The Dissertation Committee for Hugo Alberto Castellanos Certifies that this is the approved version of the following dissertation:

Sequence Stratigraphy and Tectonics of the Guantao and Minghuazhen Formations, Zhao Dong Field, Bohai Bay, Eastern China

Committee:

William L. Fisher, Supervisor

Paul Mann, Co-Supervisor

Robert H. Tatham

Ronald J. Steel

Carlos Torres-Verdin

Edgar H. Guevara

Sequence Stratigraphy and Tectonics of the Guantao and Minghuazhen Formations, Zhao Dong Field, Bohai Bay, Eastern China

by

Hugo Alberto Castellanos, B. S.

Dissertation

Presented to the Faculty of the Graduate School of

The University of Texas at Austin

in Partial Fulfillment

of the Requirements

for the Degree of

Doctor of Philosophy

The University of Texas at Austin

May, 2007

Dedication

To my wife Raquel and daughter Valeria

To my grandmother Celia

Acknowledgements

I would first like to thank my co-supervisor, Dr. Bill Fisher, for his suggestions, words of encouragement and constant support through this study. I would also like to express my gratitude to my co-supervisor Dr. Paul Mann. His dedication and guidance were always appreciated. Special thanks are due to my committee members, Dr. Robert Tatham, Dr. Ronald Steel, Dr. Carlos Torres-Verdin and Dr. Edgar Guevara for their contributions and helpful reviews.

I would like to thank Petrochina and Apache Corporation for providing the seismic and well data used in this study. Special thanks go to Alan Clare and August Lau of Apache Corporation for their long-term support of my using of these data as part of my dissertation at the University of Texas. I also want to thank Bradley Lauritsen and Claire Andrews at Apache for their technical support.

I am indebted to Khaled Fouad, Bill Ambrose, Tucker Hentz, Shinichi Sakurai, Ramon Treviño and Joseph Yeh of the Bureau of Economic Geology for their friendship and sharing their technical expertise while I was a graduate research assistant working at the Bureau of Economic Geology. It was great working with all of you. I also want to thank Emilio Garciacaro and Dr. Alejandro Escalona for many helpful discussions concerning this study.

I want to thank Jose, Romulo, Julymar, Patricia and Mary for their companionship during my time at the University of Texas at Austin.

Finally, I would like to thank my loving wife, Raquel, who has been a constant source of support in all my endeavors.

Sequence Stratigraphy and Tectonics of the Guantao and Minghuazhen Formations, Zhao Dong Field, Bohai Bay, Eastern China

Publication No._____

Hugo Alberto Castellanos, Ph.D.

The University of Texas at Austin, 2007

Supervisor: William L. Fisher

Co-Supervisor: Paul Mann

The Cenozoic tectonic evolution of the Bohai Basin in eastern China has been documented through the interpretation and integration of 8,000 km of offshore 2D seismic data, a 3D seismic volume, and 38 well logs that are tied to these reflection data. The Cenozoic stratigraphy of this basin records: 1) a late Paleocene-late Oligocene basin opening across a diffuse set of half-grabens; the widespread distribution of rifts in the Bohai Basin and adjacent areas supports a regional extension possibly related to a previously proposed rollback of the subducted Pacific plate beneath the Asian continent; 2) a late Oligocene uplift and regional erosional event marking the end of major rifting; 3) early Miocene widespread thermal subsidence manifested by a large, relatively unfaulted sag basin; and 4) middle Miocene to recent strike-slip faulting; the regional-scale "lazy-Z" map pattern of the Bohai Basin depocenter indicates the importance of right-stepping pull-apart control on the younger sag section. Initiation of strike-slip deformation in the basin is attributed to a change in the direction of the convergence

vector from WNW-ESE to E-W between the Eurasian plate and the subducting Pacific plate during early to late Miocene time.

The Miocene Guantao and Pliocene Minghuazhen Formations in Zhao Dong field, western Bohai Bay, represent a 1.7-km-thick fully continental succession deposited in a large sag basin formed during the post-rift, early Miocene and younger thermal subsidence stage of the Bohai Basin. Correlation of 38 closely spaced wells and mapping of 2D and 3D seismic data in the 280 km^2 Zhao Dong oil field allowed correlation and chronostratigraphic subdivision of these fluvial deposits into ten fieldwide and correlatable accommodation/supply cycles.

Seismic mapping, well-log correlations and total sand thickness maps estimated from impedance volumes revealed two styles of sand distribution in Zhao Dong field: channel-fill facies in the Minghuazhen Formation are intermittently and locally deposited within a background matrix of high-impedance floodplain facies. Channel-fill facies in the Guantao Formation are highly amalgamated and form areally extensive fluvial sandstone bodies that extend several hundred meters along dip and strike directions.

Table of Contents

List of Tables xv

List of Figures xvi

List of Figures xvi

CHAPTER 1 **1**

Introduction and overview of dissertation 1

CHAPTER 2 **12**

Tectonics, stratigraphy, and petroleum systems in the western offshore Bohai Basin determined from 2D and 3D offshore seismic reflection data and wells 12

2.1 INTRODUCTION 12

2.2 REGIONAL TECTONIC SETTING OF THE BOHAI BASIN 18

2.2.1 Eastern and Western Rift Groups 22

2.2.2 Significance of the Tan-Lu strike-slip fault system 22

2.3. GEOLOGIC SETTING OF THE BOHAI BASIN 26

2.3.1 Formation and evolution of the Bohai Basin and adjacent areas 26

2.3.2.1 Eocene Kongdian Formation 33

2.3.2.2 Eocene-Oligocene Shahejie Formation 33

2.3.2.3 Oligocene Dongying Formation 34

2.3.2.4 Miocene Guantao Formation 34

2.3.2.5 Pliocene Minghuazhen Formation 34

2.3.2.6 Quaternary Pingyuan Formation 35

2.4. DATABASE AND METHODOLOGY 35

2.4.1 Database 35

2.5. STRUCTURAL FRAMEWORK 36

2.5.1 Regional unconformities (megasequence boundaries) 36

2.5.1.1 Eocene megasequence boundary 1 (MB1) 38

2.5.1.2 Late Oligocene megasequence boundary 2 (MB2).....39
2.5.1.3 Pliocene – Quaternary megasequence boundary 3 39
2.5.2 Description of four megasequences in the Bohai Basin 40
2.5.2.1 Pre-rift megasequence 1 (pre-Tertiary).....40
2.5.2.2 Syn-rift megasequence 2 (late Paleocene – late Oligocene).....41
2.5.2.3 Post-rift megasequence 3 (early Miocene - Pliocene) 42
2.5.2.4 Post-rift megasequence 4 (Pliocene - Quaternary) 42
2.5.3 Cenozoic fault patterns affecting megasequences of the Bohai Basin.....43
2.5.3.1 Fault family 1: North-northeast striking faults of late Paleocene to early Eocene age 43
2.5.3.2 Fault family 2: E-W striking faults of early Eocene to late Oligocene age.....56
2.5.3.3 Fault family 3: WNW-ESE striking faults of late Miocene to recent age 56
2.5.4 Paleogene and Neogene structures formed along the Tan-Lu right-lateral strike-slip fault system.....63
2.5.4.1 Southern Tan-Lu fault in Bohai Bay (fault segment A) 63
2.5.4.2 Central Tan-Lu fault in Bohai Bay (fault segment B).....64
2.5.4.3 Northern Tan-Lu fault in Bohai Bay (fault segment C).....64
2.5.5 Tectonic interpretation of subsidence plots of wells in the Bohai Basin.....65
2.6. DISCUSSION 66
2.6.1 Main events in the geologic evolution of the Bohai Basin 66
2.6.1.1 Onset of rifting (late Paleocene – early Eocene) 71
2.6.1.2 Rifting climax (early - middle Eocene) 71
2.6.1.3 Regional erosion and post-rift thermal subsidence (late Oligocene).....72
2.6.1.4 Strike-slip deformation (late Miocene to recent).....73

2.6.2 Distinguishing the driving tectonic mechanism for Cenozoic extension in the Bohai Basin 74
2.6.2.1 Regional extension related to subduction rollback 74
2.6.2.2 Strike slip tectonism....75
2.7. PETROLEUM GEOLOGY OF THE BOHAI BASIN....75
2.7.1 Major source rocks of the Bohai Basin....75
2.7.2 Known reservoir rocks of the Bohai Basin....76
2.7.3 Known structural and stratigraphic traps of the Bohai Basin 78
2.7.4 Known hydrocarbon seals of the Bohai Basin....78
2.7.5 Main petroleum-producing regions of the Bohai Basin....79
2.8 CONCLUSIONS....92

CHAPTER 3 **94**

Sequence stratigraphy and sedimentological model of the Miocene Guantao and Pliocene Minghuazhen Formations in Zhao Dong field, Bohai Bay, eastern China 94
3.1 INTRODUCTION 94
3.2 GEOLOGIC SETTING 97
3.2.1. Tectonic and structural setting....97
3.2.2. Stratigraphy of the Zhao Dong field....98
3.3 DATABASE AND METHODOLOGY 99
3.3.1. Database used in this chapter....99
3.3.1.1 Three-dimensional seismic data....99
3.3.1.2 Well data 99
3.3.2. Methodology....100
3.3.2.1 Well log correlations....100
3.3.2.2 Seismic interpretation 107
3.4. DATA DESCRIPTION 112
3.4.1. Stratigraphic cycles – A hierarchical subdivision based on accommodation / sediment supply ratios....112
3.4.2. Orders of cyclicity....112
3.4.3. Sedimentary facies....113
3.4.3.1 Facies 1A and 1B (fluvial channel fill)....113

3.4.3.2 Facies 1C (paleosols) 114
3.4.3.3 Facies 2 (crevasse splay facies) 114
3.4.3.4 Facies 3 (floodbasin facies) 114
3.4.4 Facies associations 117
3.4.4.1 Channel-fill facies associations (FA1) 117
3.4.4.2 Point bar facies associations (FA2) 117
3.4.4.3 Crevasse splay facies associations (FA3) 119
3.4.4.4 Interdistributary facies associations (FA4) 119
3.4.5 Stratigraphic correlation and chronostratigraphic significance of turnaround points 119
3.4.5.1 Fluvial facies architecture 120
3.4.6 Seismic well tie and seismic interpretation 121
3.4.7 Amplitude extractions 122
3.4.7.1 Cycle G2 136
3.4.7.2 Cycle M5 136
3.4.7.3 Cycle M4 136
3.4.7.4 Cycle M3 137
3.4.7.5 Cycle M2 137
3.4.7.6 Cycle M1 137
3.4.7.7 Cycle M0 138
3.4.8 Subsidence analysis of Zhao Dong field 138
3.5. INTERPRETATION AND DISCUSSION 147
3.5.1 Sequence stratigraphic framework 147
3.5.1.1 Low accommodation system tract 148
3.5.1.2 High accommodation system tract 153
3.5.2 Stratigraphic forcing mechanisms 159
3.5.2.1 Eustasy 159
3.5.2.2 Climate 159
3.5.2.3 Subsidence 160
3.6 CONCLUSIONS 163

CHAPTER 4 **165**

Acoustic- and shear- impedance interpretation for fluvial sandstone distribution in the Miocene Guantao and Pliocene Minghuazhen Formations, Zhao Dong field, Bohai Bay, eastern China 165

4.1 INTRODUCTION 165

4.2 GEOLOGIC SETTING OF THE ZHAO DONG FIELD 169

4.2.1 Tectonic setting 169

4.2.2 Stratigraphy 170

4.3 DATABASE AND METHODOLOGY 171

4.3.1. Database 171

4.3.1.1 Three-dimensional seismic data 171

4.3.1.2 Well data 172

4.4 METHODOLOGY 175

4.4.1. Well log correlations 175

4.4.2. Seismic interpretation 175

4.4.3. Colored inversion 175

4.4.3.1. Extracting acoustic impedance information from available logs 176

4.5 DATA DESCRIPTION 184

4.5.1 Wire-line analysis and cross-plots 184

4.5.2 Impedance volumes 185

4.5.2.1 Impedance threshold 191

4.5.2.2 Total sand thickness maps 191

4.6 INTERPRETATION AND DISCUSSION 192

4.6.1 Architecture of reservoir sands from amplitude study 192

4.6.2 Proposed locations of new wells based on this amplitude study 196

4.6.2.1 Minghuazhen Formation 197

4.6.2.2 Guantao Formation 209

4.7 PETROLEUM GEOLOGY OF ZHAO DONG FIELD 210

4.7.1 Source rock 210

4.7.2 Reservoirs 217

4.7.3 Seal....217
4.7.4 Structural vs. stratigraphic traps....217
4.7.5 Future potential....218
4.8 CONCLUSIONS....220

CHAPTER 5 **222**

Conclusions....222
5.1 CENOZOIC TECTONIC EVOLUTION OF THE BOHAI BASIN....222
5.2 STRATIGRAPHY AND SEDIMENTOLOGY OF ZHAO DONG FIELD....223
5.3 P- AND S-IMPEDANCE SEISMIC DERIVED VOLUMES....225

References....227

Vita 242

List of Tables

Table 2.1. Summary table showing the main oil traps found in the Bohai Basin. Anticlinal and fault-related traps are the most important and common trap types in the study area. Stratigraphic traps are less important. Most of the traps occur in syn-rift and post-rift intervals although fractured and weathered pre-rift basement highs, - also known as "buried hills" by Chinese workers - also form good reservoirs in the Bohai Basin. 91

Table 3.1. Summary of the principal lithologies and facies interpretation for the five main facies associations that comprise the Guantao and Minghuazhen Formations in Zhao Dong field. 116

Table 3.2. Comparison of facies characteristics of the low- and high-accommodation system tracts in the Guantao and Minghuazhen Formations of Zhao Dong field (adapted from Catuneanu, 2006) 158

Table 3.3. Pollen assemblages identified by Yao (1994) from the Guantao and Minghuazhen Formations (climatic interpretation by O. Colmenares, personal communication, 2005). Note that there is no significant change in climatic and weathering conditions between the two formations. 162

Table 4.1 Main oil traps found in the Minghuazhen and Guantao sections of Zhao Dong field. The two main structural traps in the field are comprised by tilted-fault blocks (block C and flower structure compartments) and horst blocks (block D). 219

List of Figures

Figure 1.1 China's Oil Production and Consumption, 1986-2006 (from United States Energy Information Administration, 2007) 2
Figure 1.2 World Petroleum Consumption, 1960-2025 (from United States Energy Information Administration, International Energy Outlook, 2004).....3
Figure 1.3 Location of China's largest onshore oil producing fields. Production in Daqing and Liaohe fields has peaked, leading oil exploration activities to concentrate on developing largely untapped reserves in offshore fields in the Bohai Bay, Pearl River Delta, and South China Sea. 5
Figure 1.4. Location map showing al the data used for this study.....7
Figure 2.1. Location of the Bohai Basin and GPS velocities with respect to a fixed Eurasia plate shown in red (modified from Calais et al., 2003). In the green shaded area, from the Himalayas to the Tien Shan mountain range, the GPS vectors trend nearly north-south. Northward-directed GPS vectors show northward displacement of India and the Himalayas into Asia. In the blue shaded area, the vectors are roughly east-southeast west-northwest. These vectors show eastward and southeastward displacement of extruding continental areas of Southeast Asia in response to the India collision to the southwest. Subduction of the Pacific plate may also play a major role in the eastward motion of south and north China. The black rectangle indicates the location of figure 2.2. 14
Figure 2.2. (a) Tectonic setting of Tertiary rift basins in southeastern and northeastern China. This region is characterized by widespread Cenozoic extension and strike-slip faulting. Extension spans period from Late Cretaceous to early Oligocene and created an array of on- and offshore basins. The black rectangle indicates the location of maps shown in figures 2.4 and 2.5. Present-day convergence rates are from Northrup et al., 1995. (b) Tectonostratigraphic chart for Cenozoic basins of eastern Asia (modified from Allen et al., 1997). 16
Figure 2.3a Slab rollback model to explain Cenozoic extension of the Bohai Basin. Ye et al, (1985) proposed a two-stage extensional model to explain the Cenozoic formation of the Bohai Basin. In their model, Paleogene rifting in a WNW-ESE direction was followed by an episode of Neogene thermal subsidence that controlled less-deformed sag basins overlying the rifted section. The mechanism for two-stage rifting is generally attributed to rollback of the subducted Pacific plate beneath the Asian

continent, lithospheric extension of the overriding continental plate, and thermally-driven, regional subsidence (modified from Watson et al., 1987).....19
Figure 2.3b. Pull-apart model for the Cenozoic formation of the Bohai Basin modified from Nabelek et al. (1987). The basin is shown as a large pull-apart structure that formed at a right-step in a right-lateral shear system parallel to the east Asian continental margin during early to middle Eocene time. Smaller pull-aparts occur within the larger pull-apart basin and contribute to the overall subsidence of the basin. Regions of relative uplift can also occur as a result of either small bends in the strike-slip faults or due to the interaction between neighboring strike-slip fault. 20
Figure 2.4. Major faults, rift basins and earthquake seismicity of northeastern China. Three main actively deforming areas include: 1) the Western Rift Group; 2) the Eastern Rift Group, and 3) the active right-lateral Tan-Lu fault system. Note the intersection of faults of the Eastern Rift Group and Tan-Lu fault zone in the area of the Eocene - Oligocene rift deposits of the Bohai Basin. Recent seismicity and major structures compiled from this dissertation study, Yan et al. (1996), Allen et al. (1997) and Yang and Xu (2004). The focal mechanism solutions are compiled from Chen and Nabelek (1988) and Yang et al. (1989). 24
Figure 2.5. Surface geology of the Bohai Basin and neighboring regions (modified from Steinshouer et al., 1999). NE- and EW-striking Mesozoic folds and faults probably acted as zones of weakness for the development of later northeast- and east-striking Cenozoic faults in the Bohai Basin. The main structures relating to the Indosinian orogeny (Triassic) are characterized by northeast-striking folds and thrusts. They can be traced from east of the Taihang Mountains to the eastern part of the Yan mountains. The main structures relating to the Qinling orogeny (early Permian) are characterized by east-west-striking folds and thrusts. They can be traced from the southern Liaoning region to the eastern Tien Shan Mountains located in central Asia. 29
Figure 2.6. Stratigraphic column of the southwestern Bohai Basin. Typical well response for two of the four megasequences (MS2 and MS3) defined in the larger of the two study areas shown in Figure 2.5. Earliest rift deposits (late Paleocene deposits of the Kongdian Formation) are not present in this part of the study area. Formation names, ages and depositional environments compiled from Hu et al., (1989); Yao et al., (1994); Zhang et al., (1994); Wang Tonghe, (1995) and Allen et al., (1997). 31
Figure 2.7. Location of seismic reflection data and wells used in this study. A late 1980s regional grid of 2D seismic reflection lines (0.5-4 km spacing) cover the central part of the study area. A

2000-vintage 3D seismic survey covers the westernmost part of the study area. Seismic surveys were tied to several exploration and production wells. The heavy solid lines indicate the segments of seismic reflection profiles shown in subsequent figures. Dotted lines represent the location of seismic reflection data from Hsiao et al. (2004). Depressions or sub-basins cover unshaded areas of the Bohai Basin and are labeled in largest type; gray areas represent structural highs separating the depressions (map of depressions and highs modified from Hao et al., 2007).. Bathymetric contours are from Sundermann and Feng, 2004. Onland southern extensions of the twin traces of the Tan-Lu fault zone are from Xu, J. (1993). Trace of Taihang fault zone is compiled from Xu, J. (1993) and Hao et al. (2007). 37

Figure 2.8. A) Uninterpreted seismic line A-A' See figure 2.7 for location of line. B) Interpreted seismic line A-A'. The basin fill of the Bohai Basin in the study areas was divided into four regional unconformity bounded megasequences: 1) a pre-rift sequence of pre-Tertiary age deposited prior to the main phase of Cenozoic deformation (MS1); 2) a syn-rift sequence of early Eocene to late Oligocene age deposited during the major phase of Cenozoic deformation (MS2); and 3) two post-rift sequences of late Oligocene to Quaternary age deposited after the main phase of rifting deformation had ceased (MS3 and MS4). Circle with "x" indicates strike-slip motion with block moving away from viewer. Circle with dot indicates block moving towards viewer. 44

Figure 2.9. A) Uninterpreted seismic line B-B' See figure 2.7 for location of line. B) Interpreted seismic line B-B'. Three regional unconformities form boundaries between the four megasequences and were mapped across the study area. The megasequence boundaries correspond to: 1) the top of the pre-Tertiary "basement" (~ 43 Ma in age); 2) the top of an Oligocene sequence (~ 24.6 Ma); and 3) a late Pliocene to Quaternary regional unconformity. These megasequence boundaries are referred to as MB1, MB2 and MB3 with MB1 being the oldest boundary. 46

Figure 2.10. A) Uninterpreted seismic line C-C'. See figure 2.7 for location of line. B) Interpreted seismic line C-C'. Megasequence 1 (MS1) consists of diverse lithologies ranging in age from Archean to Mesozoic This section is normally reflection free but locally displays some well developed seismic reflections. Megasequence 2 (MS2) consists of the lacustrine and fluvio-deltaic deposits of the Eocene and Oligocene Shahejie and Dongying Formations. Seismic facies of the Shahejie Formation are generally characterized by parallel and continuous reflectors with fairly consistent amplitudes. Seismic facies of the Oligocene Dongying Formation consists mostly of sub-parallel and

discontinuous seismic reflections with variable amplitude. Megasequence 3 (MS3) consists of fluvial and lacustrine deposits of the Miocene and Pliocene Guantao and Minghuazhen Formations. Seismic facies in MS3 consists of parallel, discontinuous and variable seismic reflections. Megasequence 4 (MS4) consists of the uppermost fluvial deposits of the Pliocene Minghuazhen Formation along with loess and alluvium of the overlying Quaternary Pingyuan Formation. Megasequence 4 (MS4) consists of parallel, discontinuous and variable seismic reflections. Circle with "x" indicates strike-slip motion with block away from viewer. Circle with dot indicates block motion towards viewer. 48

Figure 2.11. A) Uninterpreted seismic line D-D'. See figure 2.7 for location of line. B) Interpreted seismic line D-D'. Megasequence 3 (MS3) was deformed by localized strike-slip faulting as shown by the presence of widespread flower structures deforming the Neogene sag section. These younger, late Neogene flower structures are commonly localized on earlier normal faults formed during Eocene to Oligocene regional extension. Circle with "x" indicates strike-slip motion with block motion away from viewer. Circle with dot indicates block motion towards viewer. 50

Figure 2.12. A) Uninterpreted seismic line E-E'. See figure 2.7 for location of seismic line. B) Interpreted seismic line E-E'. Northeast and east-striking normal faults control the distribution of major rifts in the Bohai Basin. Northeast-striking normal faults (fault family 1) are commonly restricted to the margins of the basin (e.g. Bozhong depression near the Tan-Lu fault). Normal faults extend downward into the acoustic basement and upward into Neogene and Quaternary strata and in some cases appear to cut the sea floor. East-west-striking normal faults (fault family 2) are most commonly found in the center of the Bohai Basin (e.g. Jiyang depression). Normal faults of family 2 extend downward into the basement and upward into Neogene strata. Fault family 3 consists of west-northwest-striking oblique-slip normal and reverse faults forming negative and positive flower structures, respectively. Downward, the fault strands merge near the top the Paleogene sedimentary section (MS2) and upward, they diverge and extend into Neogene and Quaternary strata and in some cases appear to cut the sea floor. Circle with "x" indicates strike-slip with block motion away from viewer. Circle with dot indicates block motion towards viewer. 52

Figure 2.13. A) Uninterpreted seismic line F-F'. See Figure 2.7 for location of seismic lines. B) Interpreted seismic line F-F. Fault family 3 consists of west-northwest-striking oblique-slip normal and reverse faults forming negative and positive flower structures,

respectively. Downward, the fault strands merge near the top the Paleogene sedimentary section (MS2) and upward, they diverge and extend into Neogene and Quaternary strata and in some cases appear to cut the sea floor. Circle with "x" indicates strike-slip displacement with block motion away from viewer. Circle with dot indicates block motion towards viewer. 54
Figure 2.14. Time structure map of MB1 (top of the pre-Tertiary "basement") with contour interval of 200 ms. MB1 represents the lower boundary of the syn-rift sequence and marks the beginning of early Cenozoic rift development in the offshore part of the Bohai Basin. Early Cenozoic basin opening occurred on a series of half-grabens with master faults striking roughly east and northeast as summarized on inset rose diagram. 57
Figure 2.15. Time structure map of MB2 (top of the Oligocene) with contour interval of 200 ms. MB2 represents the boundary between syn-rift deposits (MS2) and post-rift or sag deposits (MS3 and MS4). The MS2 surface marks the end of the main phase of Cenozoic extension. Rose diagram shows trends of strike-slip and normal faults active during this period. 58
Figure 2.16. Time structure map of MB3 (Late Miocene – early Pliocene) with contour interval of 25 ms. MB3 represents the boundary between MS3 and MS4 and its formation is related to transtensional and transpressional structures locally developed along strike slip faults including both strands of the Tan-Lu fault zone. Inset shows increase in the prevalence of northeast-striking strike-slip faults of the Tan-Lu fault zone and continued activity of east-striking normal faults. 59
Figure 2.17a. Time slice at 1643 ms level (coherency display) showing the distribution of normal faults and fault A strike-slip fault. See figure 2.7 and 2.11b for location of time slice. Colors correspond to the different megasequences exposed at this level: red = MS1; yellow = MS2 and blue = MS3. 60
Figure 2.17b. Time slice at 1273 ms level (coherency display) showing the distribution of normal faults and strike-slip fault A. See figure 2.7 and 2.11b for location of time slice. Colors correspond to the different megasequences exposed at this level: red = MS1; yellow = MS2 and blue = MS3. 61
igure 2.17c. Time slice at 758 ms level (coherency display) showing the distribution of normal faults and strike-slip fault A. See figure 2.7 and 2.11b for location. Colors correspond to the different megasequences; red = MS1; yellow = MS2 and blue = MS3. 62
Figure 2.18. Paleogene and Neogene structures of the Tan-Lu fault zone. (a) Segment A of the southern Tan-Lu fault is characterized in cross section by apparent normal faults with significant vertical separation. Most of the fault deformation occurs in Paleogene

strata where the main strand shows an eastside-down separation of about 1.2 s. (b). The central Tan-Lu fault zone in segment B is characterized by positive and negative flower structures. High-angle reverse faults associated with the positive flower structures are well developed in the Paleogene section (MS2). High-angle normal faults associated with the negative flower structures are well developed in the Neogene section (MS3). (c) Segment C of the northern Tan-Lu fault zone is characterized by a 4-km wide negative flower structure. High-angle normal faults associated with the negative flower structure are well developed in the Paleogene and Neogene sections.....67
Figure 2.19. Subsidence plots from the offshore Bohai Basin. Figure 2.19a is from this study and figures 2.19b and 2.19c are modified from Hu et al., 2001. Three main tectonic phases of basin subsidence can be identified: Phase I) an initial high rate of regional rift-related tectonic subsidence from early Eocene (~ 43 Ma) to late Oligocene; Phase II) a period of tectonic quiescence from the early Miocene until the late Miocene; and Phase III) a period of tectonic rejuvenation from the late Miocene to the present. Small differences between the subsidence histories shown on all plots are likely caused by the different geographic locations of the wells used in the subsidence calculations along with their different tectonic settings in the various depressions (rifts) and highs (intervening horst blocks) of the Bohai Basin (Figure 2.19). For example, wells used by Hu et al. (2001) in the Liaohe depression (shown on Figure 2.19c) are located on the hanging wall or downthrown blocks of normal faults. Consequently, they show an abrupt increase in the rates of tectonic subsidence resulting from the main phase of early Eocene to late Oligocene rifting. Wells in the Huanghua depression studied by Hu et al. (2001) are located on footwall or upthrown blocks of normal faults (Figures 2.11b and 2.19b). Therefore these wells record only a minor pulse of the main Eocene-Miocene subdidence event related to rifting that is better expressed from wells from the Huanghua rift.....69
Figure 2.20a. Late Paleocene-early Eocene onset of rifting in the Bohai Basin. Extension was localized on the Linqing, Jiyang, Huanghua, Jizhong and Liaohe depressions (rifts) as a result of west-northwest oblique rifting. Isopach maps are modified from Hu et al. (1989) and Yang and Xu (2004). Faults in the Liaohe depression are from Hsiao et al. (2003). 80
Figure 2.20b. Early Eocene-middle Oligocene maximum rift phase of the Bohai Basin. Rifting reached its maximum during the middle Eocene with the deposition of the Shahejie Formation in fault-bounded rifts. Half-grabens trend roughly east-west and formed as

a result of north-south oblique rifting. Isopach maps are modified from Hu et al. (1989) and Yang and Xu (2004). Inset summarizes main trends of normal faults formed during this time period.....82
Figure 2.20c. Late Oligocene tectonic evolution of the Bohai Basin. During middle to late Oligocene time, rifting began to decrease in intensity and lacustrine deposition in fault-bounded rift basins gave way to fluvial sediments of the Dongying Formation that were deposited on less faulted alluvial plains. Isopach maps are modified from Hu et al. (1989) and Yang and Xu (2004).....84
Figure 2.20d. Neogene tectonic evolution of the Bohai Basin. Late Miocene – early Pliocene marks the initiation of right-lateral strike-slip faulting across the Bohai basin. This period is characterized by the reactivation of previous rift-related normal faults as strike-slip faults and by the formation of new east-west and west-southwest-striking normal and strike-slip faults as summarized on the inset rose diagrams. Earthquakes and GPS data indicate that right-lateral strike-slip faulting continues to the present-day in a pattern consistent with the regional-scale "lazy-Z" map pattern of the Cenozoic Bohai depocenter (cf. Figure 2.4). Thick solid lines represent the present boundary of Bohai basin and Hebei Plain sediments (Chen and Nabelek, 1988). Solid circles indicate epicenters of major earthquakes (M > 6) since 1600 A.D. Recent seismicity, major structures and focal mechanism solutions are compiled Chen and Nabelek (1988), Yang et al. (1989) and Yang and Xu (2004). Faults in red are from this study. Isopach maps are modified from Hu et al. (1989) and Yang and Xu (2004). 86
Figure 2.21a. Reconstruction of Pacific - Asia plate boundary in the early Eocene about 55 Ma (courtesy of UTIG PLATES project; rates and directions of plate convergence from Northrup et al., 1995). A marked decrease in the rate of Pacific – Eurasia subduction occurred during the late Cretaceous and Paleogene, from about 120 - 140 mm/yr in the late Cretaceous to slower rates of about 30 - 40 mm/yr in Eocene time. This period of decelerating convergence correlates with a period of widespread extension along the Eastern margin of Eurasia, including the rifting that affecting the Bohai basin shown in the red boxed area. 88
Figure 2.21b. Reconstruction of Pacific - Asia plate boundary in the early to middle Miocene (courtesy of UTIG PLATES project). Note that east -west convergence occurring across the plate boundary imparts a component of right-lateral shear to the extensional deformation in the Asia continent (convergence rates from Northrup et al, 1995). 89
Figure 2.22. Location of oil and gas fields in the Bohai Basin (from Steinshouer et al., 1999). The main producing areas in the basin

are concentrated near the Yellow River delta and adjacent areas in the Jiyang Depression, the central and offshore regions of the Huanghua depression, the southeast region of the Linqing depression, the eastern portion of the Jizhong depression, the Bonan rise and neighboring regions in the Bozhong depression and the onshore and offshore portions of the Liaohe depression. Major rifts or "depressions" in Chinese literature are labeled in largest type (modified from Hao et al., 2007). Bathymetric contours are from Sundermann and Feng (2004).....90
Figure 3.1. The Zhao Dong field is located approximately 10 km offshore the western edge of the Bohai Bay, northeastern China. Depressions or sub-basins cover unshaded areas of the Bohai Basin and are labeled in largest type; gray areas represent structural highs separating the depressions (map of depressions and highs modified from Hao et al., 2007). Bathymetric contours of the seafloor of the Bohai Basin are in meters and modified from from Sundermann and Feng (2004).....96
Figure 3.2. Northwest to southeast-oriented seismic section through Zhao Dong field (western Bohai Basin). See Figure 3.14 for location of line. A major east-west-striking, rift-related normal fault of early Eocene to Miocene age, informally called "Fault A", divides the Zhao Dong field into two faulted blocks: footwall block D and hanging wall block C. Fault A was later reactivated as right-lateral strike-slip fault during the early Pliocene to recent. The basin fill (over 2-km-thick) in the Zhao Dong field can be divided into four regional-unconformity-bounded megasequences labeled on the seismic line: pre-rift megasequence 1 (MS1) of pre-Tertiary age; syn-rift megasequence 2 (MS2) of early Eocene – late Oligocene age; and post-rift megasequence 3 and 4 (MS3 and MS4) of early Miocene to recent age (MS4 is not visible in this section).....101
Figure 3.3. Stratigraphic column of the Zhao Dong field based on a representative well log response (spontaneous potential – SP and resistivity – RESD) that penetrated all three clastic megasequences shown in Figure 3.2. This figure shows the typical well response for the ten accommodation/supply (A/S) cycles identified in the study area. Red triangles pointing down on the log indicate the part of the cycle characterized by decreasing accommodation/supply conditions (taken at the bases of fluvial channels) while blue triangles pointing up depict the part of the cycle characterized by increasing accommodation/supply conditions (taken at the tops of fluvial channels). Late Paleocene – early Eocene rift-related deposits of the Kongdian Formation are not present in this part of the study area. Formation names, ages and depositional environments are compiled from Hu et al.,

(1989); Yao et al., (1994); Zhang et al., (1994); Wang Tonghe, (1995) and Allen et al., (1997). 103
Figure 3.4. Location of seismic reflection data and wells used in this study of the Zhao Dong field. A) 3D seismic data used in this chapter consists of 280 km2 two-way travel-time data recorded to 5 seconds and sampled at 4 milliseconds; bin size is 25 m. B) Time structure map of cycle M0 showing well database of 38 wells with a complete suite of well logs. Most wells are highly deviated and reach total depths at about 1600 m into Neogene channel sandstone reservoirs, which constitute the major producing reservoirs in the Zhao Dong field. Wells are concentrated on Fault A; this is an early Eocene-late Oligocene normal fault downthrown about 300 m to the north; later early Pliocene-recent right-lateral strike-slip displacement reactivated the fault and produced a strike-slip flower structure that now acts as structural trap for the Zhao Dong field. Green arrow points north C) Map view of well locations in Zhao Dong field showing their highly deviated nature from a common entry point. Red lines represent well cross-sections shown in figures 3.8, 3.9, 3.10 and 3.11. 105
Figure 3.5. Accommodation/supply (A/S) cycles. (a) In their approach, Ramon and Cross (1997) assume that the base of fluvial channels mark the initiation of increasing A/S conditions (indicated here by the base of the blue triangle that is pointing upwards) within any given cycle (modified from Ramon and Cross, 1997). (b) A counter-argument for their proposal is that the turnaround point from decreasing-to-increasing A/S conditions may actually occur higher within the fluvial channel (R. Steel, personal communication, 1997). For the interpretations shown in this chapter, I follow Ramon and Cross (1997) and select the turnaround point from decreasing-to-increasing A/S conditions to be at the bases of fluvial channels as shown in Figures 3.5c, 3.8, 3.9, 3.10 and 3.11 108
Figure 3.5c. Representative well log from the Miocene Guantao and Pliocene Minghuazhen Formations in the Zhao field showing delineation of 10 sequences in vertical sections based on the recognition of rising and falling accommodation/supply (A/S) cycles. Red triangles indicate parts of cycles inferred to represent decreasing A/S conditions while blue triangles pointing up indicate parts of cycles inferred to represent increasing A/S conditions. Yellow represents channel-fill facies. Green represents floodplain (clay and silt) facies. 110
Figure 3.6. Lateral facies relationships and comparative vertical sequences, as reflected by spontaneous potential (SP) and/or gamma ray (GR) log response of the component facies of the

fluvial systems in Zhao Dong field (modified from Galloway and Hobday, 1996): 1) Amalgamated fluvial channels; 2) channel-fill point-bar sands; 3) crevasse splays; 4) and floodbasin deposits. 115
Figure 3.7. Vertical facies associations in the Guantao and Minghuazhen Formations based on SP and GR well log responses. A) Channel-fill facies associations dominate the basal part of the Guantao Formation. This facies association commonly consists of an erosive base overlain by thin, very-coarse grained sandstone layer. They commonly display a general fining-upward grain-size distribution from coarse to fine grained sandstone, poorly to moderately sorted at the base and moderately well to well sorted at the top. These facies generally grade upward into fine to very fine grained sand with abundant kaolinite. B) Point bar facies associations consists of a scoured base overlain by a channel lag consisting of coarse grained sand. This facies associations displays a fining-upward grain-size distribution from medium- to fine-grained; moderately- to well sorted sandstone. These facies may grade upward into fine to very fine-grained sand with abundant clay that is mostly kaolinite. C) Crevasse splay facies associations are commonly preserved in the Minghuazhen Formation. Crevasse splay facies associations may show a gradual or abrupt fining-upward trend or no trend. Crevasse splay facies commonly range from 1 to 3 m in thickness and are fine to very fine-grained. See table 3.1 for legend explanation. 118
Figure 3.8. Strike well cross-section 1-1'. The turnaround points from increasing-to-decreasing and decreasing-to-increasing accommodation/supply (A/S) cycles were correlated from well to well across the Zhao Dong field and formed the basis of a 2D stratigraphic correlation framework. See figures 3.4 and 4.1 for location. 123
Figure 3.9. Strike well cross-section 2-2' showing fluvial sands in the Zhao Dong field ranging transitionally from amalgamated, multi-storied and laterally continuous sheet sandstones (Guantao Formation) to isolated fluvial sandstones encased in floodplain mudstones (Minghuazhen Formation). Gradual changes in fluvial sandstone morphology, facies, and facies successions are related to changes in tectonics and accommodation/supply conditions through time. See figures 3.4 and 4.1 for location. 125
Figure 3.10. Strike well cross-section 3-3' showing amalgamated fluvial channel sandstones in the Guantao Formation reaching up to 55 m in thickness. Channels have flat, low relief erosive bases with multiple internal scour surfaces separating individual channel bodies. Individual channel sandstones of the Minghuazhen Formation are characterized by thin, lenticular and

laterally discontinuous sand bodies encased in floodplain facies. See figures 3.4 and 4.1 for location. 127
Figure 3.11. Dip well cross-section 4-4'. Fluvial-channel sandstones of the Guantao Formation laterally and/or vertically contact one another or are separated by only a few feet of floodplain facies suggesting deposition under lower accommodation/supply (A/S) conditions (see Figure 3.5c) . Sandstone bodies in the Minghuazhen Formation are isolated within floodplain facies and show well developed splays suggesting deposition under higher accommodation/supply (A/S) conditions (see Figure 3.5c). See figures 3.4 and 4.1 for location. 129
Figure 3.12a. Uninterpreted seismic line A-A'. See figure 3.14 for location 131
Figure 3.12b. Interpreted seismic line A-A' showing the main structure of Zhao Dong field consisting of a half-graben filled by a thick early Eocene to recent non-marine clastic succession. Numerous normal faults cut the sedimentary section. Many of these faults extend downward into the pre-Tertiary "basement" and in some cases cut upwards to the seafloor. Circle with "x" indicates block motion away from viewer along right-lateral strike-slip fault A. Circle with dot indicates motion toward viewer See figure 3.14 for location. 132
Figure 3.13a. Uninterpreted seismic line B-B'. See figure 3.14 for location 134
Figure 3.13b. Interpreted seismic line B-B' showing stratigraphic cycles (reservoir intervals) in the Miocene and Pliocene Guantao and Minghuazhen Formations and main faults in Zhao Dong field. Deviated wells correspond to the well log cross section 4-4' (figure 3.11). Circle with "x" indicates block motion away from viewer. Circle with dot indicates block motion toward viewer. See figure 3.14 for location. 135
Figure 3.14. Root mean square (RMS) amplitude extraction of cycle G2 (see Figures 3.1 and 3. for location). This horizon is characterized by widespread areas of unconfined sandstone distribution throughout the Zhao Dong field. Cycle G2 is part of an interval dominated by amalgamated, multi-storied and laterally continuous sheet sandstones therefore individual fluvial channels are hardly preserved. Line A-A' is shown in Figure 312. Line B-B'is shown in Figure 3.13. 139
Figure 3.15. Root mean square (RMS) amplitude extraction of cycle M5. Cycle M5 shows depositional characteristics similar to those of cycle G2 (see Figures 3.1 and 3.4 for location). Sand-rich areas are less common and are mostly confined to the downthrown block (block C) in the field north of fault A. 140

Figure 3.16. (a) Root mean square (RMS) amplitude extraction of cycle M4 (see Figures 3.1 and 3.4 for location). (b) Cycle M4 is mostly dominated by floodplain facies. Low to moderate sinuosity channels run roughly N-S and are mostly confined to the upthrown block (block D) in the southern part of the field. A low to moderate sinuosity channel trending roughly east-west, sub-parallel to the strike of the main east-west fault (fault A) is also visible in the eastern side of block C (downthrown block). 141
Figure 3.17. (a) Root mean square (RMS) amplitude extraction of cycle M3 (see Figures 3.1 and 3.4 for location). (b) Cycle M3 is mostly dominated by floodplain facies. Low to moderate sinuosity channels run roughly N-S and are typically confined to the upthrown block of the field (block D). Small sand-rich areas are also visible in block C close to scarps formed along main east-west faults. 142
Figure 3.18. (a) Root mean square (RMS) amplitude extraction of cycle M2 (see Figures 3.1 and 3.4 for location). (b) The low to moderate sinuosity channels that run roughly N-S almost the full length of the map area in the Cycle M2 RMS amplitude extraction map are the most sharply defined river systems in the entire seismic data set. Fluvial channels are confined between broad sandstone-poor areas attributed to floodplain deposition. A prominent and widespread area of unconfined sandstone deposition in a lacustrine or alluvial fan setting is also recognized in the downthrown block of the field (block C) 143
Figure 3.19. (a) Root mean square (RMS) amplitude extraction of cycle M1 (see Figures 3.1 and 3.4 for location). (b) Cycle M1 is dominated by silty floodplain facies deposition. Weakly developed, low to moderate sinuosity fluvial channels run roughly N-S over the entire field and are confined between broad sandstone-poor areas. 144
Figure 3.20. Root mean square (RMS) amplitude extraction of cycle M0 (see Figures 3.1 and 3.4 for location). This horizon shows a significant increase in sand content. The western side of the field is characterized by broad and unconfined sandstone distribution. Floodplain facies are areally restricted and are mostly located in footwall block D and the eastern side on hanging wall block D, (see Figures 3.2 and 3.12b). 145
Figure 3.21. Subsidence analysis of Zhao Dong field based on analysis of a single exploration well penetrating the entire sedimentary sequence and top of basement (total depth 2990 m). Tectonic subsidence reflects removal of sedimentary load and compaction effects (Steckler and Watts., 1978). Bohai Basin underwent a period of slow thermal subsidence starting in late Oligocene with the deposition of the Guantao Formation in a large sag basin.

Rapid subsidence occurred during a final phase of basin development in early Pliocene during deposition of the Minghuazhen Formation. Systematic changes in the architecture of the alluvial successions between both formations reflect continuous changes in accommodation space. 146
Figure 3.22. Sedimentological model and sequence stratigraphic framework of Zhao Dong field. System tracts were recognized mainly from changes in fluvial channel stacking patterns that are shown in the well log cross sections in Figures 3.8, 3.9, 3.10 and 3.11. Systematic vertical changes in the architecture of alluvial successions clearly reflect long-term (>50 m/my) changes in accommodation space that in turn reflect changing tectonic setting and subsidence. Low accommodation system tract deposits overlying the basal sequence boundary (Guantao Formation) consist of aggrading, highly amalgamated fluvial sands deposited in alluvial plain settings. High accommodation system tract deposits (Minghuazhen Formation) consist of isolated channel-fill sandstones isolated within floodplain facies. 149
Figure 3.23. Proposed outcrop analogs from the Precambrian Karoo Basin in South Africa (from Catuneanu, 2006) of fluvial facies that are commonly found in the low- and high-accommodation system tracts in the Zhao Dong field. A) floodplain-dominated meandering stream deposits, with isolated channel fills and distal crevasse splays; B) amalgamated fluvial channel-fill; note the base of a channel scouring the top of an underlying channel-fill; C) amalgamated fluvial channel-fills. 151
Figure 3.24. (a, b) 3D perspective of the root mean square (RMS) amplitude map of cycle M2 in the Minghuazhen Formation (cf. well log section in Figure 3.5c). The sand-rich areas are represented by different tones of yellow and red (low amplitude values), whereas floodplain facies are represented by a dark gray background color (high amplitude values). Cycle M2 represents the interval of maximum accommodation/supply conditions within the Minghuazhen Formation in Zhao Dong field. Well developed non-channelized lobate amplitude anomalies in the downthrown block of the field are interpreted as fan deltas. Existing wells are concentrated along Fault A. Green arrow points to the north C) Deposition model of a fan delta in normal fault-bounded depression (modified from Evans et al., 2003).....155
Figure 3.25. Examples of shallow and deep fluvial incision and sandstone deposition (modified from Posamentier, 1999). A) Shallow fluvial incision usually forms widespread sandstone sheets of amalgamated fluvial channel-fill deposits. The base of these sheets commonly mantles a low relief regional erosion surface (cf. Minghuazhen Formation in Figures 3.5c, 3.8, 3.9,

3.10 and 3.11). B) Deep fluvial incision generally leads to narrow and deep incised valleys with high relief (modified from Posamentier, 1999). 157
Figure 4.1a. Location of Zhao Dong field (see also Figure 4.1b) and oil and gas fields in the Bohai Basin (from Steinshouer et al., 1999). The main producing areas in the basin are concentrated near the Yellow River delta and adjacent areas in the Jiyang Depression, the central and offshore regions of the Huanghua depression, the southeast region of the Linqing depression, the eastern portion of the Jizhong depression, the Bonan rise and neighboring regions in the Bozhong depression and the onshore and offshore portions of the Liaohe depression. Major rifts or "depressions" in Chinese literature are labeled in largest type (modified from Hao et al., 2007). Bathymetric contours are from Sundermann and Feng (2004). 167
168
Figure 4.1b. Depth structure map of cycle M0 showing the major faults of the Zhao Dong field. Fault A has the largest throw of the faults shown and is downthrown 300 m in a northeasterly direction. Fault A originated as a normal fault during early Eocene to late Oligocene time and was reactivated as a strike slip during late Miocene to recent time. A larger view of the faulting in the Zhao Dong field is given on Figures 2.17a, 2.17b and 2.17c. Numbered lines show locations of well-log cross sections show in figures 3.8, 3.9, 3.10 and 3.11. 168
Figure 4.2. Representative well log from the Miocene Guantao and Pliocene Minghuazhen Formations in the Zhao field showing (from left to right): 1) gamma ray (GR) log; 2) upscaled GR log; 3) spontaneous potential (SP) log; 4) upscaled SP log; 5) P-impedance trace at well location and 6) S-impedance trace at well location. Cell thickness for the upscaled logs is consistent with the vertical resolution of the impedance volumes. The vertical resolution ($\lambda/4$) of the P- and S-impedance volumes in the Minghuazhen and Guantao Formations is 17 and 21 m respectively.....173
Figure 4.3a. Acoustic impedance logs from eight exploration wells in Zhao Dong field (courtesy of August Lau). 178
Figure 4.3b Spectrum of acoustic impedance (PI). This figure shows the linear trend from the eight wells - resampled in two-way reflection time - shown in figure 4.3a. The gradient of the trend fit determines the alpha (α) value (courtesy of August Lau). 179
Figure 4.4. Mean seismic spectrum. Using the same time window as the well log analysis, sample seismic traces around all well locations were averaged to derive the mean seismic spectrum (from WesternGeco/DCS Reservoir Services, 2004).....180

Figure 4.5. Amplitude spectrum matching. The resultant amplitude spectrum obtained from the AI logs (light blue) was then used to shape the mean seismic spectrum (red). The resulting matched spectrum is shown in pink (from WesternGeco/DCS Reservoir Services, 2004). 181
Figure 4.6. Colored inversion operator. The last step in the inversion process was to apply the convolutional operator to the input seismic reflection data (from WesternGeco/DCS Reservoir Services, 2004). 182
Figure 4.7. Relative P-impedance (colored inversion) seismic section in Zhao Dong field. Sand-rich areas are represented by bright colors which in turn are inferred from low impedance values. 183
Figure 4.8a. P-impedance vs. density cross-plot in the Guantao Formation from well data. Sandy channel-fill sandstones have low P-impedance and density values while shaly floodplain facies have high P-impedance and density values. The clusters showing abnormally low P-impedance and density values represent gas bearing sands Note that oil- and water-bearing sands in both formations are indistinguishable from each other based on their P-impedance and density values. 186
Figure 4.8b. P-impedance vs. density cross-plot in the Minghuazhen Formation. Sandy channel-fill sandstones have low P-impedance and density values whereas silty floodplain facies have high P-impedance and density values. The clusters showing abnormally low P-impedance and density values represent gas bearing sands Note that oil- and water-bearing sands in both formations are indistinguishable from each other based on their P-impedance and density values. 187
Figure 4.9a. S-impedance vs. P-impedance cross-plot in the Guantao Formation (well data). Channel-fill sandstones in the Guantao Formation are characterized by low S-impedance values whereas floodplain facies are characterized by high S-impedance values. Note that oil- and water-bearing sands are indistinguishable from each other based on their S-impedance values. 188
Figure 4.9b. S-impedance vs. P-impedance cross-plot in the Minghuazhen Formation (well data). S-impedance values of the non-reservoir lithologies significantly overlap those of the reservoir sands (channel fill facies), causing uncertainty in the use of S-impedance values to predict reservoir sands in the Minghuazhen Formation. 189
Figure 4.9c. S- vs. P-impedance cross-plot in the Minghuazhen Formation (end member lithologies). When end member lithologies (channel-fill facies with Vsh < 35% and floodplain facies with Vsh > 70%) are cross-plotted we notice a clear discrimination between channel-fill facies (low S-impedance

values) and floodplain facies (high S-impedance values) in the Minghuazhen Formation based on their S-impedance values. 190
Figure 4.10a. P- vs. S-impedance cross-plot in the Minghuazhen Formation (seismic data). Using the threshold estimated from well log data (the lower one-third portion of the data distribution represent reservoir facies) the seismic-derived P- and S-impedance volumes were filtered in order to highlight and isolate reservoir bodies. 193
Figure 4.10b. P- vs. S-impedance cross-plot in the Guantao Formation (seismic data). Using the threshold estimated from well log data (the lower one-third portion of the data distribution represent reservoir facies) the seismic-derived P- and S-impedance volumes were filtered in order to highlight and isolate reservoir bodies. 194
Figure 4.11. 3D graphical representation of the filtered sand distribution corresponding to the M4 – M5 interval in the seismic data. Cell thickness of the upscaled P- and S-impedance volumes is consistent with the vertical resolution of the impedance volumes. The vertical resolution (λ4) of the P- and S-impedance volumes in the Minghuazhen and Guantao Formations is 17 and 21 m respectively. Green arrow points to the north 195
Figure 4.12. Total sand thickness map of interval M0 – M1. Sand-rich areas are represented by bright colors (low P- and S-impedance values) while floodplain (non-reservoir) facies are represented by a pink background (high P- and S-impedance values). Black dots represent well locations. The most prominent sandstone fairways in the M0 – M1 interval have already been tested and showed commercial accumulations of hydrocarbons. One additional prospect has been located in block D south. This sandstone fairway is 320 m wide and extends in a NW direction for at least 850 m. Sandstone thickness in this interval range between 17 and 30 m. 199
Figure 4.13. Total sand thickness map of interval M1 – M2. Sand-rich areas are represented by bright colors (low P- and S-impedance values) while floodplain (non-reservoir) facies are represented by a pink background (high P- and S-impedance values). Black dots represent well locations. Prospect 1 is located in the eastern side of block C. This sandstone trend is at least 470 m wide and extends northward for approximately 1340 m. Maximum sandstone thickness in this area is 22 m. Prospect 2 is located in the eastern edge of block D. This sandstone fairway (up to 28 m thick) is 250 m wide and extends in a northward direction for approximately 480 m. The last prospect is located in block D south. This fairway is 300 m wide and extends roughly E-W for about 350 m. Sandstone thickness reach up to 21 m. 201

Figure 4.14. Total sand thickness map of interval M2 – M3. Sand-rich areas are represented by bright colors (low P- and S-impedance values) while floodplain (non-reservoir) facies are represented by a pink background (high P- and S-impedance values). Black dots represent well locations. Two prospects (block C) have been identified in this interval. The first prospect is located in a sandstone fairway that runs roughly N-S. It is 250 m wide and dip-elongate, extending northward for at least 600 m. Maximum sandstone thickness is about 30 m. Prospect 2 is located in a sandstone fairway 260 m wide. It extends in a NE-SW direction for approximately 1100 m with a maximum sandstone thickness of approximately 32 m. 203
Figure 4.15. Total sand thickness map of interval M4 – M5. Sand-rich areas are represented by bright colors (low P- and S-impedance values) while floodplain (non-reservoir) facies are represented by a pink background (high P- and S-impedance values). Black dots represent well locations. This sandstone fairway is 220 m wide and extends in a NE direction for about 550 m. Maximum sandstone thickness is about 34 m. A sandstone fairway just south of prospect 1 has already been tested and showed commercial accumulations of hydrocarbons. 205
Figure 4.16. Total sand thickness map of interval M5 – G2. Sand-rich areas are represented by bright colors (low P- and S-impedance values) while floodplain (non-reservoir) facies are represented by a pink background (high P- and S-impedance values). Black dots represent well locations. One prospect (block C) has been identified in this interval. It is located in a sandstone fairway (up to 21 m thick) 500 m wide and extends in a NE direction for about 950 m. 207
Figure 4.17. Total sand thickness map of interval G2 – G3. Sand-rich areas are represented by bright colors (low P- and S-impedance values) while floodplain (non-reservoir) facies are represented by a pink background (high P- and S-impedance values). Black dots represent well locations. One prospect has been identified in this interval. The prospect is located in a sandstone fairway that runs roughly E-W in the northernmost extreme of block C. It is 450 m wide and extends for at least 1900 m. Maximum sandstone thickness in this region is about 38 m. 211
Figure 4.18. Total sand thickness map of interval G3 – G6. Sand-rich areas are represented by bright colors (low P- and S-impedance values) while floodplain (non-reservoir) facies are represented by a pink background (high P- and S-impedance values). Black dots represent well locations. Prospects 1 is located in block C, prospect 2 is located in the easternmost region of block D and prospect 3 is located in block D south. Prospect 1 is situated in a

sand prone region 450 m wide and extends for about 1800 m in an NE-SW direction. Sandstone thickness reaches up to 22 m. Prospect 2 is situated in a sandstone fairway approximately 600 m wide and extends for at least 1300 m in a NE-SW direction. Maximum sandstone thickness is 39 m. Prospect 3 is placed in a region most likely characterized by laterally continuous sheet sandstones. This area of widespread sandstone deposition is at least 1250 m wide and extends for about 2300 m in a NE-SW direction. Maximum sandstone thickness is approximately 32 m.....213

Figure 4.19. Total sand thickness map of interval G6 – G8. Sand-rich areas are represented by bright colors (low P- and S-impedance values) while floodplain (non-reservoir) facies are represented by a pink background (high P- and S-impedance values). Black dots represent well locations. Most of the sandstone fairways in this interval have already been tested and showed commercial accumulations of hydrocarbons. One additional prospect has been located in block D south. This prospect is situated in a sandstone fairway 580 m wide and extends roughly N-S for approximately 650 m. Maximum sandstone thickness is approximately 31 m.....215

CHAPTER 1

Introduction and overview of dissertation

Economic significance of the Bohai Basin. China is currently the world's second-largest consumer of oil behind the United States, and the third-largest net importer of oil after the U.S. and Japan (United States Energy Information Administration (EIA), 2007). In 2006, China consumed 7.35 million barrels of oil per day (nearly a half million barrels per day increase from 2005) while producing just about 3.8 million barrels of oil per day (Figure 1.1; United States Energy Information Administration, 2007). As a result, China's reliance on imported oil has steadily increased in recent years. China's oil import dependency level was at 47 percent in 2006, up 4.1 percentage points from 2005 (Forbes, 2007). EIA data forecasts that China's import dependency will remain high in the foreseeable future due to the country's robust economic growth. Oil consumption in the country is expected to increase 4 percent a year, and by 2025 China's oil consumption will account for 11 percent of total world consumption (Figure 1.2; United States Energy Information Administration, 2007).

As a net oil importer since 1993, China's petroleum industry is focused on meeting domestic demand. Roughly 85 percent of Chinese oil production capacity is located onshore. However China's largest onshore oil producing fields (i.e. Daqing, Liaohe) are mature and production has peaked, leading oil exploration activities to focus on developing largely untapped reserves in offshore fields in the Bohai Bay, Pearl River Delta, and South China Sea (Figure 1.3; United States Energy Information Administration, 2007). Recently, offshore oil exploration in China has been the greater focus of major oil companies. China National Offshore Oil Corporation (CNOOC) has

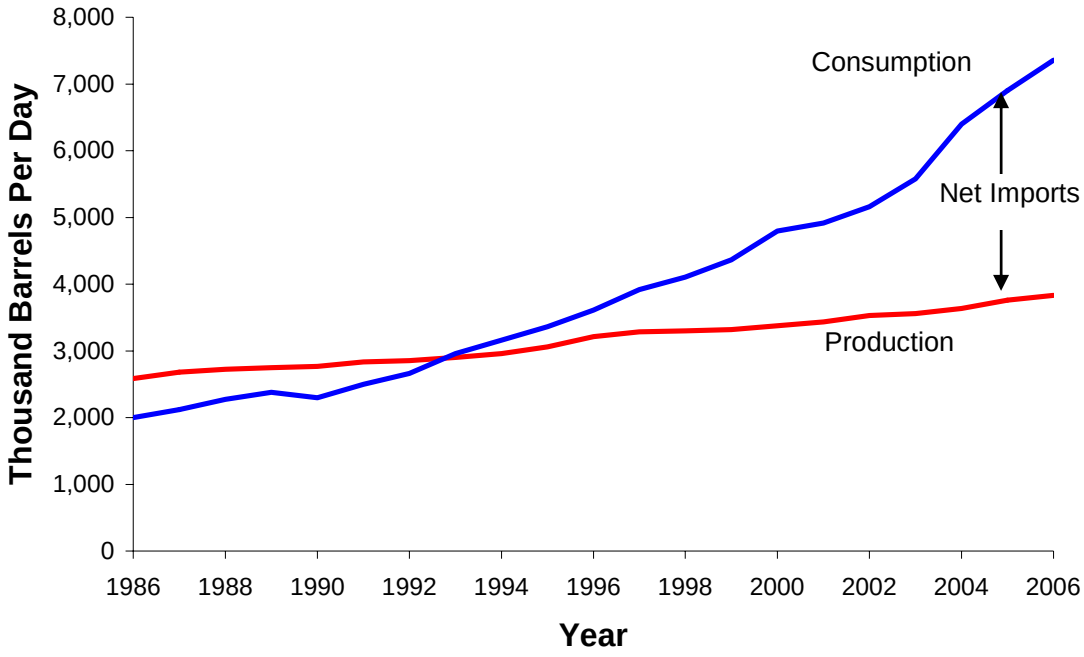

Figure 1.1 China's Oil Production and Consumption, 1986-2006 (from United States Energy Information Administration, 2007)

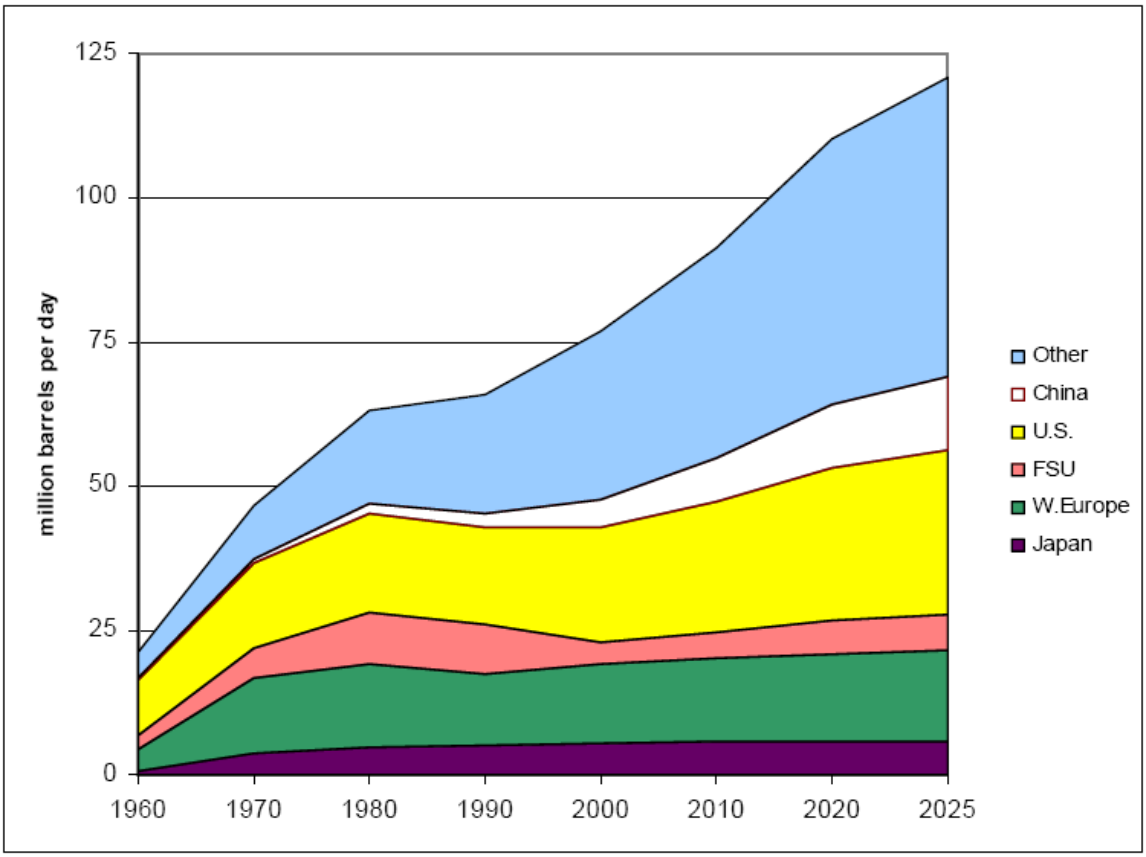

Figure 1.2 World Petroleum Consumption, 1960-2025 (from United States Energy Information Administration, International Energy Outlook, 2004)

initiated several Production Sharing Contracts with international oil companies for exploration and development in the Bohai Bay region (Figure 1.3). The Bohai Basin is currently China's third largest producing area for crude oil. As of December 31, 2005, the net proved reserves in the basin amounted to 1,044 MBOE. Average daily production in the basin is about 187,021 BOE (CNOOC Limited, 2005).

Tectonic significance of the Bohai Basin. The Cenozoic tectonic origin and evolution of the Bohai Basin has long been a source of controversy (Ye et al, 1985; Chen and Nabelek, 1988; Allen et al., 1997). The complexity and variety of tectonic events affecting this region make for a unique set of geologic and basinal parameters for which few modern basin analogs may exist. A better understanding of this important yet relatively underexplored basin is a major step towards aiding the country in meeting its future hydrocarbon demands.

Regional seismic reflection profiles tied to wells that reveal the regional character and tectonic controls on sedimentary units of the Bohai Basin have only been presented in few previous papers (Ren et al., 2002; Hsiao et al., 2004). While there are many papers by Chinese geoscientists discussing subsurface geophysical data from the Bohai Basin, the actual geophysical data is rarely included as part of their papers (Ye, 1985; Chen and Nabelek, 1988; Shanshu et al., 1992; Dongsheng et al., 2000; Zhang et al, 2004, Hu et al., 2005). This dissertation helps to address this problem of a lack of regional subsurface data from the Bohai Basin by presenting 8,000 km of offshore 2D seismic data, a 3D seismic reflection volume covering an area of 16500 km^2, and 42 wells tied to these seismic data (Figure 1.4). These data were all released by Petrochina and Apache Corporation for use in this dissertation.

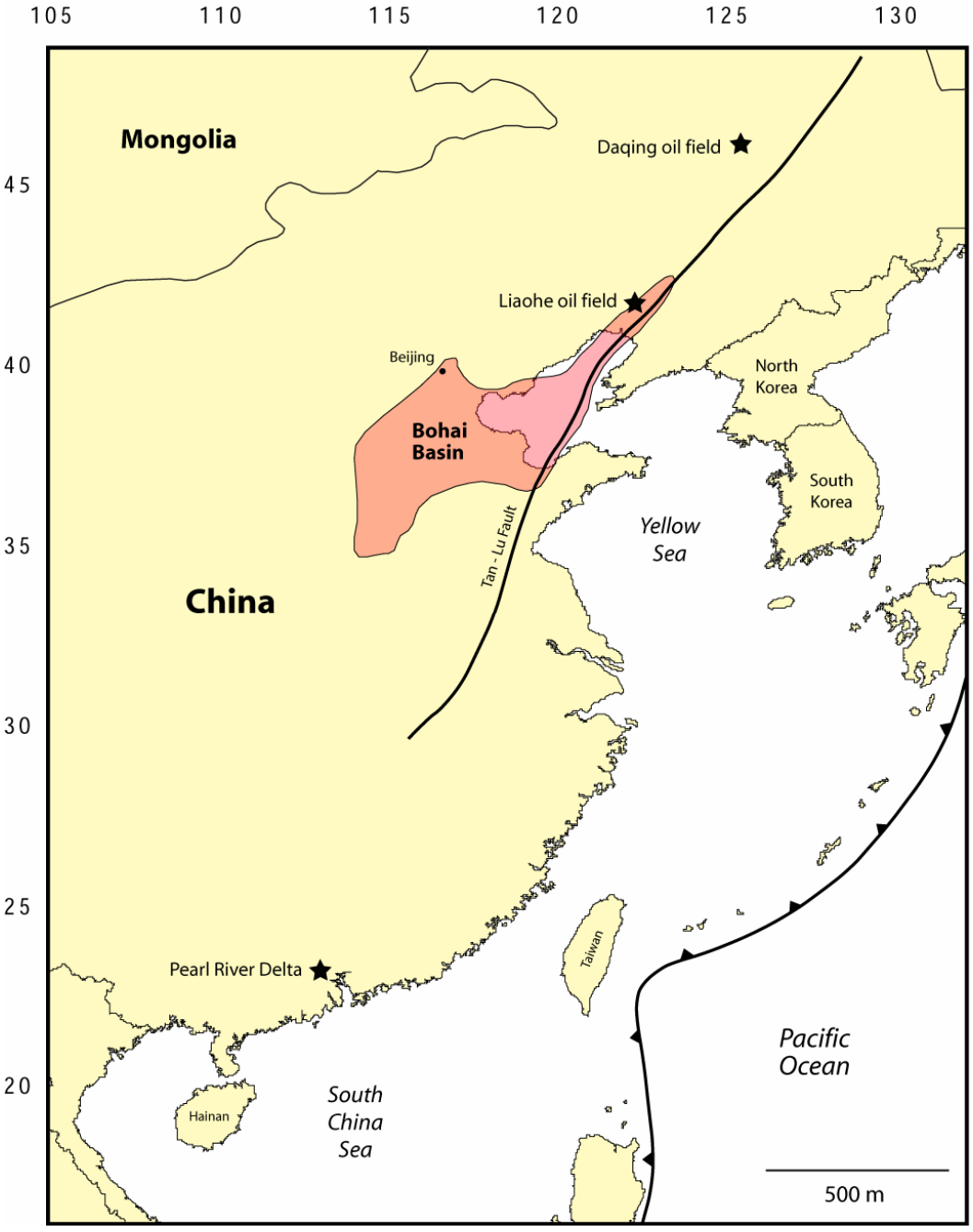

Figure 1.3 Location of China's largest onshore oil producing fields. Production in Daqing and Liaohe fields has peaked, leading oil exploration activities to concentrate on developing largely untapped reserves in offshore fields in the Bohai Bay, Pearl River Delta, and South China Sea.

Objectives of this dissertation. The main goal of my dissertation project is to document the Cenozoic stratigraphic and structural evolution of the Bohai Basin, from the plate scale to the reservoir scale using the geophysical and geologic data listed above. High-resolution sequence stratigraphy and seismic interpretation form the basis for this study. Unfortunately, data coverage is not continuous but is instead confined to two separate areas in the western part of the basin (Figure 1.4).

In order to have a better understanding of basin-wide stratigraphy and structure, I have used previously published data by Chen and Nabelek (1988); Allen et al. (1997) and Hsiao et al. (2004) in the area surrounding my study areas. I have also used the results by Li Desheng (1981); Chen and Nabelek (1988); Hu et al. (1989); Yang et al. (1989); Yan et al. (1996); Allen et al. (1997); Yang and Xu (2004) and Hao et al. (2007) in the western (onshore) part of the basin. I have also made a complete survey of the published literature from the Bohai Basin – including papers published in Chinese - and have attempted to use the most relevant results from these papers to integrate into my own observations.

Organization of this dissertation. In addition to this short introduction, this dissertation is organized into three main chapters, where each chapter considers a particular structural or stratigraphic problem at a different scale observation. The first chapter (Chapter 2) describes the basin evolution at a plate tectonic and basinal scale (>200,000 km^2), the second chapter (Chapter 3) describes how the western part of the basin (280 km^2) was infilled by continental clastic sedimentation and the last chapter (Chapter 4) focuses on geophysical imaging of reservoirs ranging in thickness from 17 to 40 m in the Zhao Dong field (50 km^2) in the western part of the basin.

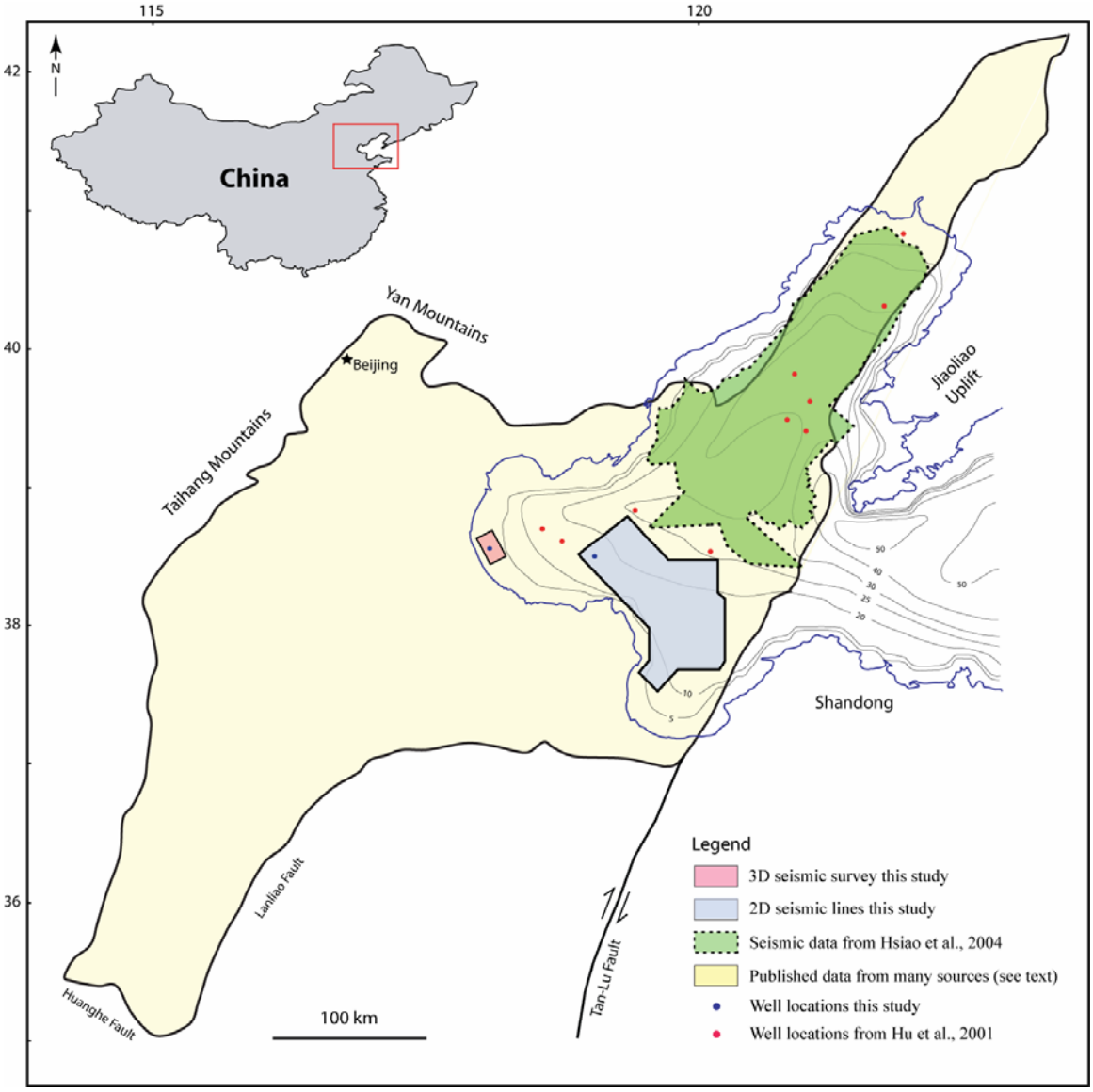

Figure 1.4. Location map showing al the data used for this study.

The three chapters that follow address these problems:

• In **Chapter Two**, I address the fundamental problem of what were the tectonic controls on the formation of the Bohai Basin. There are two ideas put forth by previous workers: Allen et al. (1997) proposed that strike-slip faulting and pull-apart basin formation was key to the basin's evolution while Ye et al. (1985) proposed that rifting without significant strike-slip faulting was the key controlling tectonic process. In order to distinguish these two models for the tectonic origin of the basin, four major unconformity-bounded megasequences were identified and mapped in the offshore region of the Bohai Basin. Thickening trends, ages and subsidence history from well data of these megasequences indicate widespread rifting in a northwest-southeast direction occurred from late Paleocene to late Oligocene. Basin opening occurred on a series of half-grabens striking from northeast to east-west. This phase of rifting ended during the late Oligocene when regional uplift and an erosional unconformity affected the basin. The Miocene to recent interval was marked by the formation of sag basins deformed by widely-spaced, northwest and roughly east-west-striking right-lateral strike-slip faults.

Given these observations a four-stage basin history is proposed: 1) late Paleocene-late Oligocene basin opening across a diffuse set of half-grabens; the widespread distribution of rifts in the Bohai Basin and adjacent plains supports a regional northwest-southeast extension possibly related to a previously proposed rollback of the Pacific plate subducted beneath the Bohai Basin (Watson et al., 1987; Northrup et al., 1995); 2) late Oligocene uplift and regional erosional event; 3) early Miocene widespread thermal subsidence; and 4) middle Miocene to recent strike-slip faulting; the regional-scale "lazy-Z" map pattern of the Bohai Basin depocenter indicates the importance of right-stepping pull-apart control on the younger sag section (Allen et al., 1997). Strike-slip deformation in the Bohai Basin is attributed to a change in the direction of the convergence vector

from west-northwest to east-west between the Eurasian plate and the subducting Pacific plate during early to late Miocene time (Northrup et al., 1995).

In summary, my work in Chapter 2 supports elements of both the rifting model and the pull-apart model. My data support the rifting origin of the basin by northwest-south extension during the period from late Paleocene to middle Oligocene. My data also support a strike-slip phase affecting the basin from middle Miocene to recent.

• In Chapter 3, I address the problem of how the Bohai Basin filled. Since the Bohai is filled by continental sedimentation that lack regional flooding surfaces and other correlative markers, the traditional approach of either eustatic sea level (Mitchum et al., 1977; Vail et al., 1977; Posamentier and Vail, 1988; Posamentier et al., 1988; Van Wagoner et al., 1988) or genetic sequences (Galloway, 1989) cannot be applied. I have adopted the approach of Ramon and Cross (1997). This methodology relies on the recognition of rising and falling accommodation/supply (A/S) cycles caused by rising or falling base level – a surface above which erosion occurs and below which deposition occurs. The turnaround points from increasing-to-decreasing and decreasing-to-increasing A/S were correlated and used to build a high-resolution chronostratigraphic framework throughout the Zhao Dong field. Applying my data to this model, I propose a new model for the filling of the western part of the basin.

The Miocene and Pliocene section in the Bohai Basin has commonly been divided into two lithostratigraphic units (Guantao and Minghuazhen Formations) based upon well logs and seismic data. In chapter three, I divide the Miocene and Pliocene section of Zhao Dong field (western Bohai Bay) into 10 (20-100 m-thick) fieldwide correlatable accommodation/supply cycles. The integrated application of fluvial sequence stratigraphic concepts with the correlation of A/S cycles on three-dimensional seismic

and well-logs have allowed a much improved understanding of reservoir architecture and connectivity within the Guantao and Minghuazhen Formations.

Guantao Formation is made up of amalgamated fluvial channels deposited under low accommodation/supply conditions while Minghuazhen Formation is characterized by isolated channel systems encased by floodplain facies deposited under high accommodation/supply conditions. The upward decrease in channel amalgamation from the basal sandstone-dominated Guantao Formation into the overlying floodplain-dominated deposits from the Minghuazhen Formation suggests a progressive increase in accommodation during deposition of this fluvial succession. This succession is interpreted as an unconformity-bounded sequence, in which the basal sandstone-dominated Guantao Formation corresponds to the low accommodation system tract of the alluvial sequence model of Dahle et al. (1997) while the upper floodplain-dominated Minghuazhen Formation represent the high accommodation system tract.

The gradual decrease in accommodation between both formations correlates with the onset of strike-slip deformation (5.1 Ma) in the Zhao Dong field that is described at a regional scale in Chapter 2. I conclude that regional tectonic subsidence and syndepositional block faulting caused by strike-slip deformation are the main controls on accommodation and stratigraphic cyclicity in the Zhao Dong field.

• In Chapter 4, I use 3D seismic data tied to wells to address the problem of imaging productive, continental sandstone reservoirs in the C and D blocks of Zhao Dong Field. Current gross production from blocks C and D is approximately 22,000 BOPD (Roc Oil Company Limited, 2007; Rigzone, 2007). The optimal development of these producing blocks requires the integration of conventional and unconventional geological and modern geophysical techniques. Accordingly, the main goal of chapter four was to apply a more robust method that more accurately delineated reservoir bodies using

multiple seismic volumes and well data. Seismic-derived P- and S-relative impedance volumes were used to image the shapes and spatial distribution of reservoir (channel-fill) facies within the Miocene Guantao and Pliocene Minghuazhen Formations in Zhao Dong field, a complex fluvial environment characterized by abrupt lateral facies changes and thin sandstone bodies that is described in detail in Chapter 3.

Total sand thickness maps estimated from P- and S-impedance volumes revealed two styles of sand distribution in Zhao Dong field: channel-fill facies in the Minghuazhen Formation appear to be intermittently and locally deposited within a background matrix of high-impedance floodplain facies. The dominant trend generally consists of narrow, confined and slightly sinuous roughly E-W and N-S oriented channel fill sandstones. Channel-fill facies in the Guantao Formation form areally extensive sandstone bodies that extend several hundred meters along dip and strike directions. Individual fluvial channels in this part of the section are hardly preserved. Geophysical imaging shows the relationship between an eroding and uplifted highland localized on a footwall block of a normal fault and subaerial channels feeding alluvial fans within a lacustrine setting on the downthrown side of the normal fault block. These images allow new prospects to be developed in the area of the sand-rich channels. Prior to this work, wells were mainly located by offsetting existing wells and there was no geologic model available to guide new prospects.

CHAPTER 2

Tectonics, stratigraphy, and petroleum systems in the western offshore Bohai Basin determined from 2D and 3D offshore seismic reflection data and wells

2.1 INTRODUCTION

Setting of the Bohai Basin. The Bohai Basin is a shallow marine embayment located in northeastern China about 200 kilometers east of Beijing (Figures 2.1 and 2.2). The basin is bounded to the east by the active, right-lateral Tan-Lu fault zone and to the west by the active, oblique-slip Taihang fault zone forming the eastern front of the Taihang Mountains (Zhang et al., 2003). The onshore extension of the Bohai Basin to the southwest is known as the Hebei Plain (Ye et al., 1987). Water depths in the Bohai basin range from less than 5 m in the coastal area of the western part to more than 30 m in the deeper eastern part of the basin (Sundermann and Feng, 2004). The delta of the Yellow River empties into the southwestern part of the basin.

The Bohai-Hebei basin covers an area of about 200,000 km^2 and forms one of a family of clastic sedimentary basins that record Cenozoic extension along the eastern margin of Asia from Viet Nam to northeastern Russia (Allen et al., 1997). Bohai Basin is currently China's third largest producing area for crude oil. As of December 31, 2005, the net proved reserves in the basin amounted to 1,044 million barrels of oil (MBOE) (CNOOC Limited, 2005). The known reservoirs of the Bohai Basin include mostly fluvial, lacustrine and deltaic sandstones of Eocene – Pliocene age (Allen et al., 1997; Yang and Xu, 2004; Kuykendall et al., 2005). The known source rocks include the

Eocene – Oligocene Shahejie Formation and the Oligocene Dongying Formation (Wang et al., 1990; Chi, 2001; Gong and Wang, 2001).

Tectonic models for the formation of the Bohai Basin. Despite extensive petroleum exploration and drilling activity in the Bohai Basin, the Cenozoic tectonic evolution of the basin remains a controversial topic in the published geologic literature (Allen, 1997). Two main deformational mechanisms have been proposed for the Cenozoic formation of the Bohai Basin. Ye et al. (1985) proposed a two-stage extensional model to explain the Cenozoic formation of the Bohai Basin. In their model, widespread Paleogene rifting in a WNW-ESE direction in the Bohai and surrounding basins (Figure 2.2a) was followed by an episode of Neogene thermal subsidence that controlled less-deformed sag basins overlying the rifted section. The mechanism for two-stage rifting is generally attributed to rollback of the subducted Pacific plate beneath the Asian continent, lithospheric extension of the overriding continental plate, and thermally-driven, regional subsidence (Watson et al., 1987)(Figure 2.3a).

Given the regional prominence of the ~3500-km-long Tan-Lu right-lateral strike-slip fault, a second model was proposed by Chen and Nabelek (1988), Schellart and Lister (2005) and Allen et al. (1997) to explain the tectonic origin of the Bohai Basin. This model invokes a more localized Cenozoic pull-apart basin formed by a right-lateral strike-slip displacement along the Taihang and Tan-Lu faults (Figure 2.3b). Earthquakes and GPS data indicate that right-lateral strike-slip faulting continues to the present-day in a pattern consistent with the regional-scale "lazy-Z" map pattern of the Cenozoic Bohai depocenter between the Taihang and Tan-Lu faults (Mann et al., 1983). Allen et al. (1997) propose that the subsurface of the large pull-apart structure contains diffuse, sub-parallel strike-slip faults offset by smaller-scale, intrabasinal pull-apart basins and localized convergent areas (Figure 2.3b).

Figure. 2.1. Location of the Bohai Basin and GPS velocities with respect to a fixed Eurasia plate shown in red (modified from Calais et al., 2003). In the green shaded area, from the Himalayas to the Tien Shan mountain range, the GPS vectors trend nearly north-south. Northward-directed GPS vectors show northward displacement of India and the Himalayas into Asia. In the blue shaded area, the vectors are roughly east-southeast west-northwest. These vectors show eastward and southeastward displacement of extruding continental areas of Southeast Asia in response to the India collision to the southwest. Subduction of the Pacific plate may also play a major role in the eastward motion of south and north China. The black rectangle indicates the location of figure 2.2.

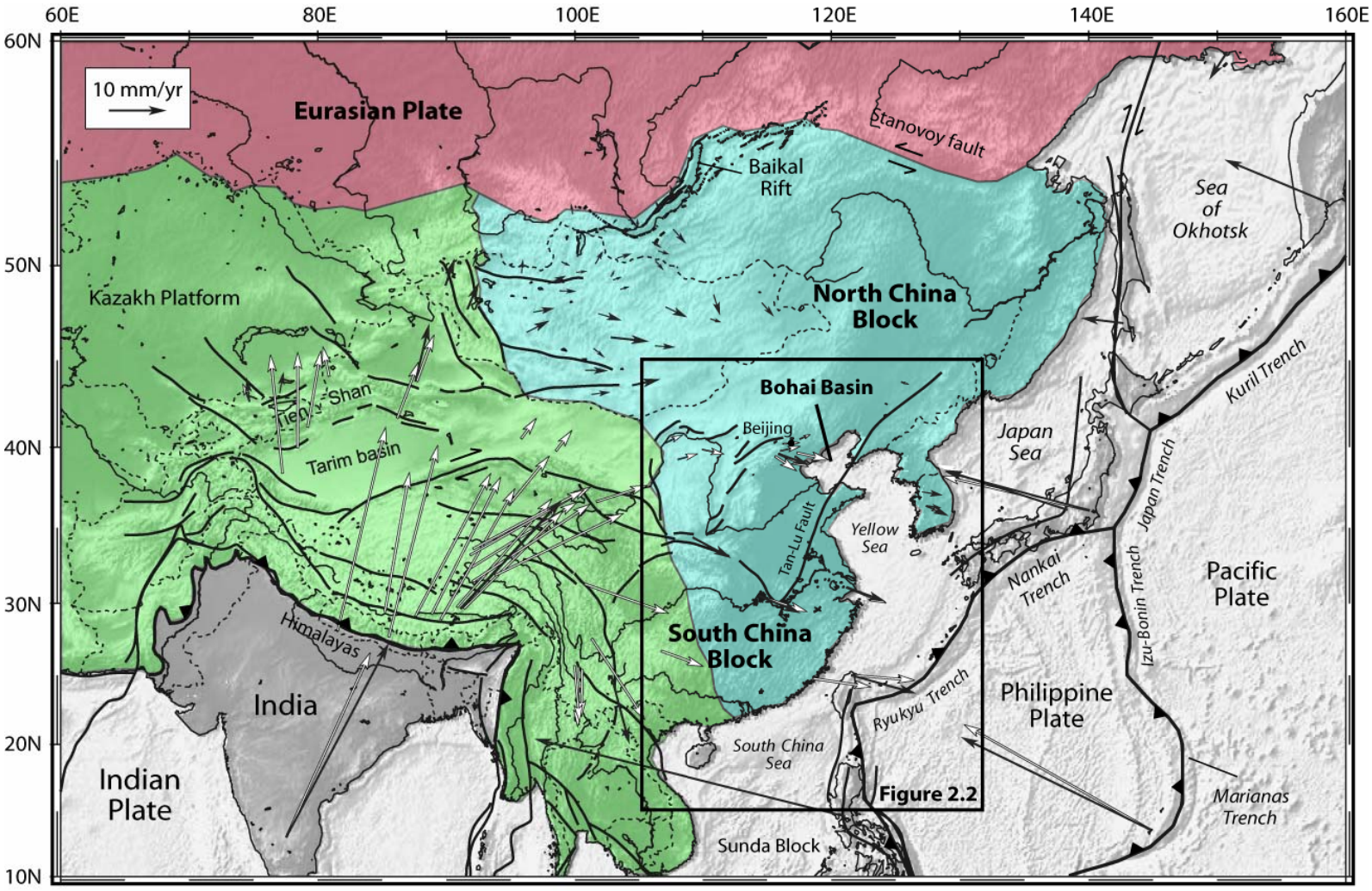
60E
80E
100E
120E
140E
160E
60N
50N
40N
30N
20N
10N
10 mm/yr
Eurasian Plate
Stanovoy fault
Baikal Rift
Sea of Okhotsk
Kazakh Platform
North China Block
Bohai Basin
Beijing
Tien Shan
Tarim basin
Japan Sea
Kuril Trench
Japan Trench
Yellow Sea
Tan-Lu Fault
Nankai Trench
Pacific Plate
Izu-Bonin Trench
South China Block
Himalayas
India
Philippine Plate
Ryukyu Trench
South China Sea
Figure 2.2
Indian Plate
Marianas Trench
Sunda Block

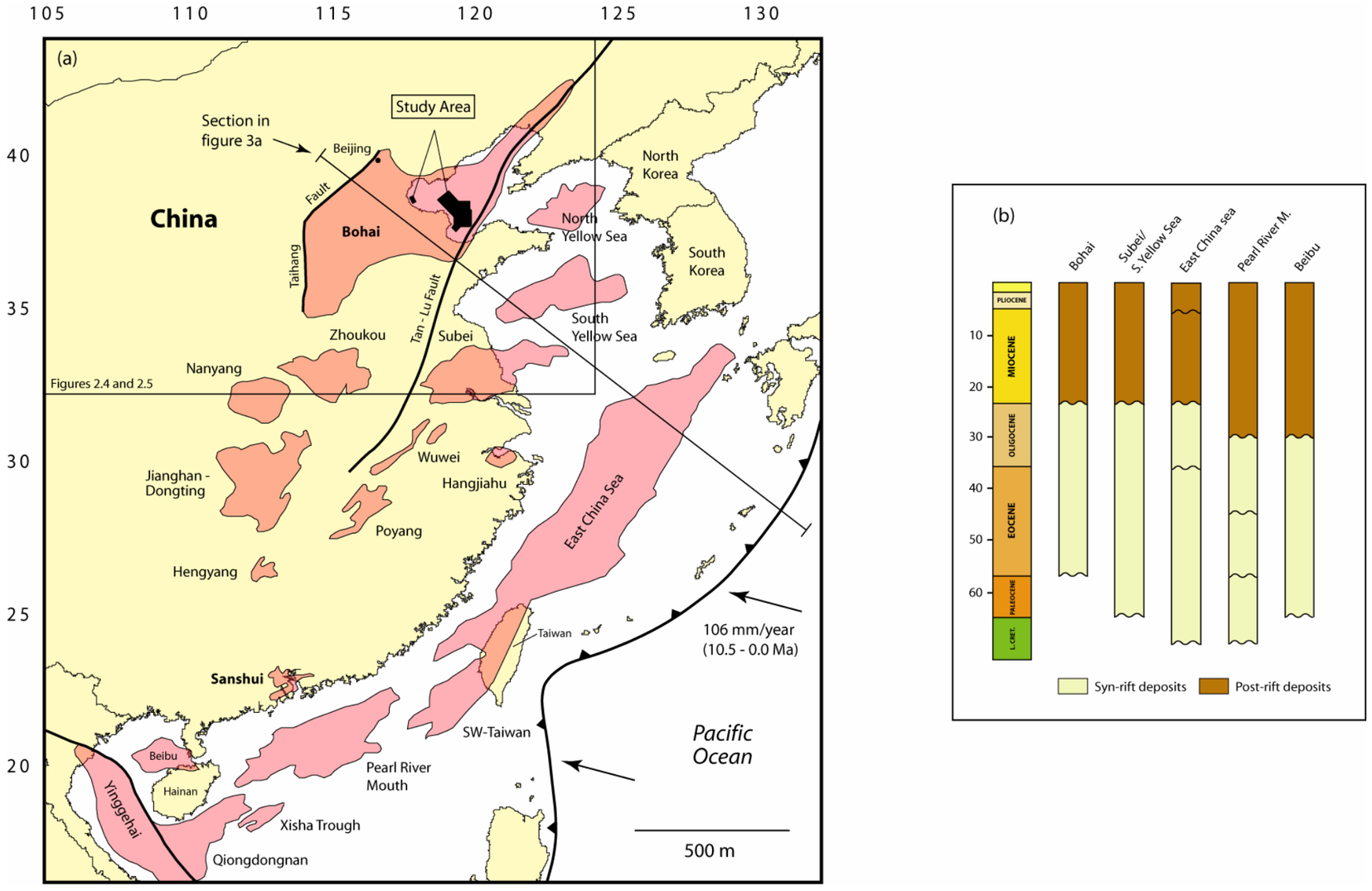

Figure 2.2. (a) Tectonic setting of Tertiary rift basins in southeastern and northeastern China. This region is characterized by widespread Cenozoic extension and strike-slip faulting. Extension spans period from Late Cretaceous to early Oligocene and created an array of on- and offshore basins. The black rectangle indicates the location of maps shown in figures 2.4 and 2.5. Present-day convergence rates are from Northrup et al., 1995. (b) Tectonostratigraphic chart for Cenozoic basins of eastern Asia (modified from Allen et al., 1997).

Each of these two classes of tectonic models has different implications for the geologic structure and stratigraphy of the Bohai Basin. For instance, longitudinal sides of pull-apart basins are predicted to be controlled by sub-parallel strike-slip faults (Mann et al., 1983; Allen et al., 1997) (Figure 2.3b). Basin-transverse faults are predicted to be dominantly normal faults that lengthen the basin with increasing strike–slip displacement along the "master" strike–slip faults (Mann et al., 1983; McClay and Dooley, 1995; Escalona and Mann, 2003). Smaller pull-aparts may occur within the larger pull-apart basin (Figure 2.3b). These smaller pull-aparts are localized depocenters but are thought to collectively contribute to the overall subsidence of the larger pull-apart basin that encloses them (Allen et al., 1997).

On the other hand, rift basins, predicted in the tectonic model by Ye et al. (1985), are defined by segmented border fault systems trending sub-parallel to the rift axis of the larger basin. Intra-rift fault systems generally form sub-perpendicular to the overall direction of extension and control distinct depocenters or sub-basins. Sub-basins are frequently elongated and less areally restricted than more localized pull-apart basins in strike-slip systems (McClay et al, 2002).

Objectives of this chapter. The objective of this chapter is to distinguish between the two alternative tectonic models for the Bohai Basin (Figures 2.3a and 2.3b) by interpreting a large amount of new subsurface 2D and 3D seismic reflection data along with 42 wells that have not previously been publicly available (Figure 2.7). I used these data, along with the results of previously published results from other workers (Li Desheng, 1981; Chen and Nabelek, 1988; Hu et al., 1989; Yang et al., 1989; Yan et al., 1996; Allen et al., 1997; 1998; Ren et al., 2002; Yang and Xu, 2004; Hsiao et al., 2004; and Hao et al., 2007), to accomplish the following objectives:

1. Establish the structural framework of the Cenozoic Bohai Basin by analyzing four seismic units or megasequences in terms of fault-patterns, depositional facies, estimated ages and the control on major depocenters.
2. Integrate subsidence analysis of one well from my data set with ten wells studied by Hu et al. (2001) in adjacent areas. These subsidence data are used to delineate major tectonic stages in the evolution of the basin.
3. Use all of the above observations to determine which basin-forming mechanism (pull-apart vs. rifting) best fits observations from the seismic reflection and well subsidence data.

2.2 REGIONAL TECTONIC SETTING OF THE BOHAI BASIN

Regional deformation of eastern Asia. Eastern Asia is characterized by widespread effects of Cenozoic extensional and strike-slip deformation (Schellart and Lister, 2005; Allen et al., 1997). Extensional and strike-slip deformation spans the period from Late Cretaceous to early Oligocene and created a diffuse array of onshore basins (Hengyang, Poyang, Jianghan-Dongting, Nanyang, Zhoukou, Wuwei, Subei, Bohai – Allen et al., 1997; Schellart and Lister, 2005) as well as offshore basins (Yinggehai, Qiongdongnan, Beibu, Pearl River Mouth, East China Sea, South Yellow Sea, North Yellow Sea – Allen et al., 1997; Schellart and Lister, 2005) (Figure 2.2a). In eastern Asia, the age of initial extension becomes progressively younger from east to west: Late Cretaceous in the East China Sea (Ren et al., 2002), Paleocene in the Subei/South Yellow Sea Basin (Ren et al., 2002) and Paleocene-Eocene in the Bohai Basin (Allen et al., 1997; Ren et al., 2002).

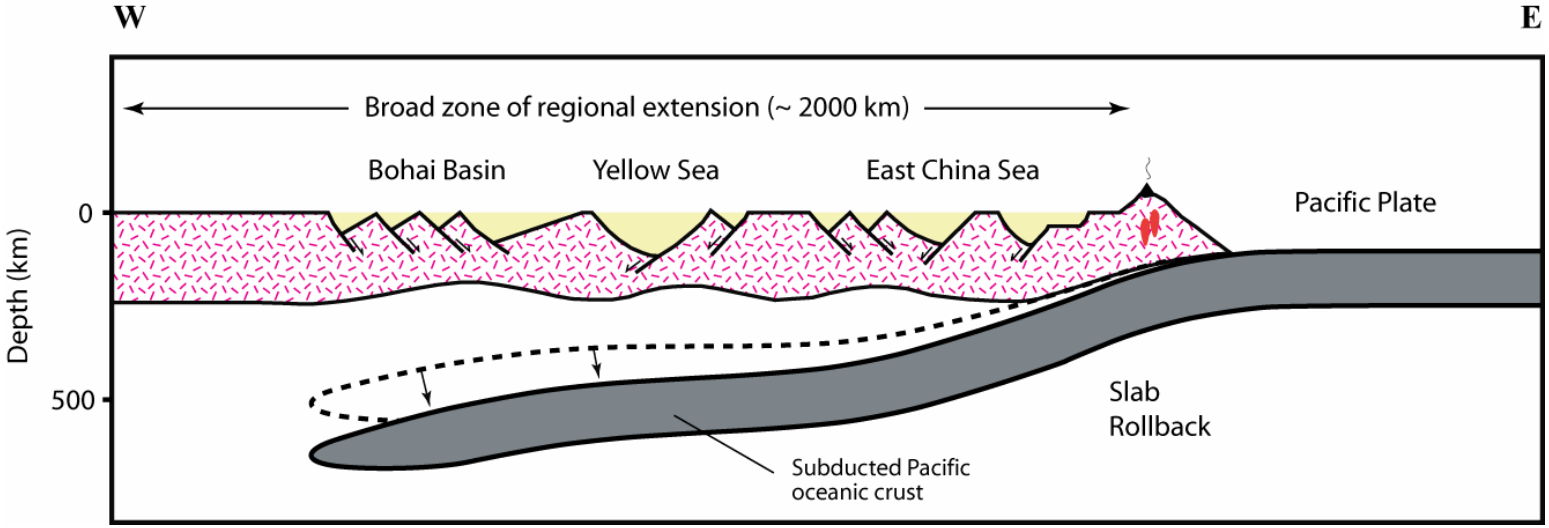

Figure 2.3a Slab rollback model to explain Cenozoic extension of the Bohai Basin. Ye et al, (1985) proposed a two-stage extensional model to explain the Cenozoic formation of the Bohai Basin. In their model, Paleogene rifting in a WNW-ESE direction was followed by an episode of Neogene thermal subsidence that controlled less-deformed sag basins overlying the rifted section. The mechanism for two-stage rifting is generally attributed to rollback of the subducted Pacific plate beneath the Asian continent, lithospheric extension of the overriding continental plate, and thermally-driven, regional subsidence (modified from Watson et al., 1987).

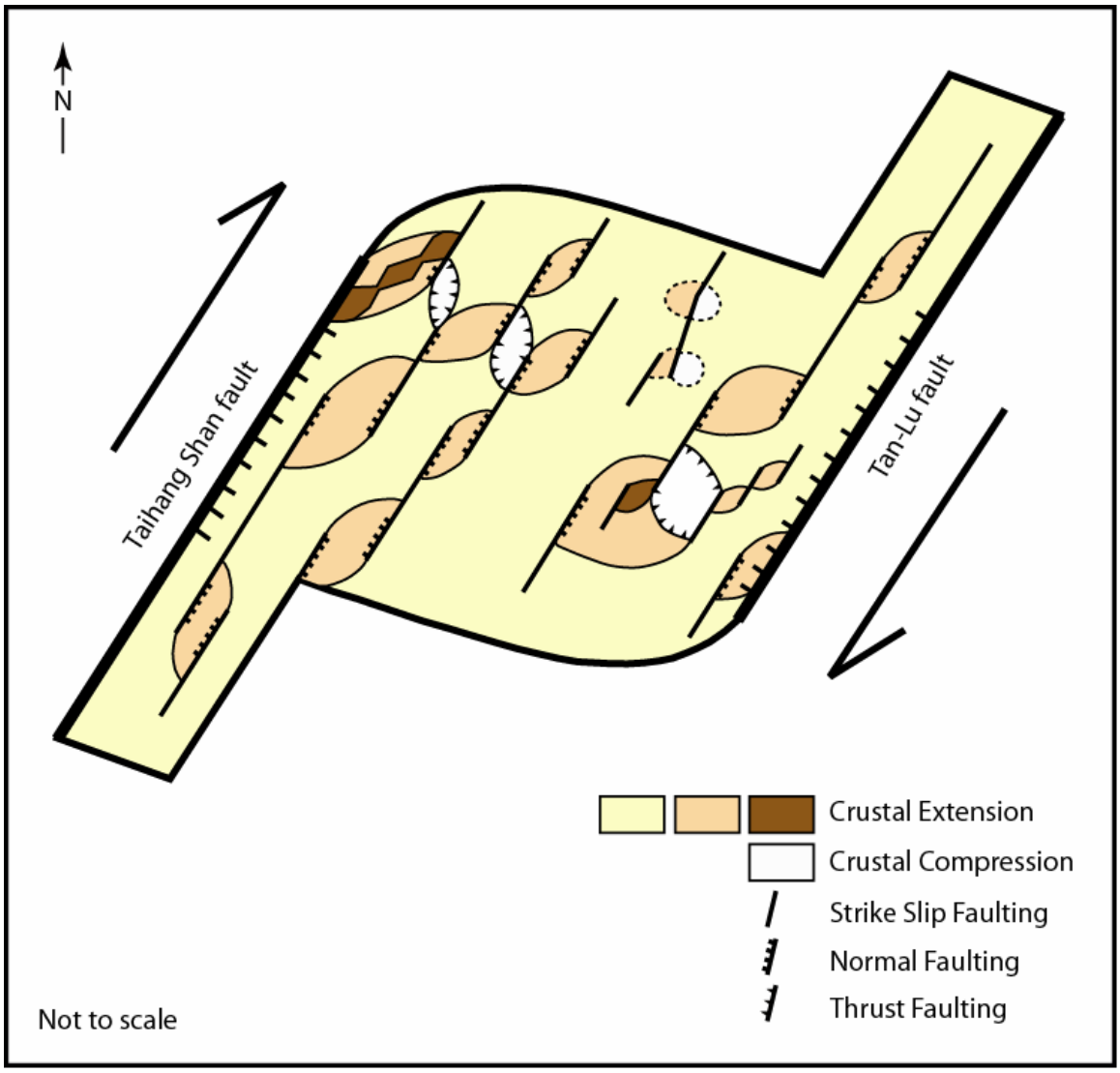

Figure 2.3b. Pull-apart model for the Cenozoic formation of the Bohai Basin modified from Nabelek et al. (1987). The basin is shown as a large pull-apart structure that formed at a right-step in a right-lateral shear system parallel to the east Asian continental margin during early to middle Eocene time. Smaller pull-aparts occur within the larger pull-apart basin and contribute to the overall subsidence of the basin. Regions of relative uplift can also occur as a result of either small bends in the strike-slip faults or due to the interaction between neighboring strike-slip fault.

Extrusion tectonics. A common tectonic model found in the literature to explain Cenozoic deformation in East Asia is the extrusion model (Molnar and Tapponnier, 1975; Tapponnier et al., 1982)(Figure 2.1). In the extrusion model, deformation is characterized by the eastward extrusion of large-scale lithospheric blocks as a consequence of the progressive India–Eurasia collision thought by most workers to have initiated in Eocene time (Searle et al., 1987; Rowley, 1996; Weinberg and Dunlap, 2000). However, GPS-derived velocities in Asia (Calais et al., 2003) show that the Bohai Basin is located in a part of eastern China where the eastward and southeastward displacement of escaping wedges related to the India - Eurasia collision is not actively occurring (Figure 2.1).

Subduction rollback. GPS observations summarized on the map in Figure 2.1 suggest that subduction rollback along the East Asian subduction zone (Schellart and Lister, 2005) may play a more important role than extrusion for the Cenozoic deformation for the area of eastern China that includes the Bohai Basin (Figure 2.2). Subducted slabs retreat or "rollback" as a consequence of their gravitational sinking into the mantle (Elsasser, 1971; Schellart, 2004). Such sinking is caused by the negative buoyancy of the slab with respect to the surrounding mantle (Elsasser, 1971; Molnar and Atwater, 1978; Schellart, 2004). Progressive retreat or rollback of the sinking slab produces a regional extension of the overriding plate in the direction of the retreating subduction hinge. The potential energy difference between the overriding plate and the retreating subducted plate causes the overriding plate to expand into the space created by the retreating subducting hinge (Lonergan and White 1997; Schellart et al., 2002; Schellart and Lister, 2004; Schellart and Lister, 2005).

2.2.1 Eastern and Western Rift Groups

Crustal extension since Eocene time has fragmented the North China block (Figure 2.1) into two diffuse extensional domains: the Eastern Rift Group and the Western Rift Group (Ye et al., 1987) (Figure 2.4). The Eastern Rift Group is located east of the Taihang Mountains and includes the North China Basin Rift System (Bohai Basin and Hebei Plain) and the Hehuai Rift Systems (now covered by younger sediments of the Hehuai Plain).

The Western Rift Group is located west of the Taihang Mountains and includes two rift systems: the Shaanxi-Shanxi and Yingchuan-Hetao rift systems (Figure 2.4). Each rift group unit has a distinct geological history and present-day morphology (Ye et al., 1987). Rifting in the Eastern Rift Group began in late Paleocene – early Eocene time and culminated in the late Oligocene (Ye et al., 1987; Xu et al., 1992). In comparison, extension in the Western Rift Group has been intermittently active since the late Eocene – early Oligocene, with a major phase of extension occurring during Neogene and Quaternary times (Ye et al., 1987; Xu et al., 1992). One of the objectives of this dissertation is to better define the timing of rifting and other major tectonic events in the Bohai Basin segment of the Eastern Rift group.

2.2.2 Significance of the Tan-Lu strike-slip fault system

The north-northeast-striking Tan-Lu right-lateral strike-slip fault zone is one of the most prominent structural features of the eastern Asian landscape (Zhang et al., 2003; Hsiao et al., 2004) (Figures 2.4 and 2.5). The fault is mapped for 3500 km from southern China, to the northeast across the eastern margin of the Bohai Basin, and as far north as eastern Siberia (Zhang et al., 2003; Hsiao et al., 2004). The exact timing of the initiation of strike-slip displacement along the Tan-Lu fault is a controversial topic in the published

literature, although there is general agreement that the fault initiated as a consequence of continent-continent collision between the North and South China Blocks (Qinlig orogeny) during early Permian to early Jurassic times (Okay and Sengor, 1992; Yin and Nie, 1993; Wan and Zhu, 1996; Wang et al., 1998; Carter et al., 2001).

During the middle Mesozoic the sense of the fault was left-lateral (Okay and Sengor, 1992; Xu, 1993; Xu, 1993; Hsiao et al., 2004). The left-lateral movement along the fault is thought to have continued during the Jurassic and Early Cretaceous with a net left-lateral displacement of about 700 – 800 km (Xu et al., 1987; Okay and Sengor, 1992; Xu, 1993). This slip direction is primarily constrained by the 700 km left-lateral offset between the Qinling-Dabie and Sulu ultra-high pressure metamorphic belts on opposite sides of the Tan-Lu fault zone (Xu et al., 1987; Okay and Sengor, 1992; Xu, 1993).

The Tan-Lu fault system was quiescent from the middle Cretaceous to the beginning of the Cenozoic (Gilder et al., 1999). However, since the early Tertiary, the Tan-Lu fault has exhibited renewed right-lateral displacement (about 40 km) within an overall extensional environment (Xu, 1993; Hsiao et al., 2004; Zhu et al., 2005). Frequent earthquakes and deformation on Quaternary strata along the fault demonstrate continued right-lateral displacement of the Tan-Lu fault (Figure 2.4). However, geodetic studies using the global positioning system (GPS) over a 4-year period have been unable to detect measurable right-lateral slip along the Tan-Lu fault, although it's possible that fault motion is episodic or occurring at a slow rate within the error of the GPS measurements (Li et al., 1998; Hsiao et al., 2004).

Figure 2.4. Major faults, rift basins and earthquake seismicity of northeastern China. Three main actively deforming areas include: 1) the Western Rift Group; 2) the Eastern Rift Group, and 3) the active right-lateral Tan-Lu fault system. Note the intersection of faults of the Eastern Rift Group and Tan-Lu fault zone in the area of the Eocene - Oligocene rift deposits of the Bohai Basin. Recent seismicity and major structures compiled from this dissertation study, Yan et al. (1996), Allen et al. (1997) and Yang and Xu (2004). The focal mechanism solutions are compiled from Chen and Nabelek (1988) and Yang et al. (1989).

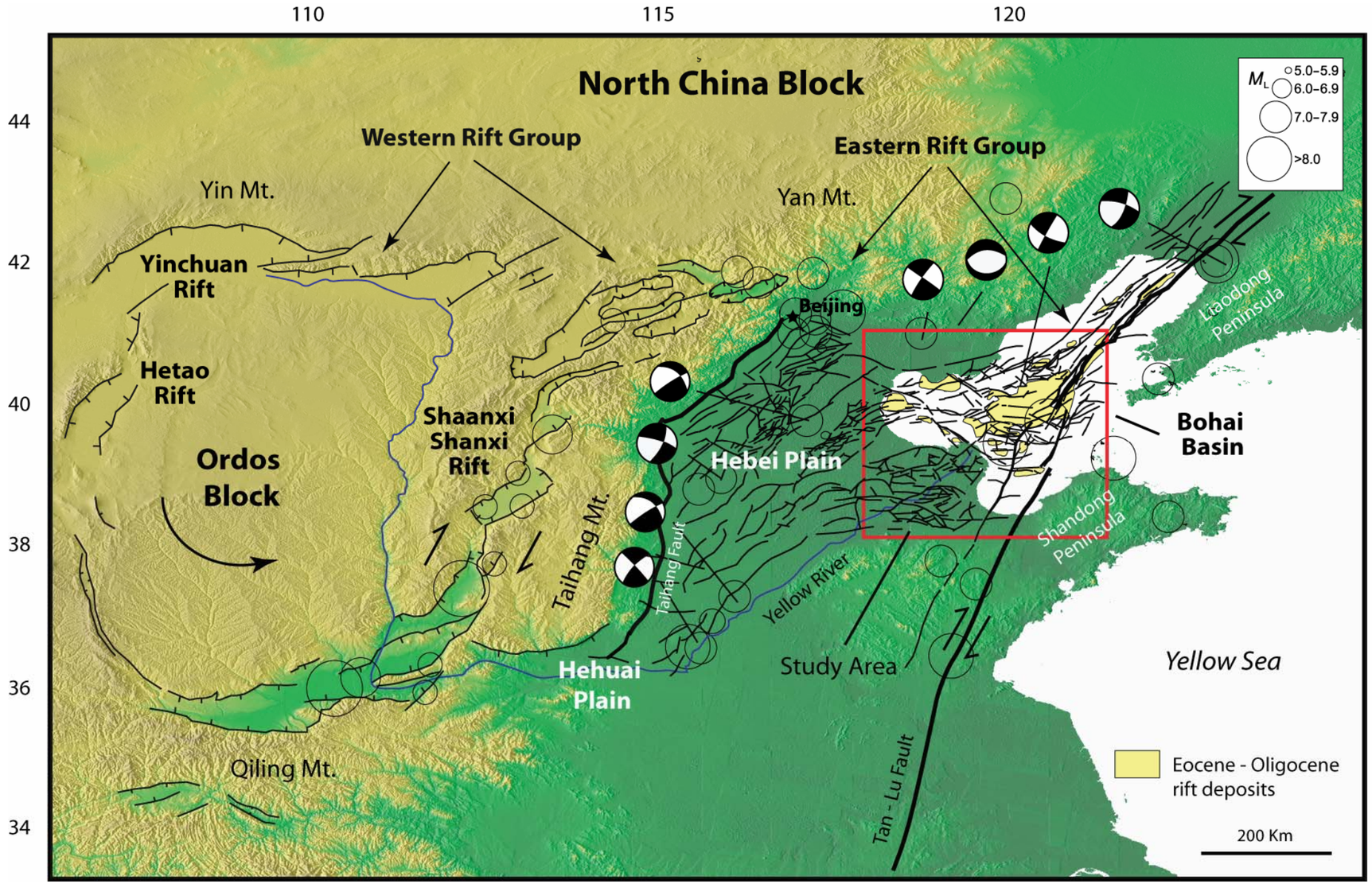
110
115
120
44
42
40
38
36
34
North China Block
Western Rift Group
Eastern Rift Group
Yin Mt.
Yan Mt.
Yinchuan Rift
Hetao Rift
Ordos Block
Shaanxi Shanxi Rift
Taihang Mt.
Taihang Fault
Hebei Plain
Beijing
Liaodong Peninsula
Bohai Basin
Shandong Peninsula
Yellow River
Study Area
Yellow Sea
Hehuai Plain
Qiling Mt.
Tan - Lu Fault
M_L
5.0–5.9
6.0–6.9
7.0–7.9
>8.0
Eocene - Oligocene rift deposits
200 Km

Figure 2.4

2.3. GEOLOGIC SETTING OF THE BOHAI BASIN

2.3.1 Formation and evolution of the Bohai Basin and adjacent areas

Proterozoic cratonic and cover rocks. The crystalline basement in mountain ranges adjacent to and underlying the Bohai Basin consists of Archean to Middle Proterozoic metamorphic rocks of the North China Craton (Hu et al., 1989; Zhai et al., 2005)(Figure 2.5). These rocks crop out extensively and constitute the metamorphic basement making up the North China continental block (Figure 2.1). Proterozoic, Paleozoic and younger rock sequences partially cover this older basement complex (Hu et al., 1989; Zhai et al., 2005). During the middle and late Proterozoic, several intracratonic basins were established over a vast area stretching from Beijing to the Shandong and Liaodong Peninsulas (Hu et al., 1989). Subsidence was rapid, with a maximum sedimentary thickness of approximately 10 km. Early sediments were dominated by clastic rocks, later grading to marine carbonate rocks (Huang, 1978; Li, 1981; Hu et al., 1989; Fletcher et al., 1995).

During the Paleozoic, the North China block was part of the stable Asian craton. In lower Cambrian to middle Ordovician time, the area was submerged beneath a shallow marine and tropical basin and received up to 1.5 km of carbonate sedimentation (Ye et al., 1985; Hu et al., 1989). Upper Ordovician to Lower Carboniferous sediments are absent, probably as the result of regional uplift and widespread erosion (Hu et al., 1989). Middle Carboniferous to Permian deposits are mainly composed of clastic sediments with thicknesses varying between 200 – 400 m (Ye et al., 1985; Hu et al., 1989).

Qinling orogeny. The diachronous collision (Qinling orogeny) between the North and South China blocks began by indentation of the northeastern South China

block into the eastern North China block during the early Permian (Yin and Nie, 1993). The collision occurred along the Qinling-Dabie-Sulu suture zone south of the study area. The main structures relating to the Qinling orogeny are characterized by east-west-striking folds and thrusts. They can be traced from the southern Liaoning region to the eastern Tien Mountains (Yin and Nie, 1996; Chen, 1998; Wang et al., 2005)(Figures 2.1 and 2.5).

Indosinian orogeny. In the Triassic, the northern part of the North China Platform was uplifted by the effects of the collision (Indosinian orogeny) between the Indochina and South China blocks. The main structures relating to the Indosinian orogeny are characterized by NE-SW striking folds and thrusts. They can be traced from east of the Taihang mountains to the eastern part of the Yan mountains region north of Beijing (Hu et al., 1989; Chung et al., 1999; Lan et al., 2003)(Figure 2.5).

Early Mesozoic rifting. Following the Indosinian orogeny in early Jurassic, the North China Platform began to deform probably as the result of the effects of Pacific plate convergence (Hu et al., 1989). The passive continental margin of the Paleozoic was transformed to an active continental margin by early Mesozoic time (Lingzhi, 1983). Intensive block faulting and magmatism led to the formation of extensive faulted depressions, controlled by northeast-southwest-striking, basement-involved normal faults (Hu et al., 1989). Varying thicknesses of terrestrial sediments were deposited in newly-formed grabens (Hu et al., 1989). Finally, the late Jurassic-early Cretaceous Yanshanian Orogeny marked the cessation of Mesozoic rifting. Regional uplift led to extensive erosion in North China resulting in the formation of a vast eroded plain (Ma et al., 1982; Ye et al., 1985; Hu et al., 1989). NE- and EW-striking Mesozoic folds and faults acted as zones of weakness for the development of NE- and EW-striking Cenozoic structures in the Bohai Basin (Ma et al., 1982; Ye et al., 1985; Wang and Tonghe; 1995)(Figure 2.5).

Cenozoic extension. Beginning in the late Cretaceous – early Oligocene, East Asia underwent a period of widespread Cenozoic extension (Allen et al., 1997; 1998; Yang and Xu, 2004). Eocene – Oligocene marks the period of highest subsidence in the Bohai Basin (Hu et al., 2001). Up to 10 km of continental clastic sediments were deposited in northeast striking faulted depressions (Hu et al., 1989; Allen et al., 1997; Hsiao et al., 2004)(Figure 2.6). Almost all the rifts or "depressions" – as they are called in the Chinese geologic literature - were formed during this period. Each depression in the basin had its own sedimentary system that was isolated from the surrounding depressions (Hu et al., 1989; Allen et al., 1997; Yang and Xu, 2004).

Major faulting culminated in the Bohai Basin by the end of the Oligocene. Regional denudation of the basin at the end of the Oligocene was followed by more uniform and less fault-controlled Neogene sedimentation. Neogene sediments form a thick, widespread blanket or sag basin of continental clastic deposits that are up to 3 km thick in the central part of the basin (Figure 2.6).

Late Tertiary and Quaternary sedimentation. The youngest clastic sediments of the Bohai Basin range between 4,000 and 10,000 m thick and are dominated by alluvial, fluvial, deltaic and lacustrine deposits (Hu et al., 1989; Allen et al., 1997; Yang and Xu, 2004). Tertiary clastic stratigraphy in the basin consists of the Paleogene Kongdian Formation that is present mostly onshore. The following clastic formations are mainly present offshore: Paleogene Shahejie and Dongying Formations, and Neogene Guantao and Minghuazhen Formations (Hu et al., 1989; Allen et al., 1997; Yang and Xu, 2004)(Figure 2.6). Quaternary stratigraphy consists of the loess and alluvium of the Pingyuan Formation (Hu et al., 1989; Allen et al., 1997).

Figure 2.5. Surface geology of the Bohai Basin and neighboring regions (modified from Steinshouer et al., 1999). NE- and EW-striking Mesozoic folds and faults probably acted as zones of weakness for the development of later northeast- and east-striking Cenozoic faults in the Bohai Basin. The main structures relating to the Indosinian orogeny (Triassic) are characterized by northeast-striking folds and thrusts. They can be traced from east of the Taihang Mountains to the eastern part of the Yan mountains. The main structures relating to the Qinling orogeny (early Permian) are characterized by east-west-striking folds and thrusts. They can be traced from the southern Liaoning region to the eastern Tien Shan Mountains located in central Asia.

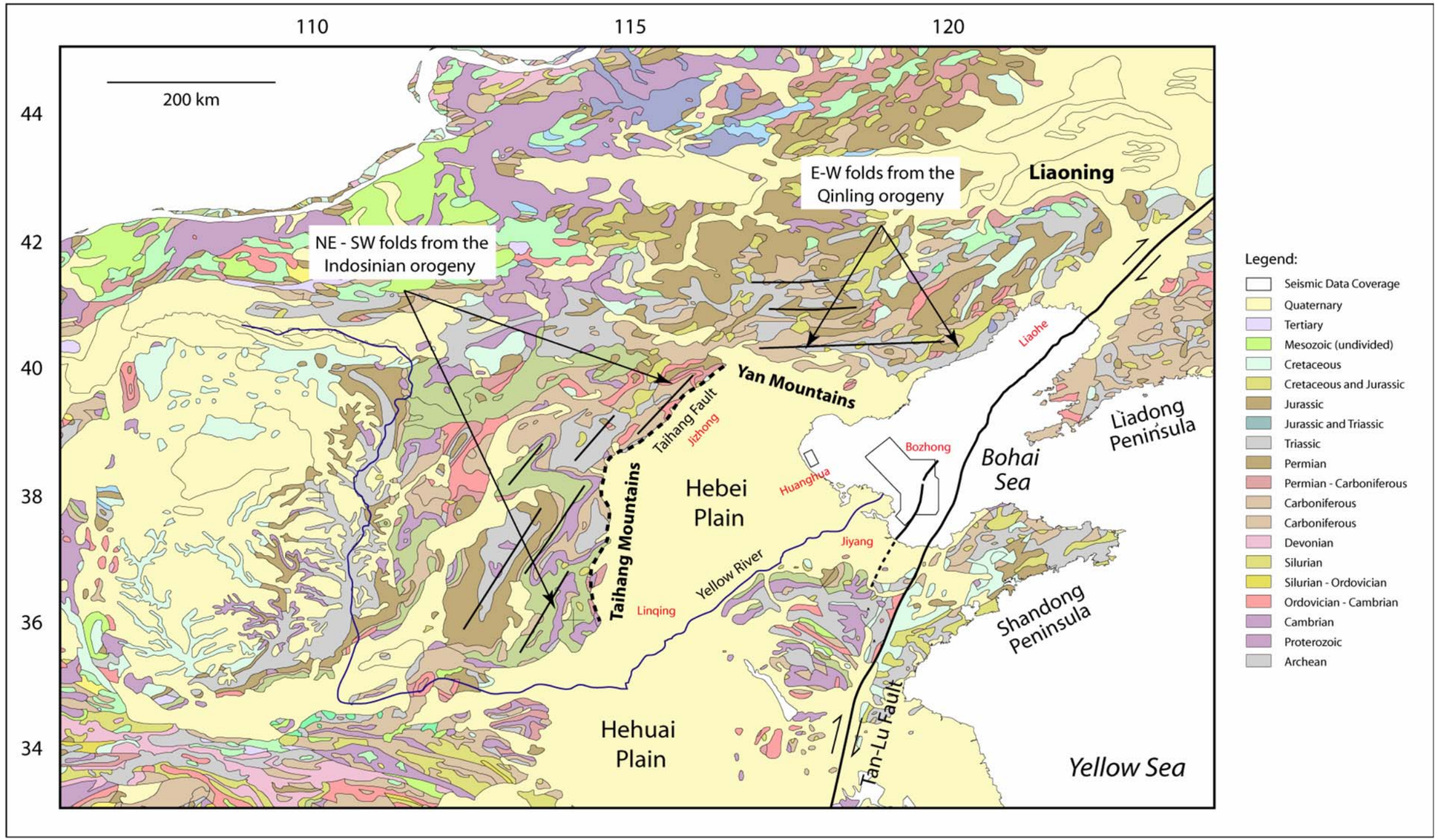
110
115
120
44
42
40
38
36
34
200 km
NE - SW folds from the Indosinian orogeny
E-W folds from the Qinling orogeny
Liaoning
Liaohe
Yan Mountains
Taihang Fault
Jizhong
Bozhong
Liadong Peninsula
Bohai Sea
Huanghua
Hebei Plain
Taihang Mountains
Jiyang
Yellow River
Linqing
Shandong Peninsula
Hehuai Plain
Tan-Lu Fault
Yellow Sea
Legend:
Seismic Data Coverage
Quaternary
Tertiary
Mesozoic (undivided)
Cretaceous
Cretaceous and Jurassic
Jurassic
Jurassic and Triassic
Triassic
Permian
Permian - Carboniferous
Carboniferous
Carboniferous
Devonian
Silurian
Silurian - Ordovician
Ordovician - Cambrian
Cambrian
Proterozoic
Archean

Figure 2.5

Figure 2.6. Stratigraphic column of the southwestern Bohai Basin. Typical well response for two of the four megasequences (MS2 and MS3) defined in the larger of the two study areas shown in Figure 2.5. Earliest rift deposits (late Paleocene deposits of the Kongdian Formation) are not present in this part of the study area. Formation names, ages and depositional environments compiled from Hu et al., (1989); Yao et al., (1994); Zhang et al., (1994); Wang Tonghe, (1995) and Allen et al., (1997).

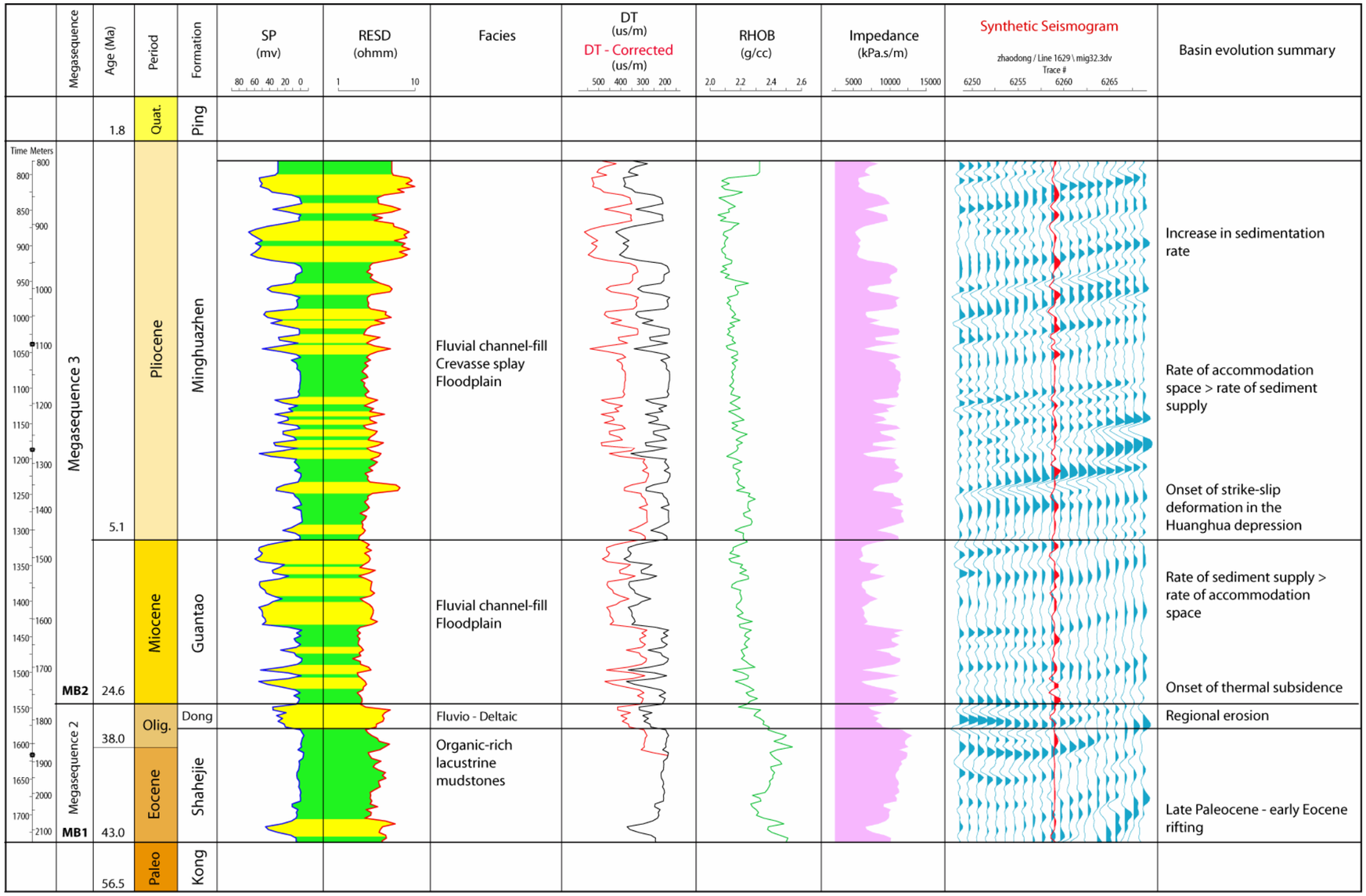
Megasequence
Age (Ma)
Period
Formation
SP
(mv)
80 60 40 20 0
RESD
(ohmm)
1 10
Facies
DT
(us/m)
DT - Corrected
(us/m)
500 400 300 200
RHOB
(g/cc)
2.0 2.2 2.4 2.6
Impedance
(kPa.s/m)
5000 10000 15000
Synthetic Seismogram
zhaodong / Line 1629 \ mig32.3dv
Trace #
6250 6255 6260 6265
Basin evolution summary
Time Meters
1.8
Quat.
Ping
Pliocene
Minghuazhen
Fluvial channel-fill
Crevasse splay
Floodplain
Increase in sedimentation rate
Rate of accommodation space > rate of sediment supply
Onset of strike-slip deformation in the Huanghua depression
Megasequence 3
5.1
Miocene
Guantao
Fluvial channel-fill
Floodplain
Rate of sediment supply > rate of accommodation space
MB2
24.6
Onset of thermal subsidence
Olig.
Dong
Fluvio - Deltaic
Regional erosion
Megasequence 2
38.0
Eocene
Shahejie
Organic-rich lacustrine mudstones
MB1
43.0
Late Paleocene - early Eocene rifting
Paleo
Kong
56.5

Figure 2.6

2.3.2.1 Eocene Kongdian Formation

This formation has been subdivided into three members: Kong-3 to Kong-1, with Kong-3 being the oldest one (Hu et al., 1989; Yang and Xu, 2004; Allen et al., 1997). The Eocene Kong-3 member was deposited largely in alluvial fan and shallow lake environments (Chen Changming et al, 1984; Allen et al, 1997). Fans were deposited at the margin of half-grabens, while ephemeral streams were located in the basin axes and probably fed small lakes (Chen Changming et al, 1984; Allen et al, 1997). The Kong-2 member rests conformably on the Kong-3 member. It consists of mudstone interbedded with carbonaceous shale and thin coal seams deposited under anoxic lacustrine conditions (Chang Chengyong, 1991; Allen et al, 1997). The Kong-1 member consists of alluvial fan-evaporitic playa lake facies associations. It is mostly composed of intercalations of mudstone and sandy conglomerate.

2.3.2.2 Eocene-Oligocene Shahejie Formation

The Shahejie Formation lies disconformably on the Kongdian Formation (Figure 2.6). It has been subdivided into four members, Sha-4 to Sha-1, with Sha-4 being the oldest (Allen et al., 1997; Yang and Xu, 2004). The Sha-4 member was mainly deposited in alluvial fan environments. It consists of grey mudstone, siltstone and fine-grained sandstone with minor gypsum (Allen et al., 1997). The Sha-3 member consists of grey mudstone, oil shale, siltstone and fine sandstone deposited in lacustrine environments of variable water depth.

The Sha-3 member comprises the main source rock in the region (Hu et al., 1989). The Sha-2 member was deposited in deltaic and shallow lacustrine environments and consists of grey and green mudstone interbedded with grey sandstone and conglomeratic

sandstone as well as intercalated organic-rich shale (Hu et al., 1989; Allen et al., 1997). The typical Sha-1 member consists of grey and green mudstone intercalated with poor quality oil-shale, fossiliferous limestone and marl deposited in shallow lacustrine environments (Hu et al., 1989; Allen et al., 1997).

2.3.2.3 Oligocene Dongying Formation

The Dongying Formation lies conformably on the Shahejie Formation (Figure 2.6). It is composed of grey and green mudstone, siltstone and fine-grained sandstone deposited in fluvial and shallow lacustrine environments (Hu et al., 1989; Allen et al. 1997). These facies represent a regression from the lacustrine-dominated sedimentation of the underlying Shahejie Formation (Hu et al., 1989; Allen et al., 1997).

2.3.2.4 Miocene Guantao Formation

The Guantao Formation lies unconformably on the Dongying Formation (Figure 2.6). Guantao Formation consists of braided and meandering river deposits and is composed of grey-green and grey-white sandstone and gravel sandstone intercalated with brown-red and grey-green mudstone (Hu et al., 1989; Allen et al., 1997).

2.3.2.5 Pliocene Minghuazhen Formation

The Minghuazhen Formation lies conformably on the Guantao Formation (Figure 2.6). Minghuazhen Formation consists of meandering fluvial deposits and is composed of silty mudstone intercalated with siltstone and fine sandstone, gravelly sandstone and mudstone (Hu et al., 1989).

2.3.2.6 Quaternary Pingyuan Formation

The Pingyuan Formation consists of loess and alluvium that covers almost the entire Bohai basin (Allen et al., 1997).

2.4. DATABASE AND METHODOLOGY

2.4.1 Database

This study uses 8,000 km of offshore 2D seismic data, a 3D seismic survey, and 42 wells that are tied to these reflection data (Figure 2.7). 2D and 3D seismic reflection data was collected during hydrocarbon exploration between 1980 and 2000. 2D and 3D seismic data covers an area of approximately 16,000 km^2 in the offshore Bohai Basin and includes the offshore part of the Jiyang Depression, the southern part of the Bozhong Depression and part of the offshore Huanghua Depression (Figure 2.7). Age control on seismic sequences is based on published biostratigraphic data (Wang Tonghe, 1995; Yao et al., 1994; Zhang et al., 1994).

2.4.2 Methodology

Conventional seismic interpretation of 2D and 3D seismic reflection lines was carried out in the study area. Structural maps, seismic cross-sections, coherency time-slices and subsidence plots allowed the delineation of four main unconformity-bounded seismic units or megasequences. For this thesis, I use the definition of "megasequence" by Hubbard (1988) as a "regional-unconformity-bounded depositional package that represents major, widespread depositional phases in a basin's history". Coherency time slices with variable seismic windows 40-120 ms were designed to measure the

incoherency in seismic markers and generate the best image of the principal faults. No additional lithologic descriptions or core analyses were carried out specifically for this study, but previous analyses were used from Apache Corporation internal well reports and were incorporated into these results.

2.5. STRUCTURAL FRAMEWORK

The basin fill of the Bohai Basin in the study areas was divided into four *megasequences* that are illustrated on the regional seismic lines shown in figures 2.8, 2.9, 2.10, 2.11, 2.12 and 2.13.

2.5.1 Regional unconformities (megasequence boundaries)

Three regional unconformities form boundaries between the four megasequences and were mapped in the study area on Figures 2.8, 2.9, 2.10, 2.11, 2.12 and 2.13. The megasequence boundaries correspond to: 1) the top of the pre-Tertiary "basement" (approximately 43 Ma in age)(Wang Tonghe, 1995; Yao et al., 1994; Zhang et al., 1994); 2) the top of the Oligocene (~ 24.6 Ma)(Wang Tonghe, 1995; Yao et al., 1994; Zhang et al., 1994); and 3) a late Pliocene to Quaternary regional unconformity (Wang Tonghe, 1995; Yao et al., 1994; Zhang et al., 1994). These megasequence boundaries are referred to as MB1, MB2 and MB3 with MB1 being the oldest and MB3 being the youngest.

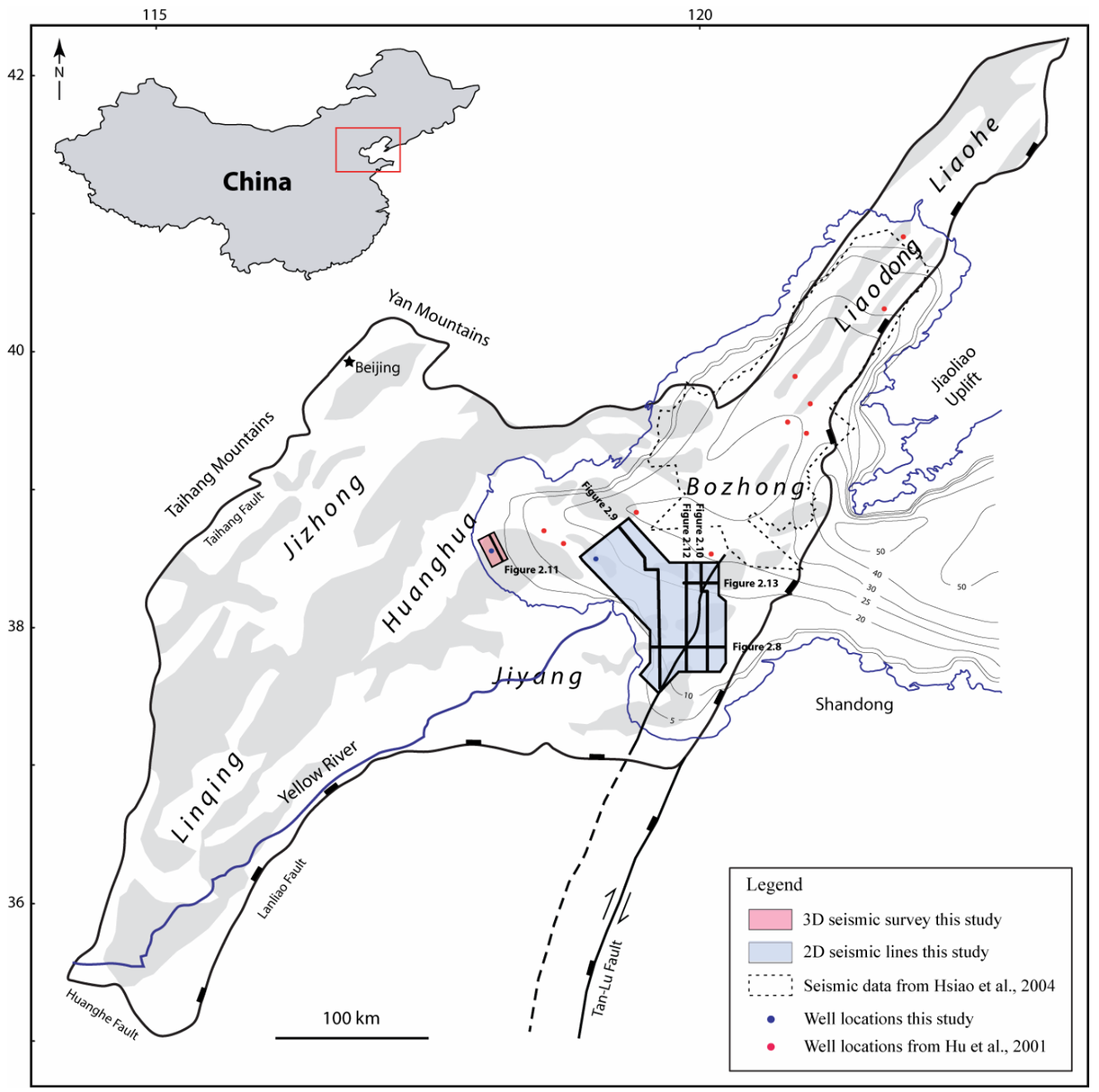

Figure 2.7. Location of seismic reflection data and wells used in this study. A late 1980s regional grid of 2D seismic reflection lines (0.5-4 km spacing) cover the central part of the study area. A 2000-vintage 3D seismic survey covers the westernmost part of the study area. Seismic surveys were tied to several exploration and production wells. The heavy solid lines indicate the segments of seismic reflection profiles shown in subsequent figures. Dotted lines represent the location of seismic reflection data from Hsiao et al. (2004). Depressions or sub-basins cover unshaded areas of the Bohai Basin and are labeled in largest type; gray areas represent structural highs separating the depressions (map of depressions and highs modified from Hao et al., 2007).. Bathymetric contours are from Sundermann and Feng, 2004. Onland southern extensions of the twin traces of the Tan-Lu fault zone are from Xu, J. (1993). Trace of Taihang fault zone is compiled from Xu, J. (1993) and Hao et al. (2007).

2.5.1.1 Eocene megasequence boundary 1 (MB1)

MB1 is the oldest identifiable unconformity and megasequence boundary in the Bohai Basin and is shown on Figures 2.8, 2.9, 2.10, 2.11, 2.12 and 2.13. MB1 represents the top of pre-Tertiary "basement" and is commonly present on seismic sections as either an angular unconformity or as a disconformity. The angular unconformity is characterized by a marked truncation of the underlying Late Mesozoic strata or Archean basement (cf. Figure 2.10b in the area of the Bozhong Sag). The disconformity is characterized by a strong and continuous reflection overlying a zone of chaotic and/or almost transparent seismic reflections (cf. Figure 2.10b; in the area of the Laizhouwan Sag).

A time-structure map for MB1 (Figure 2.14) and individual seismic cross-sections (Figures 2.8, 2.9, 2.10, 2.11, 2.12 and 2.13) show typical horst-and-graben topography at the top of MB1 and define three large depressions: the Jiyang, Bozhong and Huanghua depressions (Figure 2.14). Smaller regions of subsidence or "sags" sub-divide the major depressions. Larger depressions include the Laizhouwan, Qindong, Huanghekou and Bozhong sags (Figures 2.7 and 2.14). These four larger sags are separated by five structural highs or "rises" that have remained relatively unaffected by the effects of Tertiary deformation observed in the adjacent sags (Allen et al., 1997; 1998). The rises include the Kendong, Shaleitan, Laibel, Bonan and Weibel rises (Allen et al., 1997) (Figure 2.14).

The two-way travel-time of MB1 (Figure 2.14) ranges from 1.2 s in the southern part of the Huanghua depression (Weibel rise) to 3.8 s in the central part of the Huanghua (Laizhouwan sag) and Bozhong (Bozhong sag) depressions.

2.5.1.2 Late Oligocene megasequence boundary 2 (MB2)

MB2 separates Paleogene from Neogene sediments as seen on Figures 2.8, 2.9, 2.10, 2.11, 2.12 and 2.13. The seismic character of MB2 varies rapidly across single sub-basins and across rotated fault blocks. MB2 commonly appears as an angular unconformity around the basin margins (Figure 2.11b) and as a disconformity in the deepest, axial parts of the basin (Figure 2.8b). In some isolated faulted depressions, such as the Qindong sag (Figure 2.9b); the MB2 unconformity also appears as a flat, slightly rotated unconformity overlying rotated fault blocks. MB2 merges with MB1 on the top surface of basement highs (cf. Figure 2.9b; Kengdong rise). This relationship suggests that a major erosional event marked by the unconformity at the base of MB2 leveled the basement highs.

A time-structure map of MB2 in Figure 2.15 shows that faults cut the MB2 surface and slightly displace it up to 0.4 s in two-way travel time (Figures 2.8b and 2.9b). Displacement of the MB2 surface indicates reactivation of older fault trends in Eocene to middle Oligocene time.

The two-way travel-time of MB2 (Figure 2.15) ranges from 0.8 s in the southernmost part of the study area to 2.8 s in the center of the Bohai Basin, suggesting the main depocenter was located at the center of the Bohai Basin during this time.

2.5.1.3 Pliocene – Quaternary megasequence boundary 3

MB3 is the shallowest traceable unconformity seen on Figures 2.8, 2.9, 2.10, 2.11, 2.12 and 2.13. The age of MB3 is not well constrained but is estimated to be Pliocene to Quaternary in age (Zhang et al., 2001; Gong, 2004). The seismic character of MB3 varies widely depending on its position within the basin. MB3 is commonly expressed as a basinwide disconformity in most areas of the basin, except near the Tan-Lu fault zone

along the northeast margin of the study area (Figure 2.12b) and in structural highs in the basin (Figure 2.8b) where MB3 is manifested as an angular unconformity.

The two-way travel-time of MB3 (Figure 2.16) ranges from 0.5 s in the southernmost part of the study area to 1 s in the center of the study area, suggesting, as in the case of MB2, the main depocenter was located at the center of the Bohai Basin during late Miocene to early Pliocene time. MB3 is cut by numerous east-west and northeast oriented normal faults not present in MB2, suggesting a tectonic event following the deposition of MB2.

2.5.2 Description of four megasequences in the Bohai Basin

I identified four megasequences in the offshore part of the Bohai Basin: 1) a *pre-rift sequence* of pre-Tertiary age deposited prior to the main phase of Cenozoic deformation (MS1); 2) *a syn-rift sequence* of early Eocene to late Oligocene age deposited during the major phase of Cenozoic deformation (MS2); and 3) *two post-rift sequences* of late Oligocene to Quaternary age deposited after the main phase of rifting deformation had ceased (MS3 and MS4)(Figures 2.8, 2.9, 2.10, 2.11, 2.12 and 2.13). The depositional environment of each megasequence was interpreted from seismic and well data. Seismic facies analysis was based on the description and geologic interpretation of seismic reflection parameters, including configuration, continuity, amplitude and frequency (Mitchum et al., 1977).

2.5.2.1 Pre-rift megasequence 1 (pre-Tertiary)

Wells used in this study penetrate MS1 in only three cases (Figures 2.8, 2.9, 2.10, 2.11, 2.12 and 2.13). Despite the lack of well control, MS1 is known from outcrops

surrounding the basin to consist of diverse lithologies ranging in age from Archean to Mesozoic (Fletcher et al., 1995; Hu et al., 1989). Basement rocks include crystalline basement overlain by Paleozoic carbonates and Mesozoic terrestrial and volcanic strata (Fletcher et al., 1995; Hu et al., 1989).

On seismic lines, this pre-rift MS1 section is normally reflection-free or chaotic (Figure 2.9b), but locally displays some well developed seismic reflections (Figure 2.11b). Reflection-free configurations in MS1 most probably correspond to initially continuous sedimentary or meta-sedimentary strata that were deformed by pre-Cenozoic folding and thrusting events that disrupted their continuity as known from the folded outcrop patterns of exposed Paleozoic and Mesozoic rocks as shown on Figure 2.5.

2.5.2.2 Syn-rift megasequence 2 (late Paleocene – late Oligocene)

MS2 is confined to isolated half-grabens and is cut by numerous faults that extend upward from the basement (Figures 2.8, 2.9, 2.10, 2.11, 2.12 and 2.13). This relationship suggests that deposition of MS2 occurred during the main phase of Cenozoic rifting. Well logs and seismic cross-sections show MS2 to consist primarily of fluvio-lacustrine deposits of the Shahejie and Dongying Formations of Eocene and Oligocene age (Figure 2.6). The late Paleocene Kongdian Formation is present locally in the deepest parts of half-grabens (mostly onshore) whereas the Dongying and Shahejie Formations are more widely distributed within rifts of the Bohai Basin (Hu et al., 1989; Hsiao et al., 2004; Yang and Xu, 2004).

Seismic facies of the Shahejie Formation are generally characterized by parallel and continuous reflectors with fairly consistent amplitudes (Figures 2.8, 2.9, 2.10, 2.11, 2.12 and 2.13). This suggests that deposition of the Shahejie Formation occurred within stable and more distal areas of rifts that included lacustrine environments. The Oligocene

Dongying Formation caps the sedimentary section in MS2 and consists mostly of sub-parallel and discontinuous seismic reflections with variable amplitude, suggesting Oligocene fluvial and deltaic environments (Figures 2.8, 2.9, 2.10, 2.11, 2.12 and 2.13).

2.5.2.3 Post-rift megasequence 3 (early Miocene - Pliocene)

Well logs and seismic cross-sections show that MS3 consists primarily of fluvial and lacustrine deposits of the Miocene and Pliocene Guantao and Minghuazhen Formations (Figure 2.6)(Chapters 3, 4). Seismic cross-sections (Figures 2.8, 2.9, 2.10, 2.11, 2.12 and 2.13) show MS3 to consist of widespread sag deposits blanketing the underlying horst-and-graben topography over the entire study area. This relationship, together with the near rarity of faulting in the large areas of the sag basin indicates that an abrupt change in the tectonic style occurred between MS2 (Eocene - Oligocene) and MS3 (Miocene - Pliocene)(Chapters 3, 4).

MS3 was deformed by localized strike-slip faulting near the Tan-Lu fault zone as shown by the presence of widespread flower structures deforming the Neogene sag section. These younger, late Neogene flower structures are commonly localized on earlier normal faults formed during Eocene to Oligocene extension. The entire MS3 in the study area consists of parallel, discontinuous and variable seismic reflections suggesting deposits of alluvial and fluvial environments.

2.5.2.4 Post-rift megasequence 4 (Pliocene - Quaternary)

No well logs available for this study penetrated MS4. Therefore its age is not well constrained as shown on Figures 2.8, 2.9, 2.10, 2.11, 2.12 and 2.13. MS4 likely consists of the uppermost fluvial deposits of the Minghuazhen Formation along with

loess and alluvium of the overlying Pingyuan Formation (Hu et al., 1989). Therefore, the age of MS4 could range between late Pliocene to Quaternary (Zhang et al., 2001; Zai-sheng, 2004). The entire MS4 in the study area consists of parallel, discontinuous and variable seismic reflections suggesting deposits of alluvial and fluvial origin. Continuous or transparent reflections at the very top of MS4 are attributed to the lack of resolution in the upper parts of the multi-channel seismic reflection profiles.

2.5.3 Cenozoic fault patterns affecting megasequences of the Bohai Basin

Time-structure maps (Figures 2.14, 2.15 and 2.16) and coherency time slices (Figure 2.17 based on 3D data) reveal three distinctive fault patterns corresponding to two main tectonic phases affecting the Bohai region. Normal faults of Eocene to Oligocene age are widely distributed throughout the study area and comprise the most common fault type seen on seismic reflection lines. Strike-slip faults of early Pliocene to recent age with distinctive "flower structure" profiles are less frequent and commonly localized along older, reactivated normal faults (Figure 2.11b).

2.5.3.1 Fault family 1: North-northeast striking faults of late Paleocene to early Eocene age

Fault family 1 consists of (late Paleocene to early Eocene) high-angle normal faults with a dextral strike-slip component (Yan et al., 1996; Hsiao et al., 2004). These faults trend north-northeast and are commonly restricted to the margins of the basin (e.g., area near the Tan-Lu fault). Examples of fault family 1 are visible in seismic cross-sections in Figures 2.8b, 2.10b and 2.12b and in map view in Figures 2.14, 2.15 and 2.16.

Figure 2.8. A) Uninterpreted seismic line A-A' See figure 2.7 for location of line. B) Interpreted seismic line A-A'. The basin fill of the Bohai Basin in the study areas was divided into four regional unconformity bounded megasequences: 1) a **pre-rift sequence** of pre-Tertiary age deposited prior to the main phase of Cenozoic deformation (MS1); 2) a **syn-rift sequence** of early Eocene to late Oligocene age deposited during the major phase of Cenozoic deformation (MS2); and 3) two **post-rift sequences** of late Oligocene to Quaternary age deposited after the main phase of rifting deformation had ceased (MS3 and MS4). Circle with "x" indicates strike-slip motion with block moving away from viewer. Circle with dot indicates block moving towards viewer.

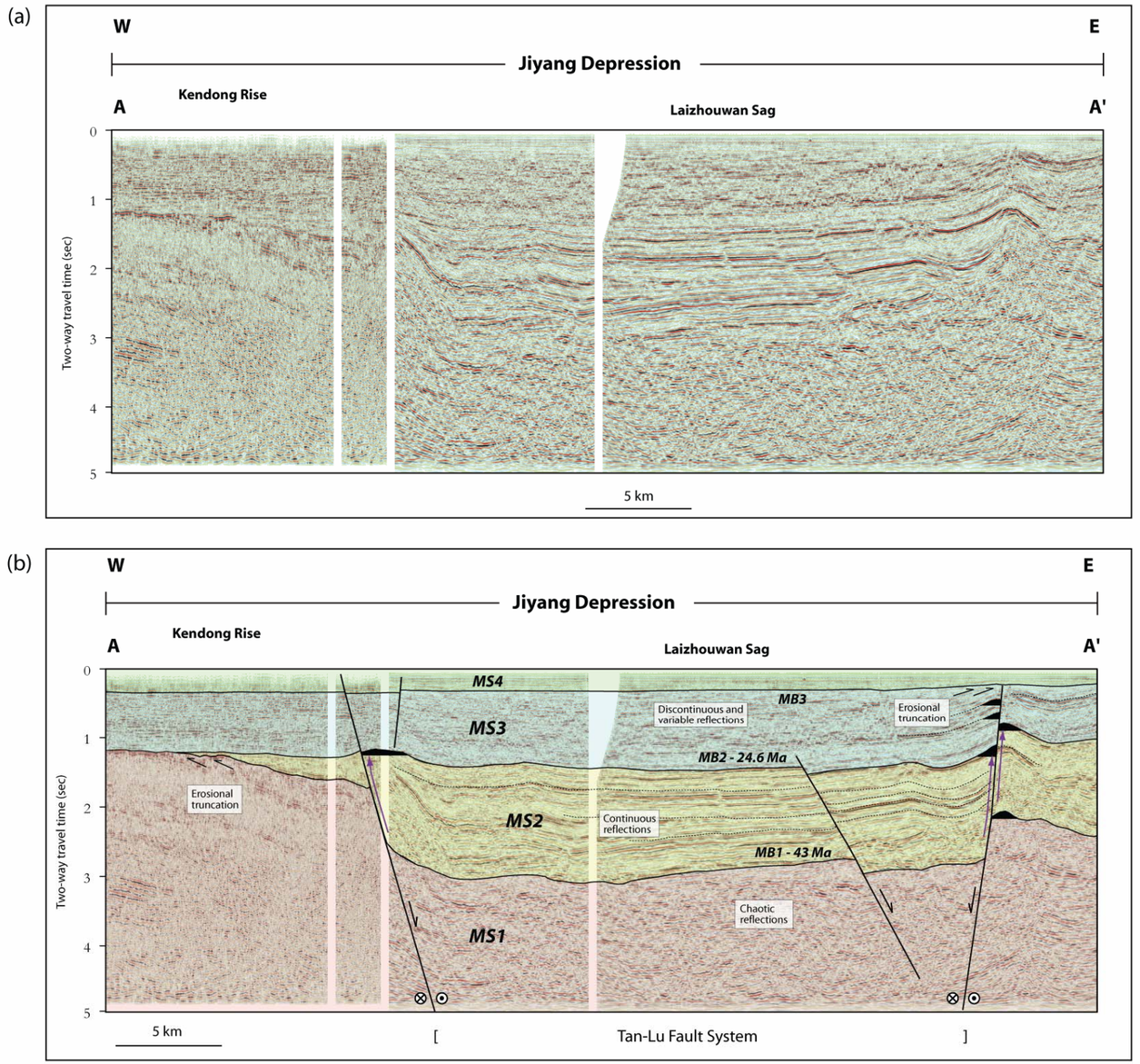
(a)
W
E
Jiyang Depression
Kendong Rise
A
Laizhouwan Sag
A'
Two-way travel time (sec)
0
1
2
3
4
5
5 km
(b)
W
E
Jiyang Depression
Kendong Rise
A
Laizhouwan Sag
A'
MS4
MS3
MS2
MS1
MB3
MB2 - 24.6 Ma
MB1 - 43 Ma
Discontinuous and variable reflections
Erosional truncation
Erosional truncation
Continuous reflections
Chaotic reflections
Two-way travel time (sec)
0
1
2
3
4
5
5 km
[
Tan-Lu Fault System
]

Figure 2.8

Figure 2.9. A) Uninterpreted seismic line B-B' See figure 2.7 for location of line. B) Interpreted seismic line B-B'. Three regional unconformities form boundaries between the four megasequences and were mapped across the study area. The megasequence boundaries correspond to: 1) the top of the pre-Tertiary "basement" (~ 43 Ma in age); 2) the top of an Oligocene sequence (~ 24.6 Ma); and 3) a late Pliocene to Quaternary regional unconformity. These megasequence boundaries are referred to as MB1, MB2 and MB3 with MB1 being the oldest boundary.

(a)

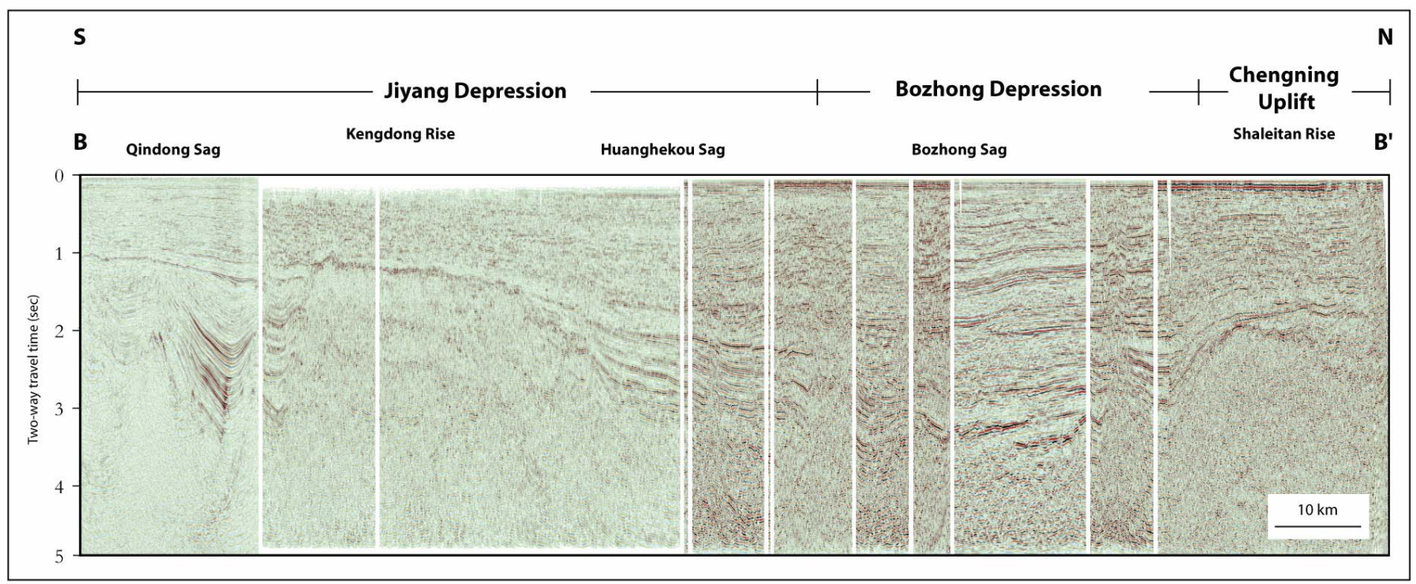
S
N
Jiyang Depression
Bozhong Depression
Chengning Uplift
B
B'
Qindong Sag
Kengdong Rise
Huanghekou Sag
Bozhong Sag
Shaleitan Rise
Two-way travel time (sec)
0
1
2
3
4
5
10 km

(b)

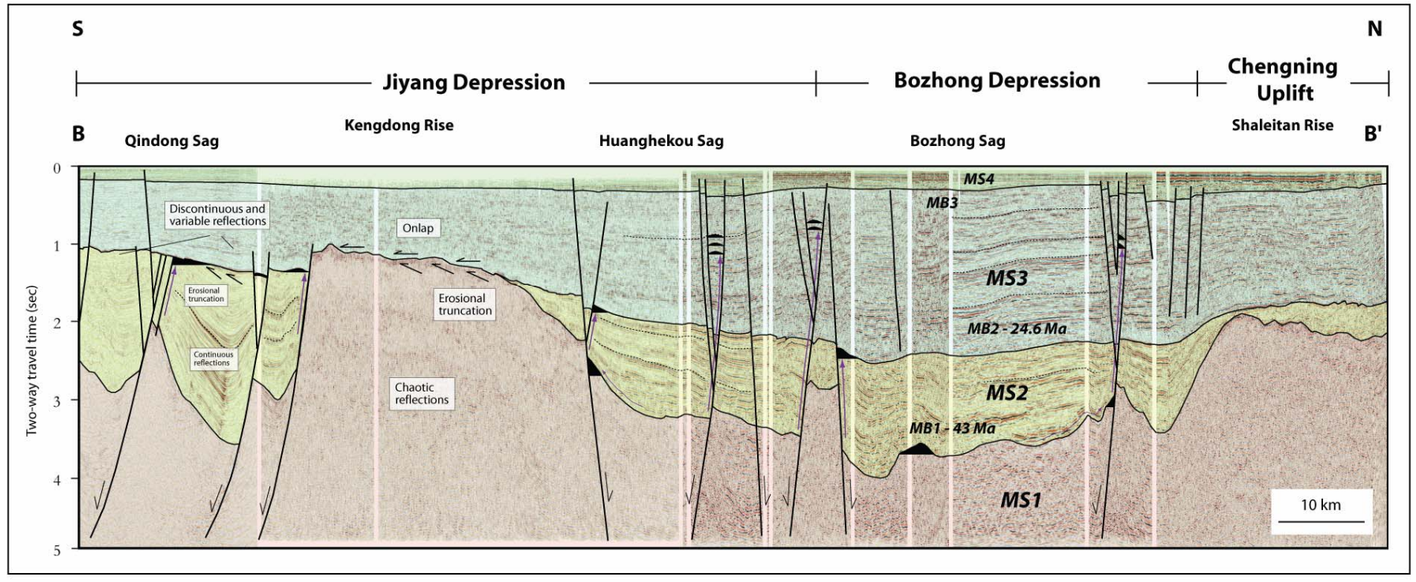
S
N
Jiyang Depression
Bozhong Depression
Chengning Uplift
B
B'
Qindong Sag
Kengdong Rise
Huanghekou Sag
Bozhong Sag
Shaleitan Rise
Two-way travel time (sec)
0
1
2
3
4
5
Discontinuous and variable reflections
Onlap
Erosional truncation
Erosional truncation
Continuous reflections
Chaotic reflections
MS4
MB3
MS3
MB2 - 24.6 Ma
MS2
MB1 - 43 Ma
MS1
10 km

Figure 2.9

Figure 2.10. A) Uninterpreted seismic line C-C'. See figure 2.7 for location of line. B) Interpreted seismic line C-C'. Megasequence 1 (MS1) consists of diverse lithologies ranging in age from Archean to Mesozoic This section is normally reflection free but locally displays some well developed seismic reflections. Megasequence 2 (MS2) consists of the lacustrine and fluvio-deltaic deposits of the Eocene and Oligocene Shahejie and Dongying Formations. Seismic facies of the Shahejie Formation are generally characterized by parallel and continuous reflectors with fairly consistent amplitudes. Seismic facies of the Oligocene Dongying Formation consists mostly of sub-parallel and discontinuous seismic reflections with variable amplitude. Megasequence 3 (MS3) consists of fluvial and lacustrine deposits of the Miocene and Pliocene Guantao and Minghuazhen Formations. Seismic facies in MS3 consists of parallel, discontinuous and variable seismic reflections. Megasequence 4 (MS4) consists of the uppermost fluvial deposits of the Pliocene Minghuazhen Formation along with loess and alluvium of the overlying Quaternary Pingyuan Formation. Megasequence 4 (MS4) consists of parallel, discontinuous and variable seismic reflections. Circle with "x" indicates strike-slip motion with block away from viewer. Circle with dot indicates block motion towards viewer.

(a)

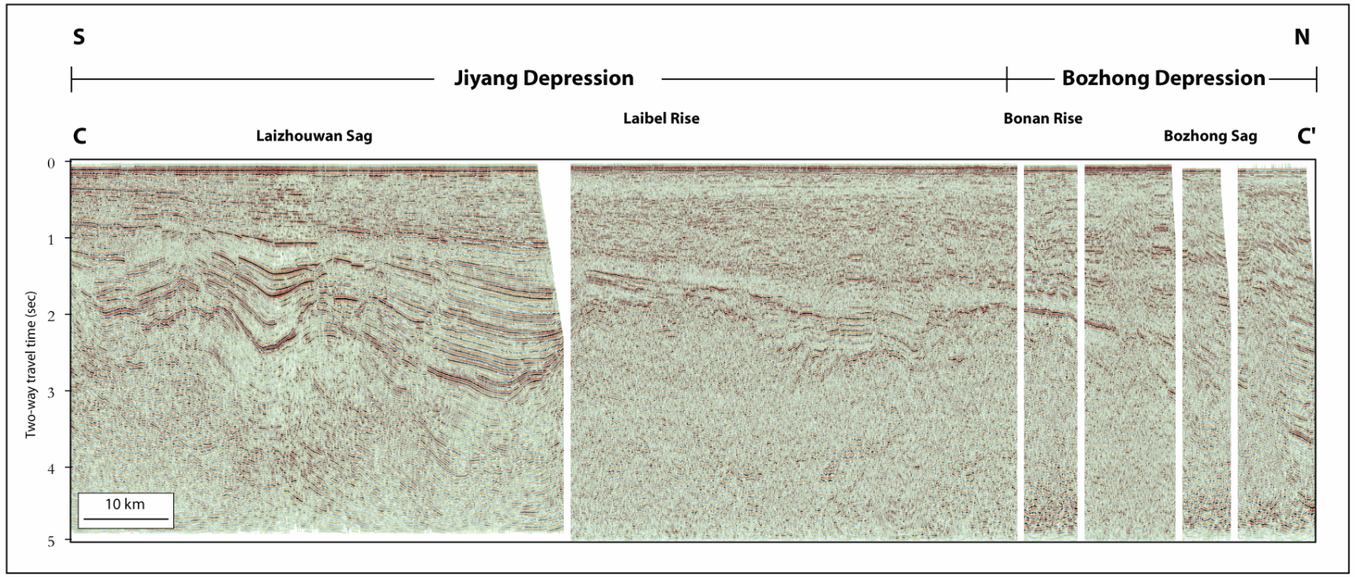

(b)

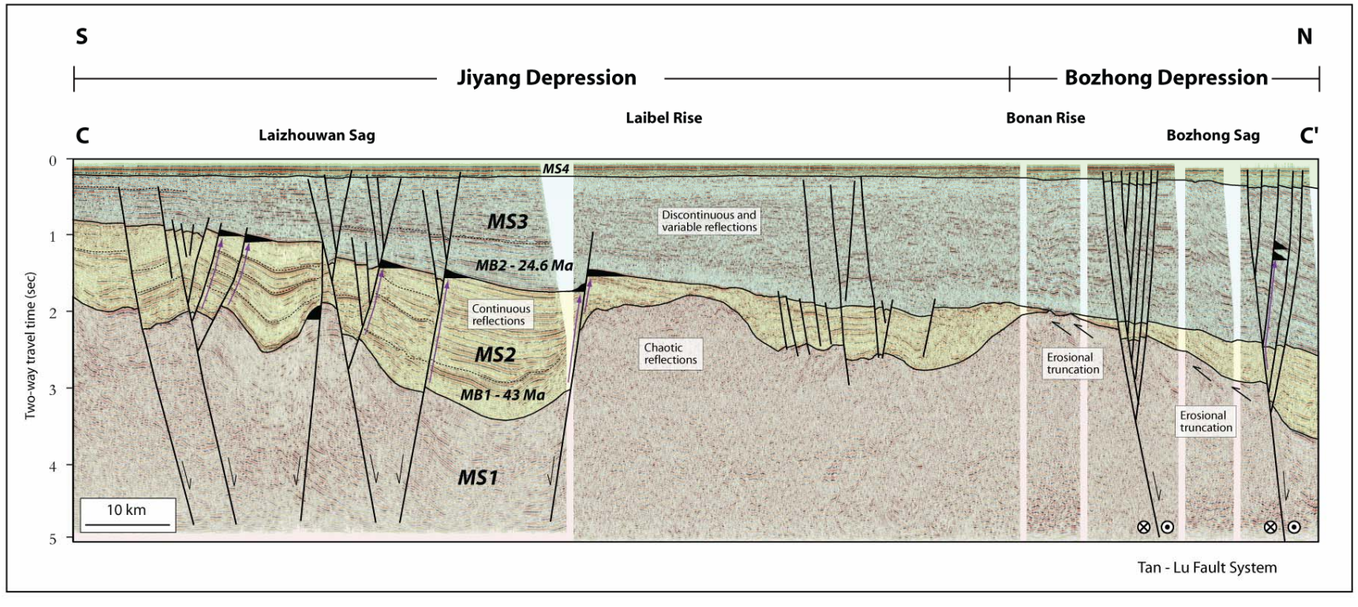

Figure 2.10

Figure 2.11. A) Uninterpreted seismic line D-D'. See figure 2.7 for location of line. B) Interpreted seismic line D-D'. Megasequence 3 (MS3) was deformed by localized strike-slip faulting as shown by the presence of widespread flower structures deforming the Neogene sag section. These younger, late Neogene flower structures are commonly localized on earlier normal faults formed during Eocene to Oligocene regional extension. Circle with "x" indicates strike-slip motion with block motion away from viewer. Circle with dot indicates block motion towards viewer.

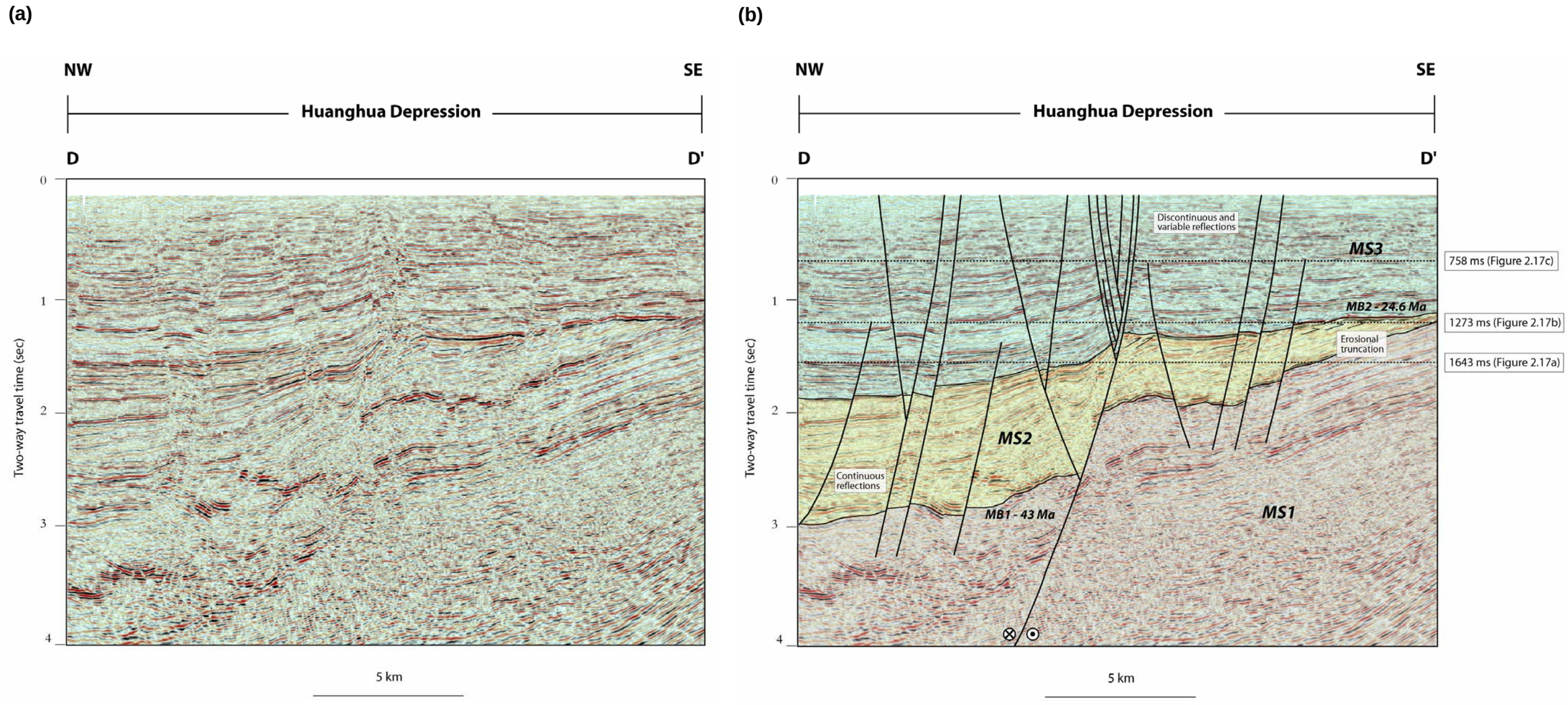
(a)
NW
SE
Huanghua Depression
D
D'
0
1
2
3
4
Two-way travel time (sec)
5 km
(b)
NW
SE
Huanghua Depression
D
D'
0
1
2
3
4
Two-way travel time (sec)
Discontinuous and variable reflections
MS3
758 ms (Figure 2.17c)
MB2 - 24.6 Ma
1273 ms (Figure 2.17b)
Erosional truncation
1643 ms (Figure 2.17a)
MS2
Continuous reflections
MB1 - 43 Ma
MS1
5 km

Figure 2.11

Figure 2.12. A) Uninterpreted seismic line E-E'. See figure 2.7 for location of seismic line. B) Interpreted seismic line E-E'. Northeast and east-striking normal faults control the distribution of major rifts in the Bohai Basin. Northeast-striking normal faults (fault family 1) are commonly restricted to the margins of the basin (e.g. Bozhong depression near the Tan-Lu fault). Normal faults extend downward into the acoustic basement and upward into Neogene and Quaternary strata and in some cases appear to cut the sea floor. East-west-striking normal faults (fault family 2) are most commonly found in the center of the Bohai Basin (e.g. Jiyang depression). Normal faults of family 2 extend downward into the basement and upward into Neogene strata. Fault family 3 consists of west-northwest-striking oblique-slip normal and reverse faults forming negative and positive flower structures, respectively. Downward, the fault strands merge near the top the Paleogene sedimentary section (MS2) and upward, they diverge and extend into Neogene and Quaternary strata and in some cases appear to cut the sea floor. Circle with "x" indicates strike-slip with block motion away from viewer. Circle with dot indicates block motion towards viewer.

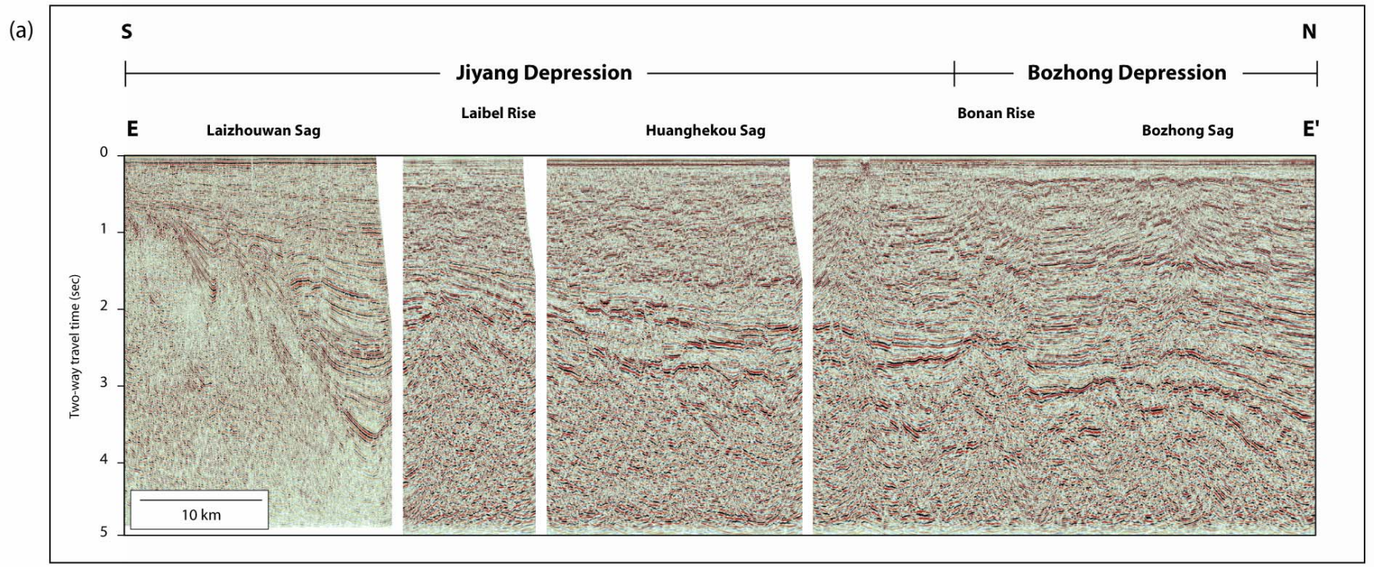
(a)
S
N
Jiyang Depression
Bozhong Depression
E
Laizhouwan Sag
Laibel Rise
Huanghekou Sag
Bonan Rise
Bozhong Sag
E'
Two-way travel time (sec)
0
1
2
3
4
5
10 km

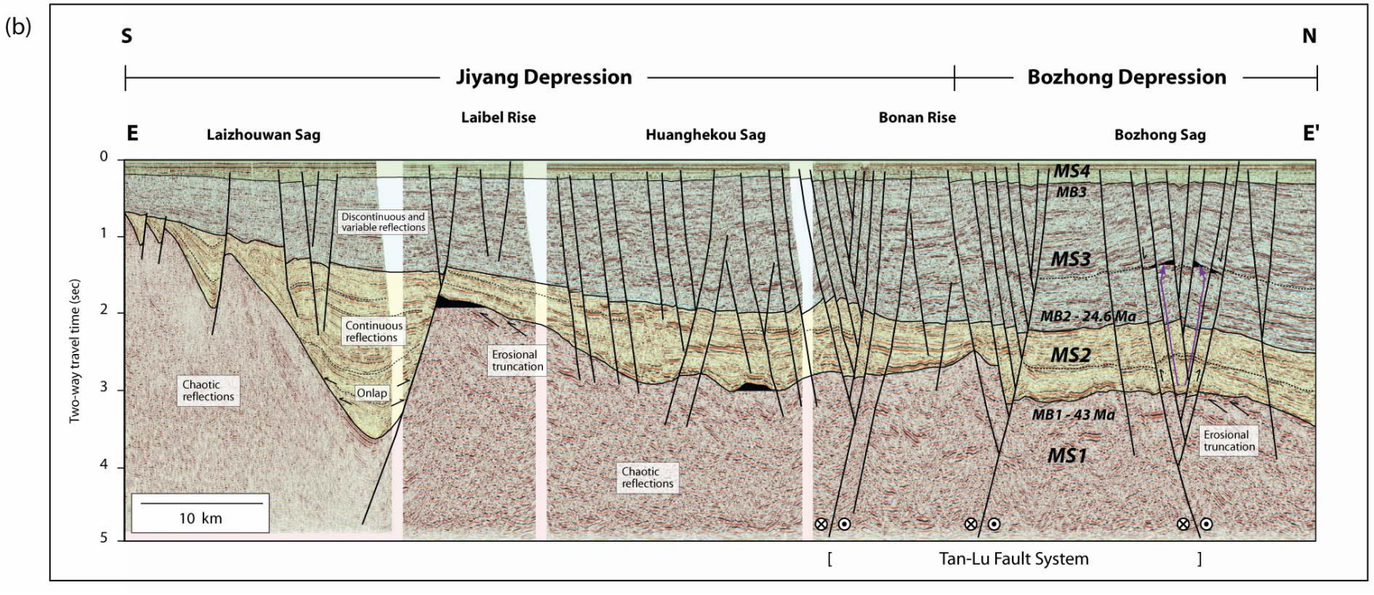
(b)
S
N
Jiyang Depression
Bozhong Depression
E
Laizhouwan Sag
Laibel Rise
Huanghekou Sag
Bonan Rise
Bozhong Sag
E'
Two-way travel time (sec)
0
1
2
3
4
5
Discontinuous and variable reflections
Continuous reflections
Chaotic reflections
Onlap
Erosional truncation
Chaotic reflections
MS4
MB3
MS3
MB2 - 24.6 Ma
MS2
MB1 - 43 Ma
MS1
Erosional truncation
10 km
[Tan-Lu Fault System]

Figure 2.12

Figure 2.13. A) Uninterpreted seismic line F-F'. See Figure 2.7 for location of seismic lines. B) Interpreted seismic line F-F. Fault family 3 consists of west-northwest-striking oblique-slip normal and reverse faults forming negative and positive flower structures, respectively. Downward, the fault strands merge near the top the Paleogene sedimentary section (MS2) and upward, they diverge and extend into Neogene and Quaternary strata and in some cases appear to cut the sea floor. Circle with "x" indicates strike-slip displacement with block motion away from viewer. Circle with dot indicates block motion towards viewer.

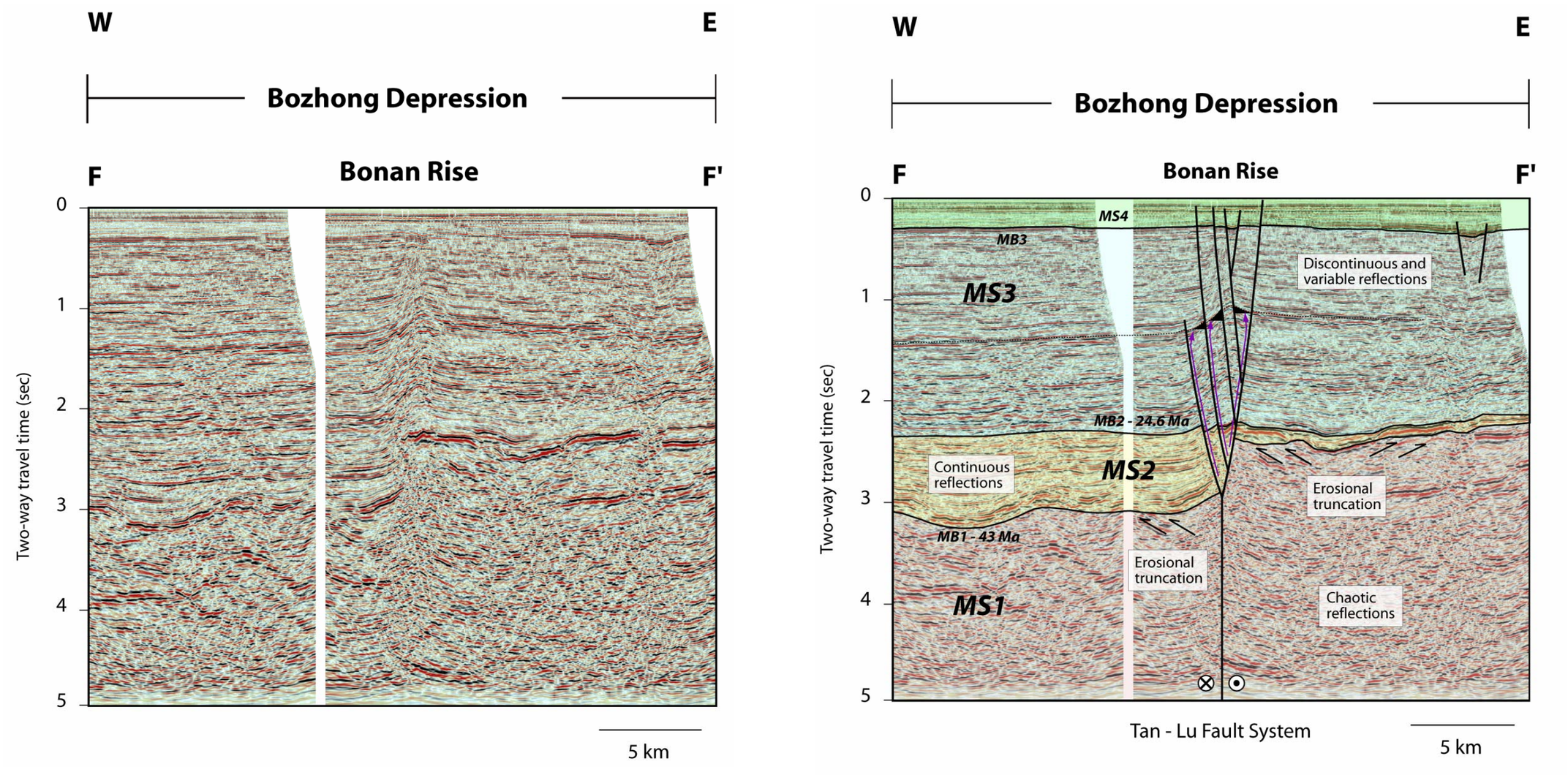
(a)
W
E
Bozhong Depression
F
Bonan Rise
F'
0
1
2
3
4
5
Two-way travel time (sec)
5 km
(b)
W
E
Bozhong Depression
F
Bonan Rise
F'
MS4
MB3
MS3
Discontinuous and variable reflections
MB2 - 24.6 Ma
Continuous reflections
MS2
Erosional truncation
MB1 - 43 Ma
Erosional truncation
MS1
Chaotic reflections
Tan - Lu Fault System
5 km

Figure 2.13

North-northeast striking faults of fault family 1 extend downward into the acoustic basement and upward into Neogene and Quaternary strata and in some cases appear to cut the sea floor. These fault systems control the distribution of major depocenters in the study area, most notably the Laizhouwan and Bozhong sags (Figures 2.8b and 2.9b). Significant downthrown side thickening of Paleogene sediments indicates these faults originated as normal faults during early Eocene to late Oligocene deposition of megasequence 2.

2.5.3.2 Fault family 2: E-W striking faults of early Eocene to late Oligocene age

This fault family is the most commonly found in the center of the Bohai Basin and consists of high-angle normal faults striking nearly E-W. These faults are visible in seismic cross-sections in Figures 2.9b and 2.10b and in map view in Figures 2.14, 2.15 and 2.16.

E-W striking faults of this family generally extend downward into the basement and upward into Neogene strata. These faults control the distribution of the Qindong, Laizhouwan and Huanghekou sags (Figures 2.9b and 2.12b). As in the case of fault family 1, significant downthrown side thickening of Paleogene sediments indicates that faults of family 2 originated as normal faults during Eocene to late Oligocene deposition of megasequence 2.

2.5.3.3 Fault family 3: WNW-ESE striking faults of late Miocene to recent age

This fault family consists of oblique-slip normal and reverse faults forming negative and positive flower structures, respectively. These faults are visible in cross-section in Figures 2.11b and 2.12b and in map view in Figure 2.16.

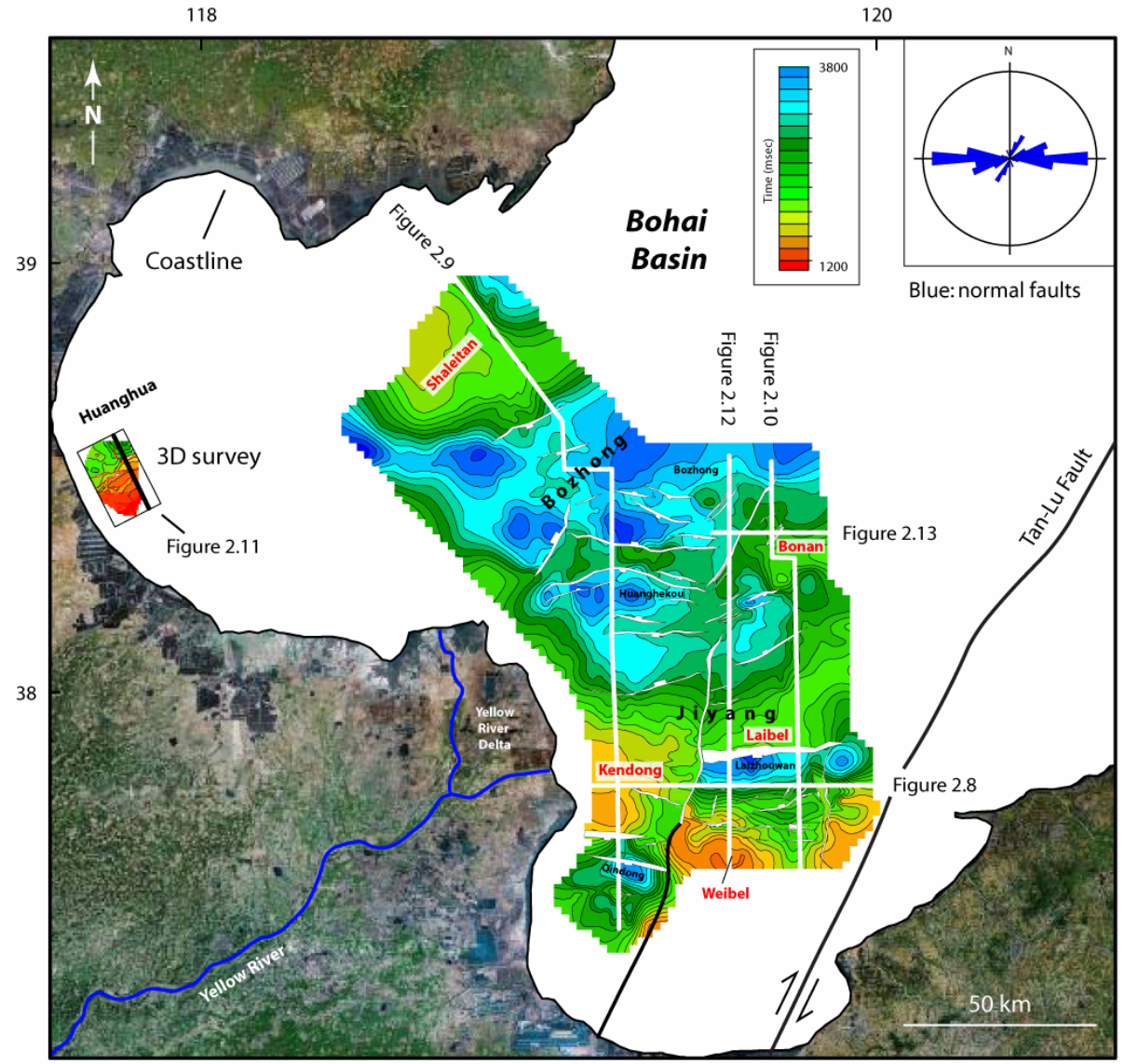

Figure 2.14. Time structure map of MB1 (top of the pre-Tertiary "basement") with contour interval of 200 ms. MB1 represents the lower boundary of the syn-rift sequence and marks the beginning of early Cenozoic rift development in the offshore part of the Bohai Basin. Early Cenozoic basin opening occurred on a series of half-grabens with master faults striking roughly east and northeast as summarized on inset rose diagram.

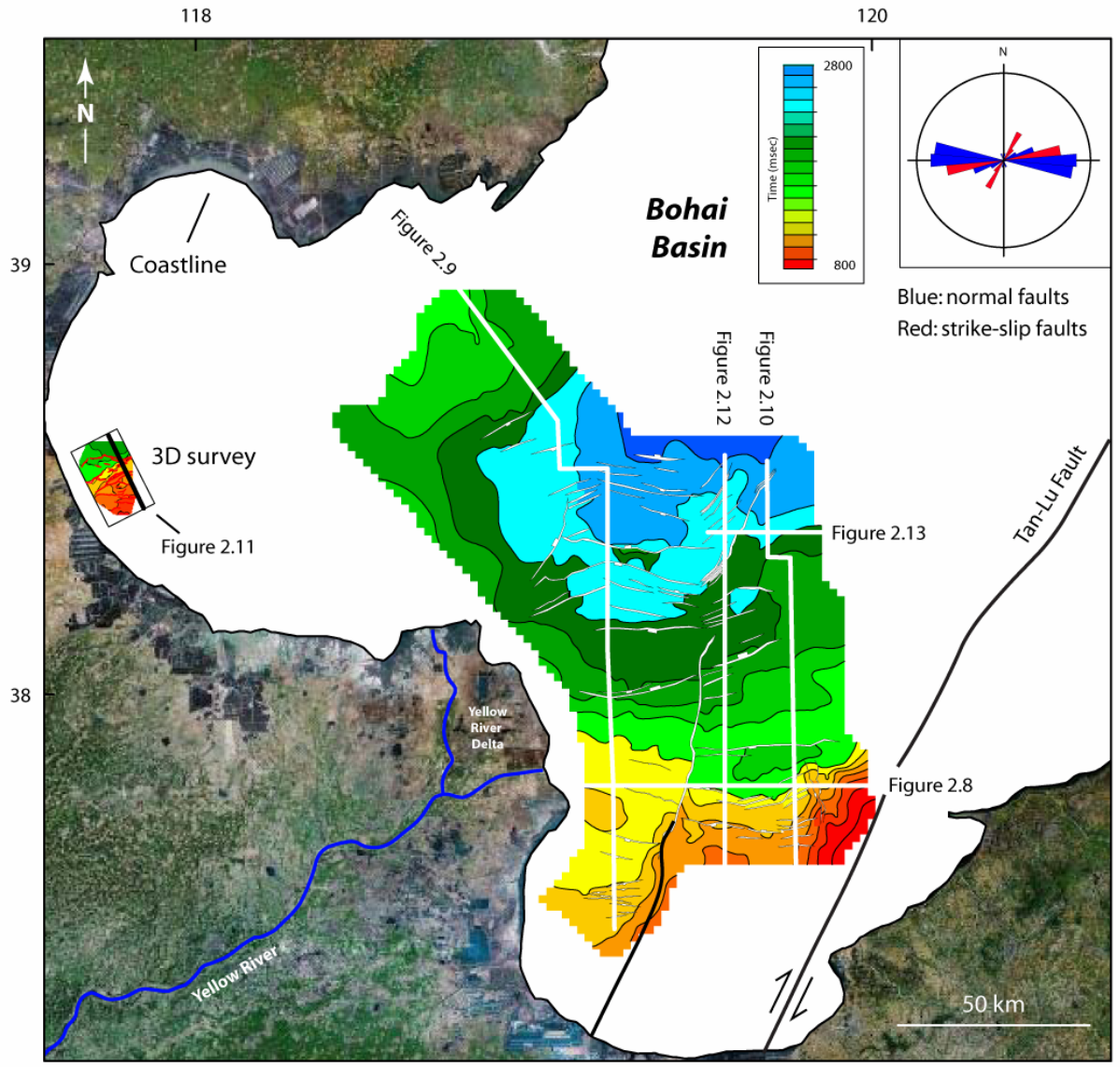

Figure 2.15. Time structure map of MB2 (top of the Oligocene) with contour interval of 200 ms. MB2 represents the boundary between syn-rift deposits (MS2) and post-rift or sag deposits (MS3 and MS4). The MS2 surface marks the end of the main phase of Cenozoic extension. Rose diagram shows trends of strike-slip and normal faults active during this period.

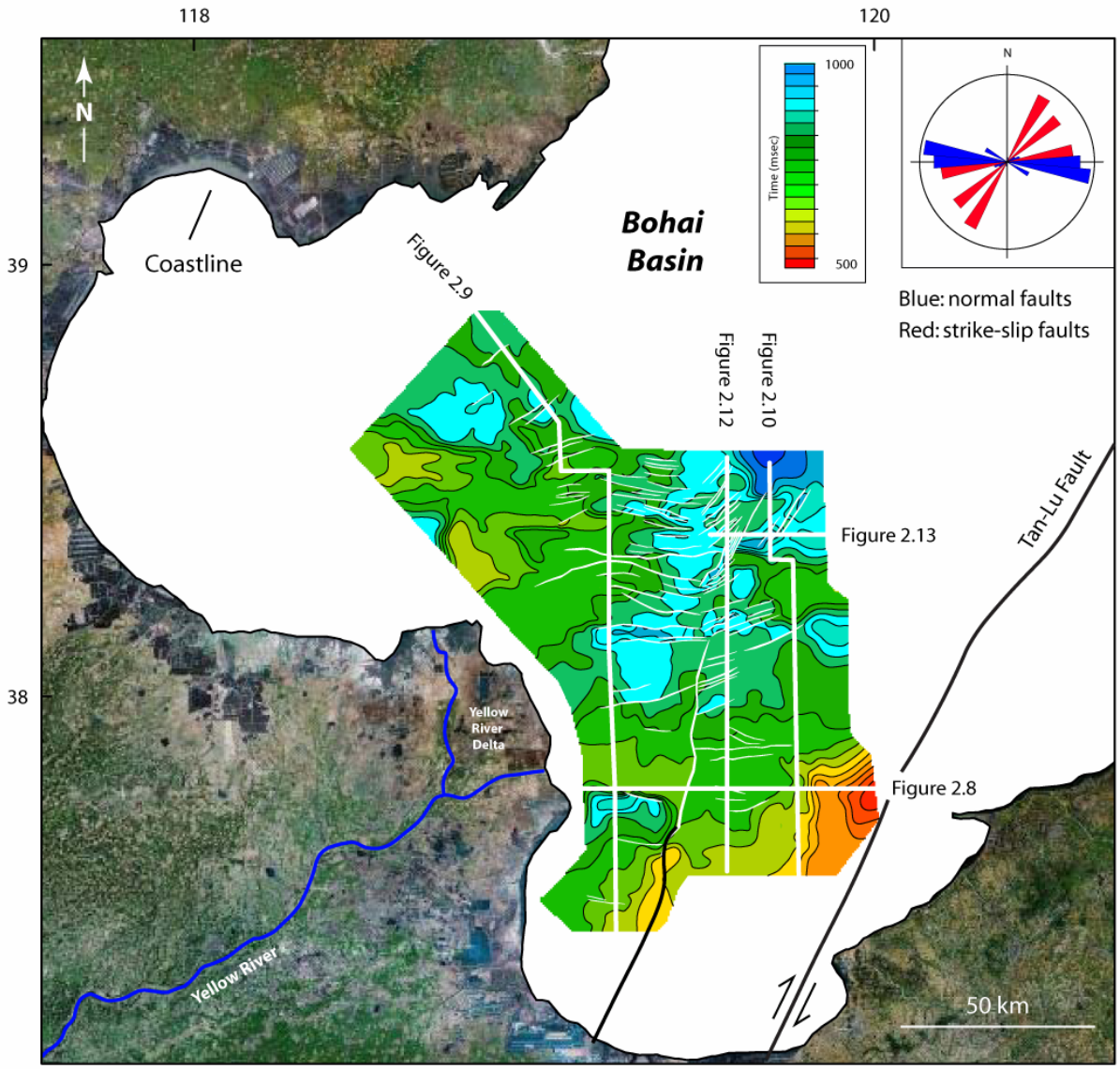

Figure 2.16. Time structure map of MB3 (Late Miocene – early Pliocene) with contour interval of 25 ms. MB3 represents the boundary between MS3 and MS4 and its formation is related to transtensional and transpressional structures locally developed along strike slip faults including both strands of the Tan-Lu fault zone. Inset shows increase in the prevalence of northeast-striking strike-slip faults of the Tan-Lu fault zone and continued activity of east-striking normal faults.

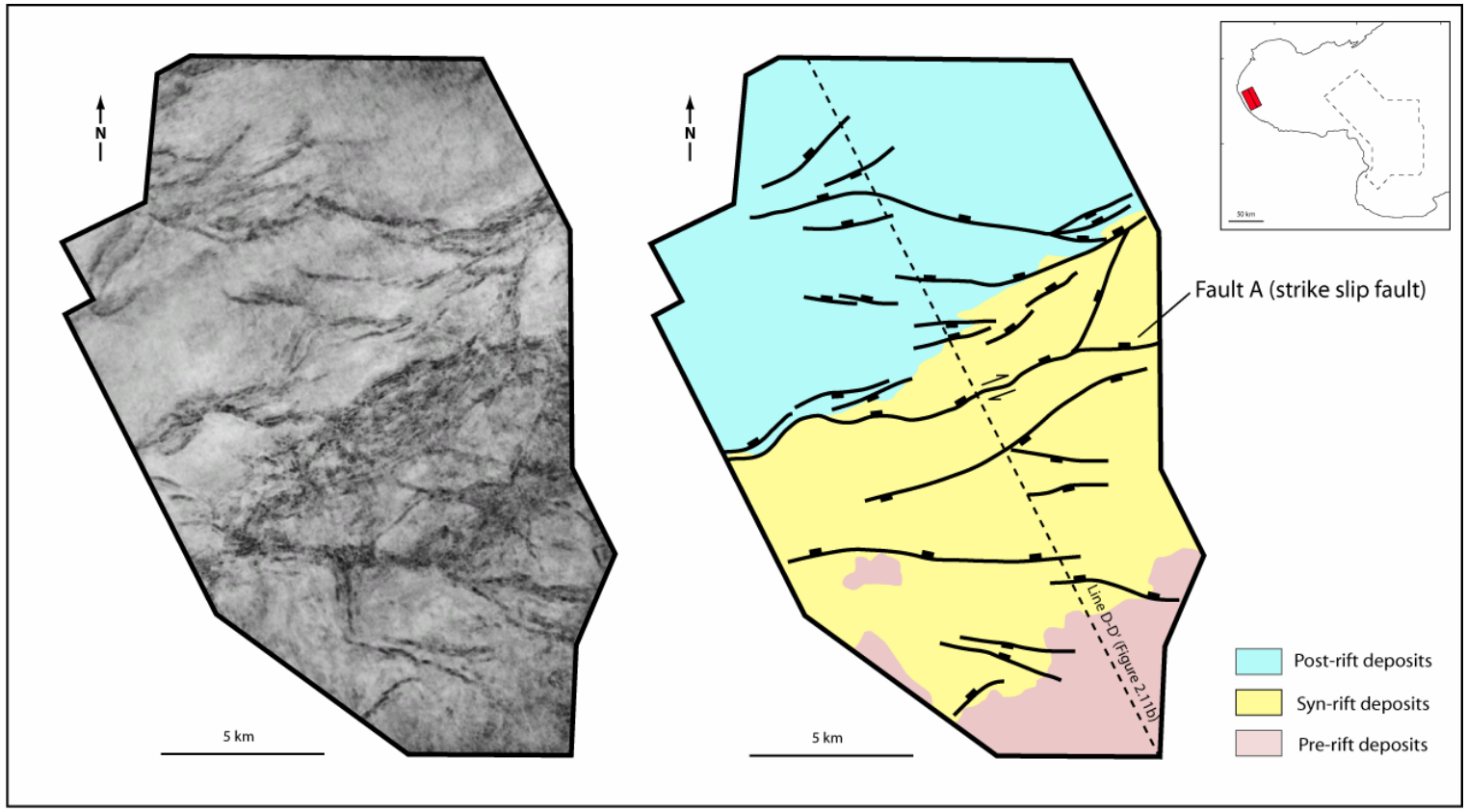

Figure 2.17a. Time slice at 1643 ms level (coherency display) showing the distribution of normal faults and fault A strike-slip fault. See figure 2.7 and 2.11b for location of time slice. Colors correspond to the different megasequences exposed at this level: red = MS1; yellow = MS2 and blue = MS3.

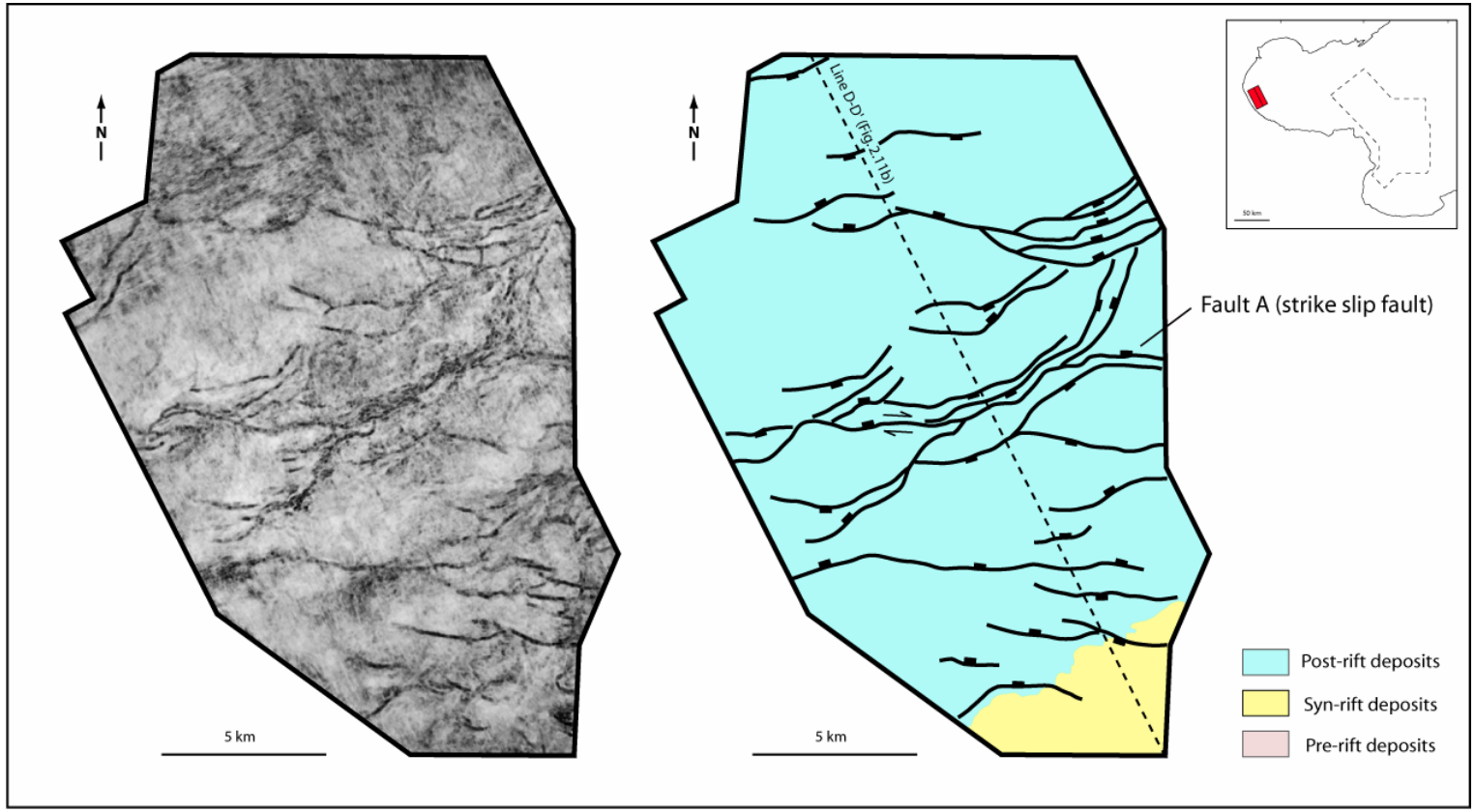

Figure 2.17b. Time slice at 1273 ms level (coherency display) showing the distribution of normal faults and strike-slip fault A. See figure 2.7 and 2.11b for location of time slice. Colors correspond to the different megasequences exposed at this level: red = MS1; yellow = MS2 and blue = MS3.

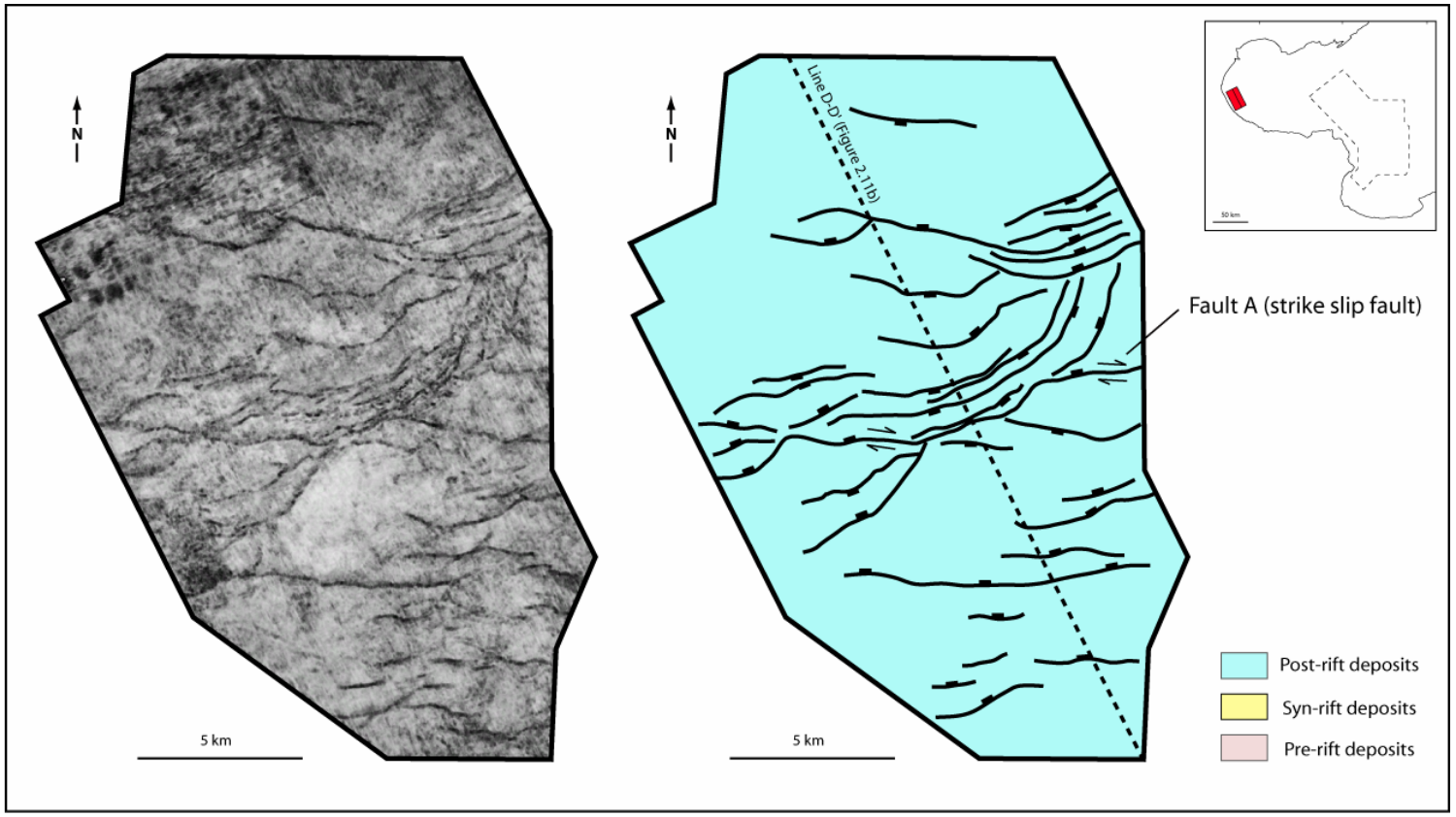

igure 2.17c. Time slice at 758 ms level (coherency display) showing the distribution of normal faults and strike-slip fault A. See figure 2.7 and 2.11b for location. Colors correspond to the different megasequences; red = MS1; yellow = MS2 and blue = MS3.

In cross section, the fault strands of this family commonly merge downward into a single strand near the top the Paleogene sedimentary section (MS2) and extend downward into basement (Figures 2.12b and 2.13b) . They diverge upward into flower structures in Neogene and Quaternary strata and in some cases the most active strands cut the sea floor (Figures 2.12b and 2.13b).

2.5.4 Paleogene and Neogene structures formed along the Tan-Lu right-lateral strike-slip fault system

In the study area, the Tan-Lu fault has been mapped in three different locations (labeled segments A, B, and C in Figure 2.18) in order to highlight the different local styles of deformation along the fault zone. The Tan-Lu fault zone shows many of the structural and stratigraphic features commonly associated with strike-slip deformation (Christie-Blick, 1985). In map view, the fault zone is characterized by a curvilinear principal displacement zone up to 3500 meters in width (Figures 2.14, 2.15 and 2.16). In cross-sectional view, the fault zone is characterized by (1) steeply dipping to vertical, basement involved faults (Figure 2.18a); (2) structurally complex, upward branching fault patterns or "flower structures" (Figure 2.18b); (3) zones of intense shear deformation isolated between relatively undeformed areas (Figures 2.18b and 2.18c); (4) contemporaneous normal and reverse faults within the same flower structure (Figure 2.18b); and (5) variable magnitude and sense of separation for different horizons offset by the same fault (Figure 2.18b).

2.5.4.1 Southern Tan-Lu fault in Bohai Bay (fault segment A)

Segment A, the southern part of the Tan-Lu fault in the study area (Figure 2.18a), is characterized by two active fault strands with significant vertical separation that are

collinear with mapped traces projecting into the basin from the Shandong Province, south of the study area (Allen et al., 1997; Yang and Xu, 2004)(Figure 2.4 and 2.7). Most of the strike-slip fault deformation occurred in Paleogene strata which show an eastside-down separation of about 1.2 s (Figure 2.18a). Vertical throw decreases upward, and deformed Paleogene strata are unconformably overlain by less deformed Neogene sediments.

2.5.4.2 Central Tan-Lu fault in Bohai Bay (fault segment B)

Segment B, the central part of the Tan-Lu fault system (Figure 2.18b), is characterized by both positive and negative flower structures. High-angle reverse faults associated with the positive flower structures are well developed in the Paleogene section (MS2)(Figure 2.18b). In contrast, high-angle normal faults associated with negative flower structures are well developed in the Neogene section (MS3)(Figure 2.18b). The fault strands merge downward and the Tan-Lu fault is inferred to be a thick-skinned, vertical fault that extends as a single strand downward into basement. Apart from the positive flower structures, a series of faulted anticlines developed in the Paleogene section may have formed during an earlier phase of (~40 Ma) of right-lateral movement of the Tan-Lu fault (Hsiao et al., 2004; Yang and Xu, 2004). Outside the Tan-Lu fault zone in segment B, Paleogene and Neogene strata are relatively flat or gently folded.

2.5.4.3 Northern Tan-Lu fault in Bohai Bay (fault segment C)

Segment C of the northern Tan-Lu fault (Figure 2.18c) is characterized by a single 4-km wide negative flower structure. High-angle normal faults associated with the negative flower structure are well developed in both the Paleogene and Neogene sections. Fault strands merge at depth close to the top of the pre-Tertiary “basement” where the

fault becomes a single, vertical fault. As in segment B, Paleogene and Neogene strata are relatively undeformed away from the Tan-Lu fault. The structure of segment C is similar to structures described by Hsiao et al. (2004) in the area of the Tan-Lu fault in Liaodong Bay, approximately 200 km north of the study area (Figure 2.7).

2.5.5 Tectonic interpretation of subsidence plots of wells in the Bohai Basin

Subsidence analysis in the Bohai area includes calculations of tectonic subsidence or subsidence caused exclusively by tectonic mechanisms. This method consists of removing the contributions of sediment loading, compaction and changes in sea level through time from the total subsidence (Steckler and Watts, 1978).

Figure 2.19 shows subsidence plots in the offshore part of Bohai Basin constructed using one well from this study (Figure 2.19a) and ten wells studied by Hu et al. (2001).

Although my well and those of Hu et al. (2001) show some minor differences three main tectonic phases in the development of the basin can be identified on all the wells: 1) an initial high rate of tectonic subsidence from early Eocene (~ 42 Ma) to late Oligocene (~ 24.6 Ma); 2) a period of tectonic quiescence with little subsidence from the early Miocene until the late Miocene (~ 5.1 Ma); and 3) a period of tectonic reactivation and uplift from the late Miocene to the present. This sequence of events is similar to the events constrained by fission track dating of sedimentary samples from the Bohai Basin (Hu et al., 2001).

Subsidence curves in the Liaohe depression (Figure 2.19c) allow further subdivision of the initial period of rapid subsidence into two episodes: (Ia) a period of high subsidence rates from previous to 42 to 38 Ma followed by a period of tectonic quiescence from 38 to 32.8 Ma; and (Ib) a period of high subsidence rates from 32.8 to

27.4 Ma and a subsequent period of tectonic quiescence until the end of the Oligocene (Hu et al., 2001). This finer subdivision of tectonic subsidence is not evident in the subsidence plots from Hu et al. (2001) in the Huanghua and Bozhong depressions to the north (Figures 2.19a and 2.19b).

Small differences between the plots are likely caused by the different geographic locations of the wells used in the subsidence calculations along with their different tectonic settings in the various depressions and highs of the basin (Figure 2.19). For example, wells used by Hu et al. (2001) in the Liaohe depression (Figure 2.19c) are located on hanging wall blocks of normal faults. Consequently, they show an abrupt increase in the rates of tectonic subsidence resulting from the main phase of early Eocene to late Oligocene rifting. Conversely, wells in the Huanghua depression shown by Hu et al. (2001) are located on footwall blocks of normal faults (Figures 2.11b and 2.19b). Therefore, these wells record only a minor pulse of the main Eocene-Miocene extensional event that is well expressed in the other areas.

2.6. DISCUSSION

2.6.1 Main events in the geologic evolution of the Bohai Basin

Based on my analysis of megasequences, regional unconformities, fault systems, and thickening trends and ages; I propose a regional rift model for the Paleocene-Oligocene formation of the Bohai Basin that is supportive of the subduction rollback extensional mechanism shown in Figure 2.3a (Watson et al., 1987).

Figure 2.18. Paleogene and Neogene structures of the Tan-Lu fault zone. (a) Segment A of the southern Tan-Lu fault is characterized in cross section by apparent normal faults with significant vertical separation. Most of the fault deformation occurs in Paleogene strata where the main strand shows an eastside-down separation of about 1.2 s. (b). The central Tan-Lu fault zone in segment B is characterized by positive and negative flower structures. High-angle reverse faults associated with the positive flower structures are well developed in the Paleogene section (MS2). High-angle normal faults associated with the negative flower structures are well developed in the Neogene section (MS3). (c) Segment C of the northern Tan-Lu fault zone is characterized by a 4-km wide negative flower structure. High-angle normal faults associated with the negative flower structure are well developed in the Paleogene and Neogene sections.

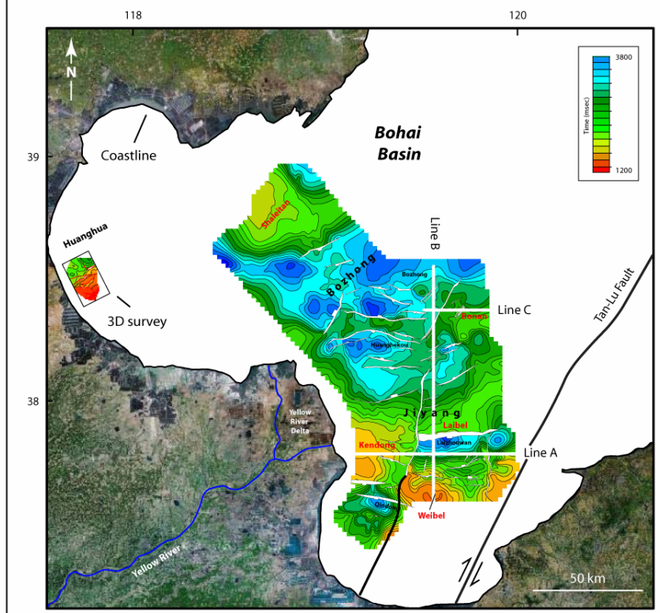
118
120
39
38
N
Coastline
Bohai
Basin
Huanghua
3D survey
Line B
Line C
Line A
Tan-Lu Fault
Bozhong
Jiyang
Kendong
Laibei
Weibei
Yellow River Delta
Yellow River
50 km
3800
1200
Time (msec)

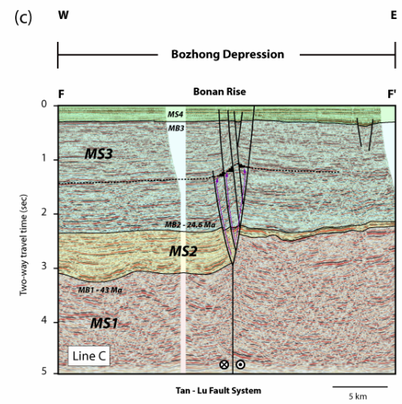
(c)
W
E
Bozhong Depression
F
Bonan Rise
F'
MS4
MB3
MS3
MB2 - 24.6 Ma
MS2
MB1 - 43 Ma
MS1
Line C
Two-way travel time (sec)
Tan - Lu Fault System
5 km

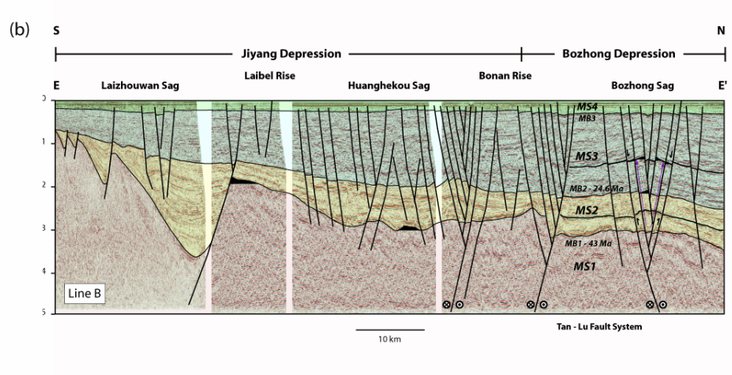
(b)
S
N
Jiyang Depression
Bozhong Depression
E
Laizhouwan Sag
Laibel Rise
Huanghekou Sag
Bonan Rise
Bozhong Sag
E'
MS4
MB3
MS3
MB2 - 24.6Ma
MS2
MB1 - 43 Ma
MS1
Line B
Tan - Lu Fault System
10 km

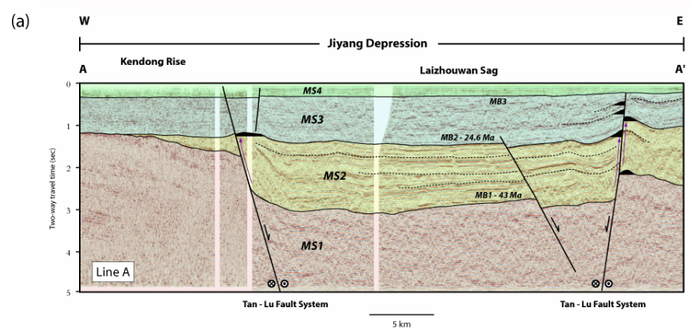
(a)
W
E
Jiyang Depression
A
Kendong Rise
Laizhouwan Sag
A'
MS4
MB3
MS3
MB2 - 24.6 Ma
MS2
MB1 - 43 Ma
MS1
Line A
Two-way travel time (sec)
Tan - Lu Fault System
Tan - Lu Fault System
5 km

Figure 2.18

Figure 2.19. Subsidence plots from the offshore Bohai Basin. Figure 2.19a is from this study and figures 2.19b and 2.19c are modified from Hu et al., 2001. Three main tectonic phases of basin subsidence can be identified: **Phase I**) an initial high rate of regional rift-related tectonic subsidence from early Eocene (~ 43 Ma) to late Oligocene; **Phase II**) a period of tectonic quiescence from the early Miocene until the late Miocene; and **Phase III**) a period of tectonic rejuvenation from the late Miocene to the present. Small differences between the subsidence histories shown on all plots are likely caused by the different geographic locations of the wells used in the subsidence calculations along with their different tectonic settings in the various depressions (rifts) and highs (intervening horst blocks) of the Bohai Basin (Figure 2.19). For example, wells used by Hu et al. (2001) in the Liaohe depression (shown on Figure 2.19c) are located on the hanging wall or downthrown blocks of normal faults. Consequently, they show an abrupt increase in the rates of tectonic subsidence resulting from the main phase of early Eocene to late Oligocene rifting. Wells in the Huanghua depression studied by Hu et al. (2001) are located on footwall or upthrown blocks of normal faults (Figures 2.11b and 2.19b). Therefore these wells record only a minor pulse of the main Eocene-Miocene subdidence event related to rifting that is better expressed from wells from the Huanghua rift.

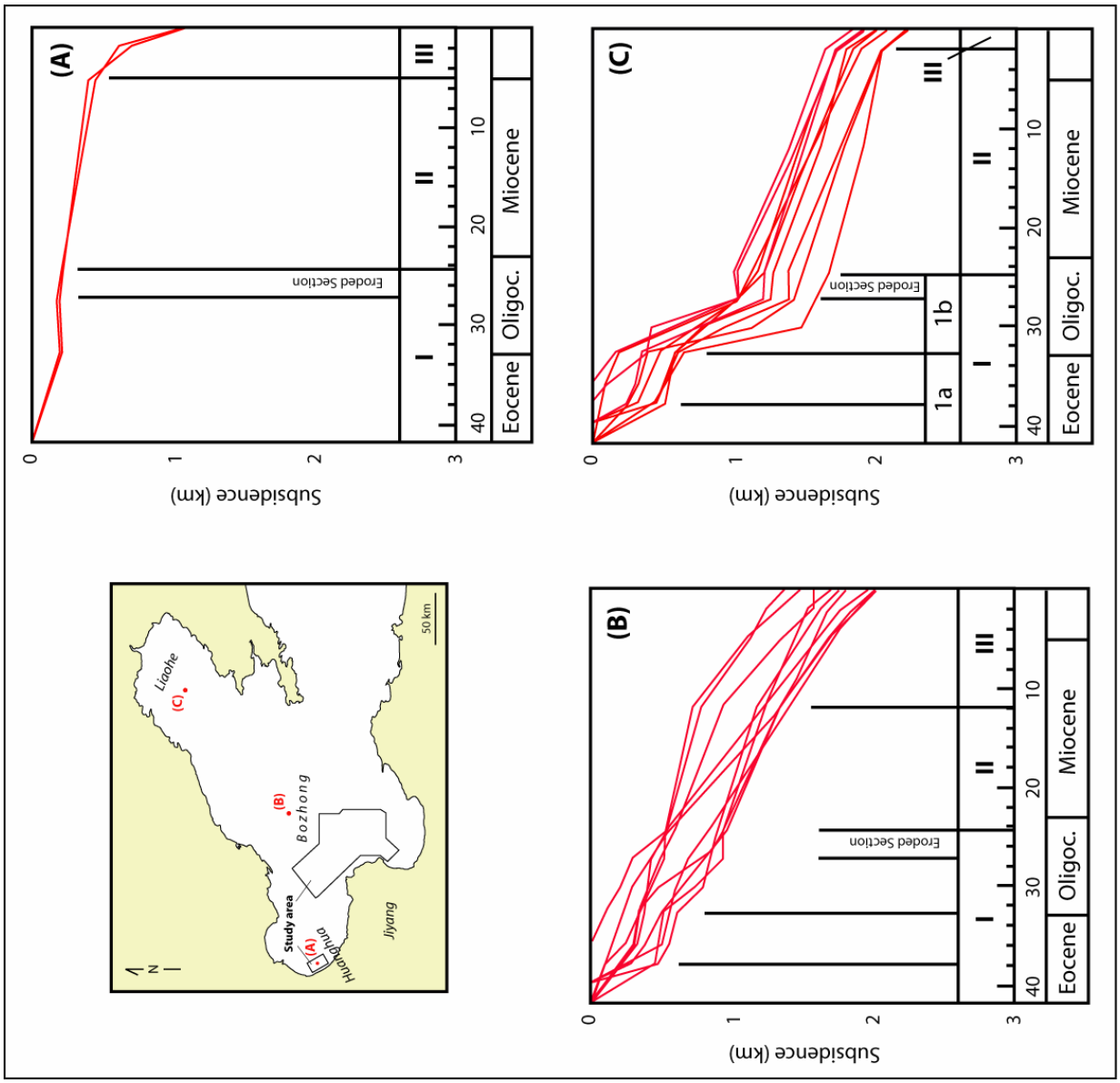
(A)
(B)
(C)
Subsidence (km)
Eroded Section
Eocene
Oligoc.
Miocene
I
II
III
1a
1b
Liaohe
Bozhong
Huanghua
Jiyang
Study area
50 km
N

Figure 2.19

2.6.1.1 Onset of rifting (late Paleocene – early Eocene)

Tertiary rifting began in the Bohai Basin during late Paleocene to early Eocene time with alluvial fan deposition of the Kongdian Formation as syn-rift deposits (Hu et al., 1989; Allen et al., 1997)(Figure 2.20a). Rift initiation was characterized by extensive faulting, subsidence, rapid sedimentation and volcanic activity (Yang and Xu, 2004). Basin opening occurred on a series of NE and E-W oriented isolated half-grabens located in the onshore part of the basin (fault family 1). The orientation of fault family 1 indicates basin-orthogonal extension in a WNW-ESE direction (Ye et al., 1985; Hsiao et al., 2004)(Figure 2.20a). Pre-existing NNE and NE Mesozoic faults and folds in the pre-rift unit (MS1)(Figure 2.5) acted as zones of weakness for the development of NE-striking Cenozoic rift structures in the Bohai Basin (Ma et al., 1982; Ye et al., 1985; Wang and Tonghe, 1995).

Erosion of the uplifted rift blocks, together with continued fault-controlled subsidence, accounts for deposition of alluvial fans of the Paleocene Kongdian Formation within the syn-rift section of the half-grabens (Figures 2.20a and 2.8b).

2.6.1.2 Rifting climax (early - middle Eocene)

Rates of subsidence in the Bohai basin increased dramatically during the middle Eocene (Figure 2.19) and thick sediments accumulated in the offshore part of the Bohai Basin (Figure 2.20b). Extension in the offshore part of the basin occurred on a series of half-grabens with master faults striking roughly E-W (fault family 2) indicating basin-orthogonal extension in a north-south direction (Figures 2.14 and 2.20b).

MB1 represents the lower boundary of the early Eocene syn-rift sequence and marks the beginning of the structural development in the offshore part of the Bohai Basin (Figure 2.14). Isolated NE- striking strike-slip faults from the Tan-Lu fault zone have

also been identified in the eastern margin of the Bohai Basin (Figure 2.14). According to Hsiao et al. (2004), right-lateral slip of the Tan-Lu fault zone initiated during the Eocene about 40 Ma but its deformational effects were confined to the Bozhong and Liaohe depressions (Figure 2.7 and 2.12b). Transpressional and transtensional anticlines related to the Tan-Lu fault zone are present in the Paleogene and Neogene strata of MS2 and MS3, respectively (Figure 2.12b).

As the rates of subsidence increased, half-grabens became sediment-starved and deep-water lacustrine shale and mudstone of the Eocene Shahejie formation were widely distributed across the entire basin (Figures 2.6 and 2.20b). Half-grabens were isolated from one another by uplifted fault blocks which also served as local source areas (Figure 2.9b). Once rifting decreased during the middle to late Oligocene, lacustrine deposition gave way to fluvial sediments of the Oligocene Dongying Formation (Hu et al., 1989; Allen et al., 1997 and Yang and Xu, 2004)(Figures 2.6 and 2.20c). These deposits represent a regression from the lacustrine-dominated sedimentation of the Shahejie Formation (Hu et al., 1989; Allen et al., 1997).

2.6.1.3 Regional erosion and post-rift thermal subsidence (late Oligocene)

Regional-scale rifting ended during the late Oligocene (Figure 2.19) when a regional uplift and erosional unconformity (MB2) affected the entire basin (Allen et al., 1997; Hsiao et al., 2004; Yang and Xu, 2004)(Figures 2.8, 2.9, 2.10, 2.11, 2.12, 2.13 and 2.15). MB2 represents the boundary between the syn-rift (MS2) and the post-rift (MS3) sequences and marks the termination of the rifting stage. Following erosion, an overall widespread thermal subsidence produced a broad subsidence and sag deposits of MS3 (Figures 2.8, 2.9, 2.10, 2.11, 2.12 and 2.13). MS3 consists of widespread Neogene fluvial deposits from the Miocene and Pliocene Guantao and Minghuazhen Formations (Figure

2.6)(Chapters 3, 4). These sand and shale deposits blanket the underlying horst-and-graben topography of the entire Bohai Basin (Figures 2.20d and 2.15).

2.6.1.4 Strike-slip deformation (late Miocene to recent)

Strike-slip deformation began in the Bohai Basin during late Miocene – early Pliocene (Figure 2.19) as a consequence of motion along the right-lateral Tan-Lu fault. Strike-slip displacement initiated at 12 Ma in the Bozhong depression (Figure 2.19b), at 5.1 Ma in the Huanghua depression (Figure 2.19a), and at 2.4 Ma in the Liaohe depression (Figure 2.19c). MB3 represents the boundary between MS3 and MS4 and its formation is probably related to transtensional and transpressional deformation and uplift locally developed along strike-slip faults.

Splays of secondary faults that branch off the main NE and E-W striking faults suggest that older normal faults formed during the period of Paleogene extension were locally reactivated as strike slip faults (Figure 2.11b and 2.12b). Strike slip-deformation is also responsible for the formation of new E-W and WSW-ENE striking faults deforming Neogene rocks (fault family 3) located in the sag basin overlying the center of the basin (Figures 2.16 and 2.20d). The Taihang Shan fault, located at the western edge of the Bohai Basin, has a southern segment striking north – south and a northern segment that strikes northeast (Allen et al., 1997)(Figures 2.2a, 2.4 and 2.7). The Taihang Shan and Tan-Lu faults give the Bohai Basin its distinctive "lazy-Z" map pattern. Recent seismicity of major earthquakes and the regional-scale "lazy-Z" map pattern of the basin indicate the importance of right-stepping pull-apart control on the younger sag section (Figures 2.4 and 2.20d). Although earthquake focal mechanisms have recorded dextral movement on two parallel faults just east of the Taihang Shan fault (Figures 2.4 and

2.20d), there is no geologic evidence for large-scale strike-slip displacement on the Taihang fault zone (Allen et al., 1997).

2.6.2 Distinguishing the driving tectonic mechanism for Cenozoic extension in the Bohai Basin

2.6.2.1 Regional extension related to subduction rollback

The development of the East China Sea and Subei-South Yellow Sea Basins (Figure 2.2) are not directly linked with the Tan–Lu fault zone, however they show similar northwest–southeast direction of early Tertiary regional extension (Lee et al., 2001; Zhang et al., 2003; Lee et al., 2006). The widespread distribution of rift basins in eastern Asia (Figure 2.2a) and the consistency of their normal fault trends and inferred extensional directions suggest that the early Tertiary rifting in northeast China was initiated by a regional subduction rollback-related extensional event (Figure 2.3a), as opposed to a more localized right-lateral strike–slip pull-apart opening (Figure 2.3b). Therefore, I favor the previously proposed rollback of the Pacific plate subducted beneath the Asian continent as the ultimate cause of Paleogene extension of the Bohai Basin (Watson et al., 1987; Allen et al., 1997)(Figure 2.3a).

Schellart and Lister (2005) based on the results from scaled physical models, demonstrated that subduction beneath the East Asian active margin is responsible for the widespread deformation in East Asia as far west as the Baikal rift zone that is 1300 km northwest of Bohai Basin and 3300 km from the site of Pacific subduction. Moreover, Northrup et al. (1985) showed a marked decrease in the convergence rate between the overriding Eurasian plate and subducting Pacific plate from about 120-140 mm/year in the Late Cretaceous to a minimum of about 30-40 mm/year in early Eocene (Figure

2.21a). In their interpretation, such a large decrease in the convergence rate reduced compressional stresses across the subduction boundary and induced extension in the overriding plate along the active margin. Schellart (2005) used dynamic modeling of subduction to demonstrate that a reduction in velocity of a subducting plate will promote slab rollback therefore supporting the idea that rollback of the Pacific slab occurred along the East Asian margin during the latest Cretaceous to middle Miocene and is indeed responsible for the widespread deformation in East Asia and for the extensional deformation of Paleogene age that I describe in this chapter from the Bohai Basin.

2.6.2.2 Strike slip tectonism

Strike-slip deformation in Bohai Bay is attributed to a change in the direction of the convergence vector between the Eurasian plate and the subducting Pacific plate during early to late Miocene time (Northrup et al., 1985)(Figure 2.21b). During this time, the convergence vector at the plate boundary changed from NWW to roughly east – west, imparting a component of dextral shear to the extensional deformation in the Asian continent.

2.7. PETROLEUM GEOLOGY OF THE BOHAI BASIN

2.7.1 Major source rocks of the Bohai Basin

Rapid subsidence in the offshore part of the Bohai Basin since late Eocene to Oligocene (Figure 2.19) provided favorable conditions for the deposition of source rocks in isolated rifts; rift subsidence and burial during the sag phase enhanced their hydrocarbon maturity and generation (Yang and Xu, 2004). The most important source

rocks in the basin are located in megasequence 2 and correspond to the lacustrine facies of the Eocene-Oligocene Shahejie and Dongying Formations (Wang et al., 1992; Yang and Xu, 2004)(Figures 2.6 and 2.10b). Three sections of source rocks include:

1) The **Sha-3 member of the Eocene-Oligocene Shahejie Formation** correlates to the basal section of megasequence 2 as shown in Figures 2.6, 2.8, 2.9, 2.10, 2.11, 2.12 and 2.13. This interval is the single most important source rock unit in the Bohai Basin (Wang et al., 1992). The Sha-3 member is 300 to 900 m thick and contains sapropelic kerogen (Wang et al., 1992). Mudrocks of the Eocene Sha-3 member are thick and widespread with an organic carbon content that ranges from 0.75 to 2.3%. Extractable hydrocarbons range from 700 to 3000 ppm (Wang et al., 1990; 1992).

2) **Mudrock of the Eocene-Oligocene Sha-1 member** also contains important source rocks although they are not as prominent and widespread as the Sha-3 member. The Sha-1 member is 800 – 1000 m thick and contains sapropelic and mixed kerogens. Organic carbon ranges from 0.41 to 1.54% and extractable hydrocarbons range from 161 to 1247 ppm (Wang et al., 1990; 1992).

3) The **Oligocene Dongying Formation** contains known source rocks although they are commonly immature (Wang et al., 1990; Chi, 2001; Gong and Wang, 2001). Organic carbon ranges from 0.28 to 1.08 and extractable hydrocarbon ranges from 500 to 900 ppm.

2.7.2 Known reservoir rocks of the Bohai Basin

There are a great variety of known clastic reservoir rocks in the Bohai Basin. Sandstone reservoirs account for approximately 70% of the total reserves in the basin. Tertiary and lower Paleozoic/Proterozoic carbonates, Mesozoic volcanic strata and

Precambrian basement all form known reservoirs of lesser importance to the sandstone reservoirs (Zha Quanheng, 1984).

The most representative example of sandstone reservoirs in the Bohai Basin are fluvial sandstones of the Miocene Guantao Formation (MS3 in Figures 2.6 and 2.11b) (Chapters 3, 4). Preserved individual channel bodies are 8 to 12 m thick and consist of coarse to fine grained, locally very coarse, poorly to moderately well sorted, subangular to subrounded quartz-rich sandstone. Porosities and permeabilities range between 28 and 32% and 240 and 5500 mD, respectively. Fluvial sandstone bodies of the Pliocene Minghuazhen Formation also provide high quality reservoir rocks although these sands are thinner and less laterally continuous (Figure 2.6, 3.8, 3.9, 3.10 and 3.11)(Chapters 3, 4).

Fluvial and alluvial fan sandstones of the Paleocene Kongdian Formation and deltaic sandstone of the Oligocene Dongying Formation (Figure 2.6), although not as important as the Guantao Formation, form known reservoir rocks in the Bohai Basin. These reservoir rocks are inferior to the fluvial sandstone of the Guantao Formation due to their common mudstone intercalations and rapid lateral facies changes. Turbiditic sandstone bodies within the Eocene Sha-1 member also form reservoir rocks commonly found along the downthrown blocks of normal faults (Zha Quanheng, 1984; Hu Jianyi et al., 1988).

Lower Paleozoic and Proterozoic carbonate reservoir rocks occur as footwall uplifts along pre-Tertiary normal fault blocks that were elevated during the main phase of Cenozoic extension (see position of MS1 in Figure 2.9b). Tertiary carbonate reservoir rocks consist of thin bioclastic limestones within the Sha-4 and Sha-1 members of the Eocene-Oligocene Shahejie Formation (Du Yunhua, 1990). Reservoir porosities are

mostly provided by fractures formed by weathering, karstification, and tectonic fracturing (Yang and Xu, 2004).

2.7.3 Known structural and stratigraphic traps of the Bohai Basin

Table 1 and Figures 2.8, 2.9, 2.10, 2.11, 2.12 and 2.13 show the main structural traps in the Bohai Basin (Figure 2.22). Anticlinal and fault-related traps are the most important trap types in the study area. Specific types of structural traps include: 1) tilted-fault blocks, 2) normal-fault hanging walls, 3) fault-controlled fault anticlines, 4) transpressional-fold anticlines and 5) flower structures (Figures 2.8, 2.9, 2.10, 2.11, 2.12 and 2.13). Fractured and weathered pre-Tertiary and pre-rift basement highs (pre-rift), also known as "buried hills" (Allen et al., 1997) also form good reservoirs in the Bohai Basin.

Stratigraphic traps are less important in the Bohai basin and include: 1) unconformity-controlled reservoirs (sub-unconformity truncations) and 2) sandstones encased in floodplain facies as in the case of the Minghuazhen Formation (Chapters 3, 4). Most stratigraphic traps occur in syn-rift as well as post-rift intervals

2.7.4 Known hydrocarbon seals of the Bohai Basin

Two rapid increases in the rate of tectonic subsidence during the late Paleocene – early Eocene and late Eocene – early Oligocene (Figure 2.19c) led to the deposition of widespread mudstone of the Sha-3 member of the Shahejie Formation and the lower Dongying Formation. Both mudstone units form regional seals on hydrocarbon accumulations (Figure 2.6). Thermal subsidence during late Oligocene – early Miocene

(Figure 2.19) formed a third regional seal, mudstones of the lower Minghuazhen Formation (Yang and Xu, 2004)(Figure 2.6, 3.8, 3.9, 3.10 and 3.11)(Chapters 3, 4).

2.7.5 Main petroleum-producing regions of the Bohai Basin

As of December 31, 2005, the net proven reserves in the Bohai Basin amounted to 1,044 million barrels of oil (MBOE) with an average daily production of 187, 021 barrels of oil (BOE)(China National Offshore Oil Corporation, 2005). Figure 2.22 shows the location of giant and major oil and gas fields in the Bohai Basin. Oil fields are scattered throughout the Bohai Basin which is the commonly observed pattern in areas of widespread normal faulting like the North Sea and Sirte rift of Libya. In general, the main producing areas are the Yellow River Delta area and adjacent areas in the Jiyang Depression, the central and offshore regions of the Huanghua depression (Figure 2.11b), the SE region of the Linqing depression, the eastern portion of the Jizhong depression, the Bonan rise and neighboring regions in the Bozhong depression (Figure 2.12b) and the onshore and offshore portions of the Liaohe depression.

In the offshore portion of the basin most major oil discoveries have been made in Neogene clastic reservoirs. The proven in-place reserves of the Guantao–Minghuazhen Formations reservoirs in the offshore portion of the basin account for 70% of the total proven in-place reserves (Gong et al., 2000). Conversely, in the onshore portion of the basin most of the major discoveries have been made in pre-Tertiary and Paleogene deposits (Gong et al., 2000). The proven in-place reserves of the pre-Tertiary and Paleogene sections in the onshore Bohai Basin accounts for an average of 77% of the total proven in-place reserves (Gong et al., 2000).

Figure 2.20a. Late Paleocene-early Eocene onset of rifting in the Bohai Basin. Extension was localized on the Linqing, Jiyang, Huanghua, Jizhong and Liaohe depressions (rifts) as a result of west-northwest oblique rifting. Isopach maps are modified from Hu et al. (1989) and Yang and Xu (2004). Faults in the Liaohe depression are from Hsiao et al. (2003).

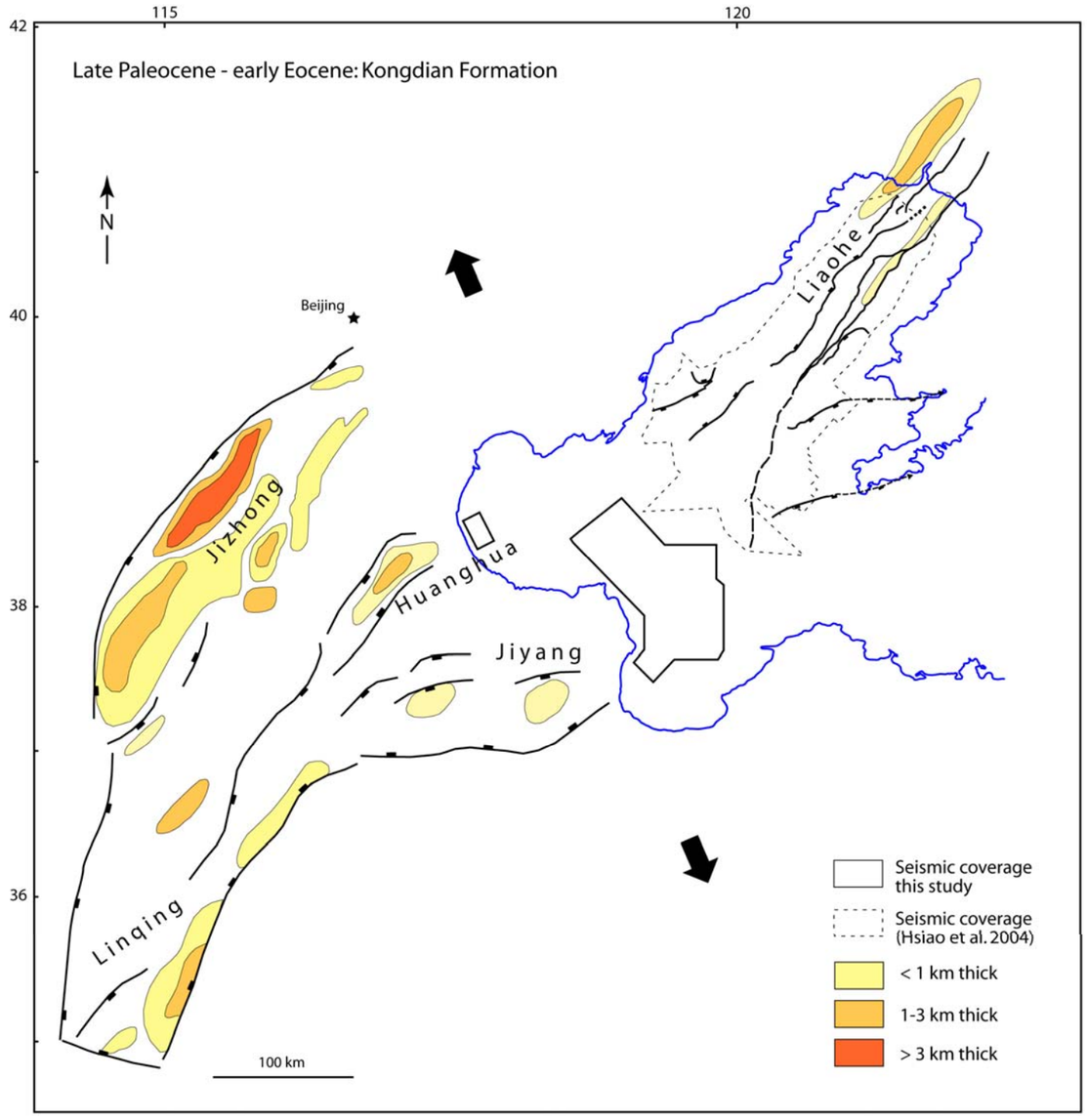
Late Paleocene - early Eocene: Kongdian Formation
115
120
42
40
38
36
N
Beijing
Liaohe
Jizhong
Huanghua
Jiyang
Linqing
100 km
Seismic coverage this study
Seismic coverage (Hsiao et al. 2004)
< 1 km thick
1-3 km thick
> 3 km thick

Figure 2.20a

Figure 2.20b. Early Eocene-middle Oligocene maximum rift phase of the Bohai Basin. Rifting reached its maximum during the middle Eocene with the deposition of the Shahejie Formation in fault-bounded rifts. Half-grabens trend roughly east-west and formed as a result of north-south oblique rifting. Isopach maps are modified from Hu et al. (1989) and Yang and Xu (2004). Inset summarizes main trends of normal faults formed during this time period.

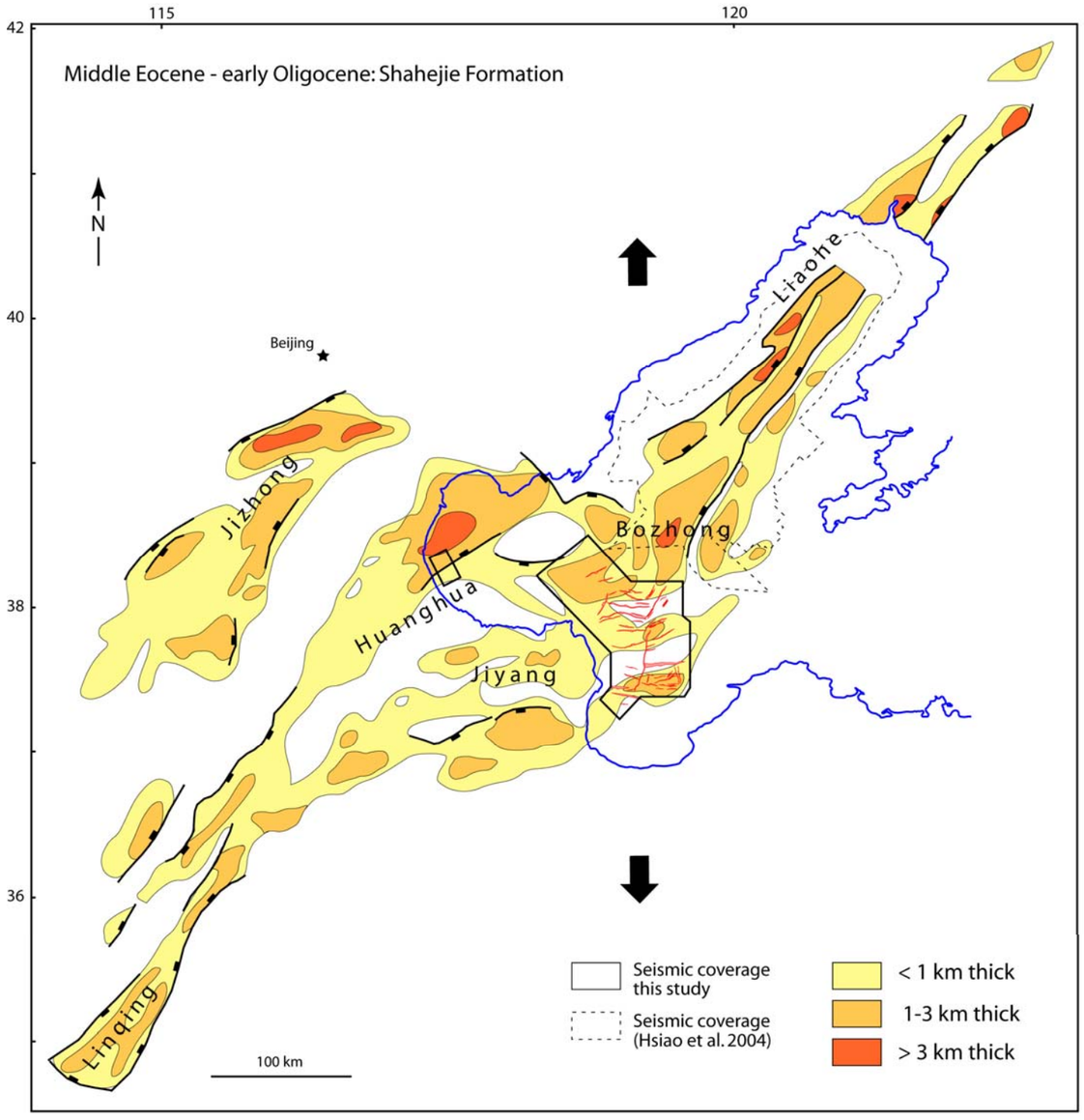
115
120
42
40
38
36
Middle Eocene - early Oligocene: Shahejie Formation
N
Beijing
Liaohe
Jizhong
Bozhong
Huanghua
Jiyang
Linqing
100 km
Seismic coverage this study
Seismic coverage (Hsiao et al. 2004)
< 1 km thick
1-3 km thick
> 3 km thick

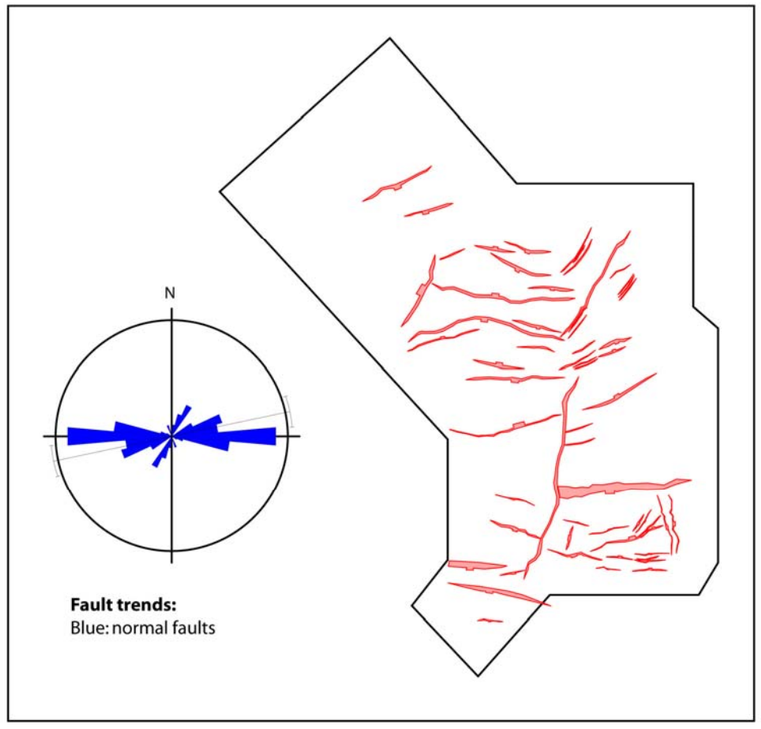
N
Fault trends:
Blue: normal faults

Figure 2.20b

Figure 2.20c. Late Oligocene tectonic evolution of the Bohai Basin. During middle to late Oligocene time, rifting began to decrease in intensity and lacustrine deposition in fault-bounded rift basins gave way to fluvial sediments of the Dongying Formation that were deposited on less faulted alluvial plains. Isopach maps are modified from Hu et al. (1989) and Yang and Xu (2004).

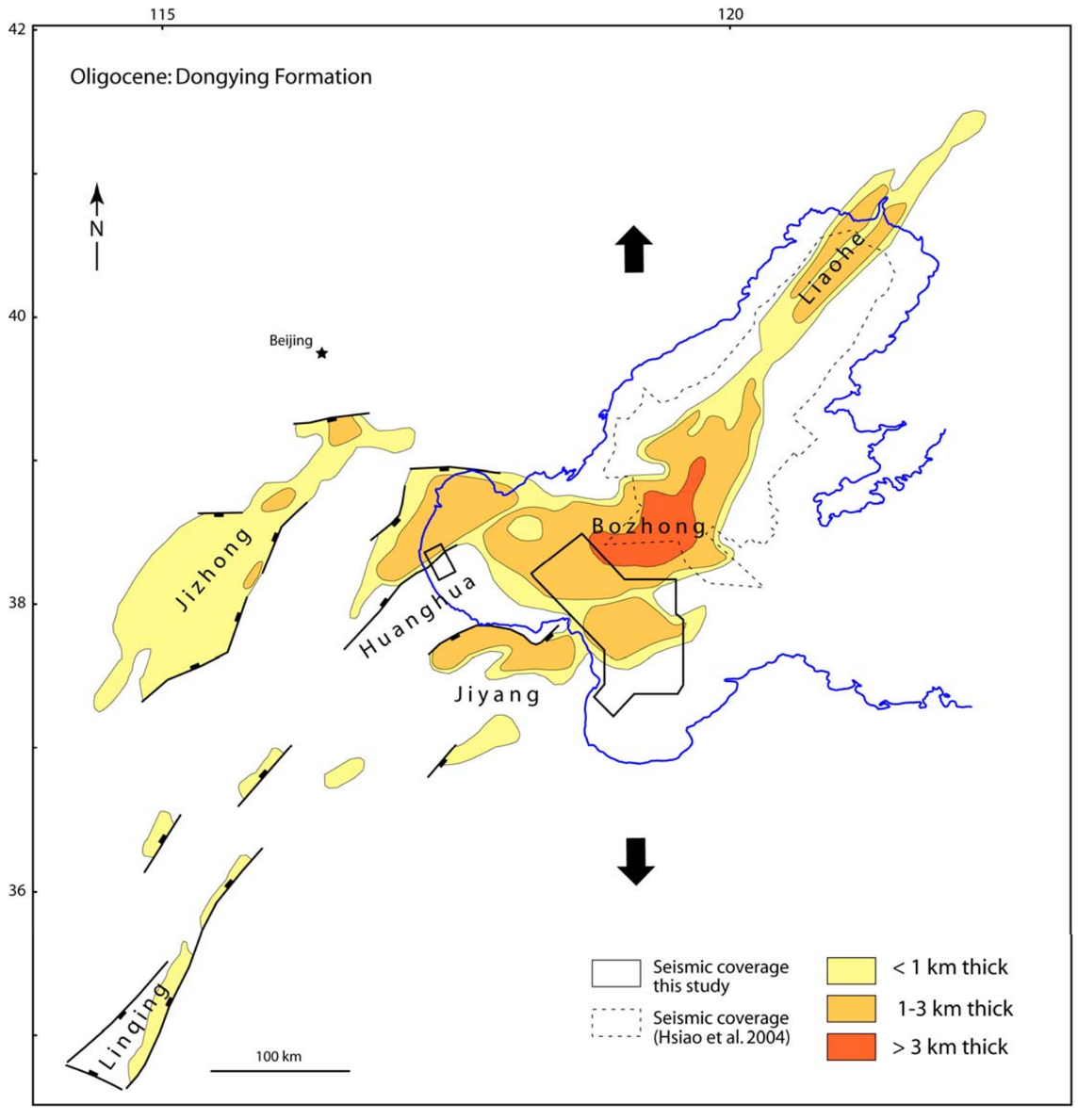
115
120
42
40
38
36
Oligocene: Dongying Formation
N
Beijing
Liaohe
Bozhong
Jizhong
Huanghua
Jiyang
Linqing
100 km
Seismic coverage this study
Seismic coverage (Hsiao et al. 2004)
< 1 km thick
1-3 km thick
> 3 km thick

Figure 2.20c

Figure 2.20d. Neogene tectonic evolution of the Bohai Basin. Late Miocene – early Pliocene marks the initiation of right-lateral strike-slip faulting across the Bohai basin. This period is characterized by the reactivation of previous rift-related normal faults as strike-slip faults and by the formation of new east-west and west-southwest-striking normal and strike-slip faults as summarized on the inset rose diagrams. Earthquakes and GPS data indicate that right-lateral strike-slip faulting continues to the present-day in a pattern consistent with the regional-scale "lazy-Z" map pattern of the Cenozoic Bohai depocenter (cf. Figure 2.4). Thick solid lines represent the present boundary of Bohai basin and Hebei Plain sediments (Chen and Nabelek, 1988). Solid circles indicate epicenters of major earthquakes (M > 6) since 1600 A.D. Recent seismicity, major structures and focal mechanism solutions are compiled Chen and Nabelek (1988), Yang et al. (1989) and Yang and Xu (2004). Faults in red are from this study. Isopach maps are modified from Hu et al. (1989) and Yang and Xu (2004).

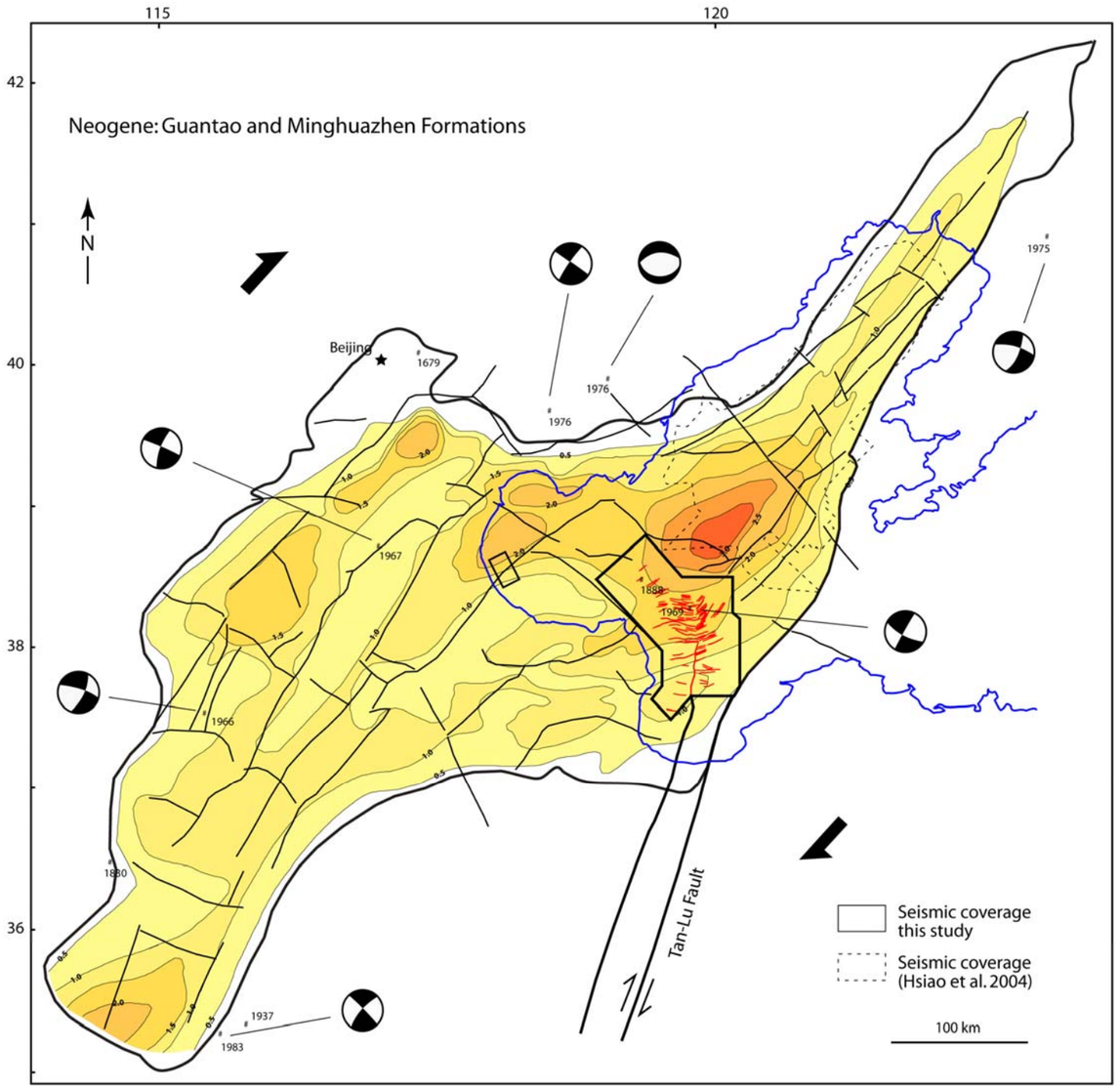
115
120
42
40
38
36
Neogene: Guantao and Minghuazhen Formations
N
Beijing
1679
1975
1976
1976
1967
1888
1969
1966
1880
1937
1983
Tan-Lu Fault
Seismic coverage this study
Seismic coverage (Hsiao et al. 2004)
100 km

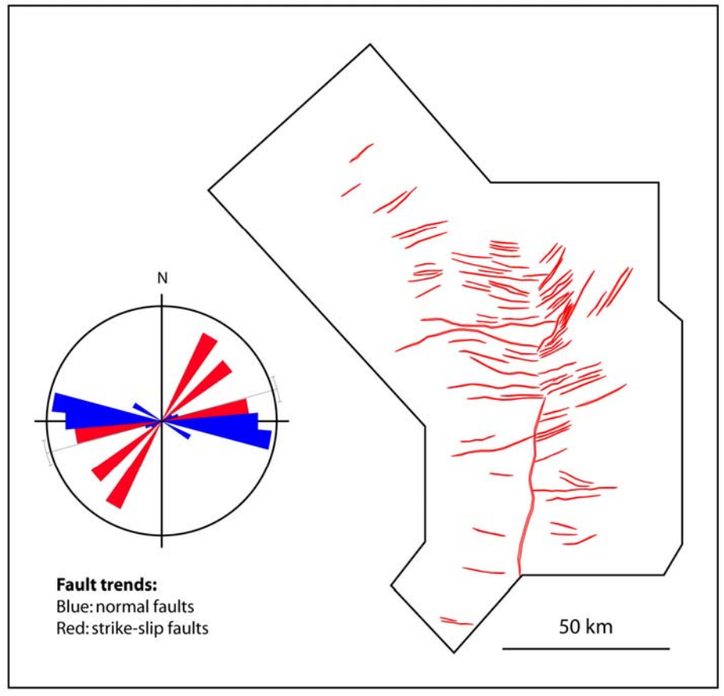
N
Fault trends:
Blue: normal faults
Red: strike-slip faults
50 km

Figure 2.20d

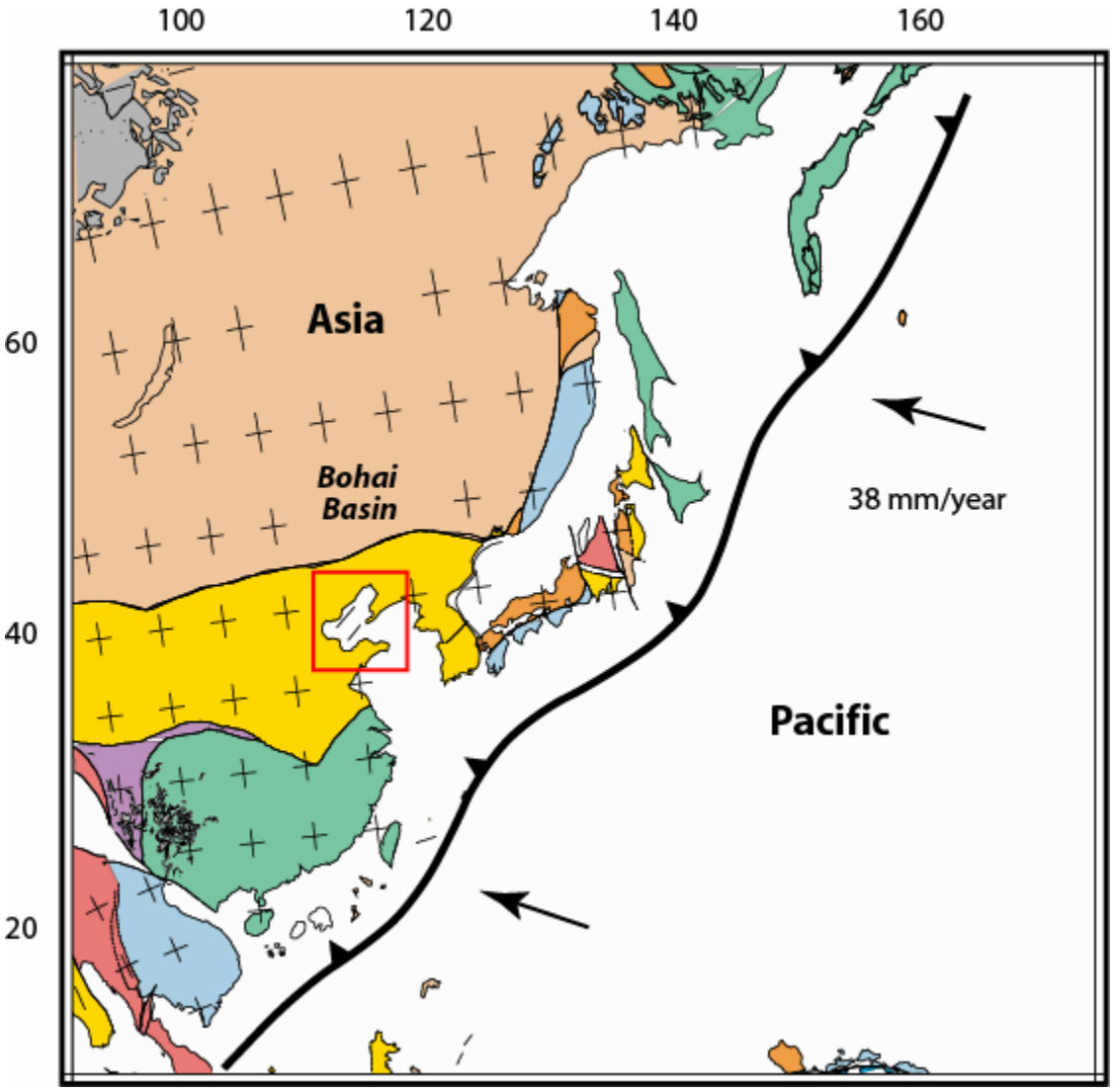

Figure 2.21a. Reconstruction of Pacific - Asia plate boundary in the early Eocene about 55 Ma (courtesy of UTIG PLATES project; rates and directions of plate convergence from Northrup et al., 1995). A marked decrease in the rate of Pacific – Eurasia subduction occurred during the late Cretaceous and Paleogene, from about 120 - 140 mm/yr in the late Cretaceous to slower rates of about 30 - 40 mm/yr in Eocene time. This period of decelerating convergence correlates with a period of widespread extension along the Eastern margin of Eurasia, including the rifting that affecting the Bohai basin shown in the red boxed area.

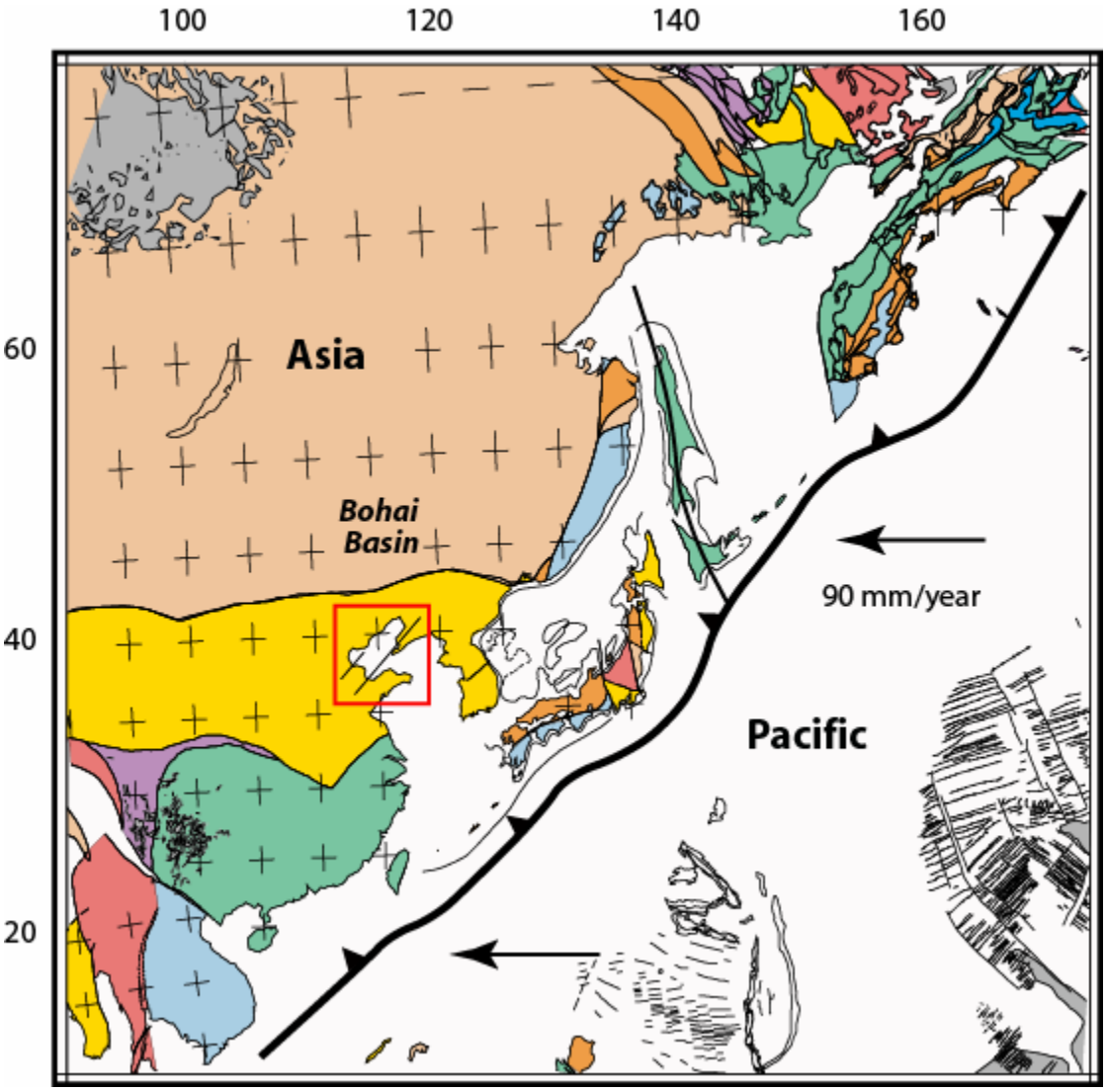

Figure 2.21b. Reconstruction of Pacific - Asia plate boundary in the early to middle Miocene (courtesy of UTIG PLATES project). Note that east -west convergence occurring across the plate boundary imparts a component of right-lateral shear to the extensional deformation in the Asia continent (convergence rates from Northrup et al, 1995).

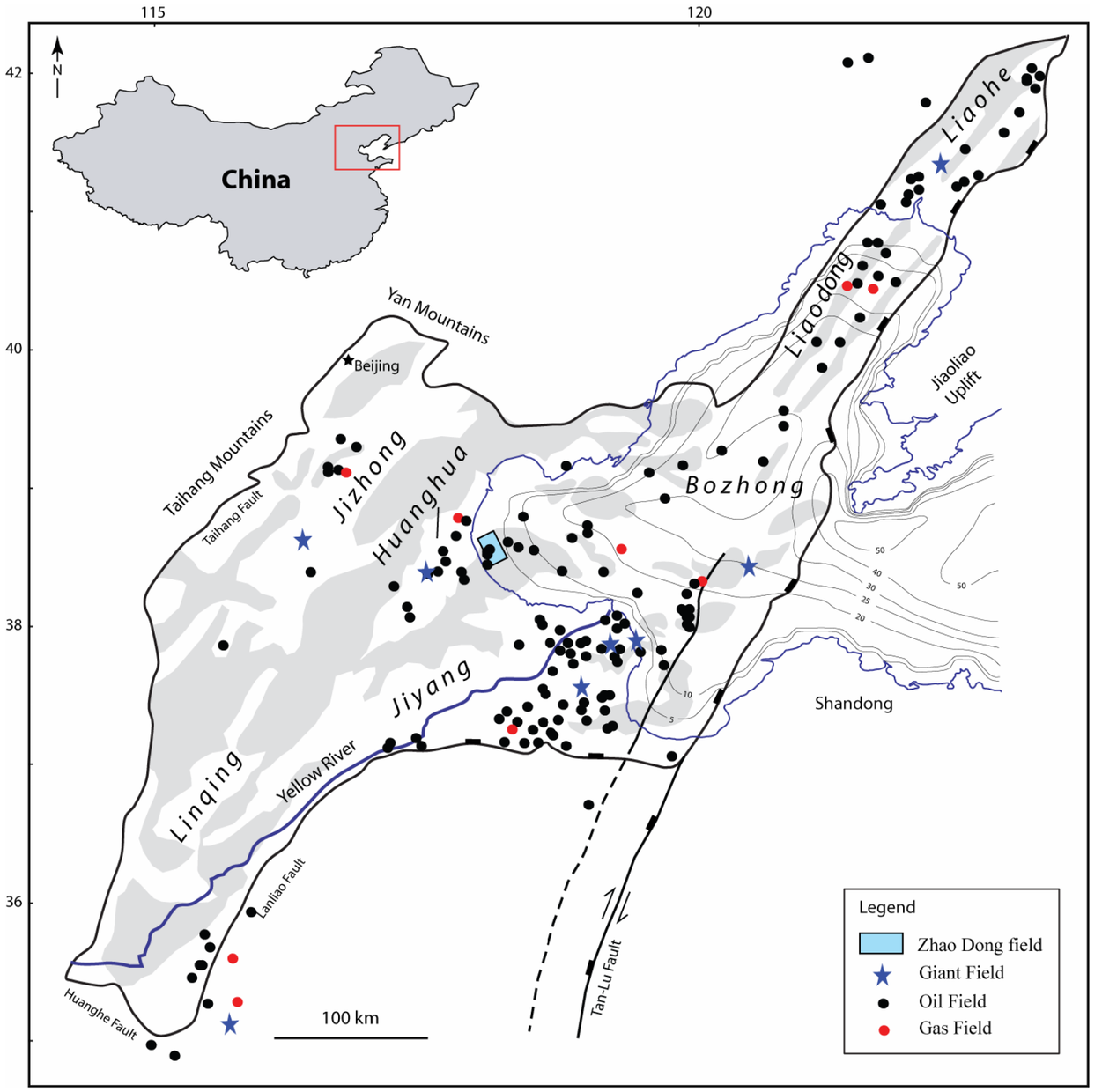

Figure 2.22. Location of oil and gas fields in the Bohai Basin (from Steinshouer et al., 1999). The main producing areas in the basin are concentrated near the Yellow River delta and adjacent areas in the Jiyang Depression, the central and offshore regions of the Huanghua depression, the southeast region of the Linqing depression, the eastern portion of the Jizhong depression, the Bonan rise and neighboring regions in the Bozhong depression and the onshore and offshore portions of the Liaohe depression. Major rifts or "depressions" in Chinese literature are labeled in largest type (modified from Hao et al., 2007). Bathymetric contours are from Sundermann and Feng (2004).

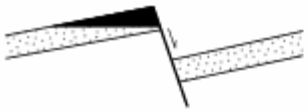	Tilted-fault block
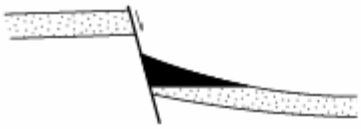	Normal fault hanging-wall
	Fault-controlled uplift anticline
	Transpressional-fold anticline
	Flower structure
	Sub-unconformity truncation
	Buried-hill

Table 2.1. Summary table showing the main oil traps found in the Bohai Basin. Anticlinal and fault-related traps are the most important and common trap types in the study area. Stratigraphic traps are less important. Most of the traps occur in syn-rift and post-rift intervals although fractured and weathered pre-rift basement highs, - also known as “buried hills” by Chinese workers - also form good reservoirs in the Bohai Basin.

2.8 CONCLUSIONS

Based on a regional basin analysis of megasequences, regional unconformities, fault systems, and, thickening trends and ages; I conclude that previously proposed models for orthogonal rifting (Ye et al., 1985) and late phase of Neogene strike-slip deformation (Hu et al., 2001) have both played important roles in the formation of the Bohai Basin.

The Cenozoic Bohai Basin contains two main depositional units, a late Paleocene to late Oligocene syn-rift section (MS2) of continental sedimentary rocks in half-grabens and an overlying early Miocene to recent post-rift sag section (MS3 and MS4) of continental sedimentary rocks deposited in broad depocenters or sag basins (Figures 2.6, 2.8, 2.9, 2.10, 2.11, 2.12 and 2.13). The syn-rift section developed in response to a regional late Paleocene – late Oligocene extension, which produced abundant basin-parallel northeast-striking and basin-oblique east-west structures (Figures 2.8, 2.9, 2.10, 2.11, 2.12, 2.13, 2.14 and 2.15). Paleogene extension was followed by a period of regional uplift and erosion during late Oligocene (Figures 2.6 and 2.11b). Subsidence analysis shows that the post-rift sag section developed in response to thermal subsidence, which was later followed by strike-slip deformation (Hu et al., 2001)(Figure 2.18).

The peak of strike-slip deformation occurred during late Miocene – early Pliocene and resulted in the reactivation of previous rift-related normal faults and in the formation of new E-W and WNW-ESE striking strike-slip faults (Figure 2.11b). Earthquakes indicate that right-lateral strike-slip faulting continues to the present-day in a pattern consistent with the regional-scale “lazy-Z” map pattern of the Cenozoic Bohai depocenter (Figure 2.4).

The widespread distribution of Eocene to Miocene rifts in the Bohai Basin and adjacent basins of east Asia (Figure 2.2a) supports the previous interpretation by Watson

et al. (1987) and Schellart and Lister (2005) that this phase of extension was related to a previously proposed rollback of the Pacific plate subducted beneath the Bohai Basin (Figure 2.3a). Strike-slip deformation is attributed to a change in the direction of the convergence vector between the Eurasian plate and the subducting Pacific plate during early to late Miocene time (Northrup et al., 1985)(Figure 2.21b).

CHAPTER 3

Sequence stratigraphy and sedimentological model of the Miocene Guantao and Pliocene Minghuazhen Formations in Zhao Dong field, Bohai Bay, eastern China

3.1 INTRODUCTION

The 198 km^2 Zhao Dong field is located 10 km offshore the western edge of the Bohai Bay, northeastern China (Figure 3.1). Water depth of wells drilled in the Zhao Dong field varies from 6 to 15 m (Sundermann and Feng, 2004). The first discovery well in the Zhao Dong field was drilled in 1994 and tested about 15,000 barrels of oil per day. Subsequent drilling of additional appraisal and development wells has proven that large accumulations of oil exist within the Zhao Dong field. Main reservoirs in the field include fluvial sandstones of the Miocene Guantao and Pliocene Minghuazhen Formations (Chapter 4).

With very few exceptions (Liangmiao Ye, 1995), most previous subsurface work has focused on the lithostratigraphic, petrographic and biostratigraphic features of the Guantao and Minghuazhen Formations in the Bohai Basin (Chen Changming et al, 1984;; Yao et al., 1994; Zhang et al., 1994; Wang Tonghe, 1995; Kuykendall et al., 2003). The focus of this chapter is to provide a more detailed sequence stratigraphic and sedimentological analysis using 2D and 3D seismic data tied to 38 wells. This scale of observation and methodology is necessary to assess the regional variability of bounding surfaces and stratal stacking patterns within the Zhao Dong field. Challenges for applying sequence stratigraphic concepts to fluvial strata include depositional complexity (i.e., rapid lateral facies change), lack of marine influence (i.e., lack of extensive shale markers

for correlation) and the unreliability of biostratigraphic control (i.e., lack of age-diagnostic marine microfauna).

In contrast to the extensive sequence and seismic stratigraphic studies of marine basinal settings (e.g., Mitchum et al., 1977; Vail et al., 1977; Posamentier and Vail, 1988; Posamentier et al., 1988; van Wagoner et al., 1988), there are far fewer studies of non-marine aggradational settings (Wright and Marriot, 1993; Hamilton and Tadros, 1994; Shanley and McCabe, 1994; Diessel et al., 2000; Plint et al., 2001; Wadsworth et al., 2002; 2003). These previous studies of non-marine basins have illustrated the significance of key lithologies such as coals, paleosols and lacustrine strata as well as the presence of marine-influenced deposits in understanding non-marine stratigraphy. Unfortunately, the lack of these types of features in Zhao Dong field make these models of little use for this particular study.

The identification of accommodation/supply (A/S) cycles (Ramon and Cross, 1997) offer the best method for developing a systematic approach to non-marine sequence stratigraphy in Zhao Dong field. The objective of this chapter is to: 1) document the influence of accommodation changes on non-marine strata in the Zhao Dong field; and 2) to define the chronostratigraphic framework and sequence stratigraphic model for the fluvial sandstone of the Miocene Guantao and Pliocene Minghuazhen Formations, using a combination of unconventional non-marine correlation techniques (Ramon and Cross, 1997) and standard sequence stratigraphic concepts developed for marine basins (Mitchum et al., 1977).

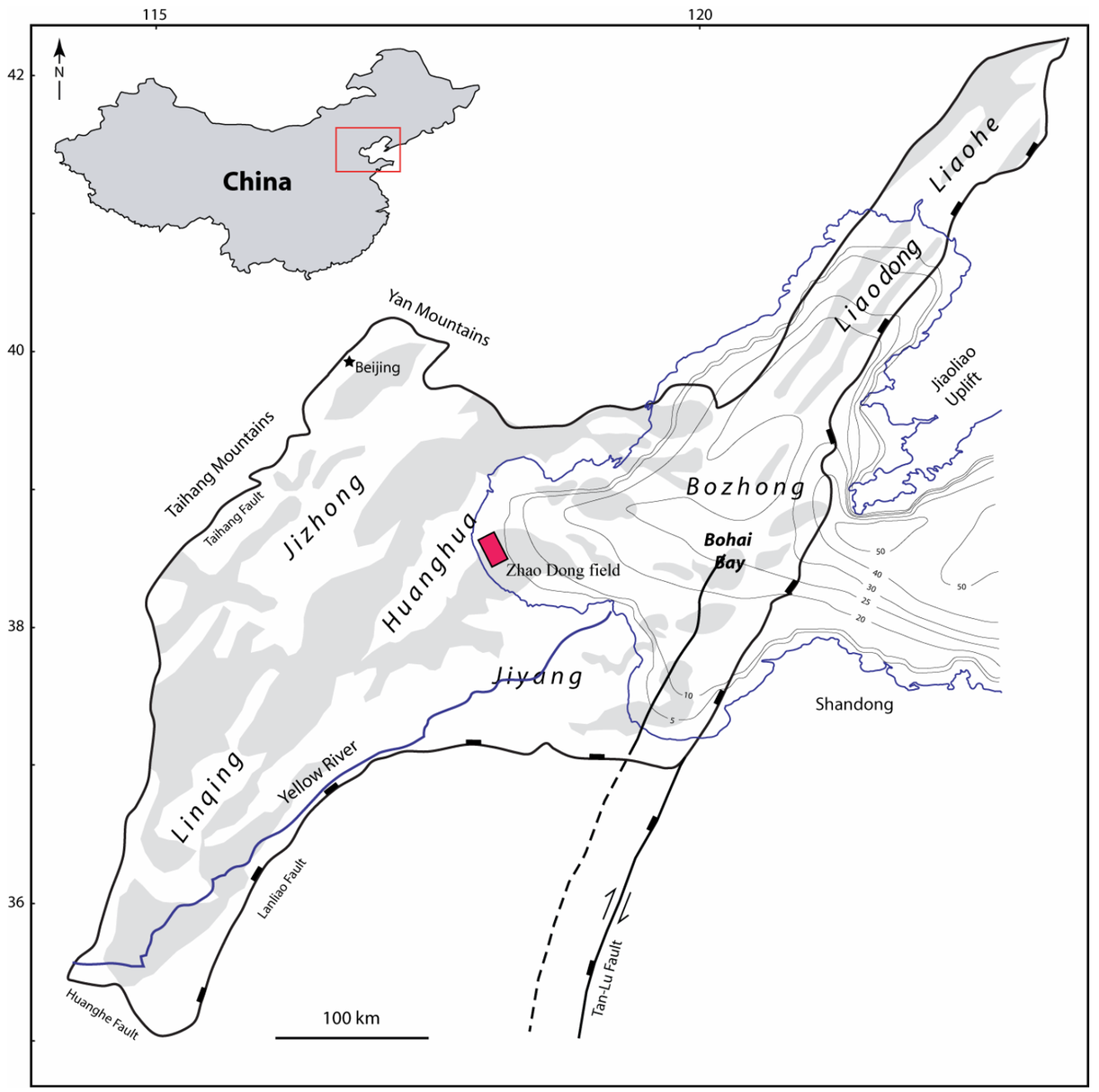

Figure 3.1. The Zhao Dong field is located approximately 10 km offshore the western edge of the Bohai Bay, northeastern China. Depressions or sub-basins cover unshaded areas of the Bohai Basin and are labeled in largest type; gray areas represent structural highs separating the depressions (map of depressions and highs modified from Hao et al., 2007). Bathymetric contours of the seafloor of the Bohai Basin are in meters and modified from from Sundermann and Feng (2004).

3.2 GEOLOGIC SETTING

3.2.1. Tectonic and structural setting

The Bohai Basin is a complex of Eocene to late Oligocene rift basins with superimposed late Miocene to recent sag and strike-slip basins that developed on the northeast margin of China. The basin consists of Paleogene, northeast and east-west-oriented rifts, which were filled with up to 10 km of non-marine clastic deposits (Ye et al., 1987; Hu et al., 1989). Six major rifts or depressions can be identified in the Bohai Basin: the Linqing depression in the south, the Jizhong, Huanghua, Jiyang and Bozhong depression in the central region and the Liaohe depression in the north (Allen et al., 1997; 1998; Hu et al., 2001) (Figure 3.1). Rifting ended during the late Oligocene when a regional uplift and erosional unconformity affected the entire Bohai Basin (Chapter 2). The Miocene to recent period of basin formation was marked by the formation of sag basins filled with up to 3 km thick of non-marine clastic deposits. The post-rift sag section developed in response to thermal subsidence, which was later followed by strike-slip deformation. The peak of strike-slip deformation initiated during middle Miocene, and resulted in the reactivation of previous rift-related normal faults (Chapter 2).

The mechanism for Eocene-late Oligocene rifting of the Bohai Basin is attributed to rollback of the subducted Pacific plate beneath the Asian continent, lithospheric extension of the overriding continental plate, and thermally-driven, regional subsidence (Watson et al., 1987) (Chapter 2). Late Miocene and younger strike-slip deformation is attributed to a change in the direction of the convergence vector between the Eurasian plate and the subducting Pacific plate from west-northwest to east – west (Northrup et al., 1995). (Figure 2.21)

The Zhao Dong field is located near the offshore part of the Huanghua depression in the western Bohai Basin (Figure 3.1). The tectonic history of the Zhao Dong field included middle Eocene basin-orthogonal extension in a north-south direction followed by early Pliocene strike-slip deformation and reactivation of older normal faults (Chapter 2).

A major east-west rift-related fault, that I have named "Fault A", divides the Zhao Dong field into two faulted blocks: footwall block D and hanging wall block C (Roc Oil Company Limited, 2007) (Figures 3.2 and 4.1). This fault was reactivated as a left-lateral strike-slip fault during the early Pliocene. Splays of secondary faults that branch off the main, reactivated east-west-striking normal fault form a prominent negative flower structure in the upper level of Neogene rocks (Figure 3.2). The flanks of this strike-slip fault currently form the main focus of hydrocarbon exploration in the Zhao Dong field.

3.2.2. Stratigraphy of the Zhao Dong field

Over 2 km of continental sediments of Eocene to Quaternary age were deposited in the area of the Zhao field during and after the major phase of Paleogene extensional rifting in the Bohai Basin (Figure 2.6). The sedimentary fill of the field can be subdivided into four regional-unconformity-bounded megasequences as discussed in detail in Chapter 2 (Figures 3.2 and 3.3):

1) A **pre-rift megasequence (MS1)** of pre-Tertiary age consisting of lithologies ranging in age from Archean to Mesozoic. These rocks include crystalline basement overlain by Paleozoic carbonates and Mesozoic terrestrial and volcanic strata (Figure 2.14; Fletcher et al., 1995; Hu et al., 1989) (Figure 2.14)

2) An early Tertiary (early Eocene – late Oligocene) **syn-rift megasequence (MS2)**, which contains 300-400 m of lacustrine and deltaic deposits of the Shahejie and

Dongying Formations bound by roughly east-west-striking normal faults of fault family 2 (Figure 2.15). This megasequence contains the primary lacustrine source-rock lithofacies as well as lacustrine reservoir and seal lithofacies (Kuykendall et al., 2003);

3) An early Miocene to Pliocene **post-rift megasequence (MS3)**, which contains 1.6-1.7 km of fluvio-lacustrine deposits of the Guantao and Minghuazhen Formations (Figure 2.16). These rocks exhibit less fault control and were deposited above a large sag basin overlying the rift-controlled rocks of MS2. Megasequence 3 contains the main reservoir and seal lithofacies in the Zhao Dong field (Kuykendall et al., 2003); and

4) A late Pliocene to recent **post-rift megasequence (MS4)** which contains at least 100 m of alluvium and loess of the Pingyuan Formation (Allen et al., 1997).

3.3 DATABASE AND METHODOLOGY

3.3.1. Database used in this chapter

3.3.1.1 Three-dimensional seismic data

3D seismic reflection data used in this chapter (Figure 3.4) consists of about 280 km^2, two-way travel-time data recorded to 5 s and sampled at 4 ms, and with a bin size of 25 m. For the study interval, the dominant frequency is between 26 and 36 Hz, giving a minimum estimated vertical resolution of 18 m (59 ft).

3.3.1.2 Well data

The well database used in this chapter includes 38 wells (Figure 3.4). Most wells are highly deviated and reach depths of about 1600 m into Neogene reservoirs, which

constitute the main reservoirs in the Zhao Dong area. Few wells reach the Paleogene interval, which lies at depths of more than 2000 m.

Four wells with core data were available for this study. Core observations were incorporated when possible to better define Neogene facies, paleoenvironments and to calibrate log curves. Age control across the Zhao Dong field is based on published palynological data (Wang Tonghe, 1995; Yao et al., 1994; Zhang et al., 1994).

3.3.2. Methodology

3.3.2.1 Well log correlations

Well log correlation in the Zhao Dong field follows the methodology proposed by Ramon and Cross (1997). Their approach is based on the recognition of rising and falling accommodation/supply (A/S) cycles caused by rising or falling base level - a surface above which erosion occurs and below which deposition occurs (Hardage and Remington, 1999). The turnaround points from increasing-to-decreasing and decreasing-to-increasing A/S were correlated and used to build a high-resolution chronostratigraphic framework throughout the field.

The A/S methodology of Ramon and Cross (1997) was adopted for this study for two main reasons. First, Minghuazhen and Guantao Formations are fully continental deposits with no marine influence and therefore the formations cannot be correlated using either conventional correlation techniques based on eustatic sea level changes (e.g., Vail et al., 1977; Van Wagoner et al., 1988) or the genetic sequence approach of Galloway (1989). Second, accommodation space and sediment supply have long been recognized by previous workers as the dominant control on non-marine deposition (Curray, 1964; Jervey, 1988; Thorne and Swift, 1991, Schlager, 1993; Shanley and McCabe, 1994).

Figure 3.2. Northwest to southeast-oriented seismic section through Zhao Dong field (western Bohai Basin). See Figure 3.14 for location of line. A major east-west-striking, rift-related normal fault of early Eocene to Miocene age, informally called "Fault A", divides the Zhao Dong field into two faulted blocks: footwall block D and hanging wall block C. Fault A was later reactivated as right-lateral strike-slip fault during the early Pliocene to recent. The basin fill (over 2-km-thick) in the Zhao Dong field can be divided into four regional-unconformity-bounded megasequences labeled on the seismic line: pre-rift megasequence 1 (MS1) of pre-Tertiary age; syn-rift megasequence 2 (MS2) of early Eocene – late Oligocene age; and post-rift megasequence 3 and 4 (MS3 and MS4) of early Miocene to recent age (MS4 is not visible in this section).

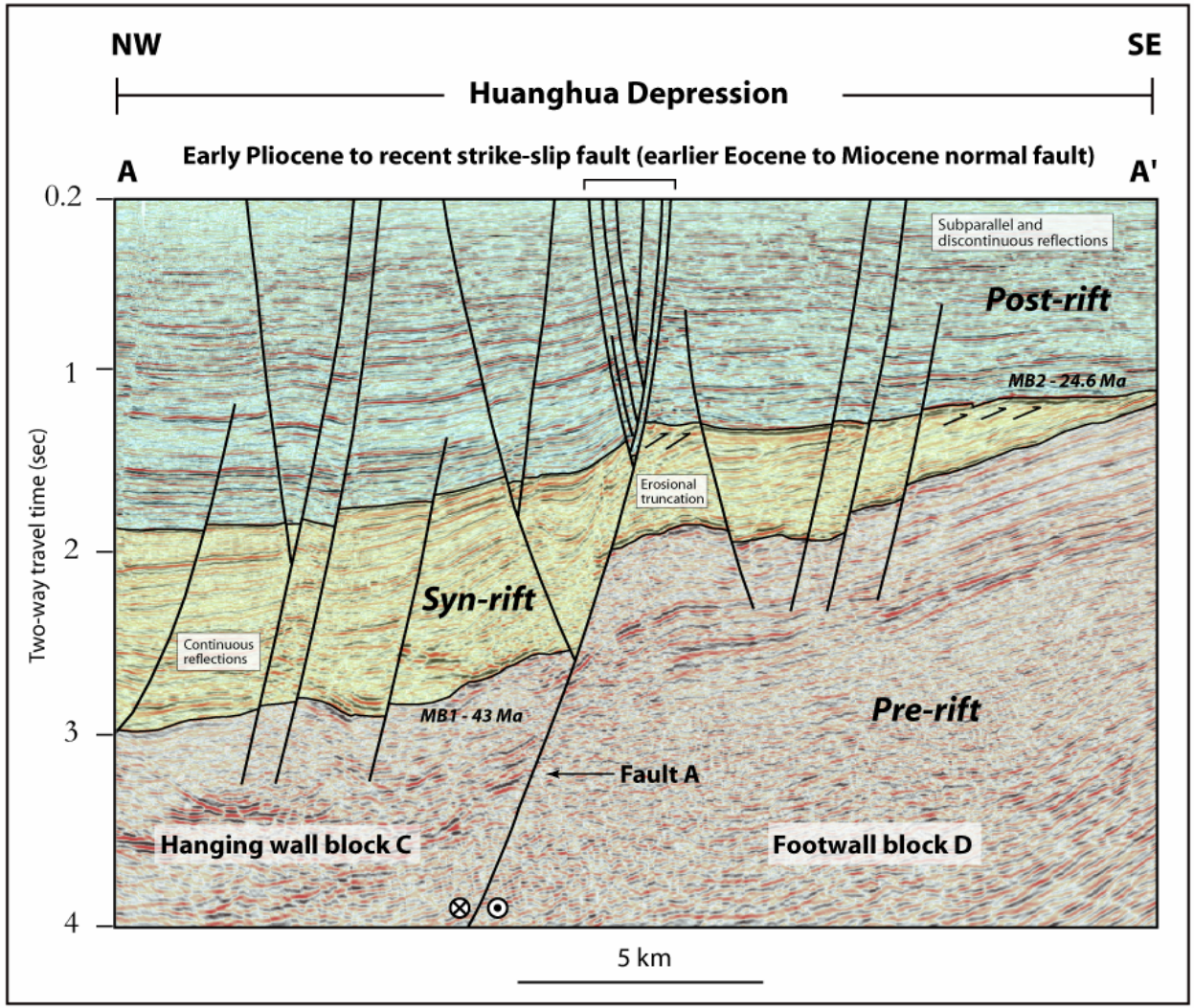
NW
SE
Huanghua Depression
Early Pliocene to recent strike-slip fault (earlier Eocene to Miocene normal fault)
A
A'
0.2
1
2
3
4
Two-way travel time (sec)
Subparallel and discontinuous reflections
Post-rift
MB2 - 24.6 Ma
Erosional truncation
Syn-rift
Continuous reflections
MB1 - 43 Ma
Pre-rift
Fault A
Hanging wall block C
Footwall block D
5 km

Figure 3.2

Figure 3.3. Stratigraphic column of the Zhao Dong field based on a representative well log response (spontaneous potential – SP and resistivity – RESD) that penetrated all three clastic megasequences shown in Figure 3.2. This figure shows the typical well response for the ten accommodation/supply (A/S) cycles identified in the study area. Red triangles pointing down on the log indicate the part of the cycle characterized by decreasing accommodation/supply conditions (taken at the bases of fluvial channels) while blue triangles pointing up depict the part of the cycle characterized by increasing accommodation/supply conditions (taken at the tops of fluvial channels). Late Paleocene – early Eocene rift-related deposits of the Kongdian Formation are not present in this part of the study area. Formation names, ages and depositional environments are compiled from Hu et al., (1989); Yao et al., (1994); Zhang et al., (1994); Wang Tonghe, (1995) and Allen et al., (1997).

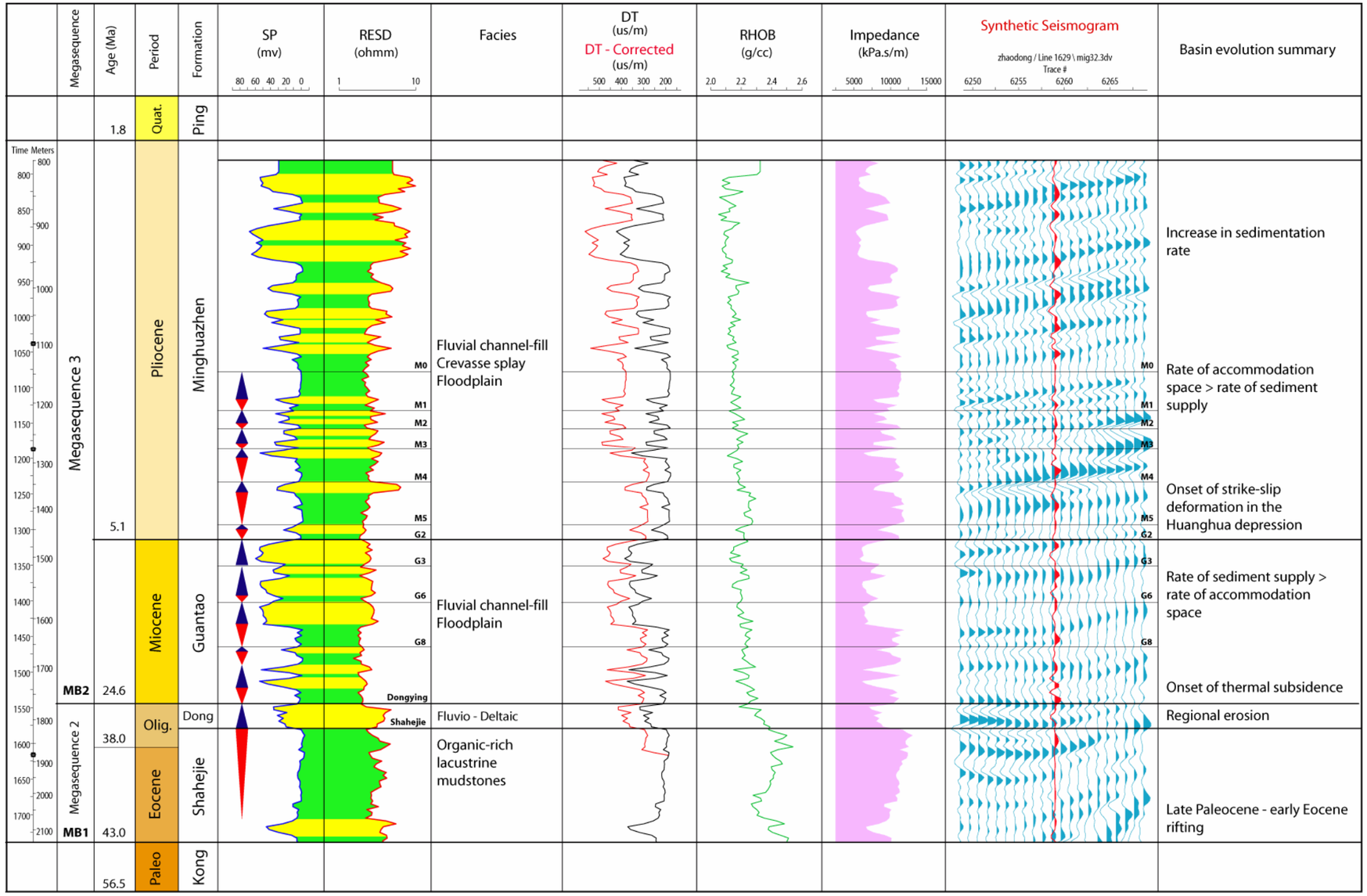
Megasequence
Age (Ma)
Period
Formation
SP
(mv)
80 60 40 20 0
RESD
(ohmm)
1 10
Facies
DT
(us/m)
DT - Corrected
(us/m)
500 400 300 200
RHOB
(g/cc)
2.0 2.2 2.4 2.6
Impedance
(kPa.s/m)
5000 10000 15000
Synthetic Seismogram
zhaodong / Line 1629 \ mig32.3dv
Trace #
6250 6255 6260 6265
Basin evolution summary
1.8
Quat.
Ping
Time Meters
Megasequence 3
Pliocene
Minghuazhen
Fluvial channel-fill
Crevasse splay
Floodplain
M0
M1
M2
M3
M4
M5
G2
Increase in sedimentation rate
Rate of accommodation space > rate of sediment supply
Onset of strike-slip deformation in the Huanghua depression
5.1
Miocene
Guantao
G3
G6
G8
Dongying
Fluvial channel-fill
Floodplain
Rate of sediment supply > rate of accommodation space
MB2
24.6
Onset of thermal subsidence
Olig.
Dong
Shahejie
Fluvio - Deltaic
Regional erosion
38.0
Megasequence 2
Eocene
Shahejie
Organic-rich lacustrine mudstones
Late Paleocene - early Eocene rifting
MB1
43.0
Paleo
Kong
56.5

Figure 3.3

Figure 3.4. Location of seismic reflection data and wells used in this study of the Zhao Dong field. A) 3D seismic data used in this chapter consists of 280 km^2 two-way travel-time data recorded to 5 seconds and sampled at 4 milliseconds; bin size is 25 m. B) Time structure map of cycle M0 showing well database of 38 wells with a complete suite of well logs. Most wells are highly deviated and reach total depths at about 1600 m into Neogene channel sandstone reservoirs, which constitute the major producing reservoirs in the Zhao Dong field. Wells are concentrated on Fault A; this is an early Eocene-late Oligocene normal fault downthrown about 300 m to the north; later early Pliocene-recent right-lateral strike-slip displacement reactivated the fault and produced a strike-slip flower structure that now acts as structural trap for the Zhao Dong field. Green arrow points north C) Map view of well locations in Zhao Dong field showing their highly deviated nature from a common entry point. Red lines represent well cross-sections shown in figures 3.8, 3.9, 3.10 and 3.11.

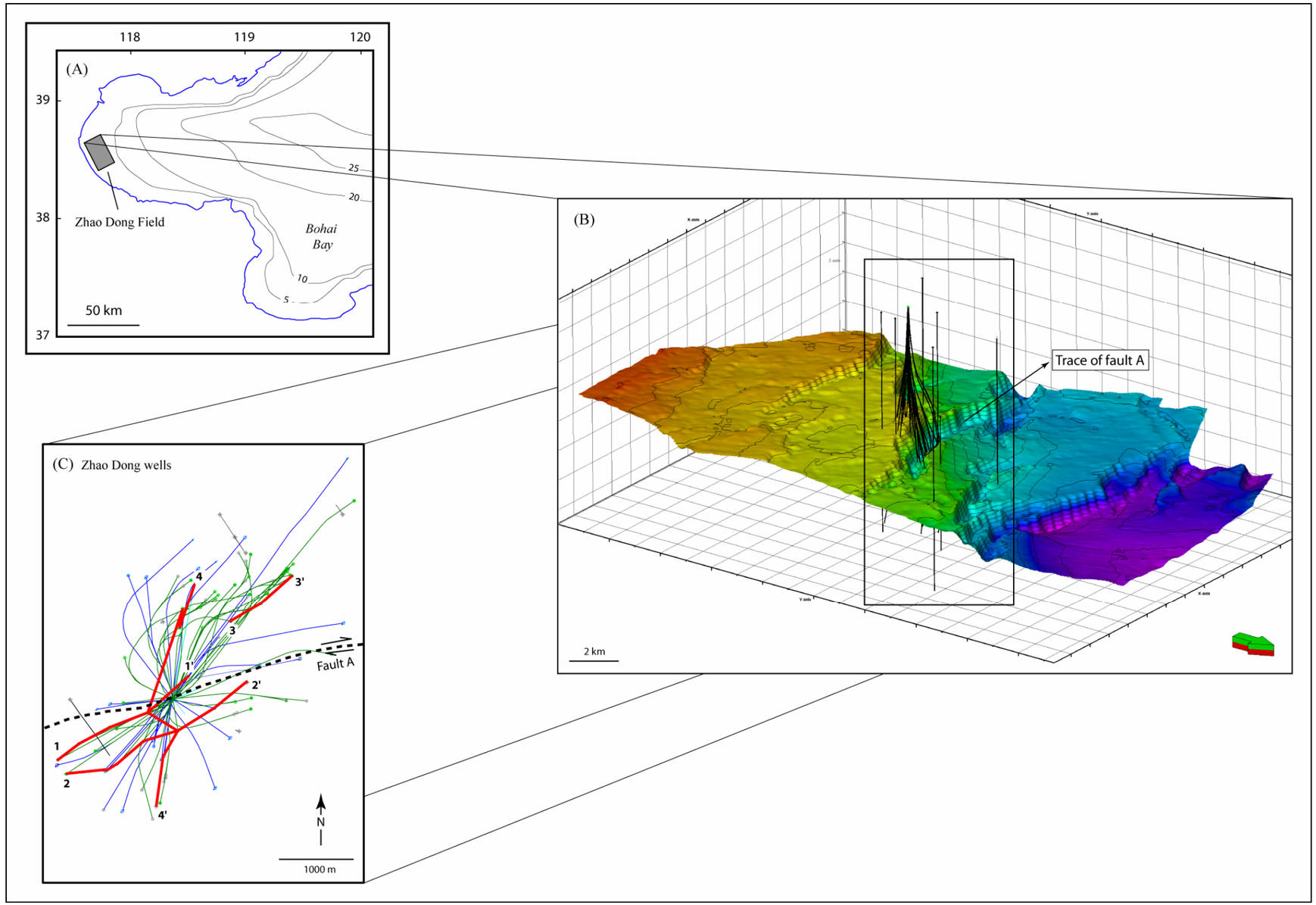
(A)
118
119
120
39
38
37
Zhao Dong Field
Bohai
Bay
25
20
10
5
50 km
(B)
Trace of fault A
2 km
(C) Zhao Dong wells
1
2
3
4
1'
2'
3'
4'
Fault A
N
1000 m

Figure 3.4

One common criticism of the A/S methodology of Ramon and Cross (1997) is where to place the turnaround point from decreasing-to-increasing A/S conditions or the hemi-cycle of base-level rise (R. Steel, personal communication, 2007). In their approach, Ramon and Cross (1997) assume that the base of fluvial channels mark the initiation of increasing A/S conditions within any given cycle (Figure 3.5a). A counter-argument for their proposal is that the turnaround point may actually occur higher within the fluvial channel (R. Steel, personal communication, 1997) (Figure 3.5b).

For the interpretations shown in this chapter, I follow Ramon and Cross (1997) and select the turnaround point from decreasing-to-increasing A/S conditions to be at the bases of fluvial channels (Figure 3.5c). One reason for this is the simplicity of correlation: because of their strong acoustic impedance contrast, the bases of fluvial channels in the Guantao and uppermost Minghuazhen Formations in Zhao Dong field are easy to identify and correlate in seismic cross-sections (Figures 3.12b and 3.13b).

3.3.2.2 Seismic interpretation

Conventional 3-D seismic data interpretation presented in this chapter includes the generation of synthetic seismograms from well logs to correlate between seismic reflectors and well data. Amplitude extractions were also used to improve the seismic interpretation and to extract additional stratigraphic information from the 3D seismic cube. Coherency time slices with variable seismic windows 40-120 ms were designed to measure the incoherency in seismic markers and generate the best possible images of the principal faults within the Zhao Dong field.

Figure 3.5. Accommodation/supply (A/S) cycles. (a) In their approach, Ramon and Cross (1997) assume that the base of fluvial channels mark the initiation of increasing A/S conditions (indicated here by the base of the blue triangle that is pointing upwards) within any given cycle (modified from Ramon and Cross, 1997). (b) A counter-argument for their proposal is that the turnaround point from decreasing-to-increasing A/S conditions may actually occur higher within the fluvial channel (R. Steel, personal communication, 1997). For the interpretations shown in this chapter, I follow Ramon and Cross (1997) and select the turnaround point from decreasing-to-increasing A/S conditions to be at the bases of fluvial channels as shown in Figures 3.5c, 3.8, 3.9, 3.10 and 3.11

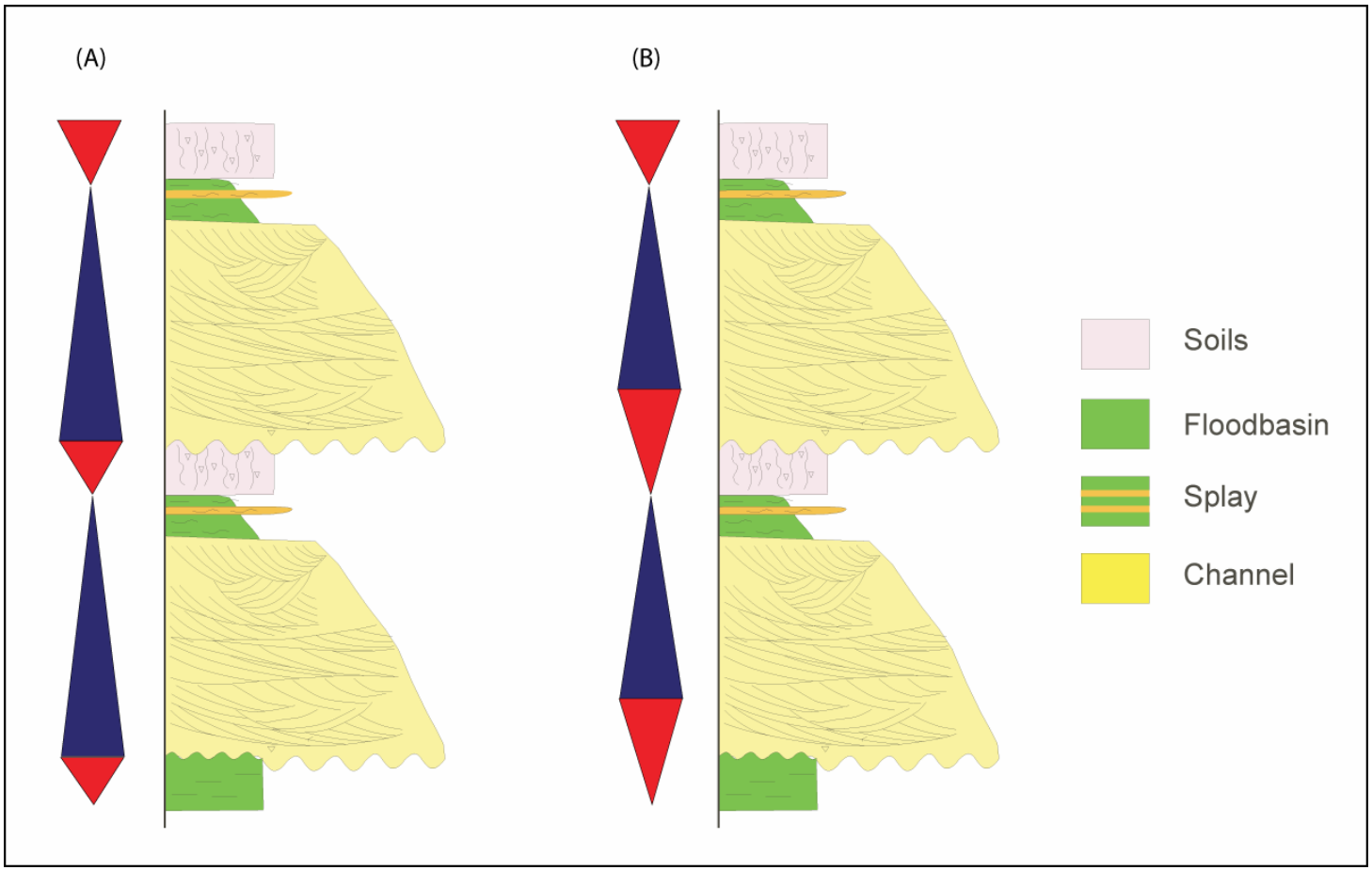

Figure 3.5(a) and (b)

Figure 3.5c. Representative well log from the Miocene Guantao and Pliocene Minghuazhen Formations in the Zhao field showing delineation of 10 sequences in vertical sections based on the recognition of rising and falling accommodation/supply (A/S) cycles. Red triangles indicate parts of cycles inferred to represent decreasing A/S conditions while blue triangles pointing up indicate parts of cycles inferred to represent increasing A/S conditions. Yellow represents channel-fill facies. Green represents floodplain (clay and silt) facies.

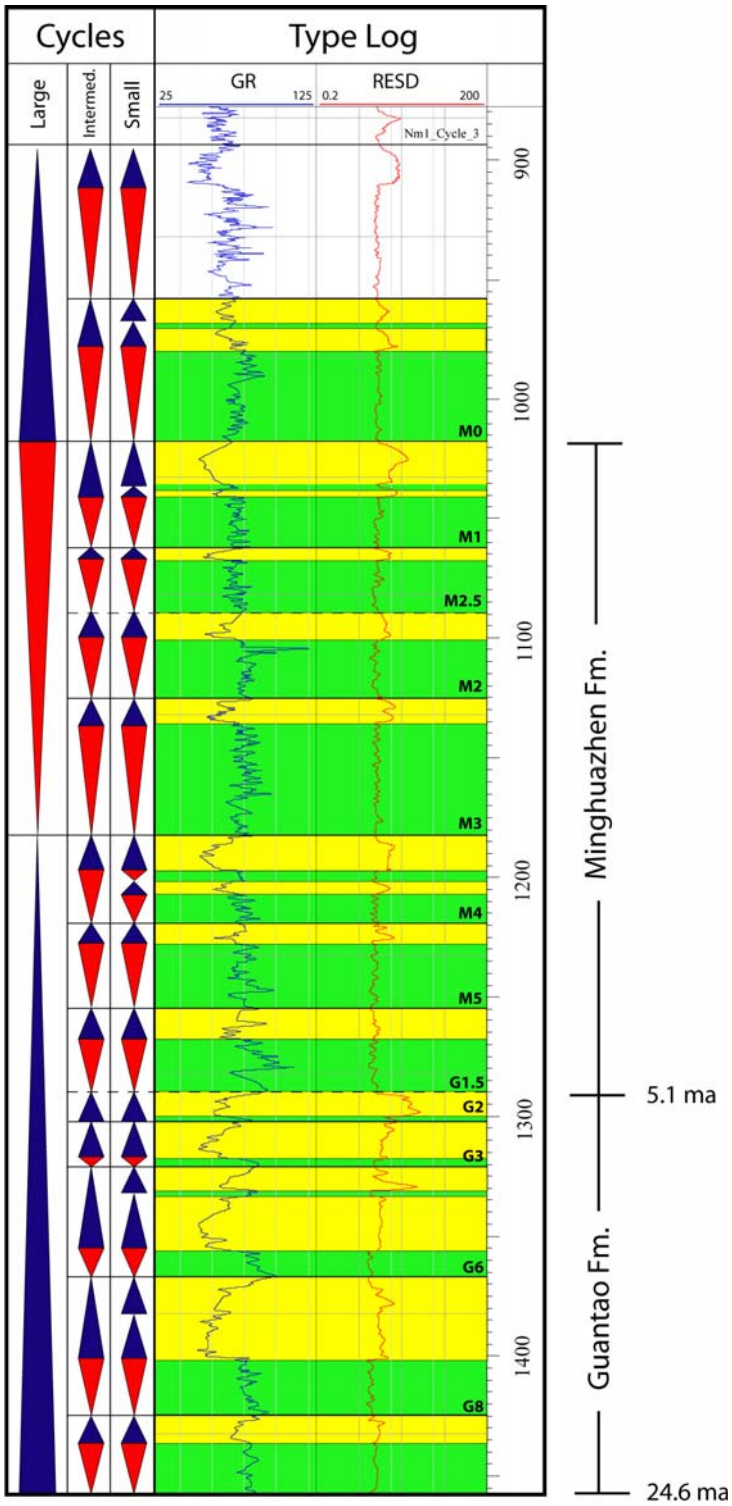
Cycles
Type Log
Large
Intermed.
Small
GR
RESD
25
125
0.2
200
Nm1_Cycle_3
900
1000
1100
1200
1300
1400
M0
M1
M2.5
M2
M3
M4
M5
G1.5
G2
G3
G6
G8
Minghuazhen Fm.
Guantao Fm.
5.1 ma
24.6 ma

Figure 3.5c

3.4. DATA DESCRIPTION

3.4.1. Stratigraphic cycles – A hierarchical subdivision based on accommodation / sediment supply ratios

The Miocene and Pliocene section in the Bohai Basin has been divided by previous workers like Wang and Zhao, 1990 and Kuykendall et al. (2005) into two lithostratigraphic units (Guantao and Minghuazhen Formations) based upon well logs and seismic data. In this chapter, the Miocene and Pliocene section of Zhao Dong field has been divided more finely into ten (20-100 m-thick) fieldwide correlatable stratigraphic cycles.

Figure 3.5c shows one example of the identification of stratigraphic cycles using a well log from the Zhao Dong field. Red triangles pointing down on the log indicate the part of the cycle characterized by decreasing accommodation/supply conditions (taken at the bases of fluvial channels) while blue triangles pointing up depict the part of the cycle characterized by increasing accommodation/supply conditions (taken at the tops of fluvial channels). The triangles provide an effective graphical tool for portraying the hierarchical embedding of sequences within sequences (Sonnenfeld, 1996). Individual cycles are also identified by changes in relative completeness of facies successions, facies proportions, cycle symmetries, and preservation of geomorphic elements (Ramon and Cross, 1997).

3.4.2. Orders of cyclicity

Sedimentologic and stratigraphic analysis of well logs from the Zhao Dong field reveals regular, recurring motifs of facies associations (Figure 3.5). These motifs, informally called “small-scale cycles”, are 15 to 30 m thick and are the smallest resolvable facies successions observed in most well logs. Small-scale cycles are grouped

by stacking patterns into "intermediate-scale cycles" of 30 to 70 m thick, which represent the highest-order cycles than can be correlated across large areas of the 198 km^2 Zhao Dong field. These "intermediate-scale cycles" are in turn are grouped into "large-scale" (80-200 m thick) stratigraphic cycles. The last two scales of cyclicity are the easiest to identify and correlate based upon one-dimensional analysis of well logs in Zhao Dong field (Figure 3.5c).

3.4.3. Sedimentary facies

Well log signatures were calibrated with facies and facies associations identified in sidewall cores, mudlogs and image logs from four wells in the field. This calibration made possible the identification of stratigraphic cycles from well logs and allowed stacking patterns of small-scale cycles to be grouped into larger-scale cycles.

Figure 3.6 shows a schematic reconstruction of the main depositional environments found in the Zhao Dong field. Four distinct facies were identified: 1) fluvial channel fill facies, 2) paleosol facies, 3) crevasse splay facies, and 4) floodplain facies.

Table 3.1 shows a lithologic classification of the sediments found in sidewall cores from four wells from the Zhao Dong field. The facies described in Table 3.1 were determined using their primary lithologic characteristics such as grain size, angularity and sorting.

3.4.3.1 Facies 1A and 1B (fluvial channel fill)

Facies 1A and 1B consist mainly of friable to firm, fine to coarse grained, locally very coarse, poorly to moderately well sorted, subangular to subrounded quartz-rich

sandstone. Facies 1A and 1B are interpreted as fluvial channel fills. Where preserved, individual channel fill sequences average between 8 and 10 m thick, with sharp, erosional bases. Porosity values commonly range between 20% and 35% and permeability values normally range between 10 and 1200 mD. Facies 1A and 1B are in general very clean sandstone. Minor amounts of clay, mostly kaolinite, are sometimes present and are probably due to early diagenesis (i.e., soil-forming processes) in the paleosol facies.

3.4.3.2 Facies 1C (paleosols)

Facies 1C is sand with abundant clay, which is mostly kaolinite. These facies are indurated due to cementation by clay minerals. Facies 1C are interpreted as to have formed as the result of soil-forming processes, probably during subaerial exposure. Where present, facies 1C are commonly underlain by facies 1A or 1B.

3.4.3.3 Facies 2 (crevasse splay facies)

Crevasse splay facies consist mainly of very fine to fine, locally medium grained, moderately to predominantly well sorted, subangular to subrounded quartz-rich sandstone. Facies 2 are commonly preserved in the Minghuazhen Formation. They occur in thin (1 to 3 m) upward fining successions.

3.4.3.4 Facies 3 (floodbasin facies)

Floodbasin facies consist of siltstone, claystone and mudstone. Internal structures in this facies include sand laminae and traces of dark brown, carbonaceous flecks. Sand fraction is very fine-grained. Facies 3 is interpreted as floodbasin deposits in floodplain and interchannel lake settings.

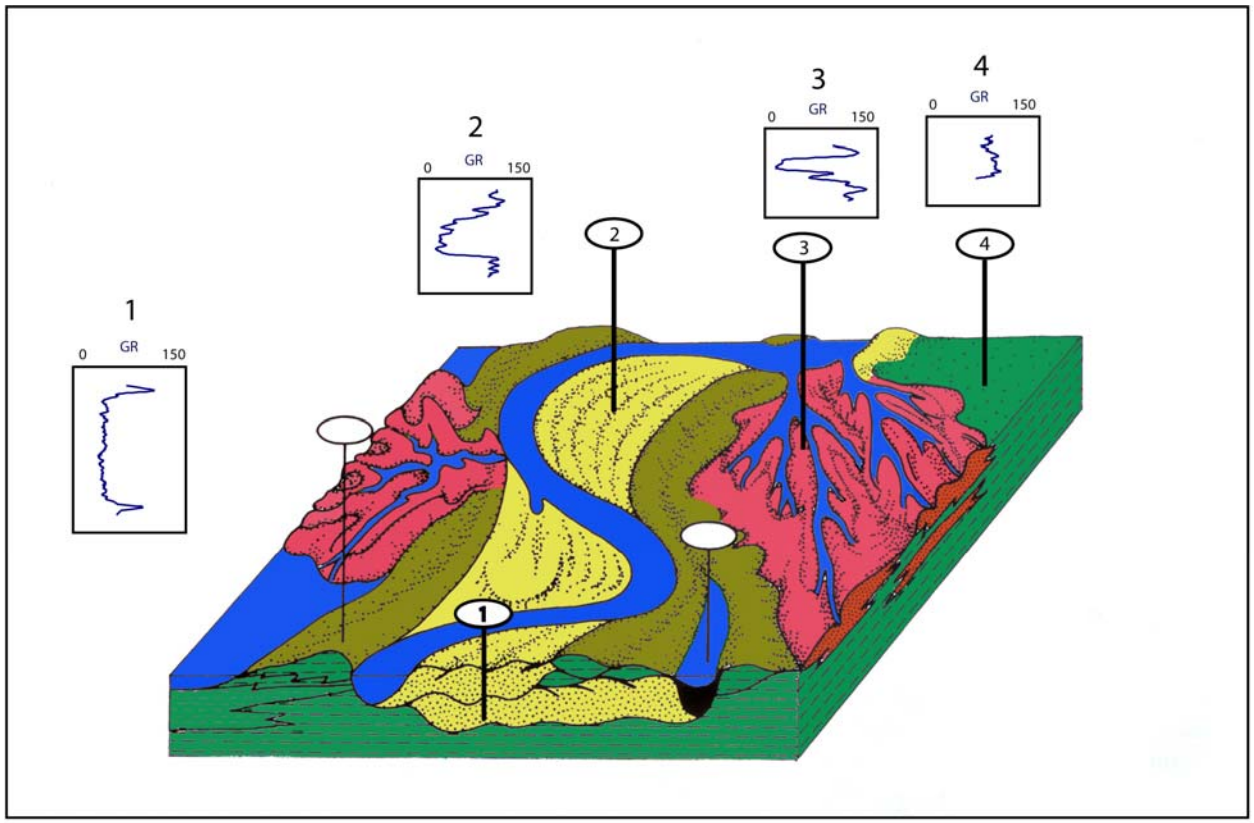

Figure 3.6. Lateral facies relationships and comparative vertical sequences, as reflected by spontaneous potential (SP) and/or gamma ray (GR) log response of the component facies of the fluvial systems in Zhao Dong field (modified from Galloway and Hobday, 1996): 1) Amalgamated fluvial channels; 2) channel-fill point-bar sands; 3) crevasse splays; 4) and floodbasin deposits.

Facies	Lithology	Interpretation
1A	**Sand**: fine-to coarse-grained, locally very coarse; poorly to moderately sorted.	Fluvial channel-fill. Minor clay content, mostly kaolinite, in Facies 1A and 1B is probably due to minor early diagenesis (soil forming processes) in paleosols.
1B	**Sand**: fine-to medium-grained, locally very fine-grained; moderately well to well sorted.	
1C	**Sand**: very fine to fine-grained, moderately well to well sorted with abundant clay, mostly kaolinite.	Sand (channel-fill or crevasse splay), highly altered by diagenesis due to soil forming processes.
2	**Sand**: very fine-to locally medium grained, moderately to well sorted.	Crevasse splay
3	**Siltstone, claystone and mudstone**.	Floodplain or lacustrine

Table 3.1. Summary of the principal lithologies and facies interpretation for the five main facies associations that comprise the Guantao and Minghuazhen Formations in Zhao Dong field.

3.4.4 Facies associations

The four facies described above are grouped together into three main facies associations (Figure 3.7): 1) channel-fill facies associations; 2) point-bar facies associations; 3) crevasse splay facies-associations; and 4) interdistributary facies-associations.

3.4.4.1 Channel-fill facies associations (FA1)

Channel-fill facies associations (Figure 3.7a) dominate the basal part of the Guantao Formation (Figure 3.5). This facies association commonly consists of an erosive base overlain by a thin very-coarse grained sandstone layer. The facies commonly displays a general fining-upward grain-size distribution from coarse to fine grained sandstone, poorly to moderately sorted at the base, and moderately well to well sorted at the top. This facies generally grades upward into fine to very fine grained sand with abundant kaolinite.

3.4.4.2 Point bar facies associations (FA2)

Point bar facies associations (Figure 3.7b) consists of a scoured base overlain by a channel lag consisting of coarse grained sand. This facies association displays a fining-upward grain-size distribution from medium- to fine-grained. Sand is moderately- to well sorted. This facies generally grades upward into fine to very fine grained sand with abundant clay, that is mostly kaolinite.

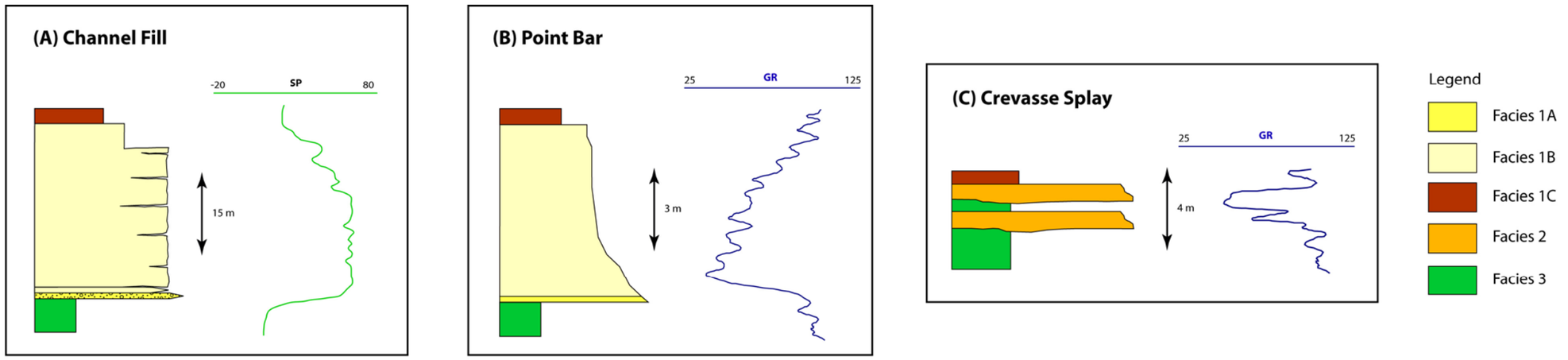

Figure 3.7. Vertical facies associations in the Guantao and Minghuazhen Formations based on SP and GR well log responses. A) Channel-fill facies associations dominate the basal part of the Guantao Formation. This facies association commonly consists of an erosive base overlain by thin, very-coarse grained sandstone layer. They commonly display a general fining-upward grain-size distribution from coarse to fine grained sandstone, poorly to moderately sorted at the base and moderately well to well sorted at the top. These facies generally grade upward into fine to very fine grained sand with abundant kaolinite. B) Point bar facies associations consists of a scoured base overlain by a channel lag consisting of coarse grained sand. This facies associations displays a fining-upward grain-size distribution from medium- to fine-grained; moderately- to well sorted sandstone. These facies may grade upward into fine to very fine-grained sand with abundant clay that is mostly kaolinite. C) Crevasse splay facies associations are commonly preserved in the Minghuazhen Formation. Crevasse splay facies associations may show a gradual or abrupt fining-upward trend or no trend. Crevasse splay facies commonly range from 1 to 3 m in thickness and are fine to very fine-grained. See table 3.1 for legend explanation.

3.4.4.3 Crevasse splay facies associations (FA3)

Crevasse splay facies associations (Figure 3.7c) are commonly preserved in the Minghuazhen Formation (Figure 3.5). Crevasse splay facies associations may show a gradual or abrupt fining-upward trend - or no vertical trend. This facies commonly ranges from 1 to 3 m thick and is fine to very fine grained. The internal structure of crevasse splays is heterogeneous, reflecting their origin by multiple flood events, shallow, chaotic flow conditions, and rapid sedimentation rates (Galloway and Hobday, 1996).

3.4.4.4 Interdistributary facies associations (FA4)

Interdistributary facies-associations include siltstone and claystone. This facies occurs throughout the sedimentary sequence although it is poorly preserved in the Guantao Formation (Figure 3.5). Accumulation of interdistributary fines occur outside the active channel and therefore form a distinctive and independent environment. Factors that influence the deposition of this facies include sediment supply, channel shape, rate of subsidence and channel migration processes (Freund, 1983).

3.4.5 Stratigraphic correlation and chronostratigraphic significance of turnaround points

A high resolution, chronostratigraphic framework was built across the Zhao Dong field from correlation of "intermediate-scale" cycles (30 to 70 m thick) identified in 38 wells and shown on Figures 3.8, 3.9, 3.10 and 3.11. Intermediate-scale cycles represent the highest-order of cyclicity than can be correlated across the entire field. Each well log was interpreted individually working from the smallest to the largest scale cycles using stacking pattern analysis, facies successions and cycle symmetries (Figure 3.5). The

turnaround points from increasing-to-decreasing and decreasing-to-increasing A/S were correlated from well to well across the Zhao Dong field and formed the basis of a 2D stratigraphic correlation framework. Four such correlations are shown in figures 3.8, 3.9, 3.10 and 3.11.

3.4.5.1 Fluvial facies architecture

The three-dimensional arrangement of channels and overbank deposits in a fluvial succession is referred as the "architecture" of the beds (Miall, 1996). The architecture is most commonly described using the proportion of channel deposits relative to the finer-grained overbank deposits (Emery and Myers, 1996; Miall, 1996). Well log cross-sections (Figures 3.8, 3.9, 3.10 and 3.11) show that fluvial sands in Zhao Dong field range transitionally from amalgamated, multi-storied and laterally continuous sheet sandstones to isolated fluvial sandstones encased in floodplain mudstones.

Amalgamated channel sandstone. Fluvial-channel sandstone bodies of the Guantao Formation laterally and/or vertically contact one another or are separated by less than one meter of floodplain facies. These relationships indicate deposition under lower A/S conditions (Ramon and Cross, 1997) (Figures 3.8, 3.9, 3.10 and 3.11). Because erosion usually preceded channel-fill deposition, only the lowermost elements of channel successions are typically preserved to produce a high sand-to-mud ratio (Ramon and Cross, 1997).

Amalgamated fluvial channel sandstone of the Guantao Formation reaches up to 55 m in thickness. These channels have flat, low relief erosive bases with multiple internal scour surfaces separating individual channel bodies about 8 to 12 m in thickness. Amalgamated fluvial channel sandstones form areally extensive bodies that extend several hundred meters along dip and strike directions.

Isolated channel sandstones. Sandstone bodies in the Minghuazhen Formation are isolated within floodplain facies and show well developed splays suggesting deposition under higher A/S conditions (Ramon and Cross, 1997) (Figures 3.8, 3.9, 3.10 and 3.11). Individual channel sandstones are characterized by thin (up to 8 m. thick), lenticular and laterally discontinuous sand bodies encased in floodplain siltstone and claystone. Sandstone preservation potential is higher in this part of the sedimentary section and results in a lower sand-to-mud ratio. An anomalously thick, sharp-based and overall fining-upward sand-body caps the Minguazhen Formation (Figures 3.8, 3.9, 3.10 and 3.11). This multistoried sandstone body (up to 25 m thick) is laterally continuous and extend several hundred meters along dip and strike directions.

3.4.6 Seismic well tie and seismic interpretation

Several synthetic seismograms were generated using well logs from the study area (Figure 3.3). A zero-phase wavelet provided the best match between synthetic seismograms and seismic data with a dominant frequency of about 30 Hz. Correlation between intermediate and large-scale cycles identified in well data and seismic data was very good. Small-scale cycles with thicknesses less than 18 m were not resolved by the seismic data.

Figures 3.12 and 3.13 show two seismic sections from the Zhao Dong field. Ten intermediate-scale cycles were identified and correlated through the 280 km^2 3D seismic volume available for the Zhao Dong field. The turnaround points from decreasing-to-increasing A/S cycles (troughs in the synthetic seismograms on Figure 3.3) were easier to identify and map in the Guantao Formation than the Minghuazhen Formation. In contrast the turnaround points from increasing-to-decreasing A/S cycles (peaks in the synthetic seismograms on Figure 3.3) were easier to identify and correlate in the Minghuazhen

Formation (Figures. 3.5, 3.12 and 3.13). The clear parallelism between the seismic reflections and the correlated intermediate-scale cycles corroborates the 2D stratigraphic correlation shown on the well logs in Figures 3.8, 3.9, 3.10 and 3.11.

3.4.7 Amplitude extractions

Seismic amplitude maps improved the interpretation of geomorphologic and depositional elements present during Mio-Pliocene deposition of the Guantao and Minghuazhen Formations in the Zhao Dong field. The root mean square (RMS) attribute was extracted over a 10 ms window above and below each interpreted horizon. Unfortunately, clear identification of geomorphologic and depositional elements were obtained only for horizons within the Minghuazhen Formation and the shallowest horizon within the underlying Guantao Formation. As interpreted from the well data (Figures 3.8, 3.9, 3.10 and 3.11), Minghuazhen Formation was deposited under high-accommodation conditions. Sediments deposited in such conditions are rarely subjected to erosion therefore they tend to provide excellent records of depositional processes and environments. Sediments deposited in high-accommodation settings are likely to be altered and modified only by normal compaction and diagenetic processes (Hardage and Remington, 1999).

The results from the RMS amplitude extractions are shown in figures 3.14, 3.15, 3.16, 3.17, 3.18, 3.19 and 3.20 in a sequence from the deepest to the shallowest horizons of the Minghuazhen Formation. These maps provided snapshots of the depositional environments during deposition of the Guantao and Minghuazhen Formations. The sand-rich areas are represented by different tones of yellow and red (low amplitude values), whereas floodplain facies are represented by a black background color (high amplitude values).

Figure 3.8. Strike well cross-section 1-1'. The turnaround points from increasing-to-decreasing and decreasing-to-increasing accommodation/supply (A/S) cycles were correlated from well to well across the Zhao Dong field and formed the basis of a 2D stratigraphic correlation framework. See figures 3.4 and 4.1 for location.

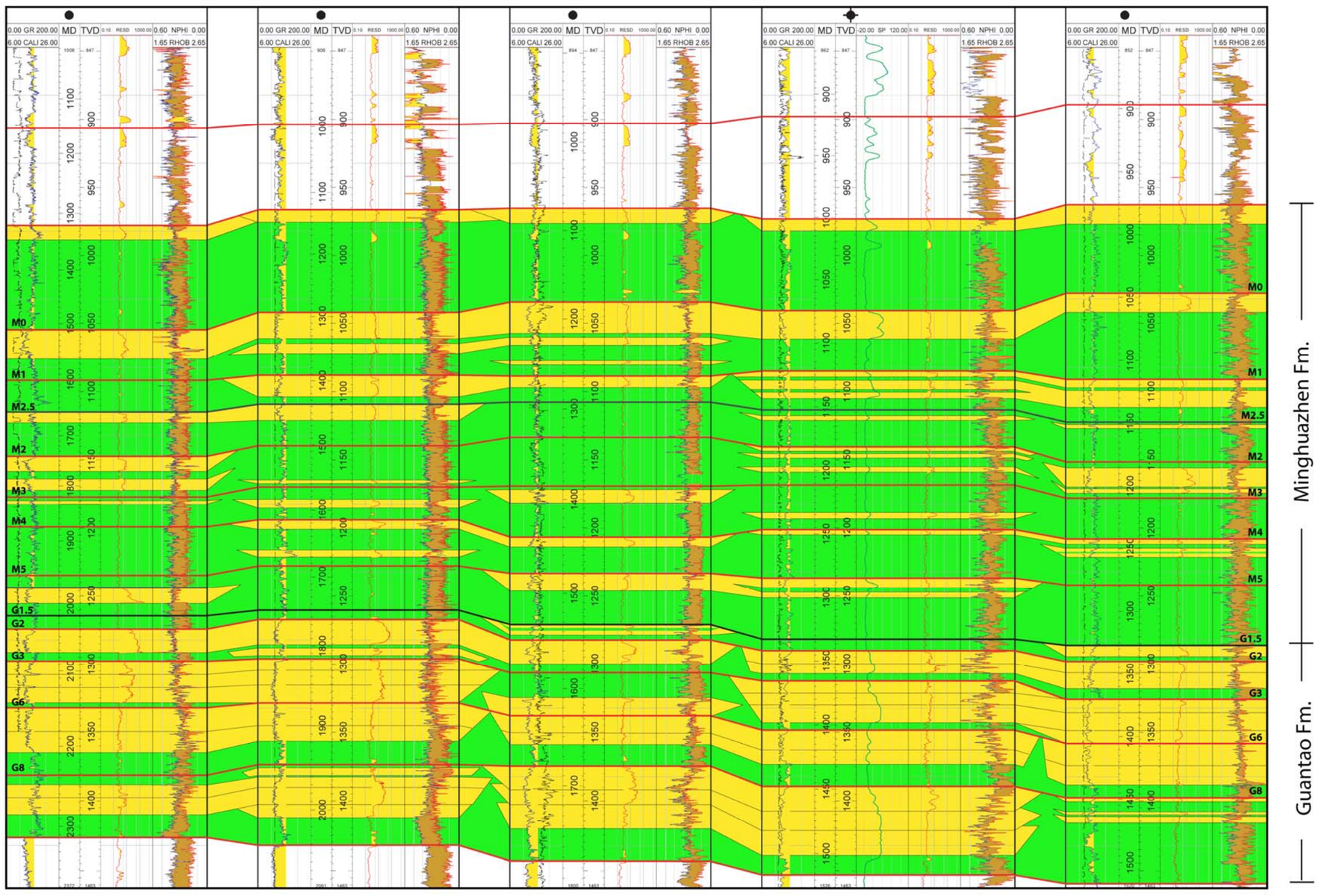
1 (SW)
Well Cross-Section 1
1' (NE)
0.00 GR 200.00
MD
TVD
0.60 NPHI 0.00
6.00 CALI 26.00
1.65 RHOB 2.65
-20.00 SP 120.00
RESD
M0
M1
M2.5
M2
M3
M4
M5
G1.5
G2
G3
G6
G8
Minghuazhen Fm.
Guantao Fm.

Figure 3.8

Figure 3.9. Strike well cross-section 2-2' showing fluvial sands in the Zhao Dong field ranging transitionally from amalgamated, multi-storied and laterally continuous sheet sandstones (Guantao Formation) to isolated fluvial sandstones encased in floodplain mudstones (Minghuazhen Formation). Gradual changes in fluvial sandstone morphology, facies, and facies successions are related to changes in tectonics and accommodation/supply conditions through time. See figures 3.4 and 4.1 for location.

2 (SW)

Well Cross-Section 2

2' (NE)

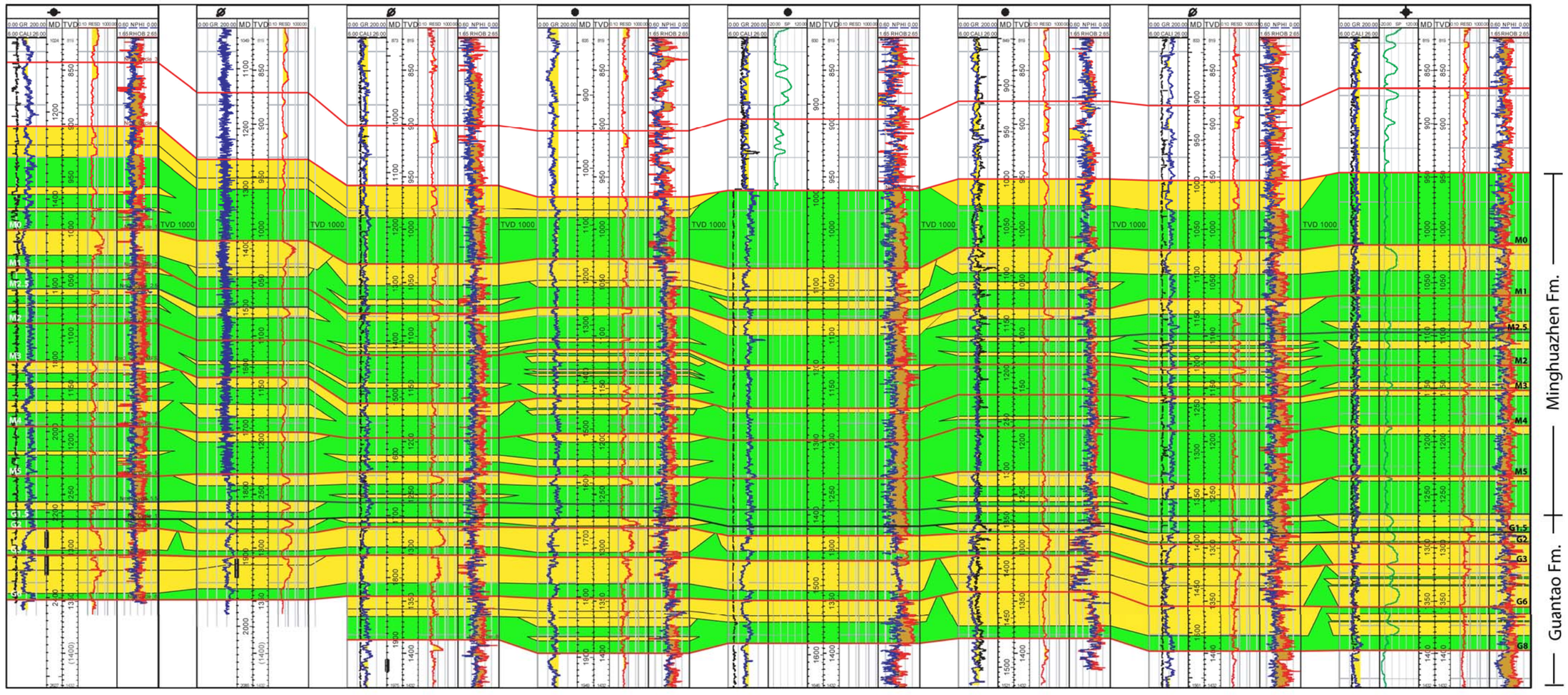

Figure 3.9

Figure 3.10. Strike well cross-section 3-3’ showing amalgamated fluvial channel sandstones in the Guantao Formation reaching up to 55 m in thickness. Channels have flat, low relief erosive bases with multiple internal scour surfaces separating individual channel bodies. Individual channel sandstones of the Minghuazhen Formation are characterized by thin, lenticular and laterally discontinuous sand bodies encased in floodplain facies. See figures 3.4 and 4.1 for location.

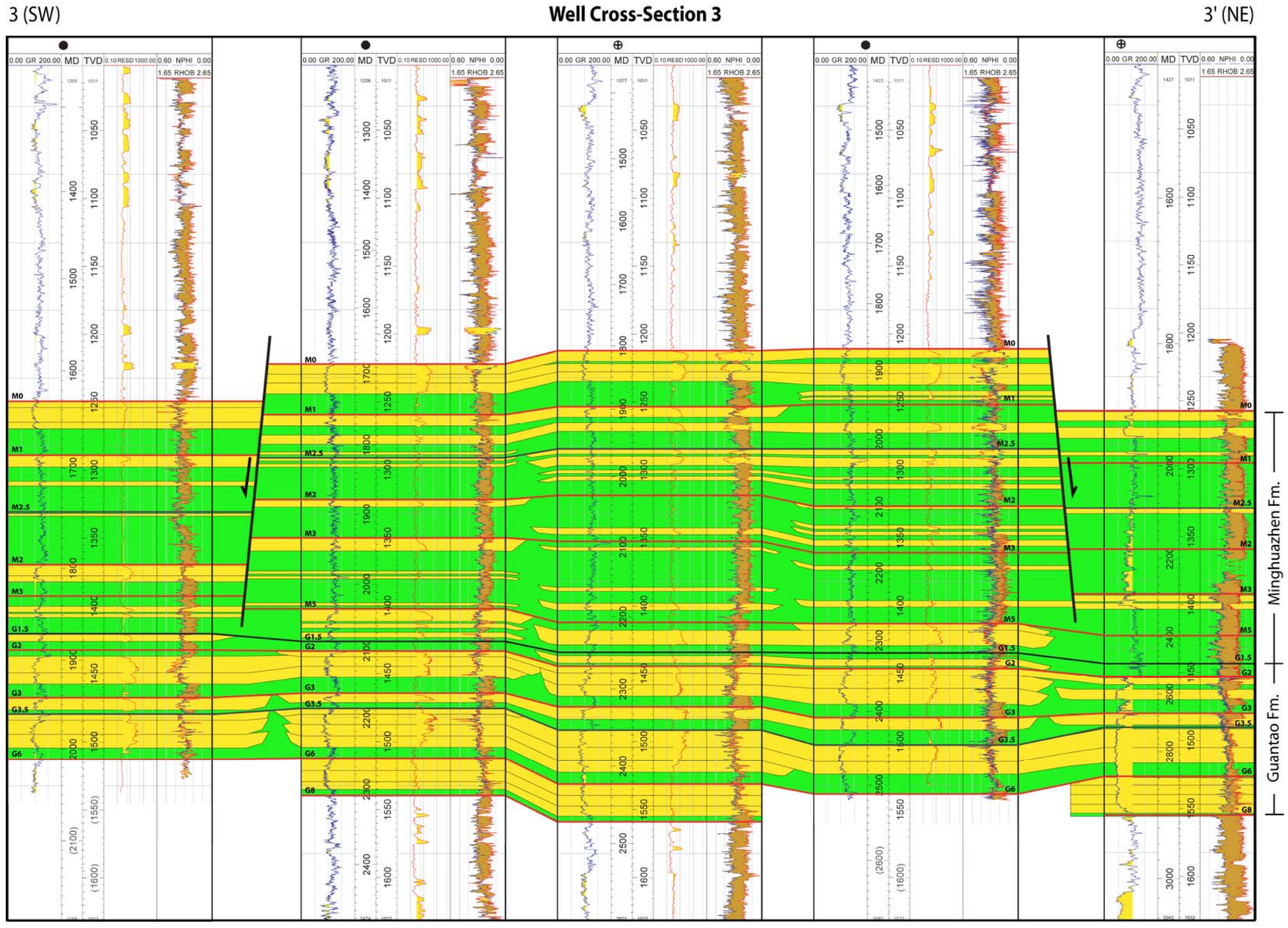
3 (SW)
Well Cross-Section 3
3' (NE)
0.00 GR 200.00
MD
TVD
0.10 RESD 1000.00
0.60 NPHI 0.00
1.65 RHOB 2.65
M0
M1
M2.5
M2
M3
M5
G1.5
G2
G3
G3.5
G6
G8
Guantao Fm.
Minghuazhen Fm.

Figure 3.10

Figure 3.11. Dip well cross-section 4-4'. Fluvial-channel sandstones of the Guantao Formation laterally and/or vertically contact one another or are separated by only a few feet of floodplain facies suggesting deposition under lower accommodation/supply (A/S) conditions (see Figure 3.5c) . Sandstone bodies in the Minghuazhen Formation are isolated within floodplain facies and show well developed splays suggesting deposition under higher accommodation/supply (A/S) conditions (see Figure 3.5c). See figures 3.4 and 4.1 for location.

4 (N)

Well Cross-Section 4

4' (S)

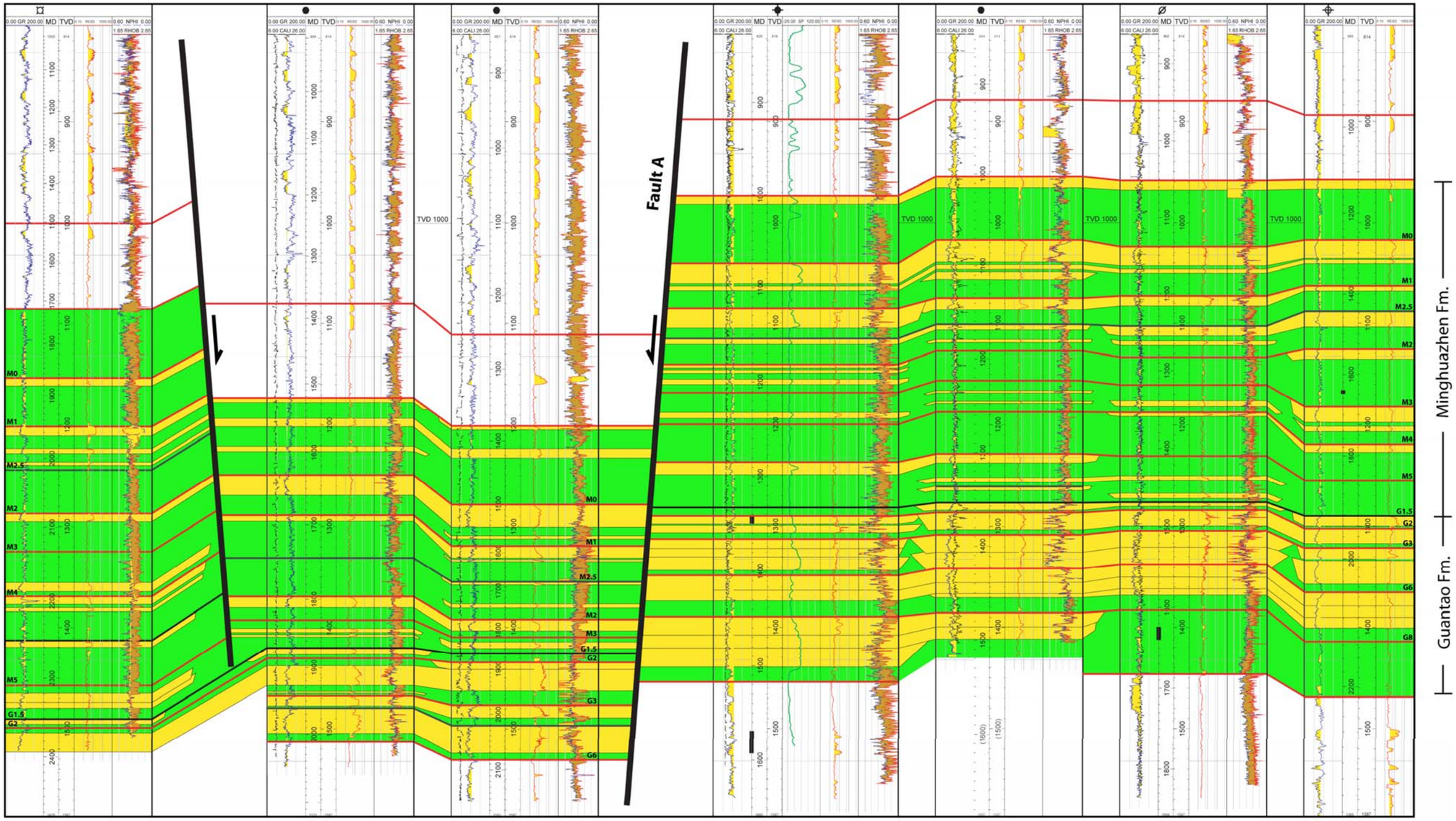

Figure 3.11

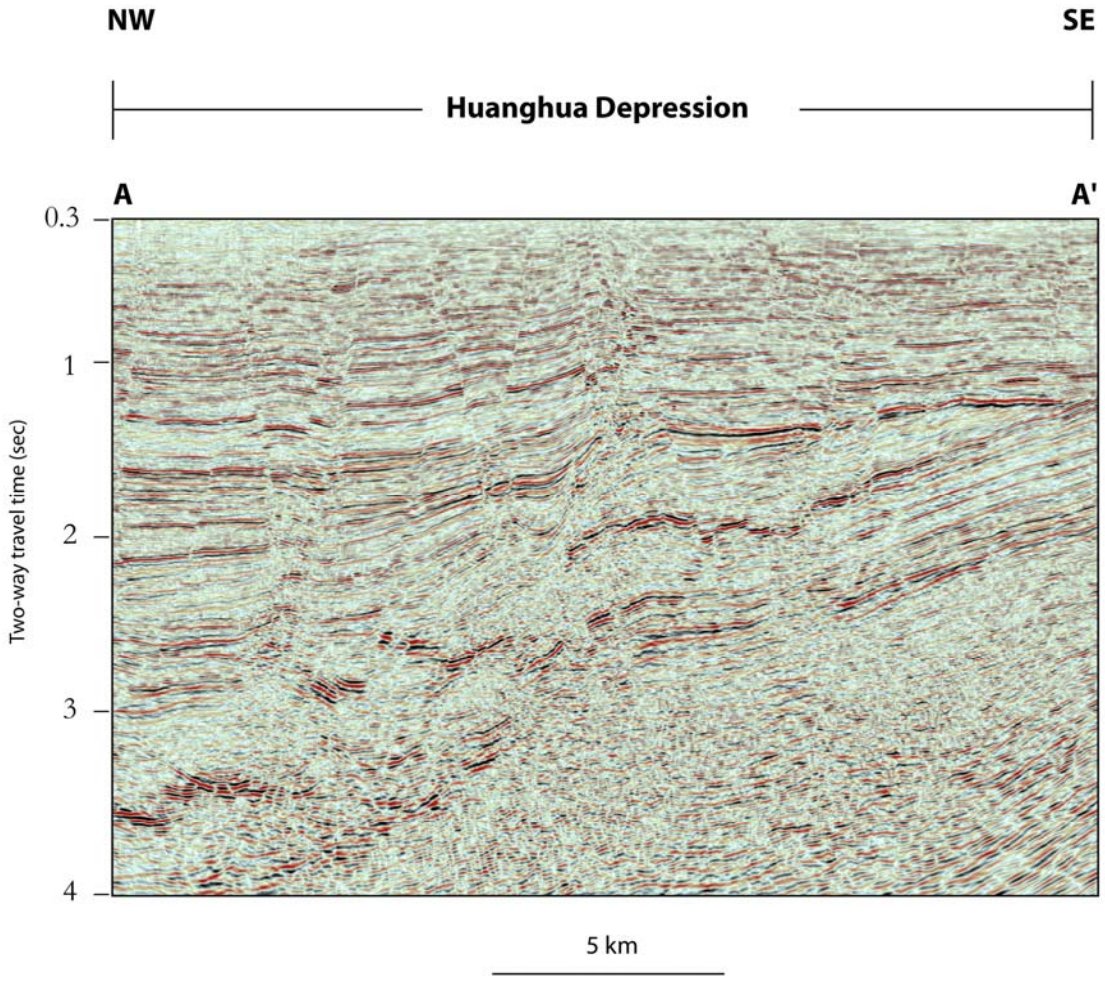

Figure 3.12a. Uninterpreted seismic line A-A'. See figure 3.14 for location

Figure 3.12b. Interpreted seismic line A-A' showing the main structure of Zhao Dong field consisting of a half-graben filled by a thick early Eocene to recent non-marine clastic succession. Numerous normal faults cut the sedimentary section. Many of these faults extend downward into the pre-Tertiary “basement" and in some cases cut upwards to the seafloor. Circle with “x” indicates block motion away from viewer along right-lateral strike-slip fault A. Circle with dot indicates motion toward viewer See figure 3.14 for location.

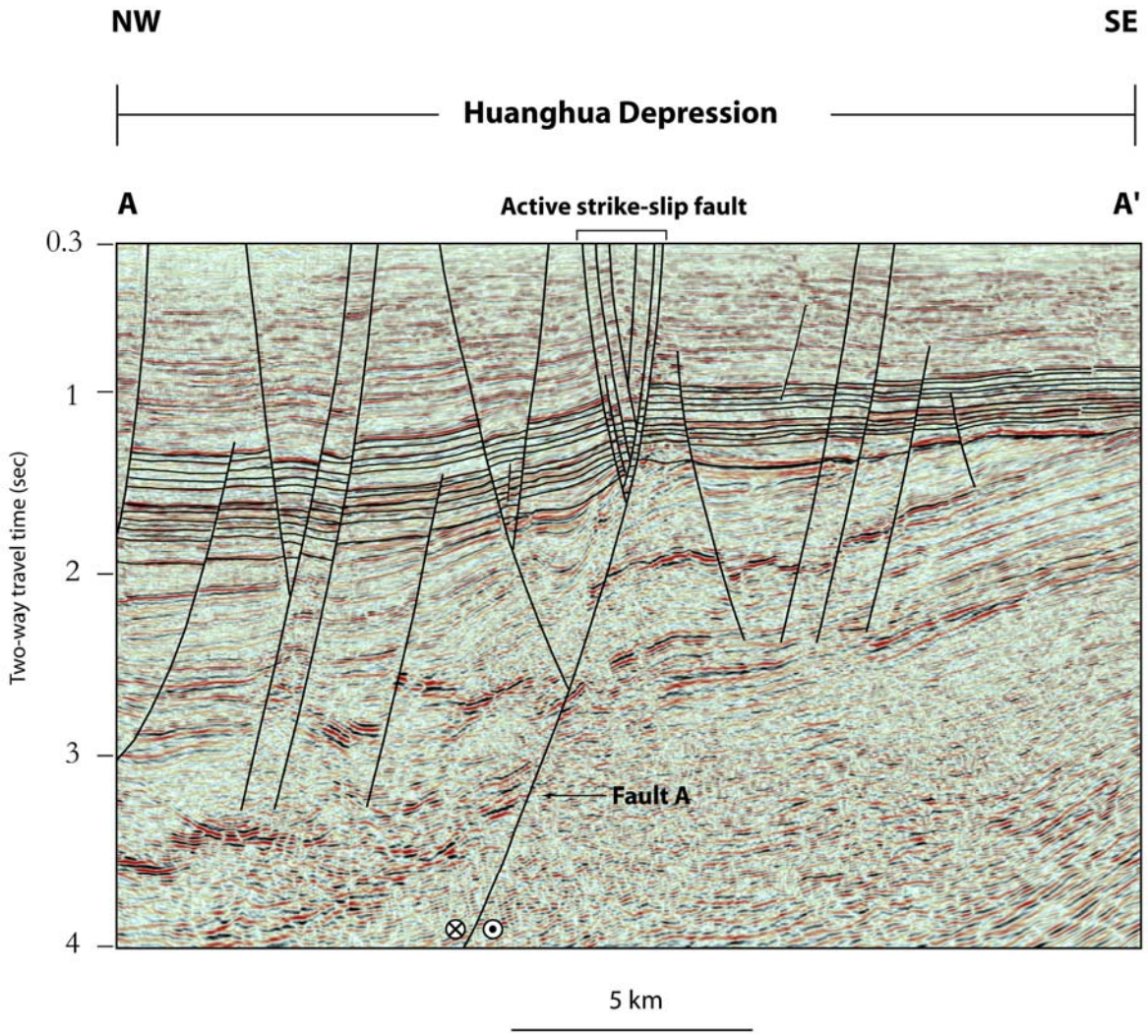
NW
SE
Huanghua Depression
A
Active strike-slip fault
A'
0.3
1
2
3
4
Two-way travel time (sec)
Fault A
5 km

Figure 3.12b

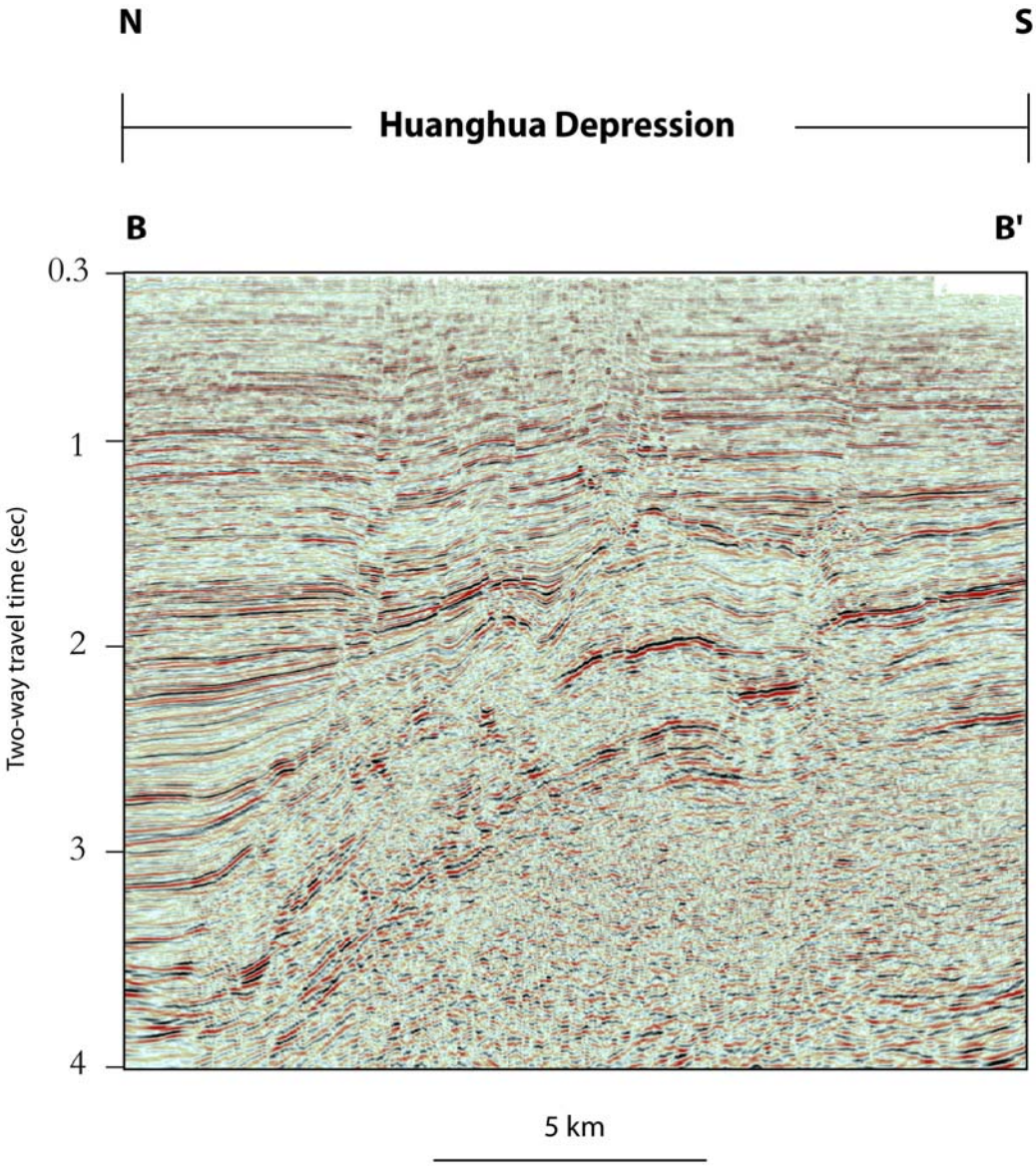

Figure 3.13a. Uninterpreted seismic line B-B'. See figure 3.14 for location

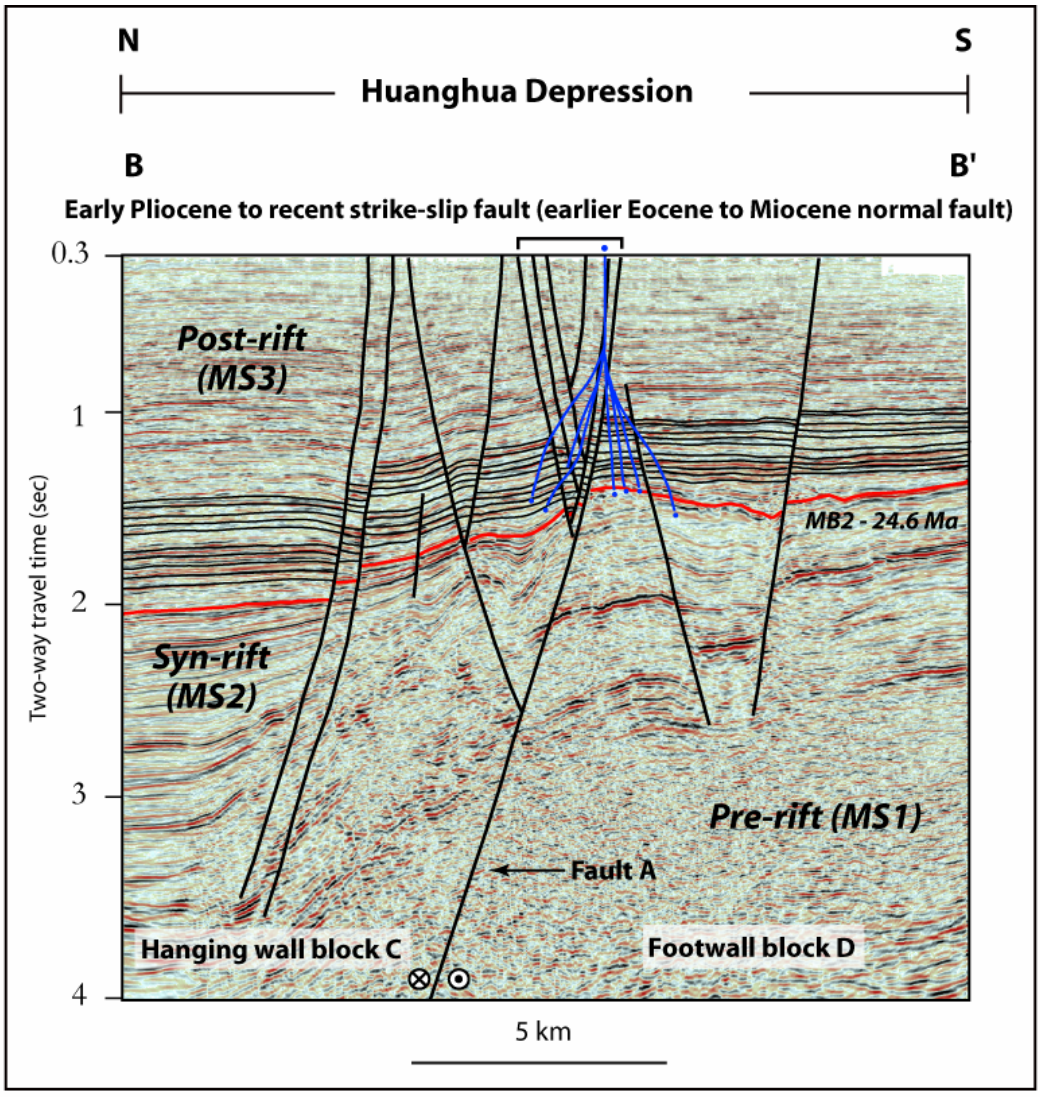

Figure 3.13b. Interpreted seismic line B-B' showing stratigraphic cycles (reservoir intervals) in the Miocene and Pliocene Guantao and Minghuazhen Formations and main faults in Zhao Dong field. Deviated wells correspond to the well log cross section 4-4' (figure 3.11). Circle with "x" indicates block motion away from viewer. Circle with dot indicates block motion toward viewer. See figure 3.14 for location.

3.4.7.1 Cycle G2

This horizon is characterized in vertical seismic sections by a strong and continuous seismic reflection. The RMS amplitude map of Cycle G2 (Figure 3.14) shows widespread areas of unconfined sandstone distribution throughout the Zhao Dong field. This is the only amplitude map constructed for the Guantao Formation. As interpreted from the well data this horizon is part of an interval dominated by amalgamated, multi-storied and laterally continuous sheet sandstones. Therefore individual fluvial channels are not preserved.

3.4.7.2 Cycle M5

This horizon is characterized on vertical seismic sections by a strong and discontinuous seismic reflection. The RMS amplitude map of the Cycle M5 (Figure 3.15) shows depositional characteristics similar to those of horizon Cycle G2, although sand-rich areas are less common and are mostly confined to the downthrown fault block in the northernmost part of the field (Figure 3.15).

3.4.7.3 Cycle M4

This horizon is characterized on vertical seismic sections by a weak and discontinuous seismic reflection. The RMS amplitude map of Cycle M4 (Figure 3.16) shows a significant decrease in sand content. The interval is mostly dominated by floodplain facies. Low to moderate sinuosity channels run roughly south to north and are mostly confined to the upthrown block (block D) in the southern part of the field. A low to moderate sinuosity channel trending roughly east-west and sub-parallel to the strike of the main east-west fault, fault A, is also visible in the eastern side of downthrown block.

3.4.7.4 Cycle M3

This horizon is characterized in vertical seismic sections by a weak and discontinuous seismic reflection. The RMS amplitude map of Cycle M3 (Figure 3.17) shows depositional characteristics similar to those of horizon Cycle M4. As in the previous horizon M4, this interval consists mostly of floodplain facies. Low to moderate sinuosity channels run roughly south to north and are mostly confined to the upthrown block D of the field area (Figure 3.17). Small sand-rich areas are also visible in the central part of the field close to the main east-west faults.

3.4.7.5 Cycle M2

This horizon is characterized by weak and discontinuous seismic reflections. The low to moderate sinuosity channels run roughly south to north across the full length of the map area (Figure 3.18). The cycle M2 RMS amplitude map reveals the most sharply defined river systems in the entire seismic data set (Figure 3.18). Fluvial channels are confined between broad sandstone-poor areas attributed to floodplain deposition. A prominent and widespread area of unconfined sandstone deposition is also recognized in the downthrown block of the field.

3.4.7.6 Cycle M1

The RMS amplitude map of the Cycle M1 (Figure 3.19) is characterized by weak and discontinuous seismic reflections inferred to be mostly floodplain facies. Weakly developed, low to moderate sinuosity fluvial channels run roughly south to north and are confined between broad sandstone-poor areas (Figure 3.19).

3.4.7.7 Cycle M0

This horizon is characterized by a strong and continuous seismic reflection over most of the seismic volume. The RMS map for Cycle M0 (Figure 3.20) shows a significant increase in sand content. The western side of the field is characterized by a broad and unconfined sandstone distribution. Floodplain facies are areally restricted and are mostly located in the upthrown block of the field, north of the main east-west fault A. In contrast, floodplain facies are dominant in the eastern side of the field. Sand rich areas are scarce and are mostly located in the upthrown block of the field (Figure 3.20).

3.4.8 Subsidence analysis of Zhao Dong field

Subsidence analysis in the Zhao Dong field includes calculations of tectonic subsidence or subsidence caused exclusively by tectonic mechanisms. This method consists of removing the effects of sediment loading, compaction and changes in sea level through time in order to isolate the tectonic subsidence (Steckler and Watts, 1978).

Figure 3.21 shows a subsidence plot I made for a single well to basement from the Zhao Dong field. The plot shows two main tectonic phases during deposition of the Neogene post-rift megasequence (MS3; Figure 3.2), which contains the fluvial deposits of the Guantao and Minghuazhen Formations: 1) a period of slow thermal subsidence (tectonic quiescence) spanning from late Oligocene until late Miocene, during deposition of the Guantao Formation; and 2) a period of gradual increase in the rates of tectonic subsidence from the early Pliocene to the present, during deposition of the Minghuazhen and Pingyuan Formations; this phase is attributed to the onset of strike-slip faulting (Chapter 2).

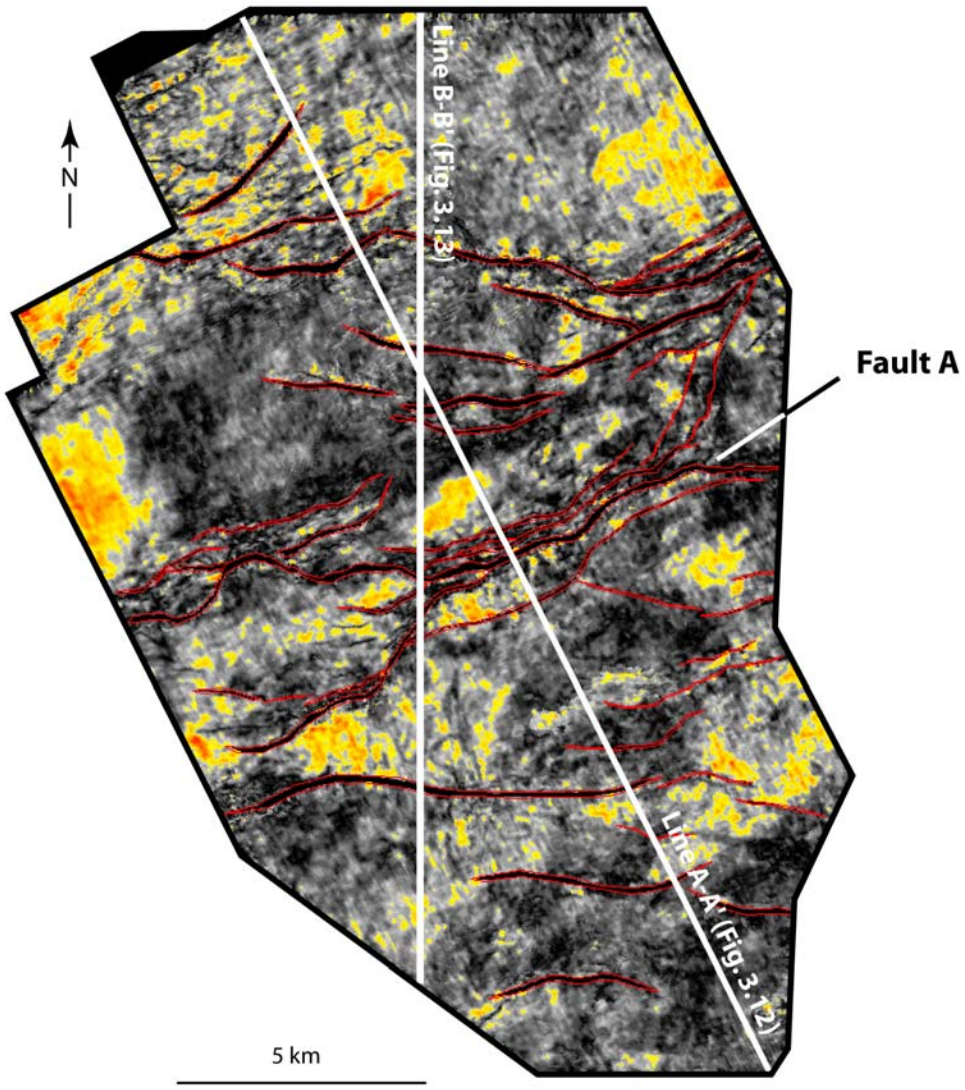

Figure 3.14. Root mean square (RMS) amplitude extraction of cycle G2 (see Figures 3.1 and 3. for location). This horizon is characterized by widespread areas of unconfined sandstone distribution throughout the Zhao Dong field. Cycle G2 is part of an interval dominated by amalgamated, multi-storied and laterally continuous sheet sandstones therefore individual fluvial channels are hardly preserved. Line A-A' is shown in Figure 312. Line B-B'is shown in Figure 3.13.

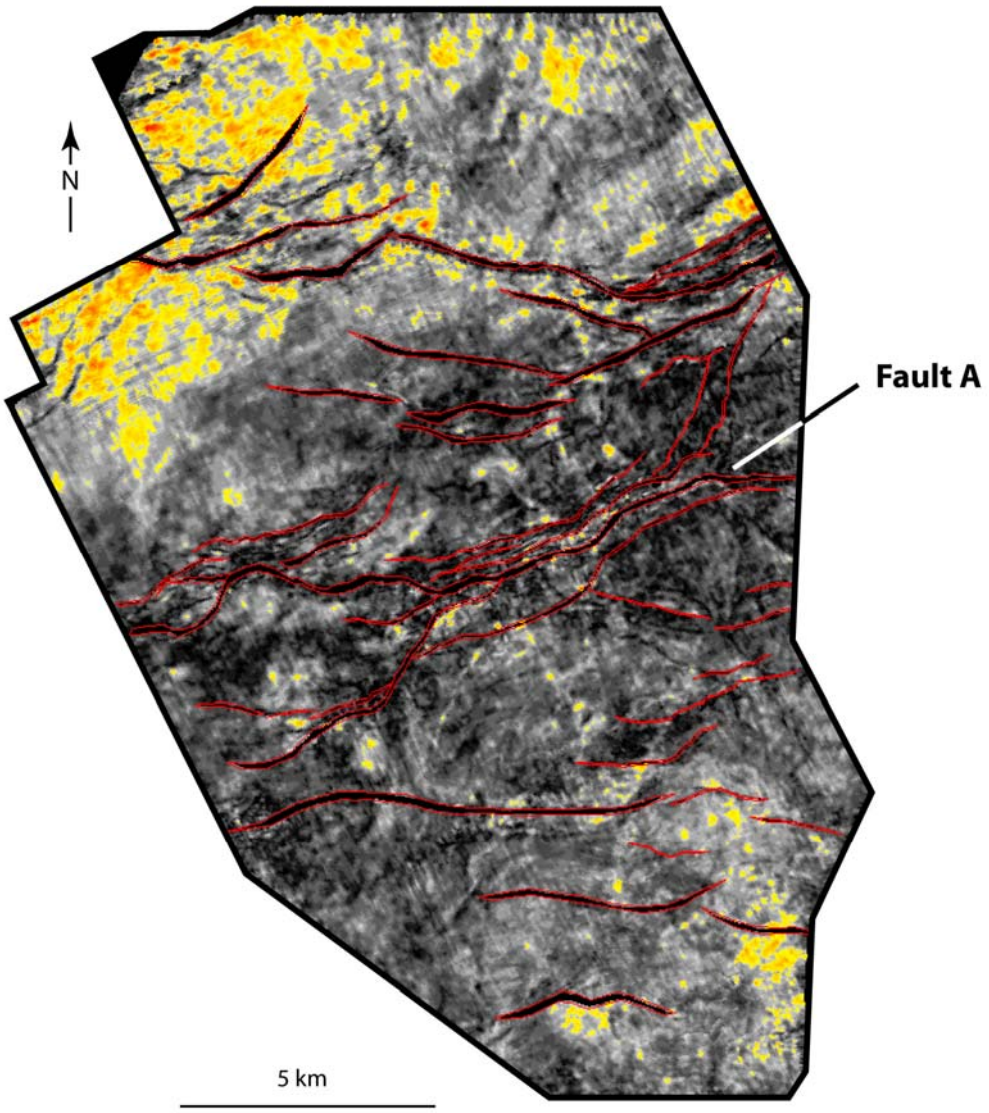

Figure 3.15. Root mean square (RMS) amplitude extraction of cycle M5. Cycle M5 shows depositional characteristics similar to those of cycle G2 (see Figures 3.1 and 3.4 for location). Sand-rich areas are less common and are mostly confined to the downthrown block (block C) in the field north of fault A.

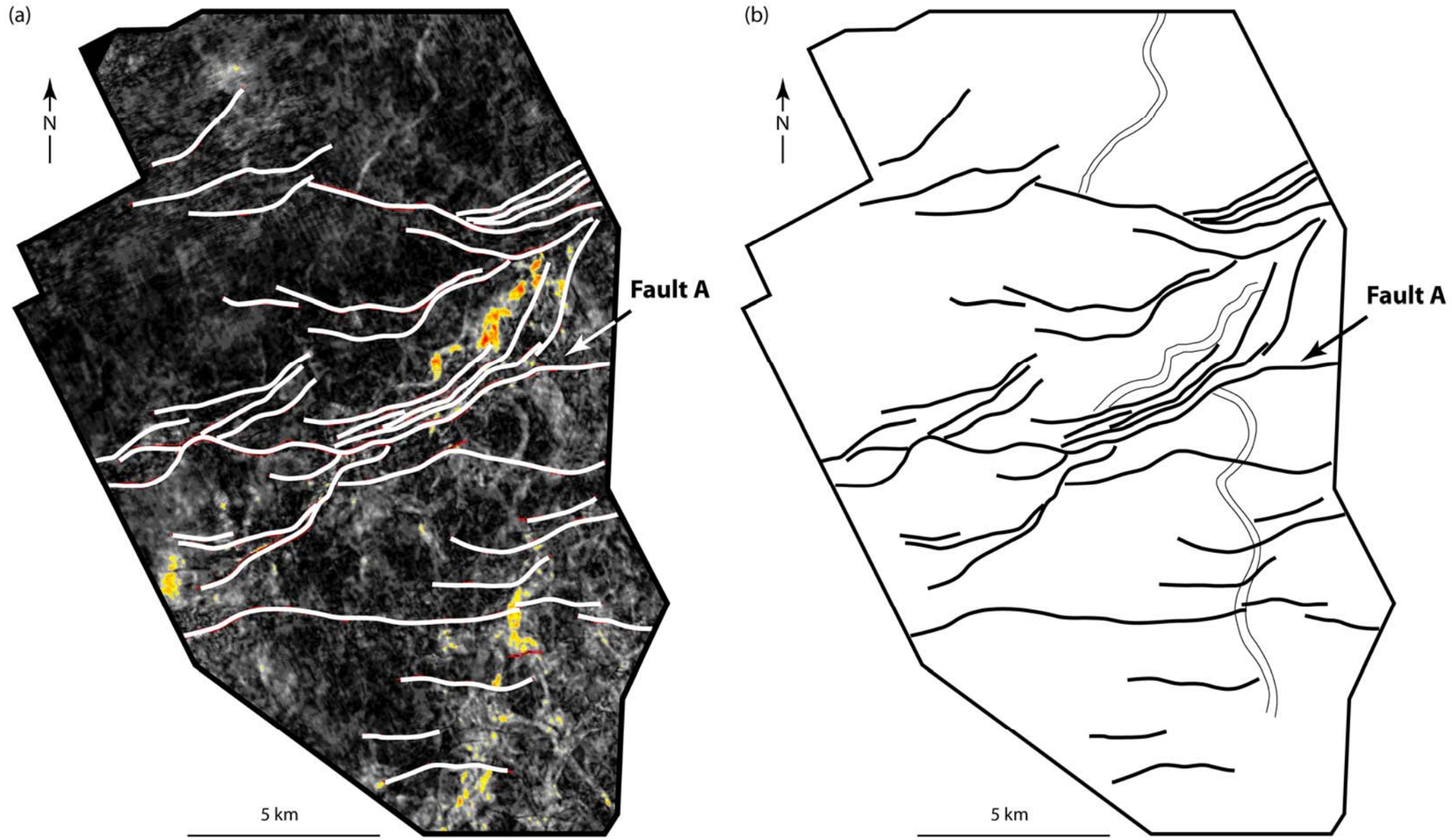

Figure 3.16. (a) Root mean square (RMS) amplitude extraction of cycle M4 (see Figures 3.1 and 3.4 for location). (b) Cycle M4 is mostly dominated by floodplain facies. Low to moderate sinuosity channels run roughly N-S and are mostly confined to the upthrown block (block D) in the southern part of the field. A low to moderate sinuosity channel trending roughly east-west, sub-parallel to the strike of the main east-west fault (fault A) is also visible in the eastern side of block C (downthrown block).

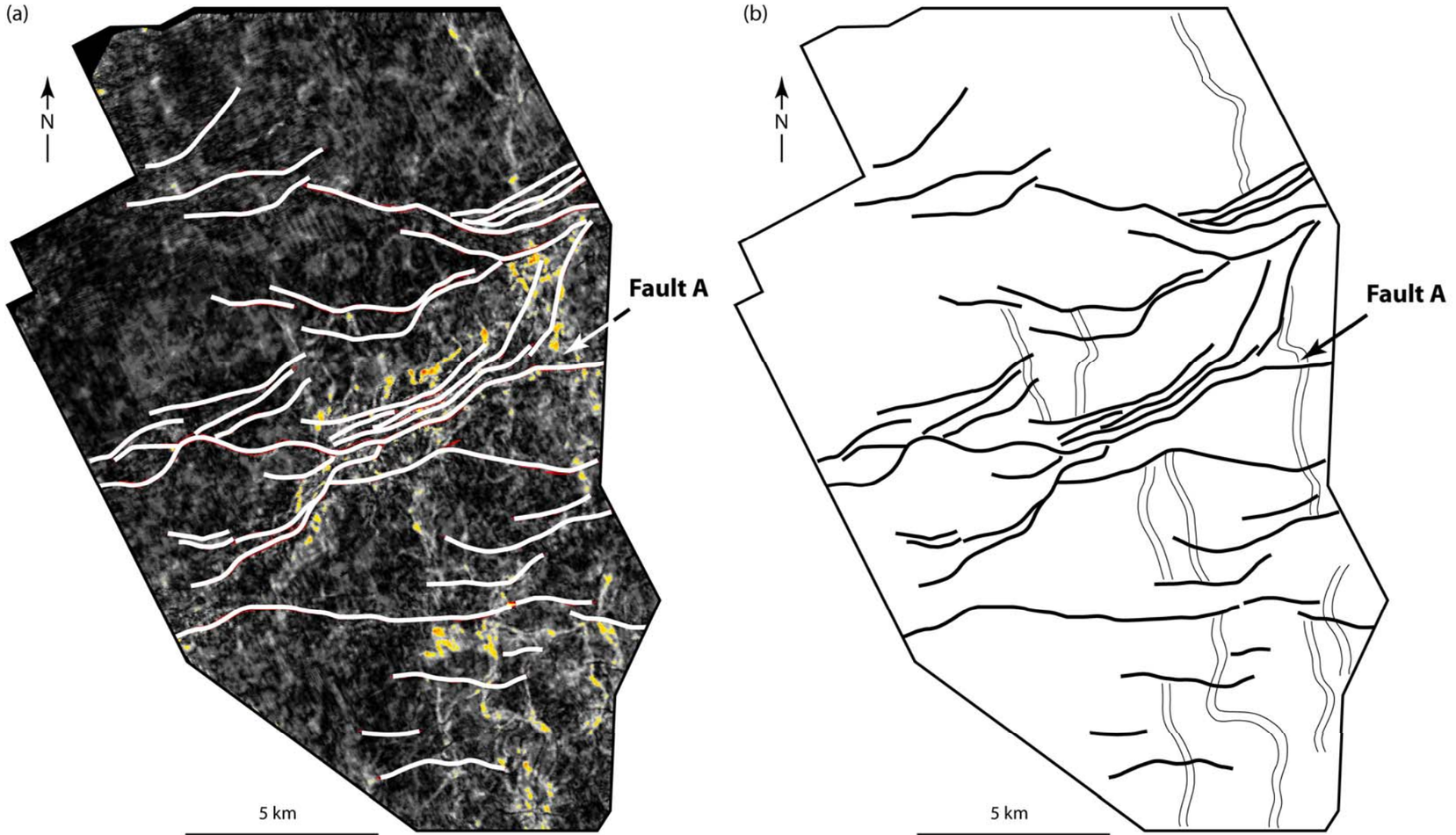

Figure 3.17. (a) Root mean square (RMS) amplitude extraction of cycle M3 (see Figures 3.1 and 3.4 for location). (b) Cycle M3 is mostly dominated by floodplain facies. Low to moderate sinuosity channels run roughly N-S and are typically confined to the upthrown block of the field (block D). Small sand-rich areas are also visible in block C close to scarps formed along main east-west faults.

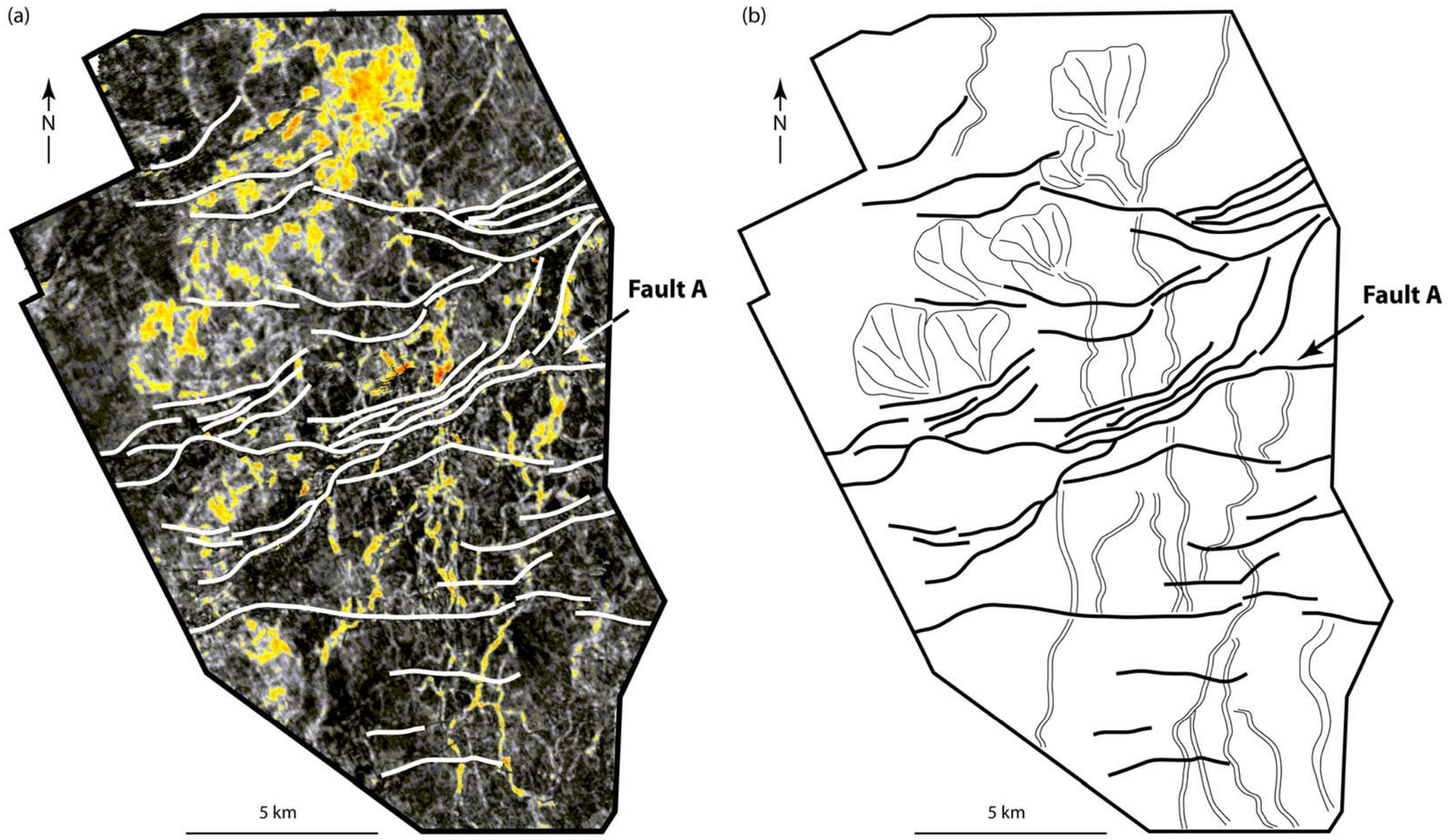

Figure 3.18. (a) Root mean square (RMS) amplitude extraction of cycle M2 (see Figures 3.1 and 3.4 for location). (b) The low to moderate sinuosity channels that run roughly N-S almost the full length of the map area in the Cycle M2 RMS amplitude extraction map are the most sharply defined river systems in the entire seismic data set. Fluvial channels are confined between broad sandstone-poor areas attributed to floodplain deposition. A prominent and widespread area of unconfined sandstone deposition in a lacustrine or alluvial fan setting is also recognized in the downthrown block of the field (block C)

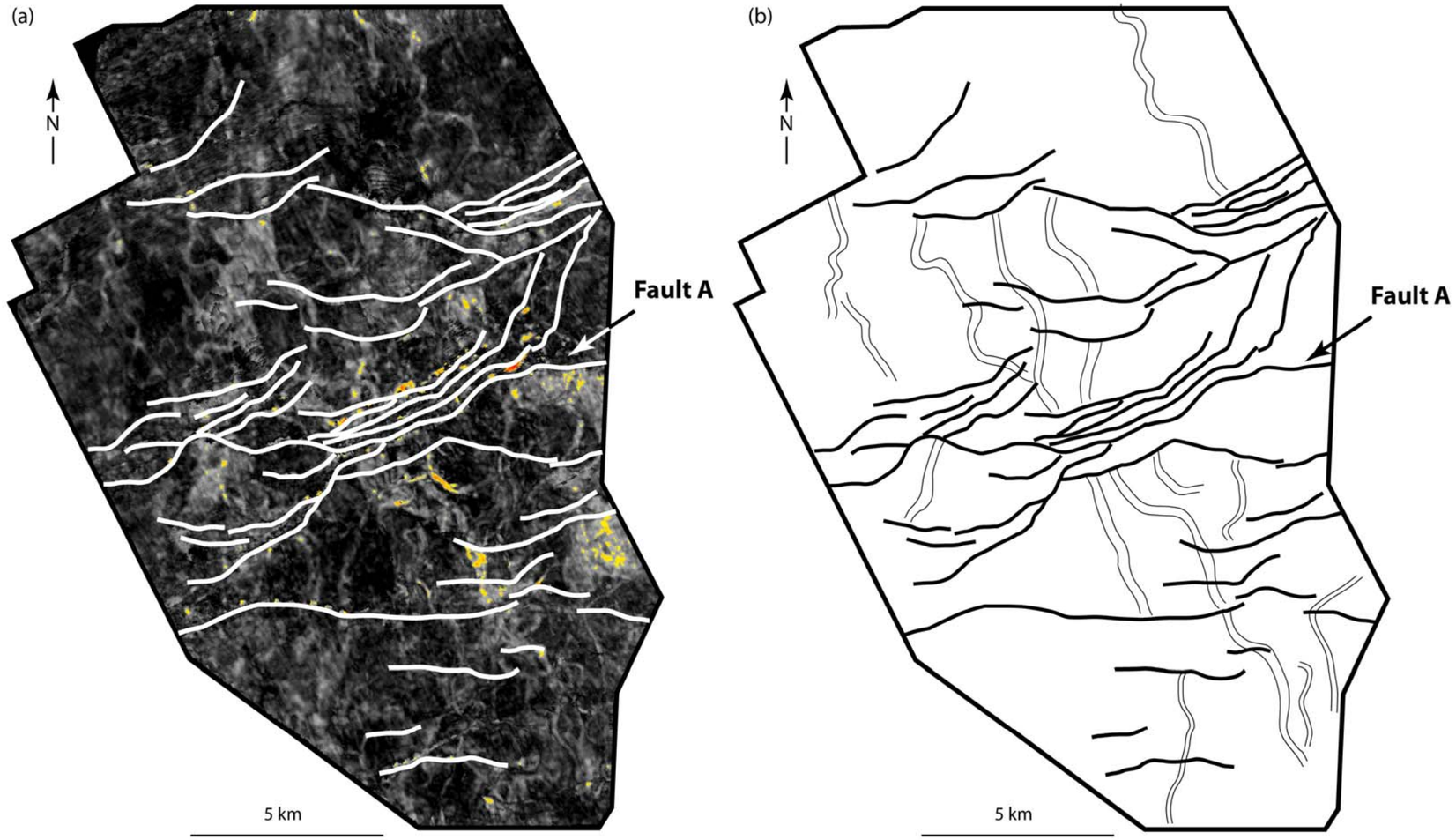

Figure 3.19. (a) Root mean square (RMS) amplitude extraction of cycle M1 (see Figures 3.1 and 3.4 for location). (b) Cycle M1 is dominated by silty floodplain facies deposition. Weakly developed, low to moderate sinuosity fluvial channels run roughly N-S over the entire field and are confined between broad sandstone-poor areas.

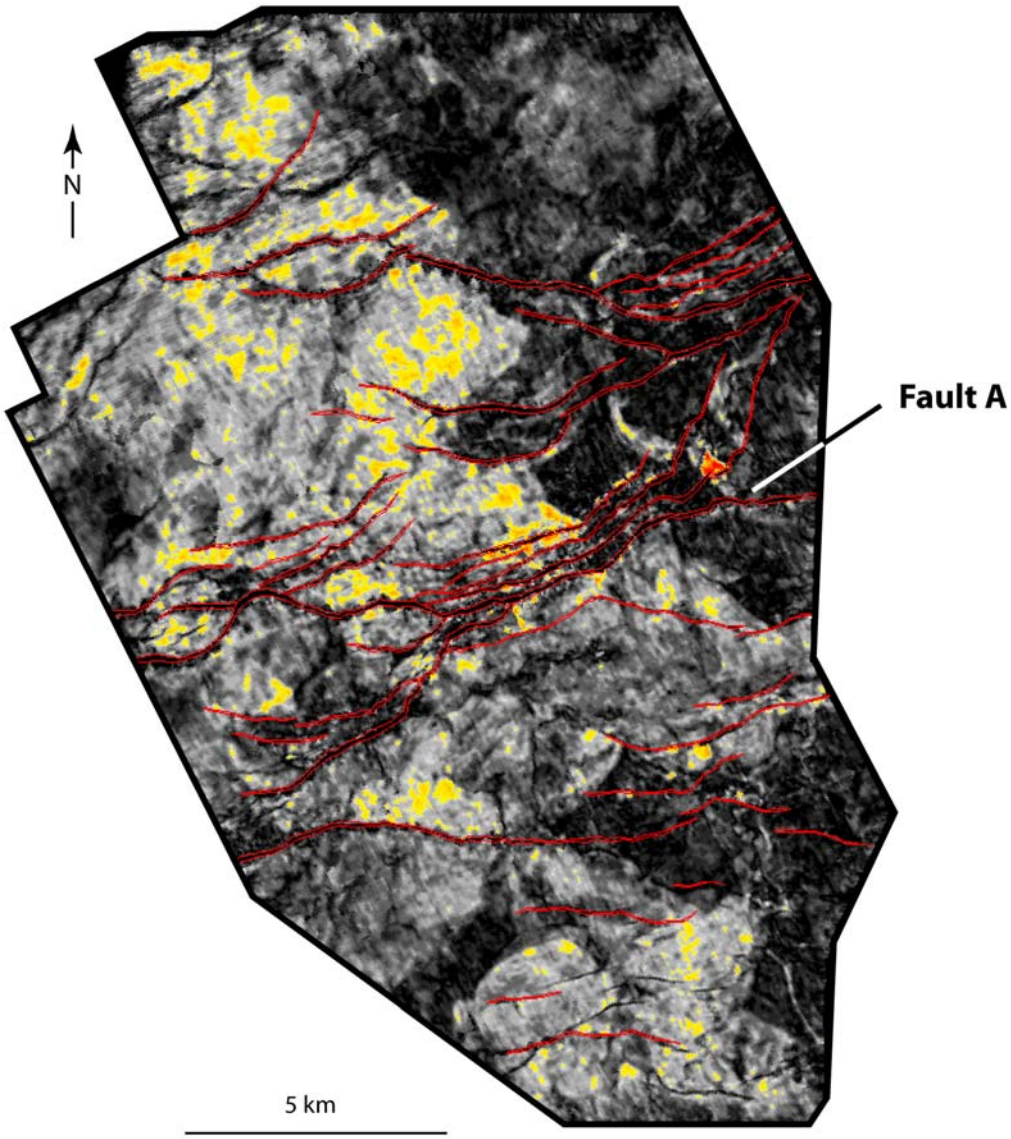

Figure 3.20. Root mean square (RMS) amplitude extraction of cycle M0 (see Figures 3.1 and 3.4 for location). This horizon shows a significant increase in sand content. The western side of the field is characterized by broad and unconfined sandstone distribution. Floodplain facies are areally restricted and are mostly located in footwall block D and the eastern side on hanging wall block D, (see Figures 3.2 and 3.12b).

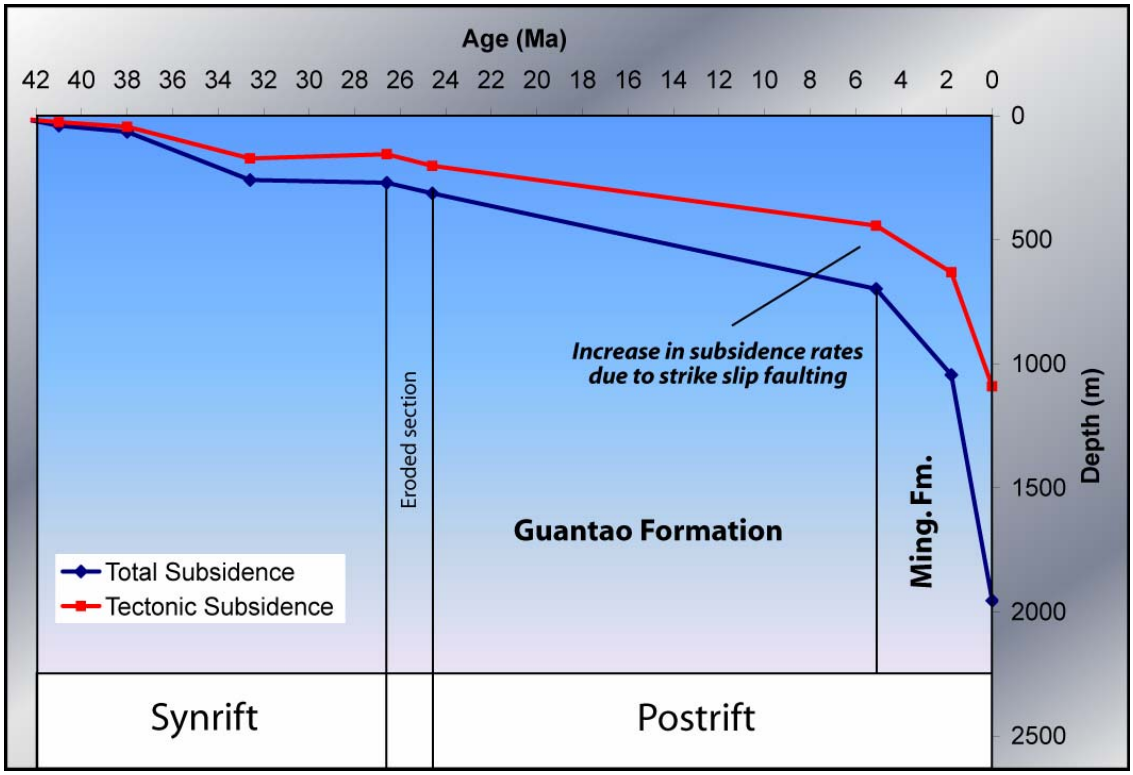

Figure 3.21. Subsidence analysis of Zhao Dong field based on analysis of a single exploration well penetrating the entire sedimentary sequence and top of basement (total depth 2990 m). Tectonic subsidence reflects removal of sedimentary load and compaction effects (Steckler and Watts., 1978). Bohai Basin underwent a period of slow thermal subsidence starting in late Oligocene with the deposition of the Guantao Formation in a large sag basin. Rapid subsidence occurred during a final phase of basin development in early Pliocene during deposition of the Minghuazhen Formation. Systematic changes in the architecture of the alluvial successions between both formations reflect continuous changes in accommodation space.

3.5. INTERPRETATION AND DISCUSSION

3.5.1 Sequence stratigraphic framework.

Neogene, post-rift deposits from the Zhao Dong field are dominated by non-marine surface processes. Therefore the use of traditional system tract nomenclature-such as lowstand, transgressive and highstand - that is linked to and dependent on the reconstruction of syndepositional shoreline shifts - is irrelevant (Catuneanu, 2006).

Dahle et al. (1997) first introduced the terms low- and high-accommodation systems tracts in an early effort to define non-marine stratigraphic units independent of marine sea-level changes and associated shoreline shifts (Catuneanu, 2006). Low- and high-accommodation systems tracts are defined mostly on the basis of changes in fluvial architectural elements, including the relative contribution and preservation of channel fills and overbank facies. Systematic changes in the architecture of alluvial successions clearly reflect changes in fluvial accommodation space through time.

The upward decrease in channel amalgamation from the basal sandstone-dominated Guantao Formation into the overlying siltstone and claystone-dominated deposits from the Minghuazhen Formation suggests that there is a progressive increase in accommodation during deposition of this succession (Figures 3.8, 3.9, 3.10 and 3.11). Thus, the sedimentary succession is interpreted as an unconformity-bounded third-order sequence, in which the basal sandstone-dominated Guantao Formation is equivalent to the low accommodation system tract as defined in the alluvial sequence model of Dahle et al. (1997). The upper siltstone-dominated Minghuazhen Formation would represent the high accommodation system tract (Figure 3.22). The entire sequence formed by cyclic variations in fluvial accommodation and its sequence boundaries result from a tectonic tilt of the fluvial profile, thereby leading to alluvial erosion.

3.5.1.1 Low accommodation system tract

Low accommodation system tract deposits overlying the basal sequence boundary are composed of aggrading, highly amalgamated fluvial sands deposited in alluvial plain settings (Figures 3.8, 3.9, 3.10, 3.11and 3.22). Fluvial channel-fill facies (FA1) are volumetrically the most important facies of the Guantao Formation, forming about 60% of its sedimentary section. Overbank deposits are poorly preserved and paleosols are common in this part of the sequence as predicted in low A/S conditions (Ramon and Cross, 1997). Log motifs are predominantly blocky reflecting amalgamation of fluvial deposits (Figures 3.8, 3.9, 3.10, 3.11and 3.22). Dipmeter analysis shows that the transport direction is northward from a southerly source area. Figures 3.23b and 3.23c shows outcrop analogs from the Karoo Basin of South Africa (Catuneanu, 2006) for the fluvial facies found in the low-accommodation system tract in the Zhao Dong field.

Highly amalgamated sandstone has been consistently interpreted in the literature as a braided-river deposit (Allen et al, 1997; Yang and Xu, 2004). However limited accommodation space during this time may have promoted slow, net aggradation and extensive cannibalization of overbank deposits. Fluvial systems during Guantao time probably migrated across the alluvial plain and eroded previously deposited channel and floodplain facies. As a result of this erosion, the depositional products of the bedload, low- and high-sinuosity channel systems may be identical. The total thickness of the channel sands may be interpreted as the result of stacking and amalgamation of several episodes of channel infill. The total thickness is probably the result of the interaction between different stratigraphic forcing mechanisms (i.e. subsidence, terrigenous sediment supply and/or climate) rather than their channel type alone.

Figure 3.22. Sedimentological model and sequence stratigraphic framework of Zhao Dong field. System tracts were recognized mainly from changes in fluvial channel stacking patterns that are shown in the well log cross sections in Figures 3.8, 3.9, 3.10 and 3.11. Systematic vertical changes in the architecture of alluvial successions clearly reflect long-term (>50 m/my) changes in accommodation space that in turn reflect changing tectonic setting and subsidence. Low accommodation system tract deposits overlying the basal sequence boundary (Guantao Formation) consist of aggrading, highly amalgamated fluvial sands deposited in alluvial plain settings. High accommodation system tract deposits (Minghuazhen Formation) consist of isolated channel-fill sandstones isolated within floodplain facies.

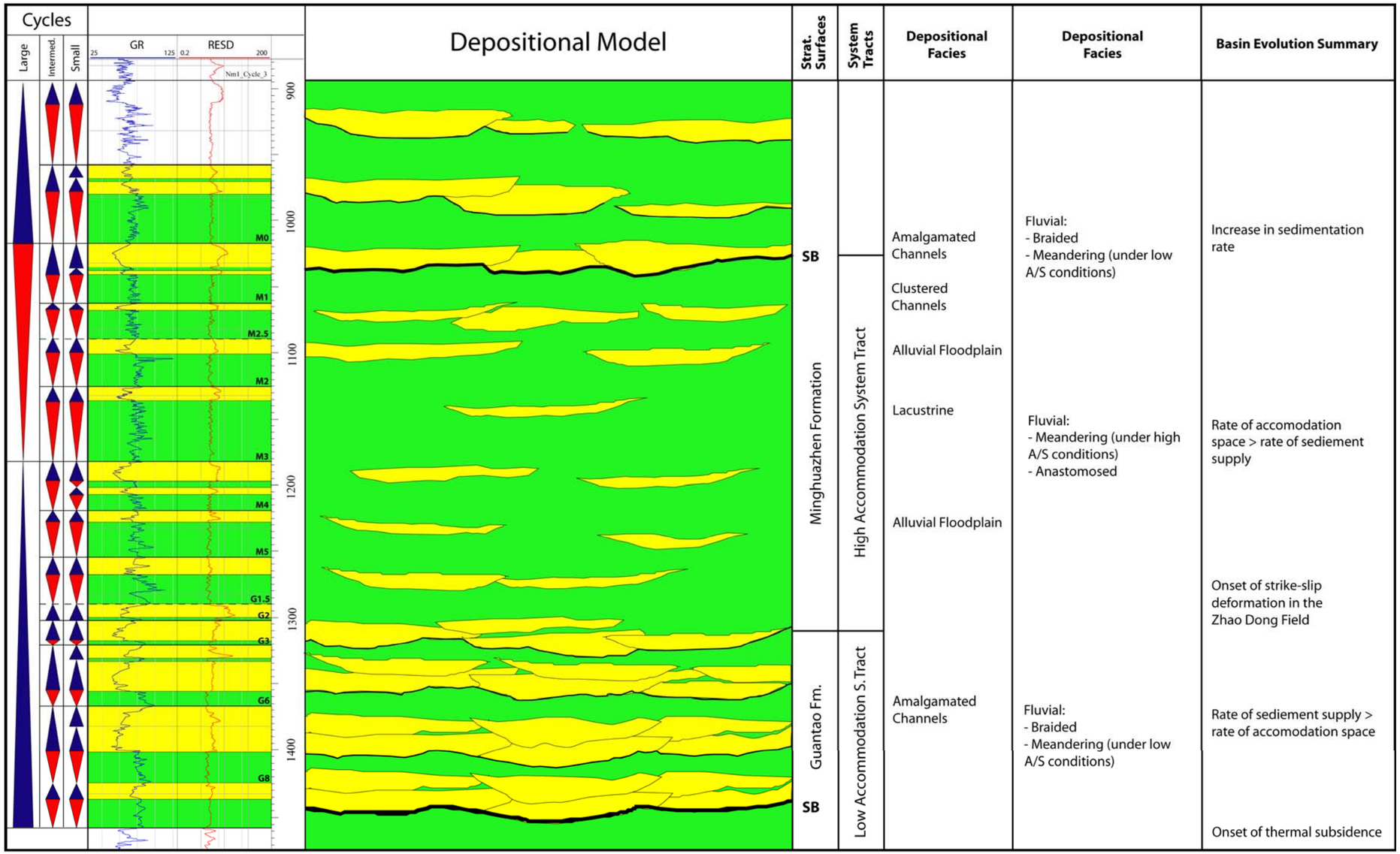
Cycles
Large
Intermed.
Small
GR
RESD
25
125
0.2
200
Nm1_Cycle_3
900
1000
1100
1200
1300
1400
M0
M1
M2.5
M2
M3
M4
M5
G1.5
G2
G3
G6
G8
Depositional Model
Strat. Surfaces
System Tracts
Depositional Facies
Depositional Facies
Basin Evolution Summary
SB
Minghuazhen Formation
Guantao Fm.
SB
High Accommodation System Tract
Low Accommodation S.Tract
Amalgamated Channels
Clustered Channels
Alluvial Floodplain
Lacustrine
Alluvial Floodplain
Amalgamated Channels
Fluvial:
- Braided
- Meandering (under low A/S conditions)
Fluvial:
- Meandering (under high A/S conditions)
- Anastomosed
Fluvial:
- Braided
- Meandering (under low A/S conditions)
Increase in sedimentation rate
Rate of accomodation space > rate of sediement supply
Onset of strike-slip deformation in the Zhao Dong Field
Rate of sediement supply > rate of accomodation space
Onset of thermal subsidence

Figure 3.22

Figure 3.23. Proposed outcrop analogs from the Precambrian Karoo Basin in South Africa (from Catuneanu, 2006) of fluvial facies that are commonly found in the low- and high-accommodation system tracts in the Zhao Dong field. A) floodplain-dominated meandering stream deposits, with isolated channel fills and distal crevasse splays; B) amalgamated fluvial channel-fill; note the base of a channel scouring the top of an underlying channel-fill; C) amalgamated fluvial channel-fills.

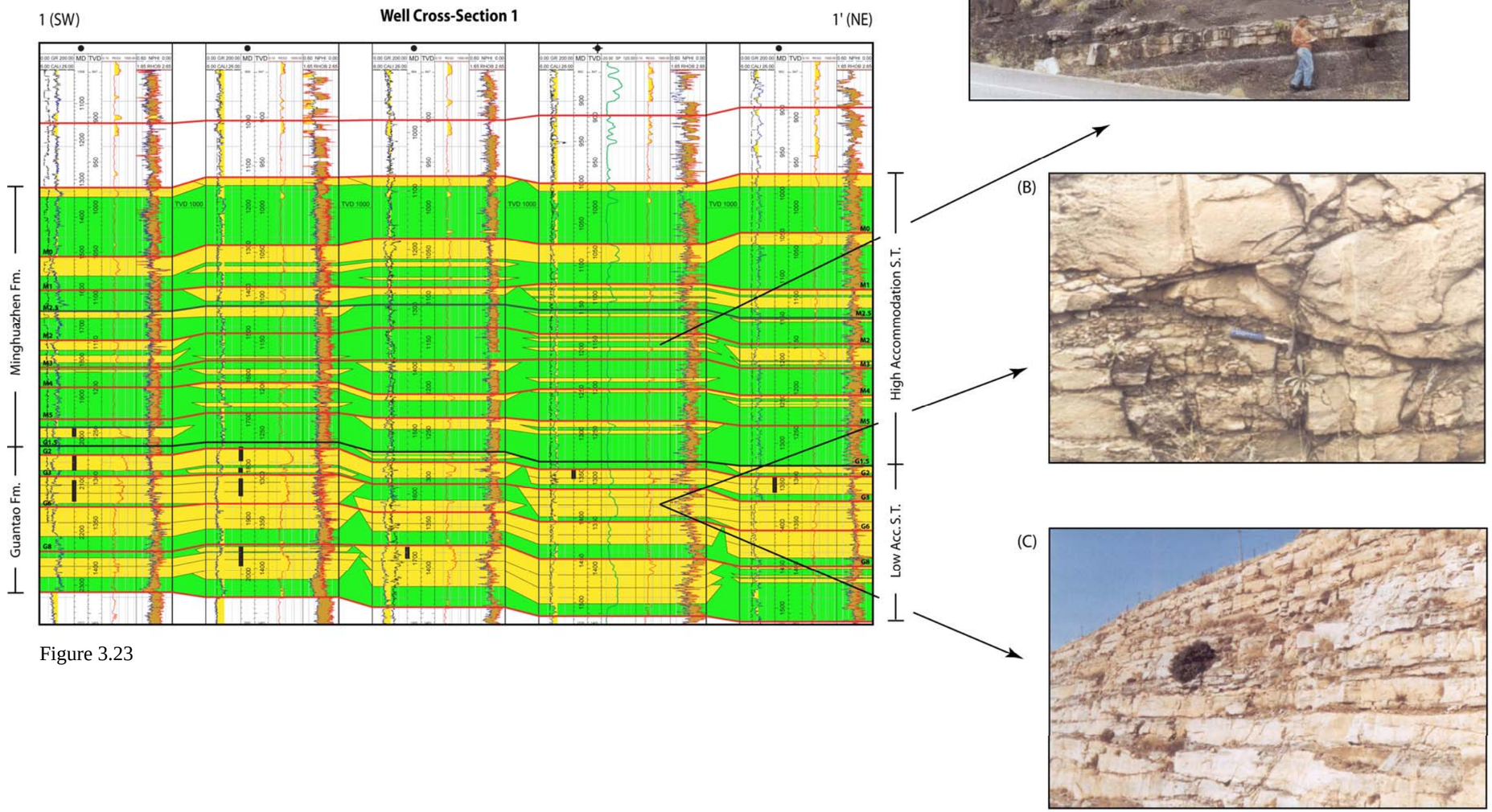
1 (SW)
Well Cross-Section 1
1' (NE)
Minghuazhen Fm.
Guantao Fm.
High Accommodation S.T.
Low Acc.S.T.
(A)
(B)
(C)

Figure 3.23

3.5.1.2 High accommodation system tract

High accommodation system tract deposits consist of isolated channel-fill sandstones (FA2) isolated within floodplain facies (Figures 3.8, 3.9, 3.10, 3.11and 3.22). Sand bodies are generally thinner and less laterally continuous than in any other part of the sedimentary section. Accordingly floodplain (FA4) and crevasse-splay facies (FA3) become more prominent as a result of increasing A/S conditions. Preservation potential is higher in this part of the sedimentary section and results in a lower sand-to-mud ratio. Isolated channel fill sandstone displays a fining-upward grain-size distribution on well logs and reflects lateral migration of channel meanders. Dipmeter analysis and seismic amplitude maps (Figures 3.16, 3.17, 3.18 and 3.19) show a northward transport direction. Figure 3.23a shows an outcrop analog from the the Karoo Basin of South Africa of the fluvial facies (Catuneanu, 2006) found in the high-accommodation system tract in the Zhao Dong field.

Fluvial channels during Minghuazhen time appear to have been low to moderately sinuous mixed-load types (Figures 3.16, 3.17, 3.18 and 3.19). Lateral migration of channel meanders resulted in accretion of point bars along the margin of relatively narrow channels. Crevasse splays formed under flood conditions where flow was partly channelized as it topped stream channel margins and spread onto the floodplain.

Cycle M2 represents the interval of maximum accommodation/supply conditions within the sedimentary section (Figures 3.5, 3.8, 3.9, 3.10, 3.11 and 3.22). Rapid generation of nonmarine accommodation during this time may have favored the formation of lacustrine conditions in the downthrown normal fault block of the Zhao Dong field (Figure 3.18). None of the wells available for this study penetrates this part of

the field but the presence of well developed non-channelized lobate sandstone bodies indicative of fan deltas help support this interpretation (Figures 3.18 and 3.24).

The high-accommodation system tract in Zhao Dong field is capped by a sharp based, multistoried (up to 25 m thick) and laterally continuous sand-body (Figures 3.8, 3.9, 3.10, 3.11). This sandstone body is interpreted as amalgamated fluvial channel-fill deposits probably overlying a low-relief fluvial incision surface. Shallow fluvial incision usually forms widespread sandstone sheets of amalgamated fluvial-channel deposits and can form sandstone units that are continuous over tens or hundreds of kilometers along strike as well as dip (Posamentier and Allen; 1999) (Figure 3.25a). The number of sandstone bodies and the degree of channel amalgamation increases above this sequence boundary so the boundary probably marks the time of initiation for a new fluvial sequence.

There is no a clear system tract boundary that defines the change from low- to high-accommodation system tracts in Zhao Dong field. Despite the lack of a marker, the stratigraphic record of both system tracts is easily differentiated due to the increased partitioning of channel and floodplain deposits and the decreasing connectivity of fluvial channel deposits in the high-accommodation system tract (Minghuazhen Formation). Reduction of fluvial gradients in response to increased A/S conditions may have promoted not only an evolution in channel styles to more mixed load or meandering fluvial systems, but also promoted an increase in the proportion of splay deposits in the stratigraphic record as rivers attempted to maintain grade with rising base level conditions. Table 3.2 summarizes a list of key features that distinguish between the low- and high-accommodation systems tracts in Zhao Dong field.

Figure 3.24. (a, b) 3D perspective of the root mean square (RMS) amplitude map of cycle M2 in the Minghuazhen Formation (cf. well log section in Figure 3.5c). The sand-rich areas are represented by different tones of yellow and red (low amplitude values), whereas floodplain facies are represented by a dark gray background color (high amplitude values). Cycle M2 represents the interval of maximum accommodation/supply conditions within the Minghuazhen Formation in Zhao Dong field. Well developed non-channelized lobate amplitude anomalies in the downthrown block of the field are interpreted as fan deltas. Existing wells are concentrated along Fault A. Green arrow points to the north C) Deposition model of a fan delta in normal fault-bounded depression (modified from Evans et al., 2003).

(A)

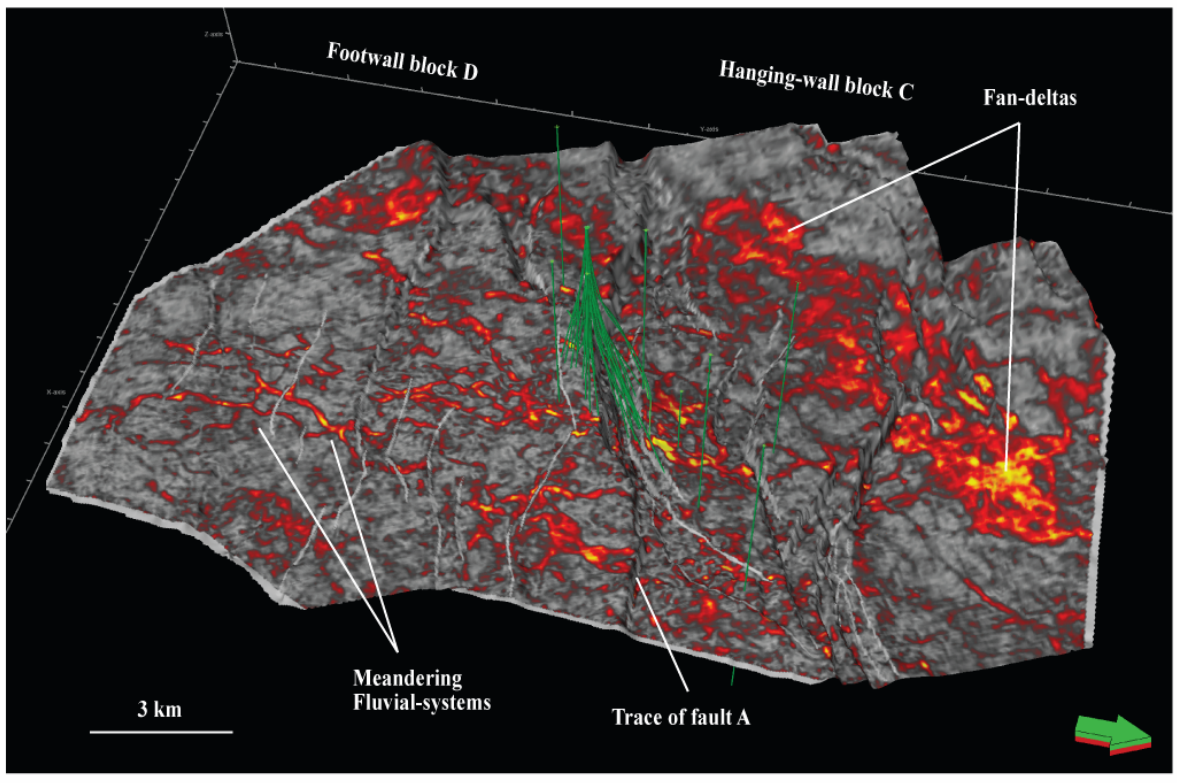

(B)

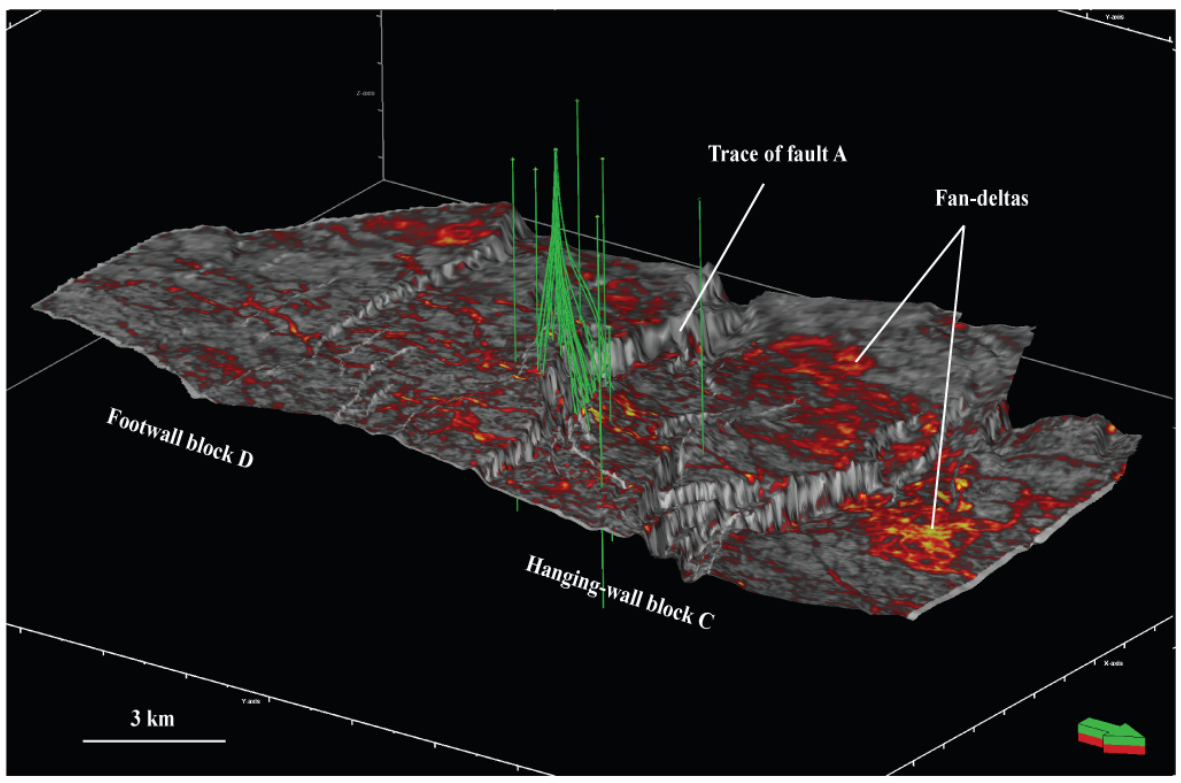

(C)

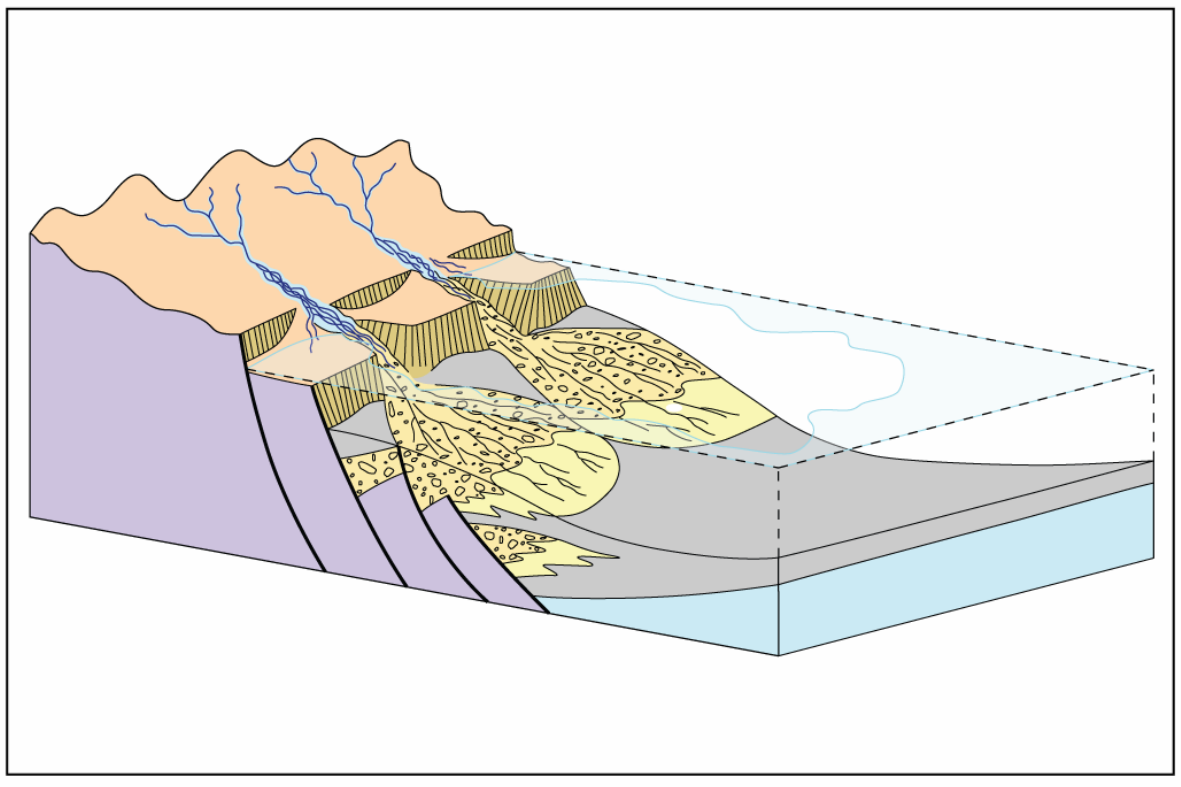

Figure 3.24

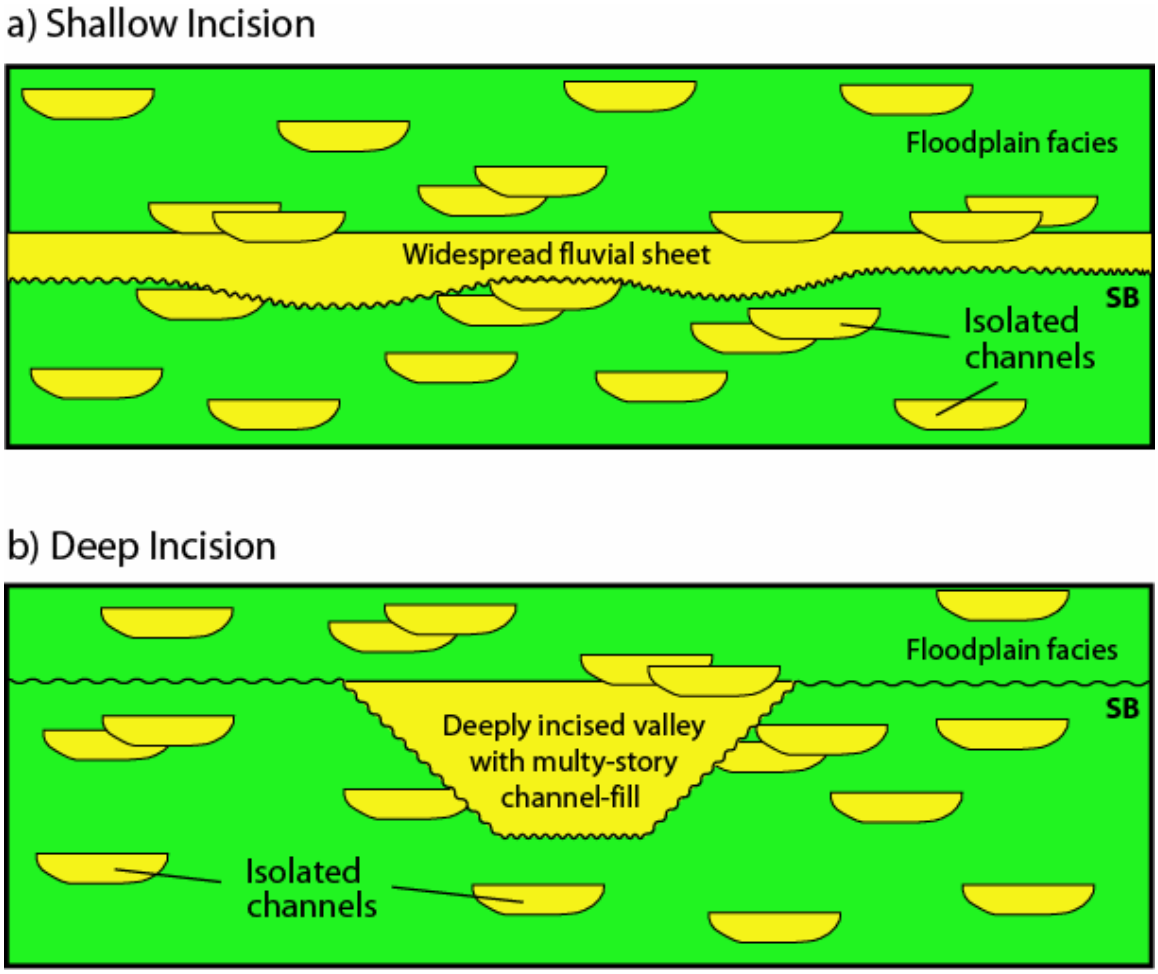

Figure 3.25. Examples of shallow and deep fluvial incision and sandstone deposition (modified from Posamentier, 1999). A) Shallow fluvial incision usually forms widespread sandstone sheets of amalgamated fluvial channel-fill deposits. The base of these sheets commonly mantles a low relief regional erosion surface (cf. Minghuazhen Formation in Figures 3.5c, 3.8, 3.9, 3.10 and 3.11). B) Deep fluvial incision generally leads to narrow and deep incised valleys with high relief (modified from Posamentier, 1999).

Systems tract / Features	Low-accommodation system tract (Guantao Fm.)	High-accommodation system tract (Minghuazhen Fm.)
Grain size	Coarser	Finer
Sand to mud ratio	High	Low
Reservoir architecture	Amalgamated channel fills	Isolated sandstones
Floodplain facies	Sparse	Abundant
Thickness	Thinner	Thicker
Paleosols	Somewhat developed	Minor or absent

Table 3.2. Comparison of facies characteristics of the low- and high-accommodation system tracts in the Guantao and Minghuazhen Formations of Zhao Dong field (adapted from Catuneanu, 2006).

3.5.2 Stratigraphic forcing mechanisms

Fluvial systems respond to a number of allogenic controls on sedimentation, which include eustasy, climate, source area tectonism and basin subsidence (Shanley and McCabe, 1994; Galloway, 1996). The interplay of these variables, in addition to sediment compaction, defines the stratigraphic architecture of the sediments that fill the accommodation space within a basin (Vail et al., 1977; Galloway, 1989; Emery and Myers, 1996). In order to understand the origin and stratigraphic architecture interpreted in the Zhao Dong field, these variables are discussed below.

3.5.2.1 Eustasy

The Guantao and Minghuazhen Formations in Zhao Dong field are fully continental fluvial successions (Chen Changming et al, 1984; Allen et al., 1997; Yang and Xu, 2004) and accumulated in isolation from any marine influences. Eustasy can therefore be ruled out as an external control on accommodation and stratigraphic patterns in the Zhao Dong field.

3.5.2.2 Climate

Fluvial sequences reflecting climate changes are mainly controlled by orbital forcing - that is, Milankovitch cycles of glaciation and deglaciation at temporal scales of 10^4 – 10^5 years (Miall, 1996; Catuneanu, 2006). Climate fluctuations affect the river discharge which in turn affects the balance between the transport capacity of the river and its sediment load. Increased transport capacity relative to sediment load triggers fluvial incision whereas increased sediment load relative to transport capacity triggers fluvial

aggradation (Miall, 1996; Blum and Tornqvist, 2000; Lukie et al., 2002; Catuneanu, 2006).

Evidence for climatic changes during deposition of the Guantao and Minghuazhen Formations in the Zhao Dong field is limited. The available literature postulates an unchanging warm and humid climate during the Miocene and Pliocene in northeast China with no significant fluctuations (Liu and Leopold, 1994; Yang et al., 2006). This conclusion is also supported in this study based on the following arguments: 1) kaolinite is the primary authigenic clay found in both formations, which is known to be preferentially formed in places with humid climate (Millot, 1979; Miall, 1996); and 2) pollen assemblages from the Guantao and Minghuazhen Formations (Table 3.3) indicate humid and temperate climatic conditions with no significant fluctuations between both formations (O. Colmenares, personal communication, 2005)

3.5.2.3 Subsidence

Differential tectonic subsidence or basin tilting, such as typically occuring near active normal fault blocks, affects channel pattern and facies preservation (Galloway and Hobday, 1996). These tectonic effects influence the fluvial equilibrium profile, leading to stream deflection and the shift of the channel course in the direction of maximum subsidence. Such channel-belt movements have the potential of increasing the proportion and connectedness of channel-belt deposits within a basin fill (Alexander et al, 1994).

The sedimentary fill in Zhao Dong field is dominated by repetitive, upward coarsening stratigraphic cycles (Figure 3.5). These stratigraphic cycles appear to be controlled by tectonically-induced changes in base-level that induced progradation of axial coarse-grained facies over axial finer-grained facies. The change from low (Guantao Formation) to high (Minghuazhen Formation) accommodation conditions seen in the

Zhao Dong field correlate with an abrupt increase in the rates of tectonic subsidence during the onset of deposition of the Minghuazhen Formation (Figures 3.8, 3.9, 3.10, 3.11 and 3.21). This period of increased subsidence rates is attributed to the onset of strike-slip deformation in the field (Chapter 2).

Formation	Pollen Assemblages	Climate
Minghuazhen (Pliocene)	*Quercus sp, Ceratopteris, Pinus, Picea, Tsuga, Abies, Artemisia, Salix, Liquidambar, Polygonaceae, Fagaceae, Ulmaceae, Juglandaceae, Betulaceae, Tiliaceae, Chenopodiaceae, Gramineae, Leguminosae, Rosaceae, Compositae, Cruciferae, Labiatae, Convovulacea.*	Subtropical, humid
Guantao (Miocene)	*Ceratopteris, Juglandaceae, Pinus, Juglans, Ulmus, Larix, Taxaceae, Taxodiacea, Chenopodiaceae, Gramineae, Betulaceae, Polypodiaceae, Pteris, Osmunda.*	Subtropical, warm/humid and hot

Table 3.3. Pollen assemblages identified by Yao (1994) from the Guantao and Minghuazhen Formations (climatic interpretation by O. Colmenares, personal communication, 2005). Note that there is no significant change in climatic and weathering conditions between the two formations.

3.6 CONCLUSIONS

The Miocene Guantao and Pliocene Minghuazhen Formations in Zhao Dong field developed during the post-rift thermal subsidence stage of the Bohai Basin in northeastern China (Chapter 2). These deposits are entirely fluvial in origin and can be grouped into four main facies associations: FA1 - channel-fill, FA2 - point-bar, FA3 - crevasse splay; and FA4 - interdistributary facies-associations (Figure 3.7).

The integrated application of fluvial sequence stratigraphic concepts together with the identification and correlation of A/S cycles (Ramon and Cross, 1997) on three-dimensional seismic and well-log data has resulted in a revised chronostratigraphic subdivision of the fluvial deposits of the Guantao and Minghuazhen Formations in Zhao Dong field, Bohai Bay; northeastern China. The revised chronostratigraphic subdivision results in a more detailed prediction of reservoir sand distribution and connectivity and therefore increases the likelihood for successful wells drilled in the Zhao Dong field (Chapter 4).

Ten fieldwide correlatable accommodation/supply cycles were identified and correlated in the Guantao and Minghuazhen sections of Zhao Dong field (Figure 3.5c). Guantao Formation is made up of highly amalgamated fluvial sands deposited under low accommodation/supply conditions (Figures 3.8, 3.9, 3.10, 3.11 and 3.21). Amalgamated fluvial channel sandstone forms areally extensive bodies that extend several hundred meters along dip and strike directions. Minghuazhen Formation on the other hand is characterized by isolated channel systems encased by floodplain facies deposited under high accommodation/supply conditions (Figures 3.8, 3.9, 3.10, 3.11 and 3.21). The changes in the fluvial architecture between both formations are interpreted to reflect a

progressive increase in accommodation space produced by strike-slip faulting (Chapter 2) that led to successively less amalgamation of the channel deposits.

Because Guantao and Minghuazhen Formations are fully fluvial successions, eustasy can be ruled out as an external control on their accommodation and stratigraphic cyclicity. Climatic fluctuations also appear to have been minor since climatic indicators such as paleosols and pollen assemblages did not vary markedly during their span of deposition (ref).

On the basis of data presented in this chapter, I conclude that regional tectonic subsidence - including syndepositional block faulting caused by strike-slip deformation - is the main control on changing accommodation and stratigraphic cyclicity of Miocene-Pliocene non-marine deposits of the Zhao Dong field. Autogenic processes such as lateral migration and avulsion may also be superimposed effects on the autogenic processes recorded in the fluvial stratigraphy of the basin.

CHAPTER 4

Acoustic- and shear- impedance interpretation for fluvial sandstone distribution in the Miocene Guantao and Pliocene Minghuazhen Formations, Zhao Dong field, Bohai Bay, eastern China

4.1 INTRODUCTION

Exploration history. Exploration activity in the Zhao Dong oil field, located at the western edge of the Bohai Bay, northeastern China (Figures 4.1a and 4.1b), began in 1994. During the exploration and drilling campaign, eight out of eleven wildcat wells encountered commercial oil accumulations proving that large accumulations of oil exists within the field (Roc Oil Company Limited, 2007; Rigzone, 2007) (Figures 4.1a and 4.1b). Production commenced in 2003 and to date approximately 20 million barrels of oil (MMBO) have been produced (Roc Oil Company Limited, 2007). The waxy oil, which has a low pour point and a low acid content, is currently sold for the export market (Roc Oil Company Limited, 2007; Rigzone, 2007). Oil gravities range from 18° to 38° API with the higher gravity oil being in the deeper part of the section (Rigzone, 2007).

Problem and objectives of this chapter. Main reservoir rocks of the Zhao Dong field consist of the fluvial sandstone of the Miocene Guantao and Pliocene Minghuazhen Formations that have been described in detail in Chapter 3 of this dissertation. Fluvial sands in the Zhao Dong field transition from amalgamated, multi-storied and laterally continuous sheet sandstones in the underlying Guantao Formation to isolated fluvial sands encased within floodplain mudstones in the Minghuazhen Formation (cf.

Figures.3.8, 3.9, 3.10 and 3.11). Because of the complexity and lateral variability of the fluvial sandstones in both formations, the objective of this chapter is to develop a more robust method of seismic interpretation that can be used to more accurately delineate fluvial reservoir sandstone bodies in both formations and therefore improve the number of successful wells in the Zhao Dong field.

Interpretation on acoustic impedance volumes, a product of the inversion of post-stack seismic data, has substantial advantages compared to conventional seismic amplitude interpretation (Latimer et al., 2000). Acoustic impedance - the product of P-wave velocity and density - is a rock property, not an interface property (Latimer et al., 2000). Therefore interpretations should be made from lithological units rather than on lithologic boundaries at formation contacts (Latimer et al., 2000). Moreover, inversion to acoustic impedance may increase the vertical resolution of the seismic data and can then be correlated with other rock properties, such as porosity (Brown, 1996; Ronghe and Trung, 2000; Ronghe and Surarat, 2002).

Unfortunately, acoustic impedance by itself is of limited value because of its inability to reliably discriminate between lithologies and fluids. The simultaneous analysis of acoustic- and shear-impedance - the product of S-wave velocity and density - can be obtained from the inversion of multi-offset pre-stack seismic data and can significantly reduce the inability to distinguish between lithologies and fluids. The advantage of this simultaneous analysis is based on the fact that P-impedance is primarily sensitive to lithology, porosity and fluid content, whereas S-impedance is primarily sensitive to lithology.

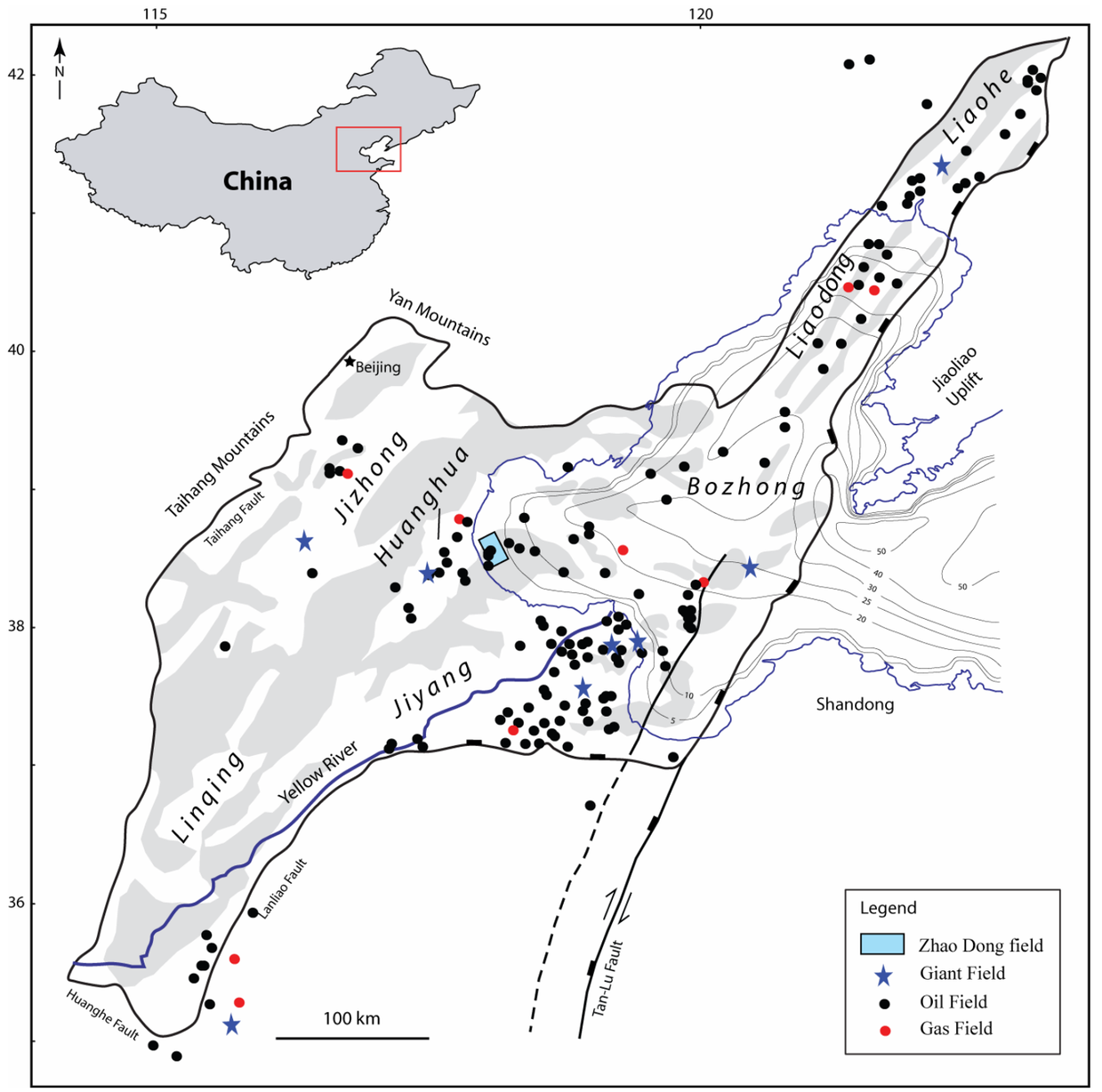

Figure 4.1a. Location of Zhao Dong field (see also Figure 4.1b) and oil and gas fields in the Bohai Basin (from Steinshouer et al., 1999). The main producing areas in the basin are concentrated near the Yellow River delta and adjacent areas in the Jiyang Depression, the central and offshore regions of the Huanghua depression, the southeast region of the Linqing depression, the eastern portion of the Jizhong depression, the Bonan rise and neighboring regions in the Bozhong depression and the onshore and offshore portions of the Liaohe depression. Major rifts or "depressions" in Chinese literature are labeled in largest type (modified from Hao et al., 2007). Bathymetric contours are from Sundermann and Feng (2004).

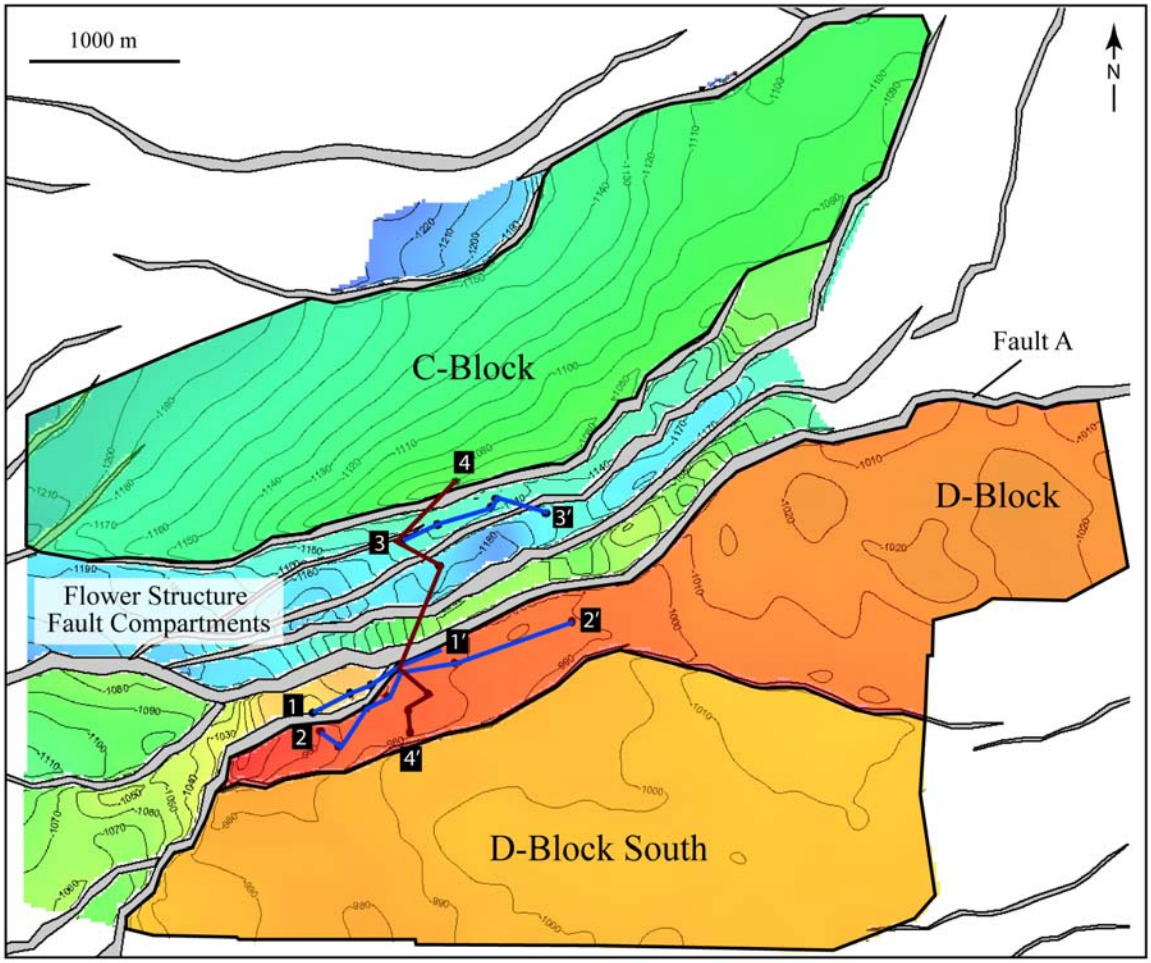

Figure 4.1b. Depth structure map of cycle M0 showing the major faults of the Zhao Dong field. Fault A has the largest throw of the faults shown and is downthrown 300 m in a northeasterly direction. Fault A originated as a normal fault during early Eocene to late Oligocene time and was reactivated as a strike slip during late Miocene to recent time. A larger view of the faulting in the Zhao Dong field is given on Figures 2.17a, 2.17b and 2.17c. Numbered lines show locations of well-log cross sections show in figures 3.8, 3.9, 3.10 and 3.11.

Because of its continental setting with Type I kerogen types and thermal history (Kuykendall et al., 2003), the Zhao Dong field is exceptionally oil prone. Oil has been discovered wherever a suitable reservoir and trap exists (Roc Oil Company Limited, 2007) (Figures 3.5 and 3.13b). Hence the primary focus of this chapter is to qualitatively explore the seismic differences in acoustic and shear response between floodplain and channel-fill facies from a 50 km^2 3D seismic data set and then use these differences to map the distributions of sandstone and shale lithologies within the Miocene Guantao and Pliocene Minghuazhen Formations. This is a challenging task given the complex fluvial environment characterized by abrupt lateral facies changes and thin sandstone bodies in the Zhao Dong field (Figures 3.8, 3.9, 3.10 and 3.11). In this chapter, I present gross sandstone maps derived from mapping the 3D seismic volume and use these maps to both develop new prospects for drilling along with increasing our understanding of the tectonic influences on sandstone distribution in the Zhao Dong field (Figure 4.1).

4.2 GEOLOGIC SETTING OF THE ZHAO DONG FIELD

4.2.1 Tectonic setting

The primary structural features that characterize the Zhao Dong field includes: 1) normal faults produced during late Paleocene to middle Oligocene time by north-south extension related to the subduction rollback of the Pacific plate beneath the Asian continent (Watson et al., 1987; Allen et al., 1997) (Figures 2.20a and 2.20b); and (2) northeast and east-west strike slip faulting produced during Miocene to recent time by a change in the direction of the plate tectonic convergence vector between the Eurasian plate and the subducting Pacific plate (Northrup et al., 1985) (Figures 2.20d and 2.21 a 2.21b).

A major east-west rift-related, south-dipping normal fault formed during late Eocene to late Oligocene time - herein called "Fault A" - divides the Zhao Dong field into two NNE-trending fault blocks: fault block D (footwall) and block C (hanging wall) (Roc Oil Company Limited, 2007) (Figures 3.2 and 4.1b). Fault A was later reactivated by strike-slip motion during the early Pliocene (Figure 2.20d). Splays of secondary faults that branch off the main east-west fault (fault A) form a prominent negative flower structure (Figure 3.2). This complex flower structure and its flanks contain many structural and stratigraphic traps that are currently the main focus of hydrocarbon prospectivity in the Zhao Dong development block.

4.2.2 Stratigraphy

Over 2 km of continental sediments of Eocene to Quaternary age were deposited in the area of the Zhao field during and after the major phase of Paleogene extensional rifting in the Bohai Basin (Figure 2.6). The sedimentary fill of the field can be subdivided into four regional-unconformity-bounded megasequences previously described in detail in Chapter 2 (Figures 3.2 and 3.3):

1) A **pre-rift megasequence (MS1)** of pre-Tertiary age consisting of lithologies ranging in age from Archean to Mesozoic. They include crystalline basement overlain by Paleozoic carbonates and Mesozoic terrestrial and volcanic strata (Fletcher et al., 1995; Hu et al., 1989) (Figure 2.14).

2) An early Tertiary (early Eocene – late Oligocene) **syn-rift megasequence (MS2)**, which contains 300-400 m of lacustrine and deltaic deposits of the Shahejie and Dongying Formations bound by roughly east-west-striking normal faults of fault family 2 (Figure 2.15). This megasequence contains the primary lacustrine source-rock lithofacies as well as lacustrine reservoir and seal lithofacies (Kuykendall et al., 2003).

3) An early Miocene to Pliocene **post-rift megasequence (MS3)**, which contains 1.6-1.7 km of fluvio-lacustrine deposits of the Guantao and Minghuazhen Formations (Figure 2.16). These rocks exhibit less fault control and were deposited above a large sag basin overlying the rift-controlled rocks of MS2. Megasequence 3 contains the main reservoir and seal lithofacies in the Zhao Dong field (Kuykendall et al., 2003); and

4) A late Pliocene to recent **post-rift megasequence (MS4)** which contains at least 100 m of alluvium and loess of the Pingyuan Formation (Allen et al., 1997).

The Miocene and Pliocene fluvial deposits of megasequence 3 (Guantao and Minghuazhen Formations) are the main focus of this chapter. Using 38 well logs, the complete section has been divided into ten (20-100 m-thick) fining or coarsening upward cycles and are interpreted as representing rising and falling accommodation/supply (A/S) cycles (Ramon and Cross, 1997) (Figures 3.3 and 3.5). Guantao Formation is characterized by amalgamated fluvial channel sandstones up to 55 m thick. The Guantao Formation has flat, low relief erosive bases with multiple internal scour surfaces separating individual channel bodies. Minghuazhen Formation is characterized by thin, lenticular and laterally discontinuous sand bodies encased in floodplain facies.

4.3 DATABASE AND METHODOLOGY

4.3.1. Database

4.3.1.1 Three-dimensional seismic data

Three separate 3D seismic volumes from the Zhao field were released to me in 2005 by Petrochina and Apache Corporation for the purpose of this dissertation study (Figure 3.4). 3D seismic reflection data consists of 280 km^2, two-way travel-time data

recorded to 5 s and sampled at 4 ms, and with a bin size of 25 m. For the study interval of the Guantao and Minghuazhen formations, the dominant frequency is between 26 and 36 Hz, giving a maximum estimated vertical resolution (λ_4) of 18 m (59 ft). The 3D seismic reflection volume is in an 8-bit display format that is not useful for more detailed quantitative analysis including simultaneous inversion. Additionally, two seismic-derived (50 km^2) relative acoustic- and shear-impedance volumes were provided by Apache for this dissertation study. The vertical resolution (λ_4) of the P- and S-impedance volumes in the Pliocene (Minghuazhen Formation) and Miocene (Guantao Formation) sections are about 17 and 21 m respectively (Figure 4.2).

4.3.1.2 Well data

The well database used in this study includes 38 wells (Figure 3.4). Most wells are highly deviated and reach total depths of about 1700 m in Neogene reservoirs, which constitute the main reservoirs in the Zhao Dong area. Few wells reach the Paleogene interval, which lies at depths of more than 1700 m (Figure 2.6). Four wells with core data were made available by Apache for this study. Core observations were incorporated when possible to better define Neogene facies, paleoenvironments and to calibrate log curves. Age control is based on published biostratigraphic data (Wang Tonghe, 1995; Yao et al., 1994; Zhang et al., 1994).

Figure 4.2. Representative well log from the Miocene Guantao and Pliocene Minghuazhen Formations in the Zhao field showing (from left to right): 1) gamma ray (GR) log; 2) upscaled GR log; 3) spontaneous potential (SP) log; 4) upscaled SP log; 5) P-impedance trace at well location and 6) S-impedance trace at well location. Cell thickness for the upscaled logs is consistent with the vertical resolution of the impedance volumes. The vertical resolution ($\lambda/4$) of the P- and S-impedance volumes in the Minghuazhen and Guantao Formations is 17 and 21 m respectively.

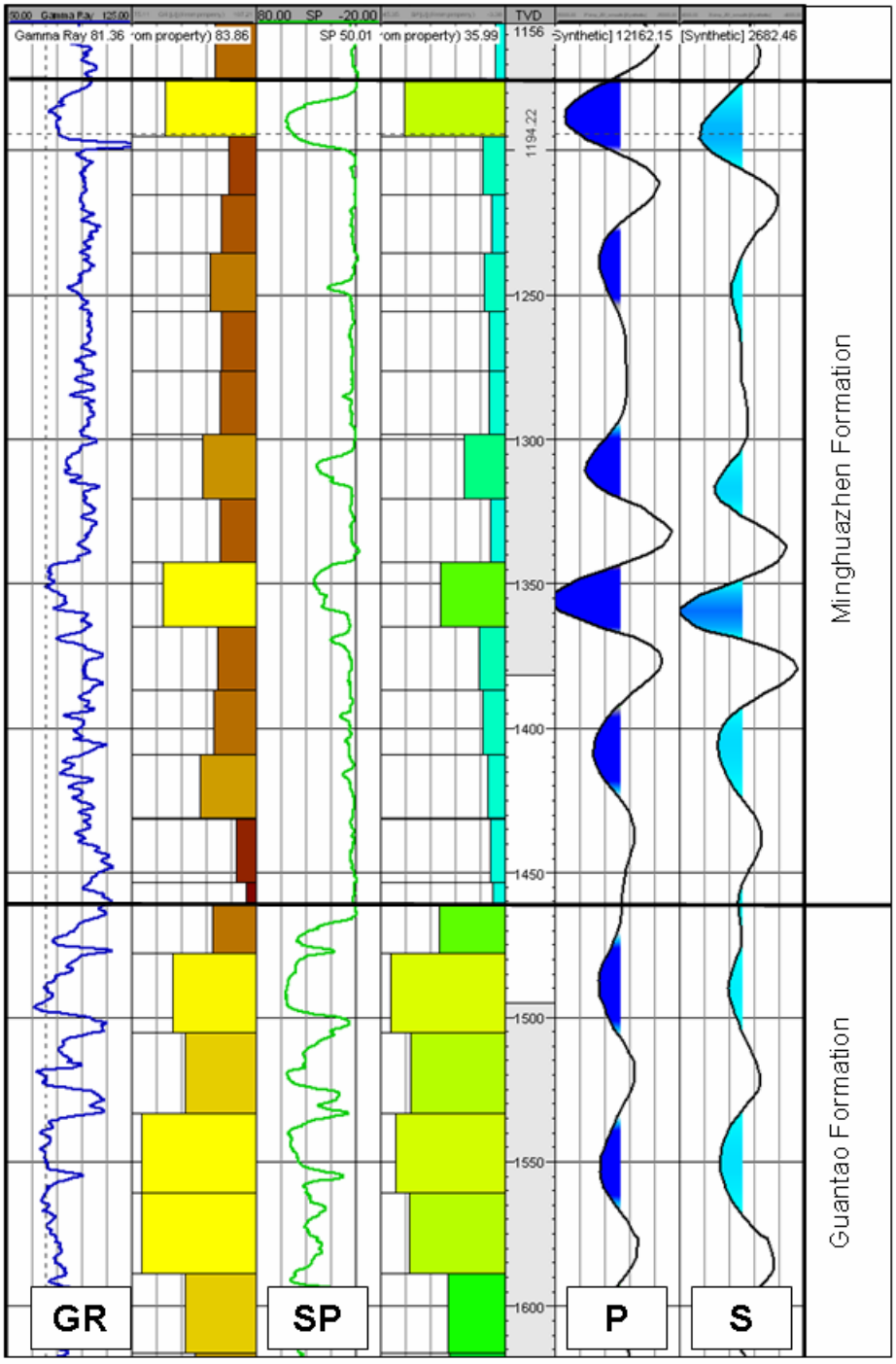
Gamma Ray 81.36
SP 50.01
TVD
1156
1194.22
1250
1300
1350
1400
1450
1500
1550
1600
Minghuazhen Formation
Guantao Formation
GR
SP
P
S

Figure 4.2

4.4 METHODOLOGY

4.4.1. Well log correlations

In Chapter 3, the fluvial sandstones of the Miocene Guantao and Pliocene Minghuazhen Formations have been subdivided into ten (20-100 m-thick) fieldwide correlatable accommodation/supply (A/S) cycles (Ramon and Cross, 1997) (Figures 3.8, 3.9, 3.10 and 3.11). This approach has proved useful where conventional correlation techniques do not work because of a lack of marker beds (coals, paleosols, and marine shale incursions) and biostratigraphic information.

4.4.2. Seismic interpretation

In Chapter 3, the turnaround points from increasing-to-decreasing and/or decreasing-to-increasing accommodation/supply cycles (Figures 3.12b and 3.13b) were identified and correlated within the 280 km^2 post-stack time migrated seismic volume, and the 50 km^2 P- and S-impedance seismic volumes. Seismic-well ties were achieved through the generation of synthetic seismograms. In addition, cross-plot analyses were performed to corroborate the existence of intrinsic correlations between lithology and impedance values (Torres-Verdin et al., 1999).

4.4.3. Colored inversion

The seismic inversion of post-stack seismic data to acoustic impedance for the Zhao Dong 3D data was completed by WesternGeco and Apache Corporation during the exploration phase (2003) using a post-stack colored inversion process (Lancaster and Whitcombe, 2000). The limited amount of well data and inconsistent seismic-well ties

available for this effort would have made an absolute inversion unreliable at best. Since 2003, several development wells have been drilled in Zhao Dong field and the seismic-well ties problems were improved significantly (Figure 3.3). Unfortunately, the 3D seismic reflection data available for this study is in an 8-bit display format which is limited in its usefulness for a more quantitative inversion (e.g. simultaneous inversion, sparse spike inversion)

The method of "colored inversion" converts the seismic data to a relative impedance data set (Lancaster and Whitcombe, 2000). The advantages of colored inversion are the speed of calculation and avoidance of artifacts that may be introduced by a preexisting model (Maynard et al., 2003; Veeken and Da Silva, 2004). However, since colored inversion is a relative measure of impedance changes, it cannot provide a quantitative estimate of reservoir properties (Veeken and Da Silva, 2004). Despite this limitation, more than 30 development wells drilled in the Zhao field up to 2006 have proved that this fast-track inversion technique is very useful for mapping lithologies from 3D seismic data.

4.4.3.1. Extracting acoustic impedance information from available logs

The first step in any "colored inversion" process is to estimate the correct alpha (α) value by curve-fitting to acoustic impedance logs (Lancaster and Whitcombe, 2000). For the Zhao Dong field, acoustic impedance logs, constructed from sonic and density logs, from eight exploration wells were examined (WesternGeco/DCS Reservoir Services, 2004) (Figure 4.3a). A general consistency between the wells could be observed, and a representative alpha value for the whole field was derived by fitting a trend curve to this data (WesternGeco/DCS Reservoir Services, 2004) (Figure 4.3b).

Next, using the same time window as the well log analysis, sample seismic traces around all well locations were averaged to derive the mean seismic spectrum (Figure 4.4). The resultant amplitude spectrum obtained from the acoustic time-sampled impedance logs was then used to shape the mean seismic spectrum. The resulting matched spectra, after bringing them in scale with the time-sampled log spectra is shown in Figure 4.5 (WesternGeco/DCS Reservoir Services, 2004).

The last step in the inversion process was to apply the convolutional operator obtained in the previous step (Figure 4.6) to the input seismic reflection data. The result of this process was a relative impedance seismic volume (Figure 4.7), which has in effect been shaped to well data in terms of amplitude and frequency (WesternGeco/DCS Reservoir Services, 2004).

A relative shear-impedance volume was also obtained through detailed log-analysis, 3-term angle versus offset (AVO), and the application of colored impedance. Using well-based AVO modeling and angle decomposition of the migrated seismic gathers, it was determined that the maximum angle of incidence at the basal section of the Minghuazhen Formation was about 45^{o} (WesternGeco/DCS Reservoir Services, 2004).

It is important to keep in mind that coloured inversion is a quick and imprecise inversion method – yet with good predictive power as shown by its comparison with actual well data from the Zhao Dong and other fields (Lancaster and Whitcombe, 2000). Accordingly, any result obtained from the interpretation of seismic derived P- and S-impedance volumes based on coloured inversion should be considered suspect in the absence of supporting well data. A more sophisticated and robust inversion method (e.g. simultaneous inversion) is necessary to increase the confidence of the inversion results in Zhao Dong field. Unfortunately, I was not able to perform this type of inversion because of the lack of availability of 32 bit seismic data for this dissertation study.

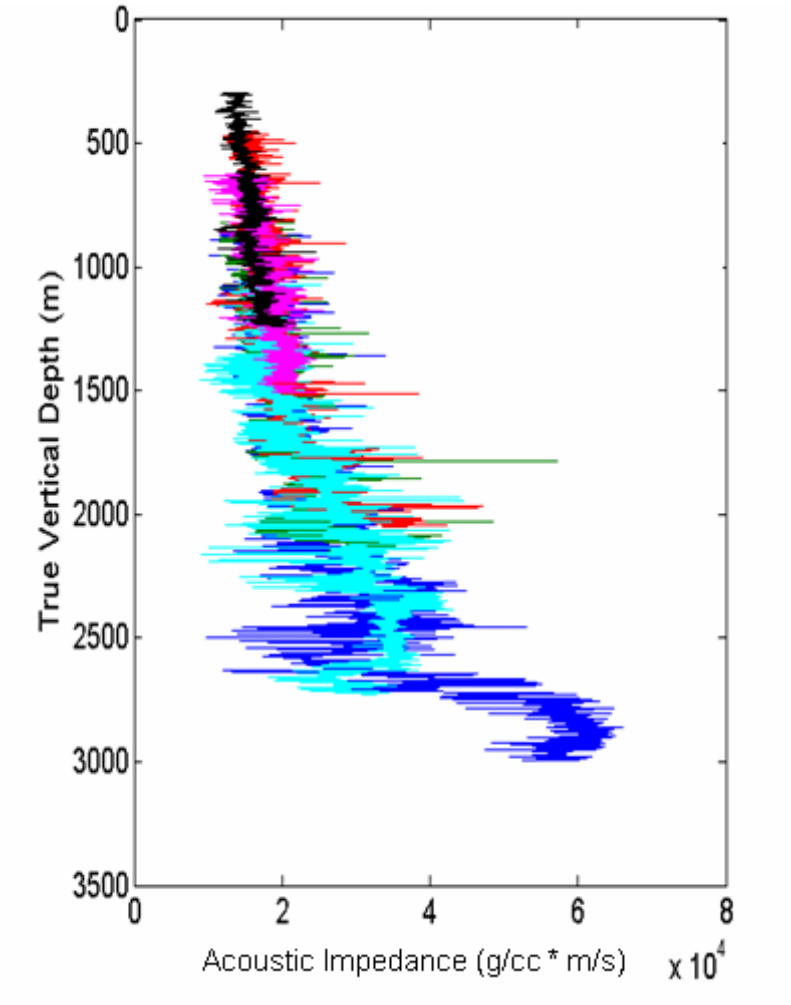

Figure 4.3a. Acoustic impedance logs from eight exploration wells in Zhao Dong field (courtesy of August Lau).

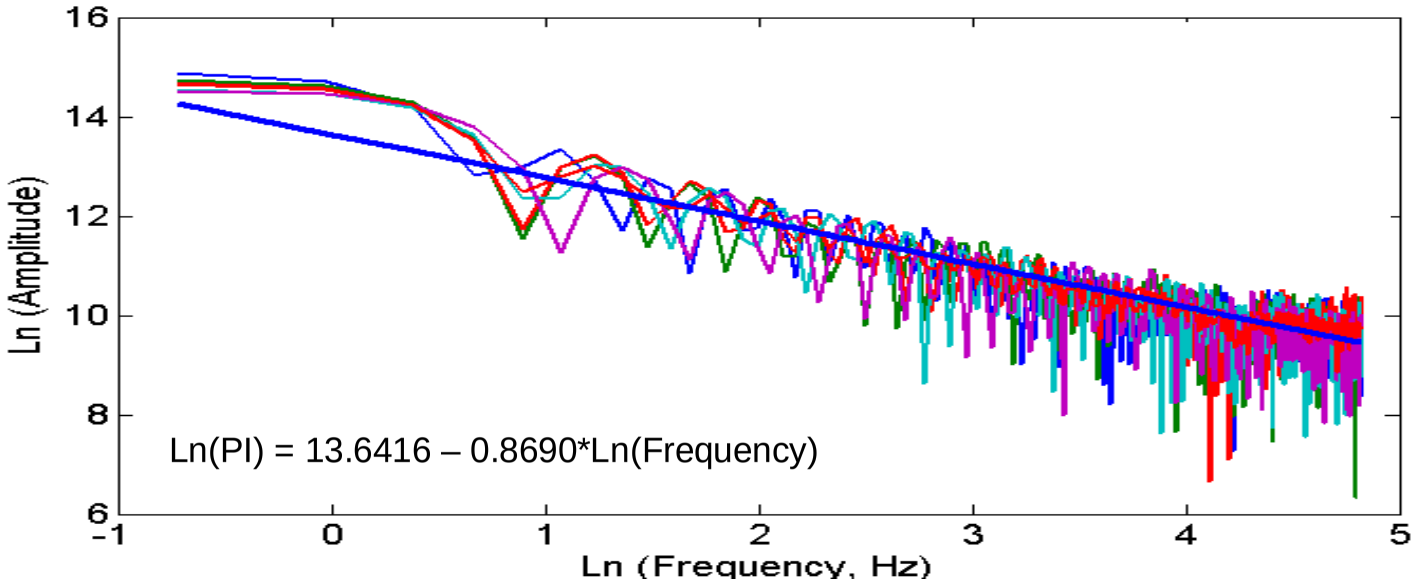

Figure 4.3b Spectrum of acoustic impedance (PI). This figure shows the linear trend from the eight wells - resampled in two-way reflection time - shown in figure 4.3a. The gradient of the trend fit determines the alpha (α) value (courtesy of August Lau).

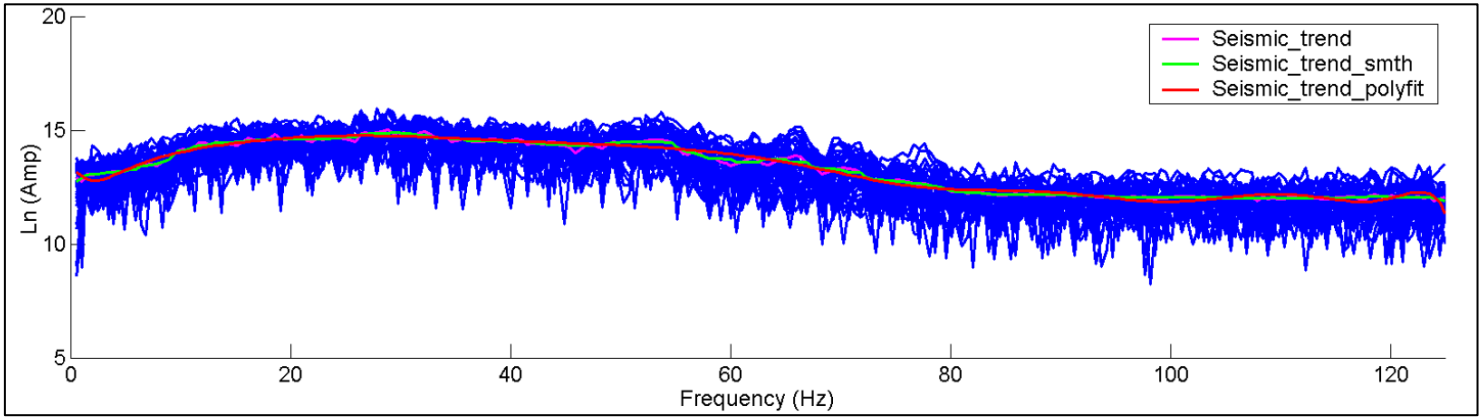

Figure 4.4. Mean seismic spectrum. Using the same time window as the well log analysis, sample seismic traces around all well locations were averaged to derive the mean seismic spectrum (from WesternGeco/DCS Reservoir Services, 2004).

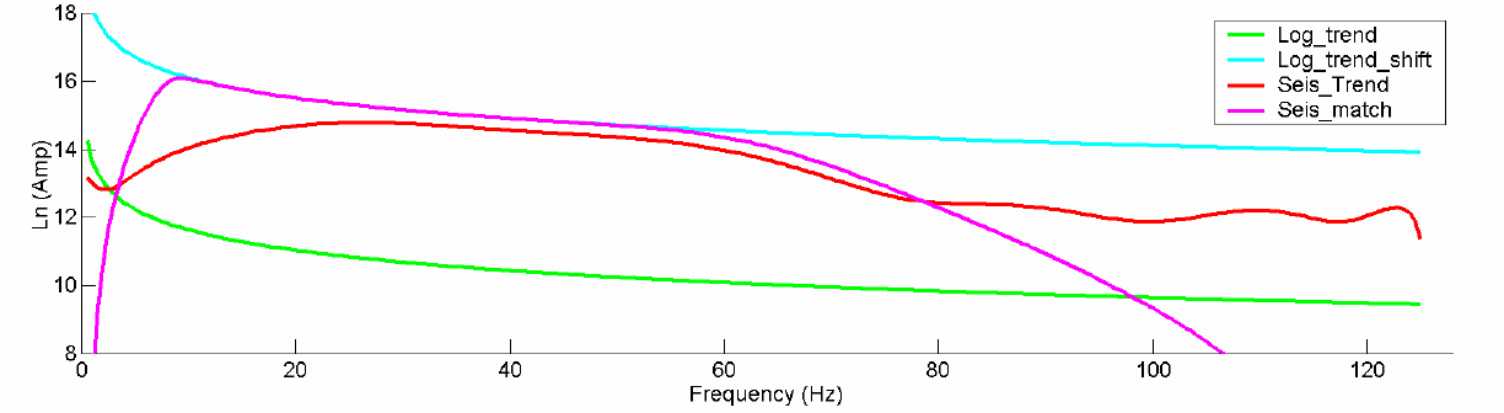

Figure 4.5. Amplitude spectrum matching. The resultant amplitude spectrum obtained from the AI logs (light blue) was then used to shape the mean seismic spectrum (red). The resulting matched spectrum is shown in pink (from WesternGeco/DCS Reservoir Services, 2004).

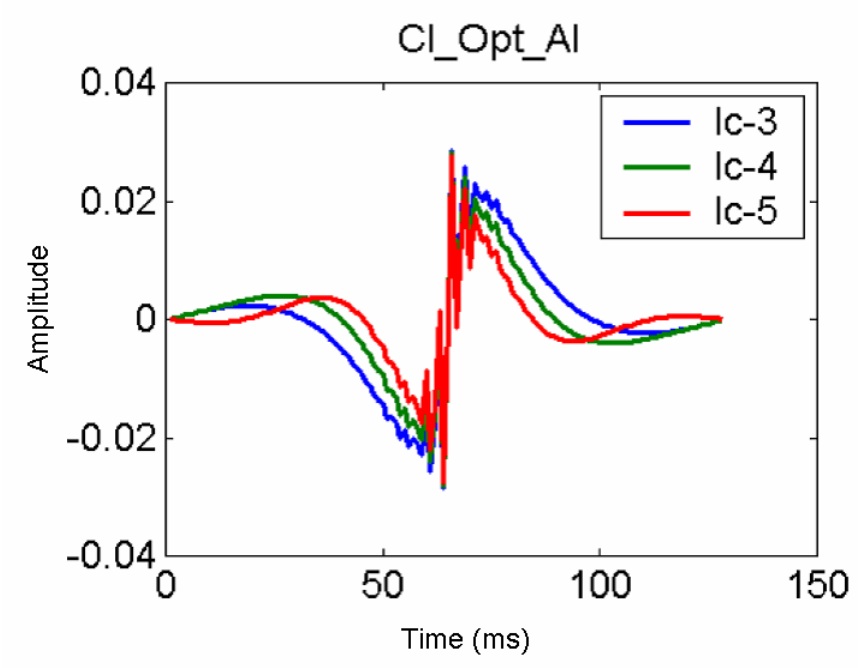

Figure 4.6. Colored inversion operator. The last step in the inversion process was to apply the convolutional operator to the input seismic reflection data (from WesternGeco/DCS Reservoir Services, 2004).

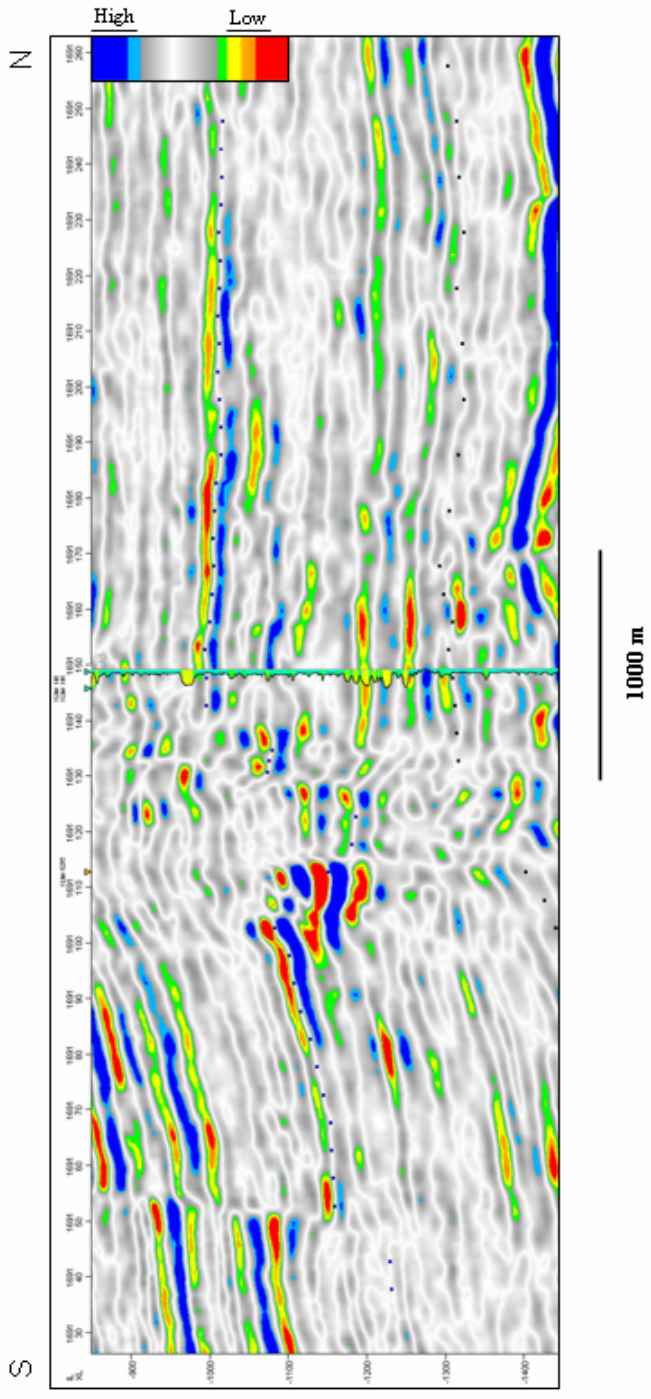

Figure 4.7. Relative P-impedance (colored inversion) seismic section in Zhao Dong field. Sand-rich areas are represented by bright colors which in turn are inferred from low impedance values.

4.5 DATA DESCRIPTION

4.5.1 Wire-line analysis and cross-plots

The purpose of making cross-plots is to establish a qualitative procedure to discriminate channel-fill facies from floodplain facies in the Zhao Dong field exclusively on the basis of their differences in acoustic (P) and shear (S) impedance response. P- and S-impedance, being the product of the density times P- and S-velocity, respectively, were computed from dipole sonic and density logs made available for this study. Subsequently, these values were cross-plotted with density and volume of shale logs (computed from gamma ray logs) in order to study the acoustic and shear impedance responses to lithology variations in the Zhao Dong field. The two wells used in making the cross-plots are a good representation of the different fluid types (gas, oil and water) present in the sands.

Figures 4.8a and 4.8b illustrate P-impedance vs. density logs in the Guantao and Minghuazhen Formations, respectively. These cross-plots indicate that channel-fill sandstones in both formations have low P-impedance and density values while floodplain facies (clay and silt) have high P-impedance and density values. The clusters showing abnormally low P-impedance and density values in both formations represent gas-bearing sands. The occurrence of gas in the formation lowers the velocity of sonic wave propagation and, consequently, gas sands exhibit very low impedance values. Note that oil- and water-bearing sands in both formations are indistinguishable from each other based on their P-impedance and density values (Figures 4.8a and 4.8b).

Figure 4.9 illustrates P-impedance vs. S-impedance logs in the Guantao and Minghuazhen Formations. Figure 4.9a shows that sandstone in the Guantao Formation is characterized by low S-impedance values whereas floodplain facies (clay and silt) are

characterized by high S-impedance values. Figure 4.9b shows the S-impedance values of the non-reservoir lithologies significantly overlap those of the reservoir sands, causing uncertainty in the use of S-impedance values to predict reservoir sands. However, when end member lithologies (i.e., channel-fill facies with volume of shale values less than 30% and floodplain facies with volume of shale values greater than 70%) are cross-plotted (Figure 4.9c) we notice a clear discrimination between channel-fill facies with low S-impedance values and floodplain facies with high S-impedance values in the Minghuazhen Formation based on their S-impedance values. Note that oil- and water-bearing sands in both formations are indistinguishable based exclusively on their S-impedance values.

Cross-plot analysis provided the following conclusions: 1) sandstone and floodplain lithologies can be clearly differentiated in the Zhao Dong field on the basis of their P- and S-impedance values; 2) mixed lithologies (shaley sand and/or sandy shale) in the Minghuazhen Formation cause significant overlap in the S-impedance cross-plots; and 3) the non-unique characteristic of P- and S-impedance values for oil- and water-bearing sands does not allow discriminate fluids based on their impedance values.

4.5.2 Impedance volumes

I use the cross-plot analysis of well logs to establish the framework within which the inverse modeling-derived P- and S-impedance volumes can be interpreted. Threshold filters on P- and S-impedance estimated from well log data were used to efficiently map the three-dimensional spatial distribution and shapes of sandstone bodies within each reservoir level in the Guantao and Minghuazhen Formations.

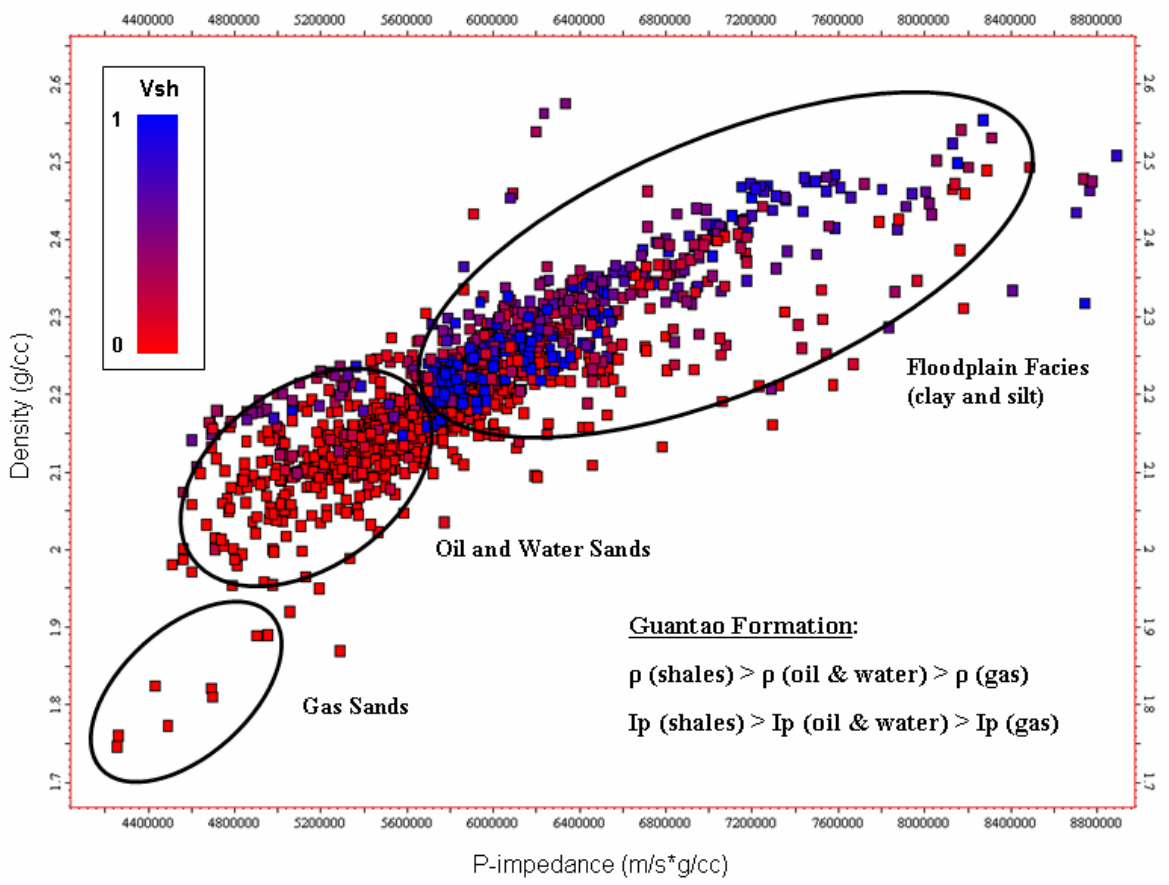

Figure 4.8a. P-impedance vs. density cross-plot in the Guantao Formation from well data. Sandy channel-fill sandstones have low P-impedance and density values while shaly floodplain facies have high P-impedance and density values. The clusters showing abnormally low P-impedance and density values represent gas bearing sands Note that oil- and water-bearing sands in both formations are indistinguishable from each other based on their P-impedance and density values.

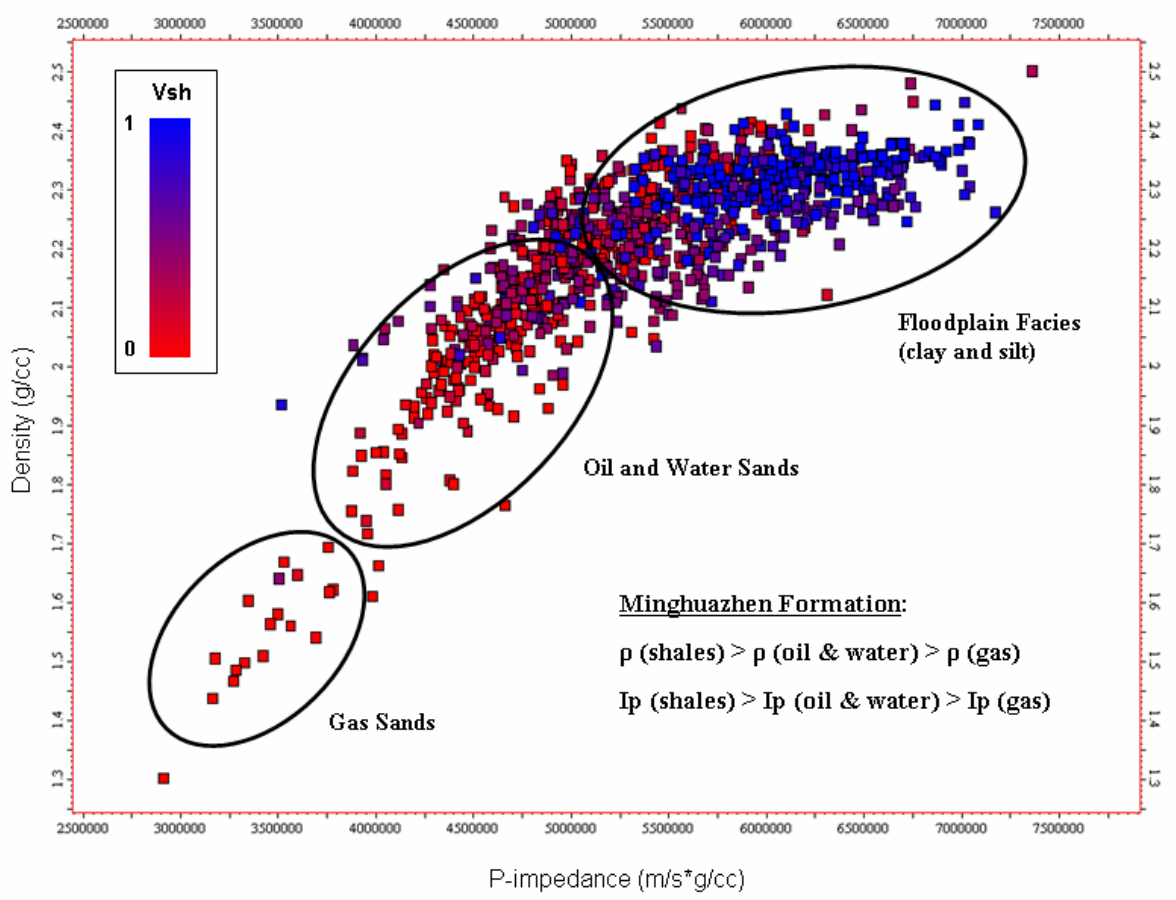

Figure 4.8b. P-impedance vs. density cross-plot in the Minghuazhen Formation. Sandy channel-fill sandstones have low P-impedance and density values whereas silty floodplain facies have high P-impedance and density values. The clusters showing abnormally low P-impedance and density values represent gas bearing sands Note that oil- and water-bearing sands in both formations are indistinguishable from each other based on their P-impedance and density values.

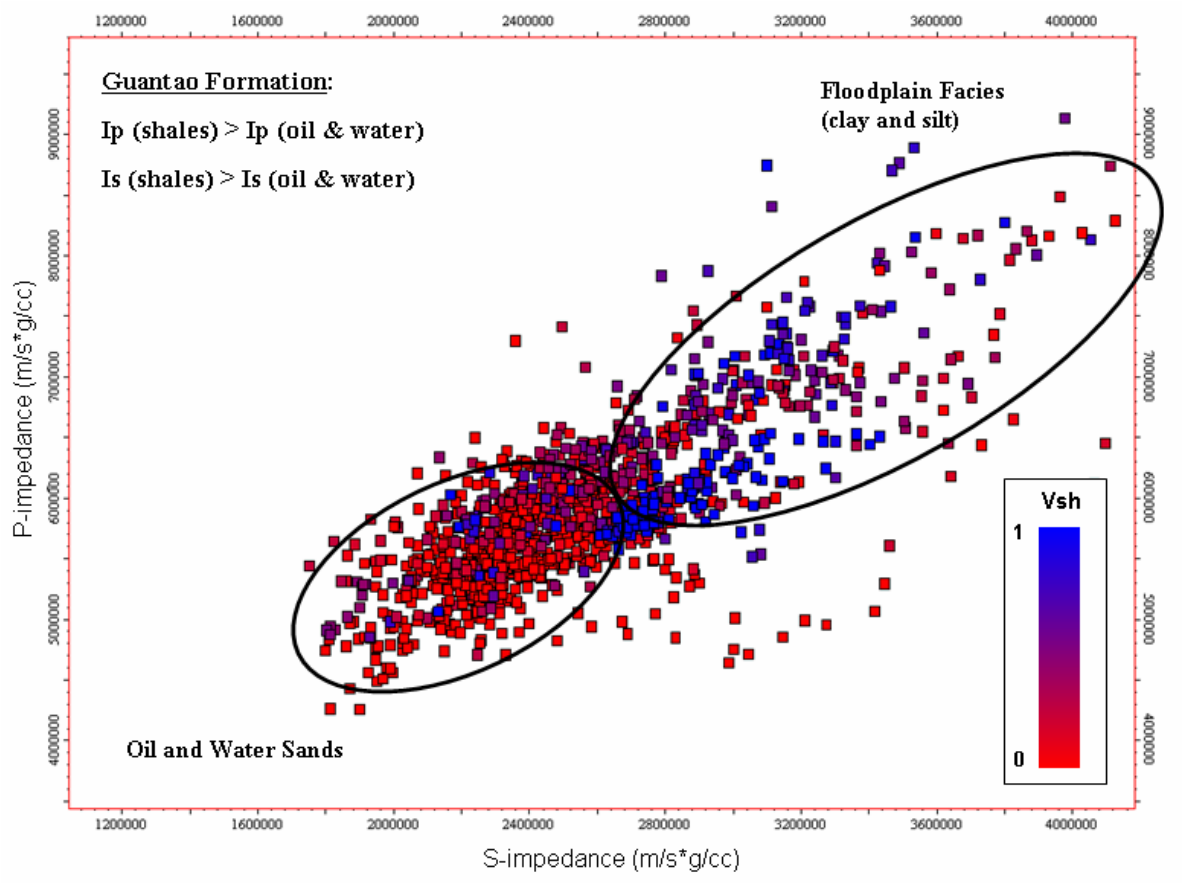

Figure 4.9a. S-impedance vs. P-impedance cross-plot in the Guantao Formation (well data). Channel-fill sandstones in the Guantao Formation are characterized by low S-impedance values whereas floodplain facies are characterized by high S-impedance values. Note that oil- and water-bearing sands are indistinguishable from each other based on their S-impedance values.

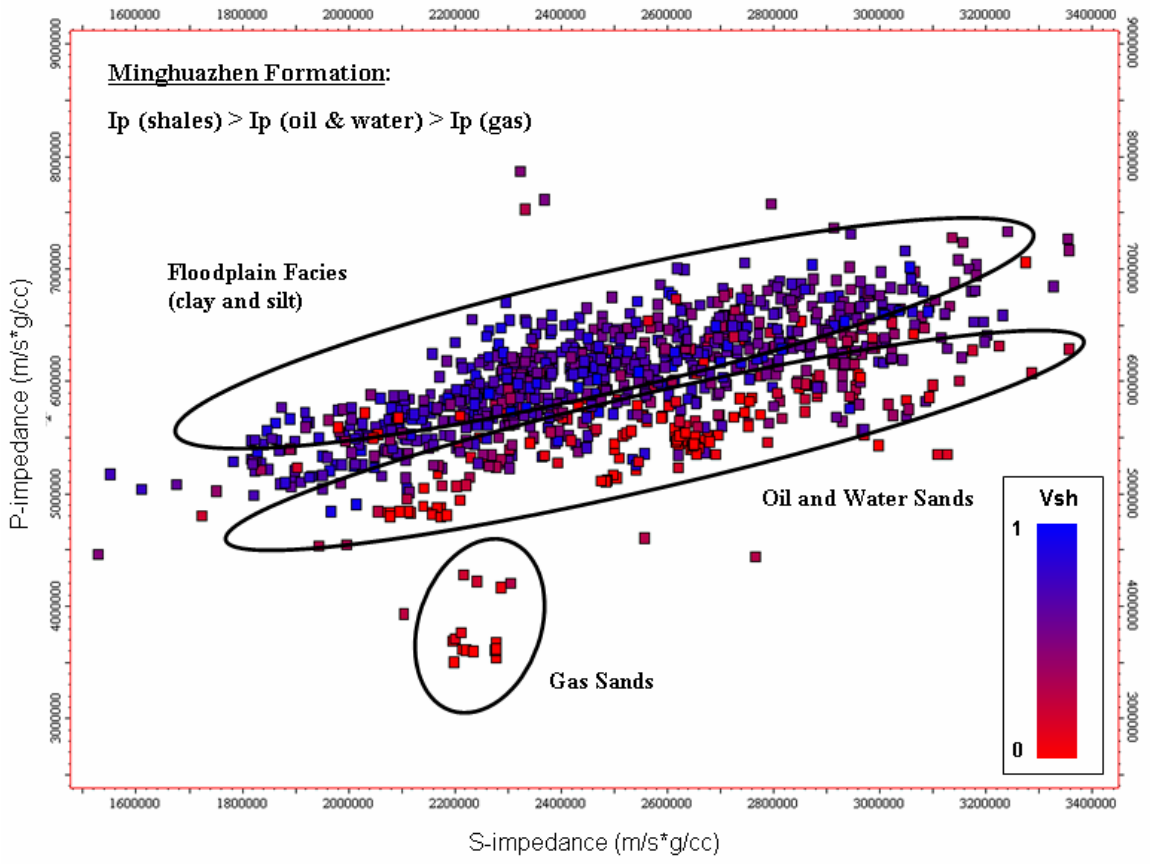

Figure 4.9b. S-impedance vs. P-impedance cross-plot in the Minghuazhen Formation (well data). S-impedance values of the non-reservoir lithologies significantly overlap those of the reservoir sands (channel fill facies), causing uncertainty in the use of S-impedance values to predict reservoir sands in the Minghuazhen Formation.

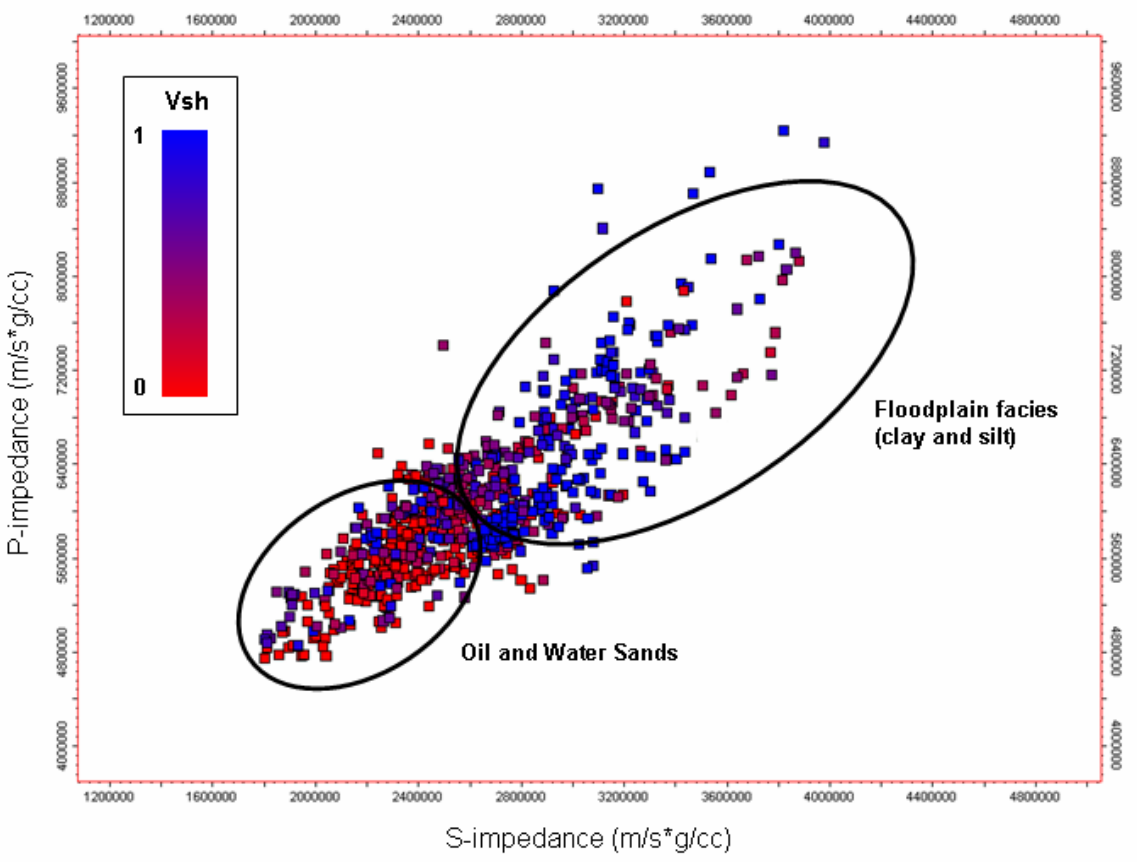

Figure 4.9c. S- vs. P-impedance cross-plot in the Minghuazhen Formation (end member lithologies). When end member lithologies (channel-fill facies with Vsh < 35% and floodplain facies with Vsh > 70%) are cross-plotted we notice a clear discrimination between channel-fill facies (low S-impedance values) and floodplain facies (high S-impedance values) in the Minghuazhen Formation based on their S-impedance values.

4.5.2.1 Impedance threshold

Since colored inversion converts the seismic data to a relative P-impedance data set, the P- and S-impedance volumes available in this study are not suitable for use in quantitative estimation of reservoir properties. As a result, it is not possible to establish P- and S-impedance cutoff values from well log data in order to discriminate reservoir from non-reservoir facies using seismic-derived impedance volumes. However, it is still possible to establish a qualitative threshold based on well-log information.

Figures 4.8 and 4.9 show reservoir facies (channel-fill sandstones) in the Minghuazhen and Guantao Formations are characterized by low P- and S-impedance values. From these cross-plots it has been estimated that the lower one-third of the data distribution for both formations represent potential reservoir facies. Using this information, the seismic-derived P- and S-impedance volumes were upscaled into a geocellular model and then filtered (Figure 4.10) in order to highlight and isolate all potential reservoir bodies. Figure 4.11 shows an example of the graphical representation of the filtered sand distribution corresponding to the M4 – M5 interval (Figure 3.5), which is clearly identified by relatively low P- and S-impedance values. Cell thickness for the filtered sandstone bodies is consistent with the vertical resolution of the impedance volumes (Figure 4.2). The vertical resolution (λ_4) of the P- and S-impedance volumes in the Minghuazhen and Guantao Formations is 17 and 21 m respectively.

4.5.2.2 Total sand thickness maps

Given the laterally discontinuous character of the sandstone bodies within the Zhao Dong field, the best exploration strategy is to drill wells where total sand thickness is greatest and the enclosing geologic structures, such as faults and shale seals, are most favorable. Figures 4.12, 4.13, 4.14, 4.15, 4.16, 4.17, 4.18 and 4.19 show total sand

thickness maps for eight prospective sand rich cycles within both formations that range in thickness from 17 to 40 m (Figures 3.3 and 3.5). These maps were created by the vertical summation of the sand thickness that corresponds to each of the individual sand units identified within every stratigraphic interval (Figure 4.11). Sand-rich areas are represented by bright colors which in turn correspond to low P- and S-impedance values. Floodplain (non-reservoir) facies, on the other hand, are represented by a pink background color which in turn corresponds to high P- and S-impedance values.

4.6 INTERPRETATION AND DISCUSSION

The purpose of the simultaneous analysis of the amplitude and P- and S-impedance volumes in Zhao Dong field was to: 1) discriminate reservoir sands from non-reservoir lithologies in the Guantao and Minghuazhen Formations; 2) assess the lateral continuity and shapes of channel-fill facies; and 3) use this information to identify new prospects and hence improve the success ratio of wells to be drilled.

4.6.1 Architecture of reservoir sands from amplitude study

Figures 4.12, 4.13, 4.14, 4.15 and 4.16 reveal that channel-fill facies of the Minghuazhen Formation appear to be intermittently and locally deposited within a background matrix of high-impedance floodplain facies. This result is consistent with the well log correlation discussed in Chapter 3 and summarized on Figure 3.8, 3.9, 3.10 and 3.11.

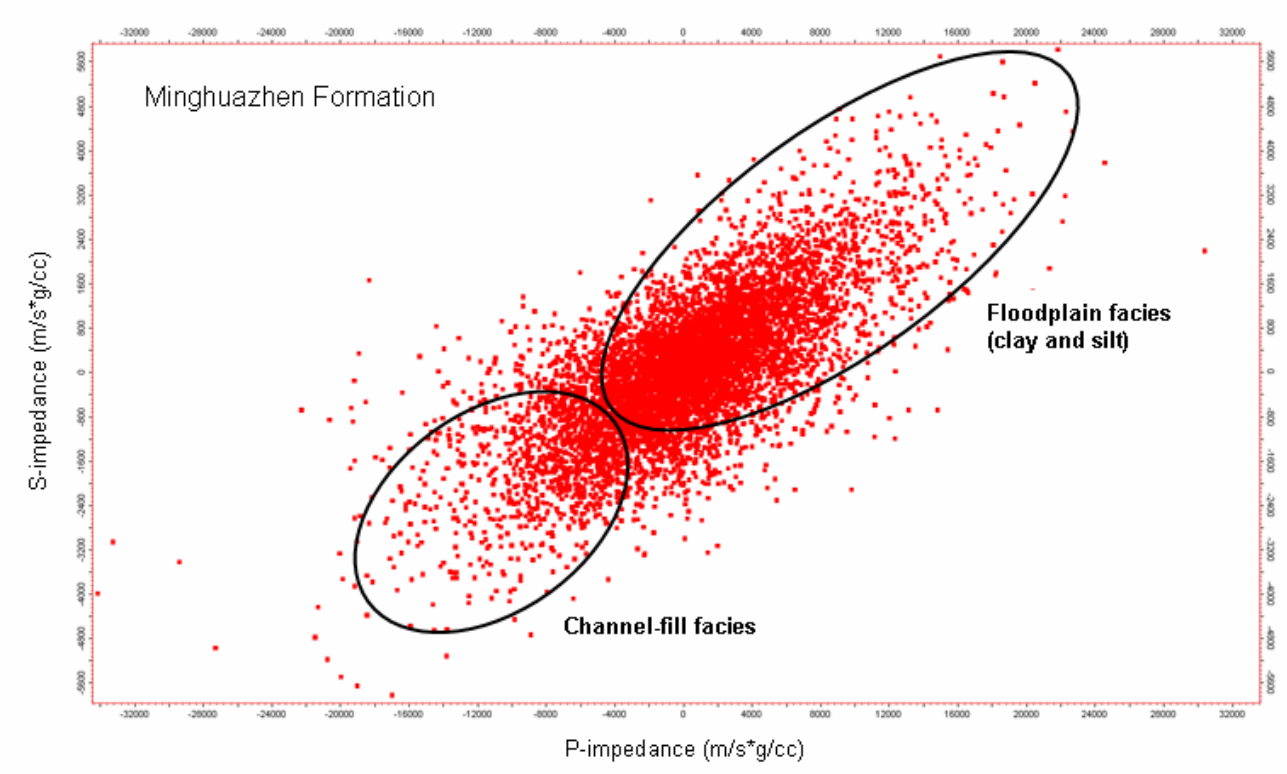

Figure 4.10a. P- vs. S-impedance cross-plot in the Minghuazhen Formation (seismic data). Using the threshold estimated from well log data (the lower one-third portion of the data distribution represent reservoir facies) the seismic-derived P- and S-impedance volumes were filtered in order to highlight and isolate reservoir bodies.

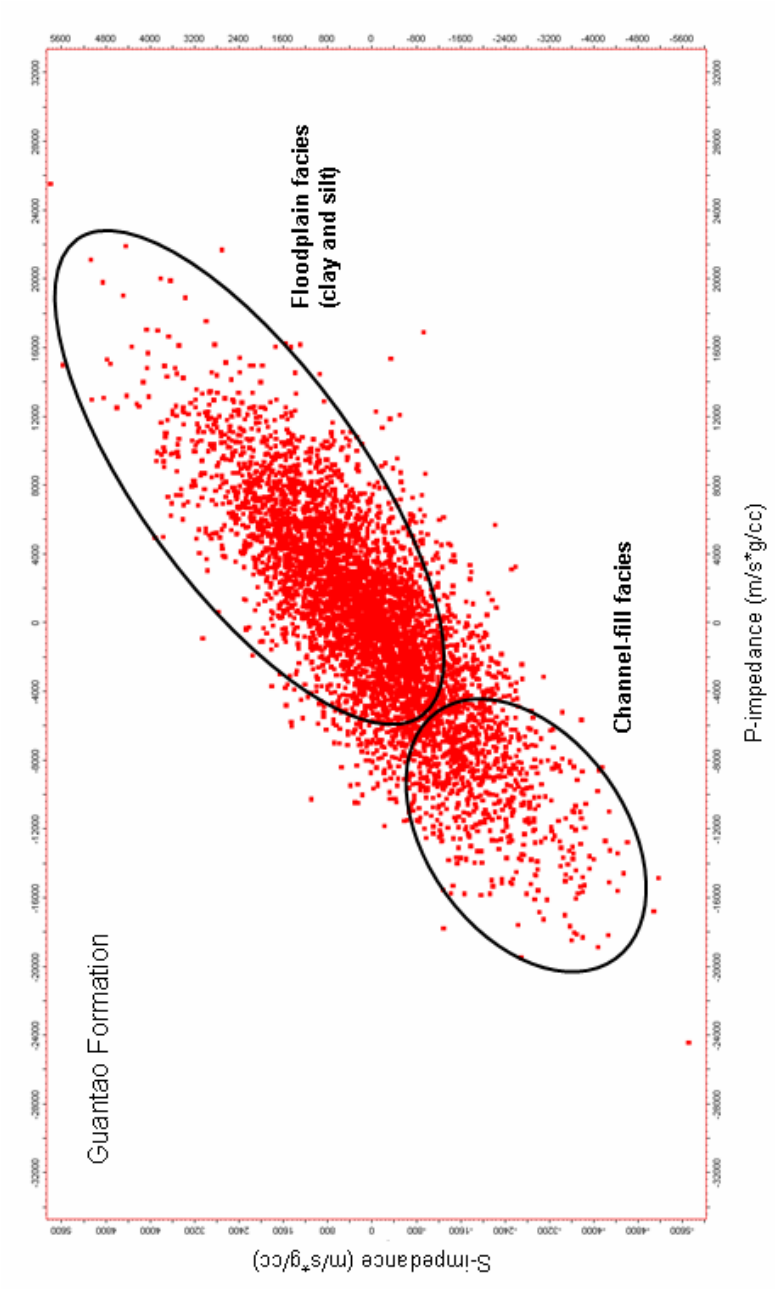

Figure 4.10b. P- vs. S-impedance cross-plot in the Guantao Formation (seismic data). Using the threshold estimated from well log data (the lower one-third portion of the data distribution represent reservoir facies) the seismic-derived P- and S-impedance volumes were filtered in order to highlight and isolate reservoir bodies.

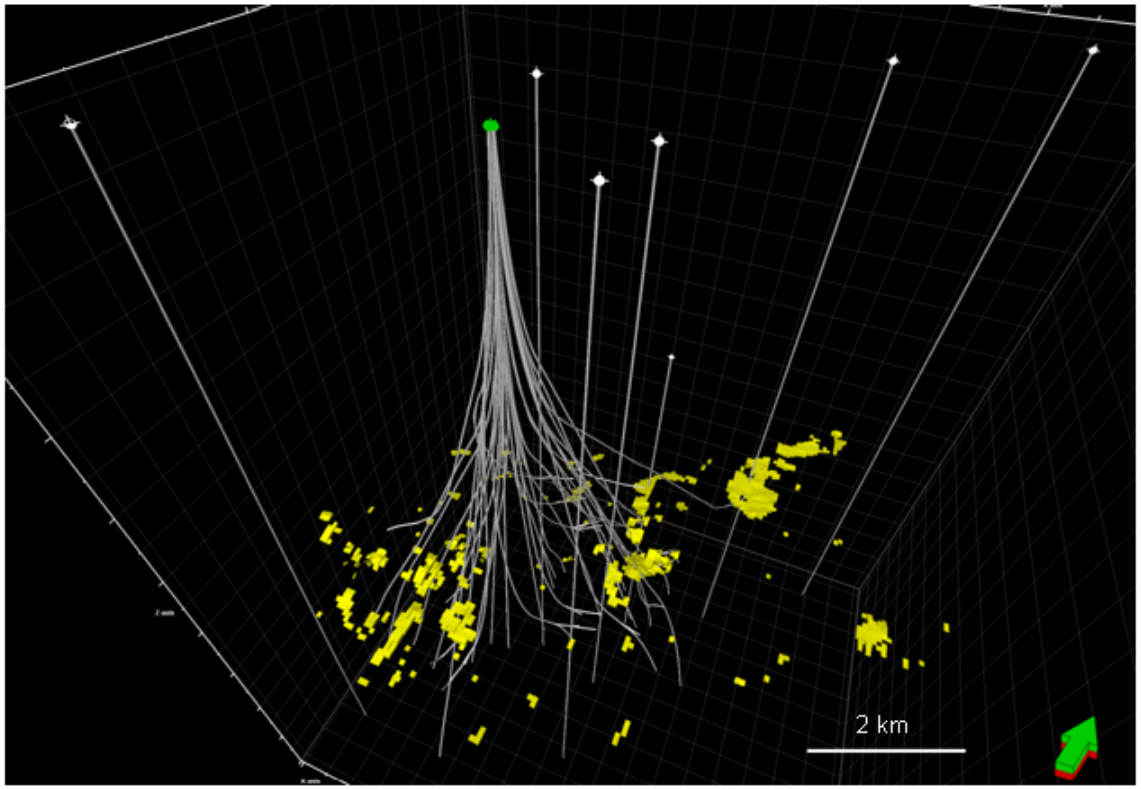

Figure 4.11. 3D graphical representation of the filtered sand distribution corresponding to the M4 – M5 interval in the seismic data. Cell thickness of the upscaled P- and S-impedance volumes is consistent with the vertical resolution of the impedance volumes. The vertical resolution ($\lambda/4$) of the P- and S-impedance volumes in the Minghuazhen and Guantao Formations is 17 and 21 m respectively. Green arrow points to the north

The dominant depositional trend of sand bodies consists of relatively narrow (up to 470 m wide), confined, and slightly sinuous, roughly E-W or N-S-oriented sandstone-filled fluvial channels (Figures 4.13, 4.14, 4.15 and 4.16). Wells penetrating the channels record up to 25 m of gross sandstone and display fining-upward and serrate well log patterns (Figure 3.5). These sandstone trends pinch out into low-impedance, extensive floodplain areas.

An anomalous thick, sharp based and overall fining upward sand-body caps the Minghuazhen Formation in the study interval (Figures 3.8, 3.9, 3.10 and 3.11). This laterally continuous stacked sandstone body covers over 18 km^2 of the western side of the Zhao Dong development block.

Channel-fill facies in the Guantao Formation (Figures 4.18, 4.19 and 4.20) form areally extensive sandstone bodies that extend several hundred meters along dip and strike directions. Individual fluvial channels are hardly preserved. Wells in these trends reach up to 55 m of gross sandstone and display blocky or coarsening-upward well log patterns (Figures 3.8, 3.9, 3.10 and 3.11). These sandstone trends pinch out into low-impedance, floodplain areas characterized by silt and clay.

4.6.2 Proposed locations of new wells based on this amplitude study

The Zhao Dong field is exceptionally oil prone; and oil is generally found wherever a suitable reservoir and trap exist. As a result, most drilling locations during the early development of the field were selected based on the identification of low-amplitude anomalies from post-stack seismic volumes (i.e., indicators of reservoir sands) combined with structural closures at the reservoir level. Although the recognition of low-amplitude anomalies has proven successful, it has also resulted in some non-commercial wells. Postdrill appraisals show that these failures are commonly due to one or more of the

following factors: 1) unreliable seismic amplitude information was available; 2) superposition of seismic reflections and tuning effects led to unreliable imaging; 3) the prospect was not adequately tested by the well (i.e. well was drilled off structure).

I propose thirteen new drilling locations (Figures 4.12, 4.13, 4.14, 4.15, 4.16, 4.17, 4.18 and 4.19) based on the impedance-derived total thickness maps of eight different intervals (Figures 3.3 and 3.5) within the Guantao and Minghuazhen Formations. Prospects from each interval are discussed below.

4.6.2.1 Minghuazhen Formation

1) Interval M0 – M1

The most prominent sandstone fairways in the M0 – M1 interval of the Minghuazhen formation (Figure 4.12) have already been tested by drilling and show commercial accumulations of hydrocarbons. I propose one additional prospect at this level in block D south (Figure 4.12). This sandstone fairway is 320 m wide and extends in a NW direction for at least 850 m. Sandstone thickness in this interval range from 17 to 30 m.

2) Interval M1 – M2

Three prospects have been identified based on the total sand thickness map of interval M1 – M2 (Figure 4.13). Prospect 1 is located in the eastern side of block C. This sandstone trend is at least 470 m wide and extends northward for approximately 1340 m. Maximum sandstone thickness in this area is 22 m. Prospect 2 is located in the eastern edge of block D. This sandstone fairway (up to 28 m thick) is 250 m wide and extends in a northward direction for approximately 480 m. The last prospect is located in block D

south. This fairway is 300 m wide and extends roughly E-W for about 350 m. Sandstone thickness reach up to 20 m.

3) Interval M2 – M3

Two prospects (block C) have been identified based on the total sand thickness map of interval M2 – M3 (Figure 4.14). The first prospect is located in a sandstone fairway that runs roughly N-S. It is 250 m wide and dip-elongate, extending northward for at least 600 m. Maximum sandstone thickness is about 30 m. Prospect 2 is located in a sandstone fairway 260 m wide. It extends in a NE-SW direction for approximately 1100 m with a maximum sandstone thickness of approximately 32 m.

4) Interval M4 – M5

One block C prospect was identified based on the total sand thickness map of interval M4 – M5 (Figure 4.15). This sandstone fairway is 220 m wide and extends in a NE direction for about 550 m. Maximum sandstone thickness is about 34 m. A sandstone fairway just south of prospect 1 has already been tested and showed commercial accumulations of hydrocarbons.

5) Interval M5 – G2

The total sand thickness map of interval M5 – G2 allowed the identification of one new prospect in block C (Figure 4.16). The prospect is located in a sandstone fairway (up to 21 m thick) 500 m wide and extends in a NE direction for about 950 m.

Figure 4.12. Total sand thickness map of interval M0 – M1. Sand-rich areas are represented by bright colors (low P- and S-impedance values) while floodplain (non-reservoir) facies are represented by a pink background (high P- and S-impedance values). Black dots represent well locations. The most prominent sandstone fairways in the M0 – M1 interval have already been tested and showed commercial accumulations of hydrocarbons. One additional prospect has been located in block D south. This sandstone fairway is 320 m wide and extends in a NW direction for at least 850 m. Sandstone thickness in this interval range between 17 and 30 m.

.

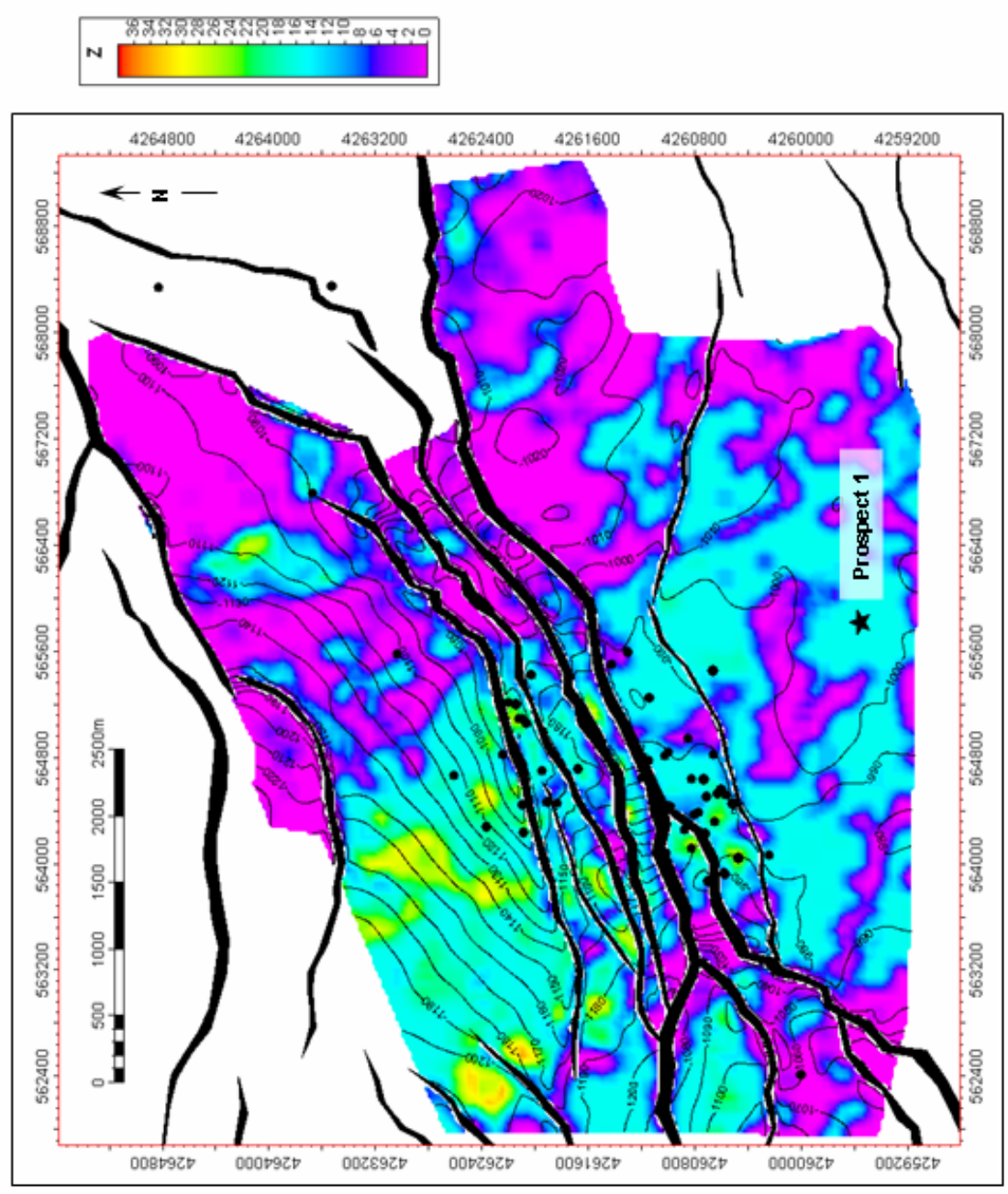
Z
36
34
32
30
28
26
24
22
20
18
16
14
12
10
8
6
4
2
0
4264800
4264000
4263200
4262400
4261600
4260800
4260000
4259200
568800
568000
567200
566400
565600
564800
564000
563200
562400
N
Prospect 1
0
500
1000
1500
2000
2500m

Figure 4.12

Figure 4.13. Total sand thickness map of interval M1 – M2. Sand-rich areas are represented by bright colors (low P- and S-impedance values) while floodplain (non-reservoir) facies are represented by a pink background (high P- and S-impedance values). Black dots represent well locations. Prospect 1 is located in the eastern side of block C. This sandstone trend is at least 470 m wide and extends northward for approximately 1340 m. Maximum sandstone thickness in this area is 22 m. Prospect 2 is located in the eastern edge of block D. This sandstone fairway (up to 28 m thick) is 250 m wide and extends in a northward direction for approximately 480 m. The last prospect is located in block D south. This fairway is 300 m wide and extends roughly E-W for about 350 m. Sandstone thickness reach up to 21 m.

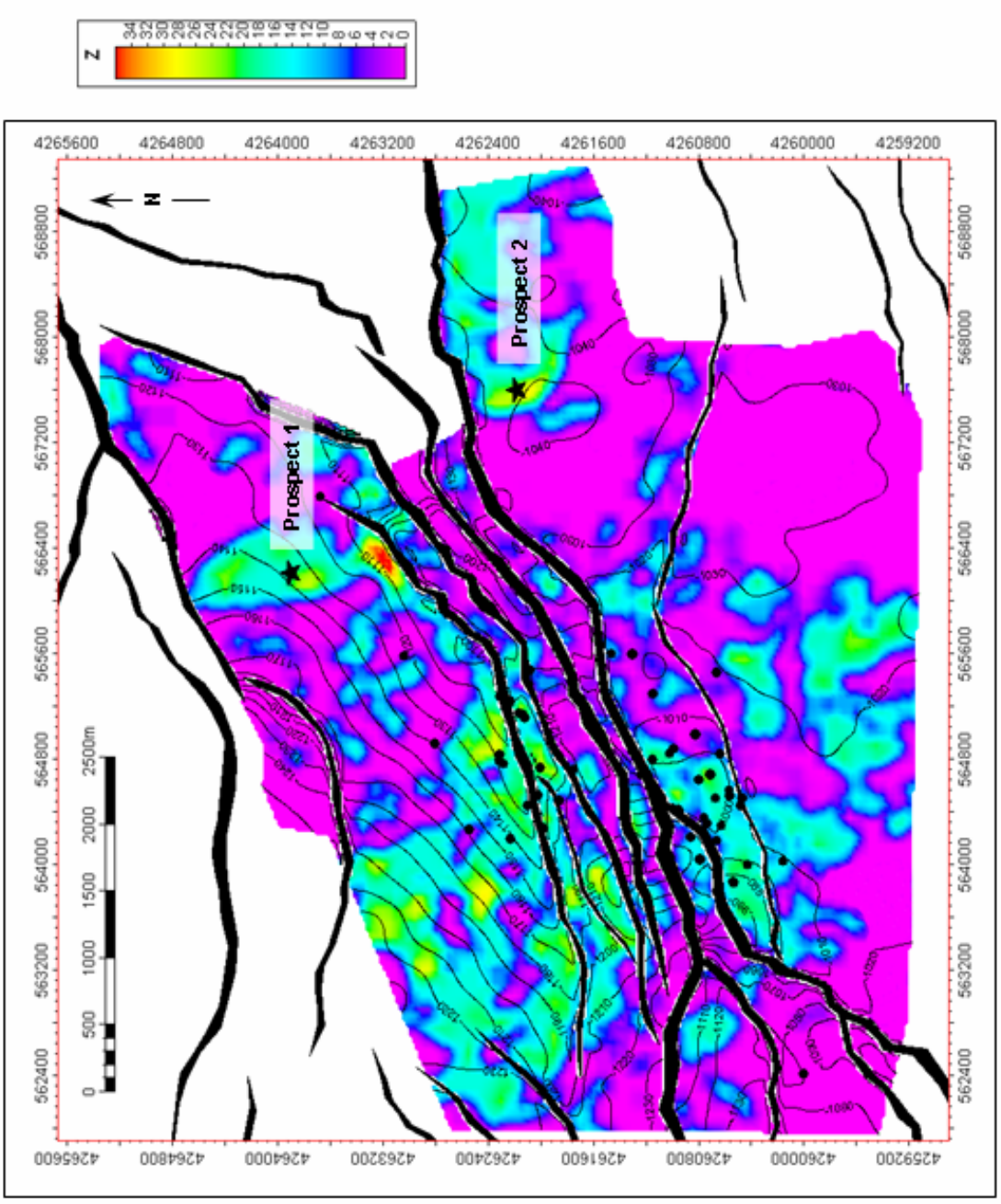
Z
34
32
30
28
26
24
22
20
18
16
14
12
10
8
6
4
2
0
4265600
4264800
4264000
4263200
4262400
4261600
4260800
4260000
4259200
N
Prospect 1
Prospect 2
568800
568000
567200
566400
565600
564800
564000
563200
562400
0
500
1000
1500
2000
2500m

Figure 4.13

Figure 4.14. Total sand thickness map of interval M2 – M3. Sand-rich areas are represented by bright colors (low P- and S-impedance values) while floodplain (non-reservoir) facies are represented by a pink background (high P- and S-impedance values). Black dots represent well locations. Two prospects (block C) have been identified in this interval. The first prospect is located in a sandstone fairway that runs roughly N-S. It is 250 m wide and dip-elongate, extending northward for at least 600 m. Maximum sandstone thickness is about 30 m. Prospect 2 is located in a sandstone fairway 260 m wide. It extends in a NE-SW direction for approximately 1100 m with a maximum sandstone thickness of approximately 32 m.

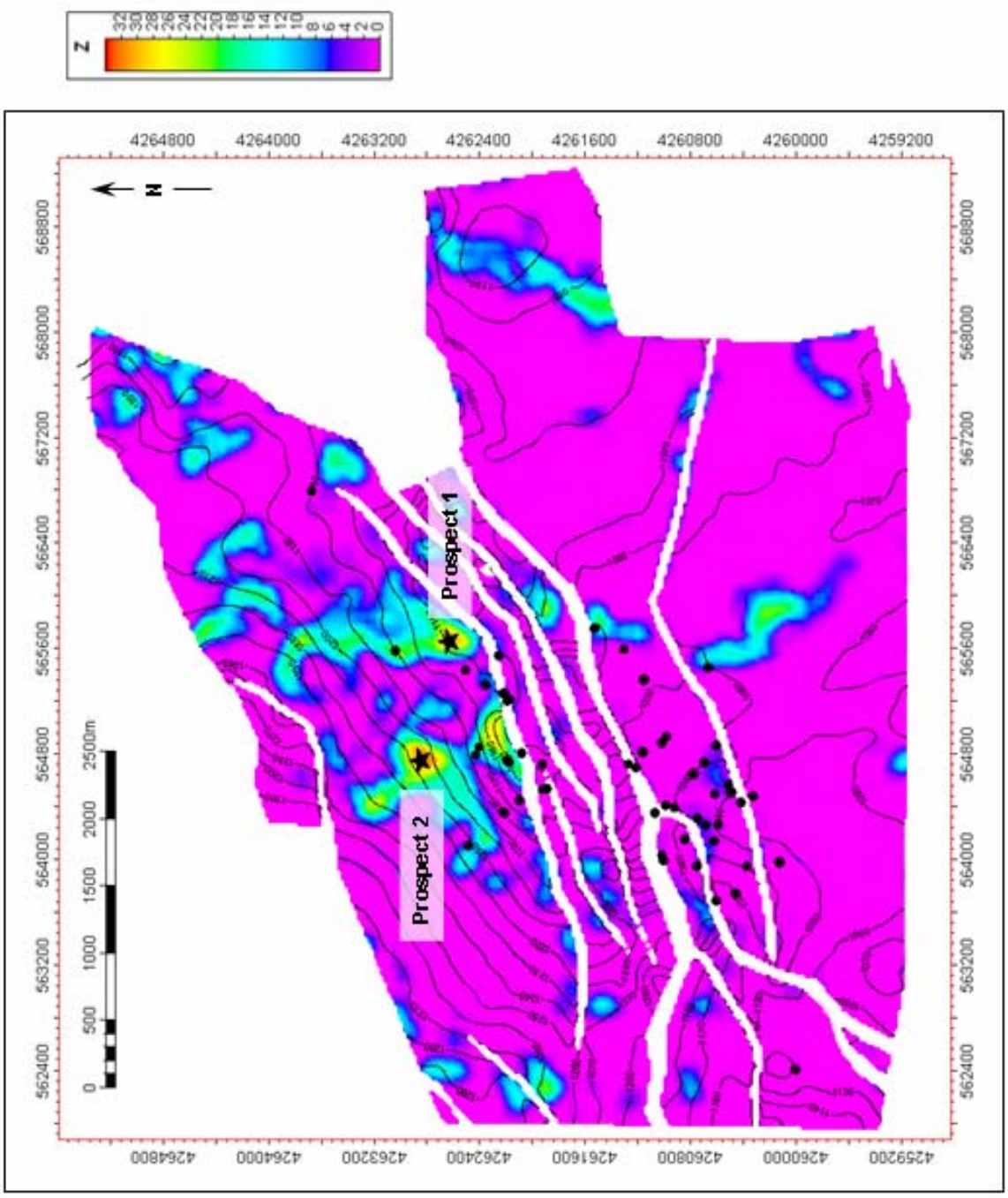
Z
32
30
28
26
24
22
20
18
16
14
12
10
8
6
4
2
0
4264800
4264000
4263200
4262400
4261600
4260800
4260000
4259200
N
568800
568000
567200
566400
565600
564800
564000
563200
562400
Prospect 1
Prospect 2
0
500
1000
1500
2000
2500m

Figure 4.14

Figure 4.15. Total sand thickness map of interval M4 – M5. Sand-rich areas are represented by bright colors (low P- and S-impedance values) while floodplain (non-reservoir) facies are represented by a pink background (high P- and S-impedance values). Black dots represent well locations. This sandstone fairway is 220 m wide and extends in a NE direction for about 550 m. Maximum sandstone thickness is about 34 m. A sandstone fairway just south of prospect 1 has already been tested and showed commercial accumulations of hydrocarbons.

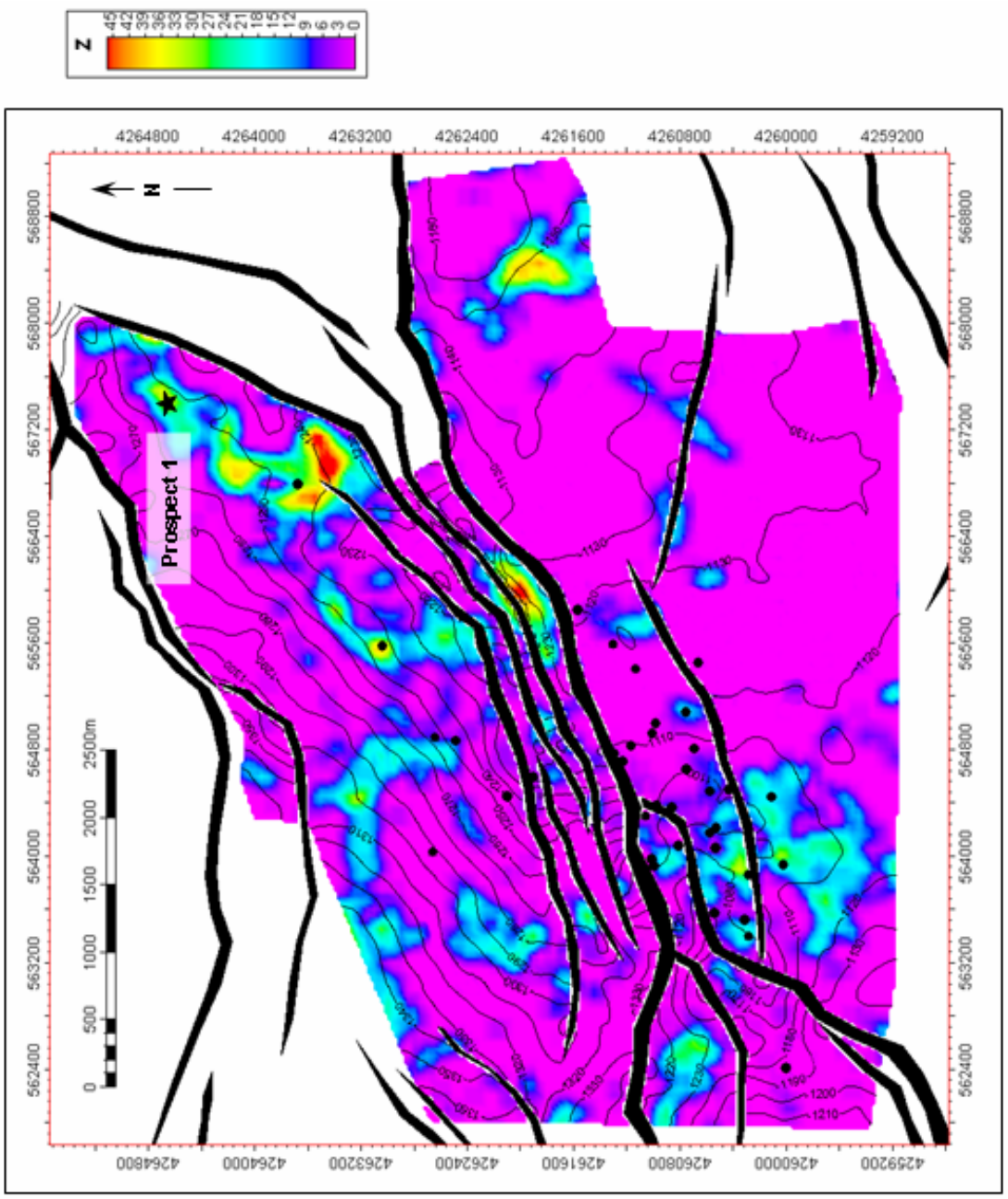
Z
45
42
39
36
33
30
27
24
21
18
15
12
9
6
3
0
4264800
4264000
4263200
4262400
4261600
4260800
4260000
4259200
N
Prospect 1
0
500
1000
1500
2000
2500m

Figure 4.15

Figure 4.16. Total sand thickness map of interval M5 – G2. Sand-rich areas are represented by bright colors (low P- and S-impedance values) while floodplain (non-reservoir) facies are represented by a pink background (high P- and S-impedance values). Black dots represent well locations. One prospect (block C) has been identified in this interval. It is located in a sandstone fairway (up to 21 m thick) 500 m wide and extends in a NE direction for about 950 m.

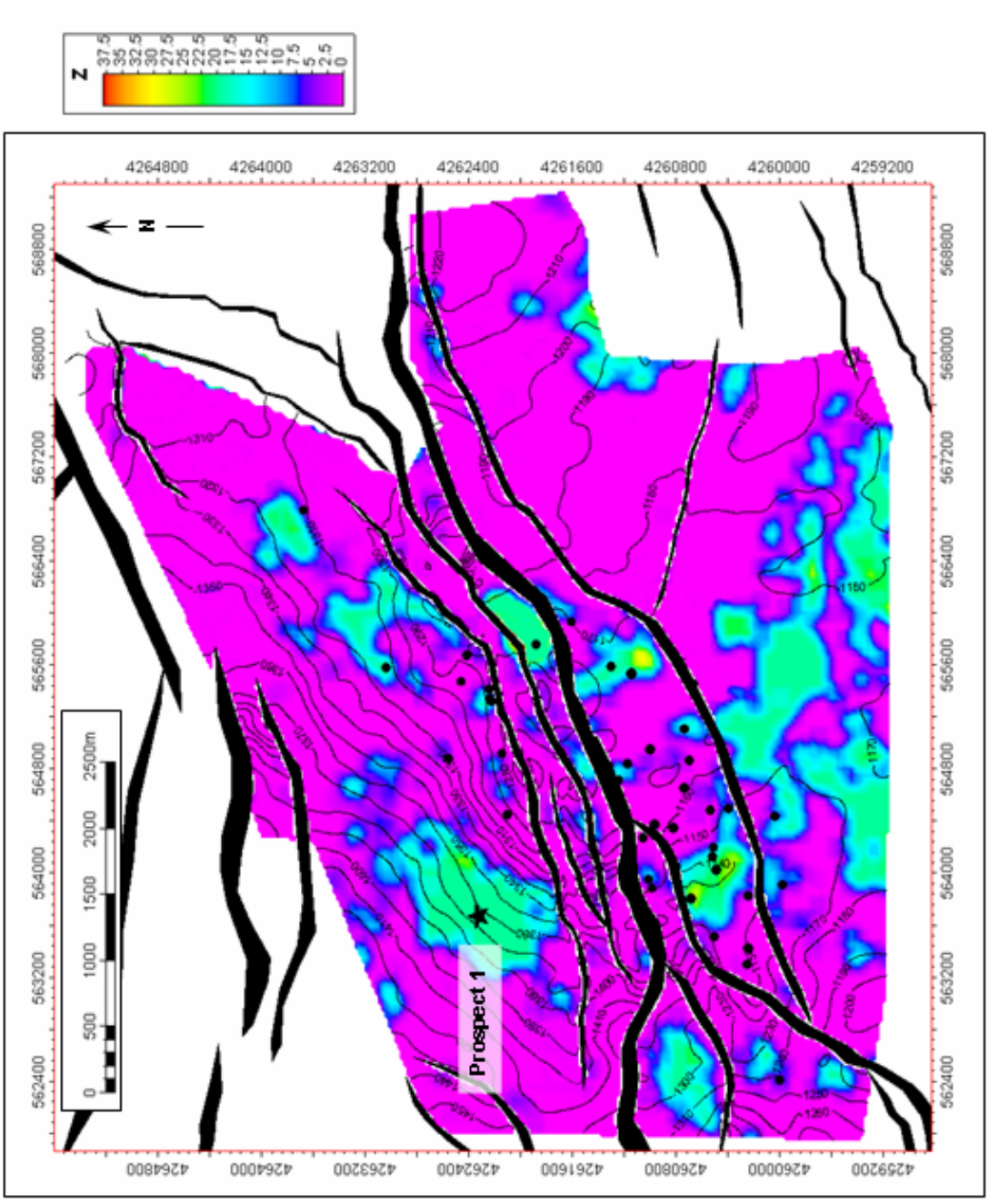
N
37.5
35
32.5
30
27.5
25
22.5
20
17.5
15
12.5
10
7.5
5
2.5
0
4264800
4264000
4263200
4262400
4261600
4260800
4260000
4259200
568800
568000
567200
566400
565600
564800
564000
563200
562400
0
500
1000
1500
2000
2500m
Prospect 1

Figure 4.16

4.6.2.2 Guantao Formation

1) Interval G2 – G3

I identified one new prospect based on the total sand thickness map of interval G2 – G3 (Figure 4.17). The prospect is located in a sandstone fairway that runs roughly E-W in the northernmost extreme of block C. It is 450 m wide and extends for at least 1900 m. Maximum sandstone thickness in this region is about 38 m.

2) Interval G3 – G6

Three prospects have been identified based on the total sand thickness map of interval G3 – G6 (Figure 4.18). Prospect 1 is located in block C, prospect 2 is located in the easternmost region of block D and prospect 3 is located in block D south. Prospect 1 is situated in a sand prone region 450 m wide and extends for about 1800 m in an NE-SW direction. Sandstone thickness reaches up to 22 m. Prospect 2 is situated in a sandstone fairway approximately 600 m wide and extends for at least 1300 m in a NE-SW direction. Maximum sandstone thickness is 39 m. Prospect 3 is sited in a region most likely characterized by laterally continuous sheet sandstones. This area of widespread sandstone deposition is at least 1250 m wide and extends for about 2300 m in a NE-SW direction. Maximum sandstone thickness is approximately 32 m.

3) Interval G6 – G8

The total sand thickness map of interval G6 – G8 (Figure 4.19) shows the thickest sand intervals (up to 41 m thick) within the Guantao Formation. Most of these sandstone fairways have been tested by previous drilling and showed commercial accumulations of hydrocarbons. I have identified one additional prospect in block D south (Figure 4.19).

This prospect is situated in a sandstone fairway 580 m wide and extending 650 m in a roughly N-S direction. Maximum sandstone thickness is approximately 31 m.

4.7 PETROLEUM GEOLOGY OF ZHAO DONG FIELD

Over twelve different stratigraphic levels, ranging in age from Palaeozoic to Tertiary, are known to contain commercial accumulations of oil and attest to the high quality of the petroleum system present in Zhao Dong field (Rigzone, 2007). Since production initiated in 2003, approximately 20 MMBO has been produced from the C and D blocks and there is an estimated 57.5 MMBO of gross proved and probable reserves yet to be produced (Roc Oil Company Limited, 2007; Rigzone, 2007). Current gross production from the two producing blocks in the field is approximately 22,000 BOPD (Roc Oil Company Limited, 2007; Rigzone, 2007).

4.7.1 Source rock

Paleogene lacustrine sediments are the main source rocks in the Bohai Bay region (Wang et al., 1992; Yang and Xu, 2004). In Zhao Dong field, fine-grained lacustrine deposits from the Eocene-Oligocene Shahejie Formation are the principal source rock (Yang and Xu, 2004). The moderate- to high-amplitude seismic reflectors in megasequence 2 most likely represent intervals of lacustrine rocks acting as source rocks (Figure 3.2; MS2). The source rock in Zhao Dong field is rich and generative (Roc Oil Company Limited, 2007). Oil gravities range from 18° to 38° API with the higher gravity (lighter) oil present in the deeper part of the section.

Figure 4.17. Total sand thickness map of interval G2 – G3. Sand-rich areas are represented by bright colors (low P- and S-impedance values) while floodplain (non-reservoir) facies are represented by a pink background (high P- and S-impedance values). Black dots represent well locations. One prospect has been identified in this interval. The prospect is located in a sandstone fairway that runs roughly E-W in the northernmost extreme of block C. It is 450 m wide and extends for at least 1900 m. Maximum sandstone thickness in this region is about 38 m.

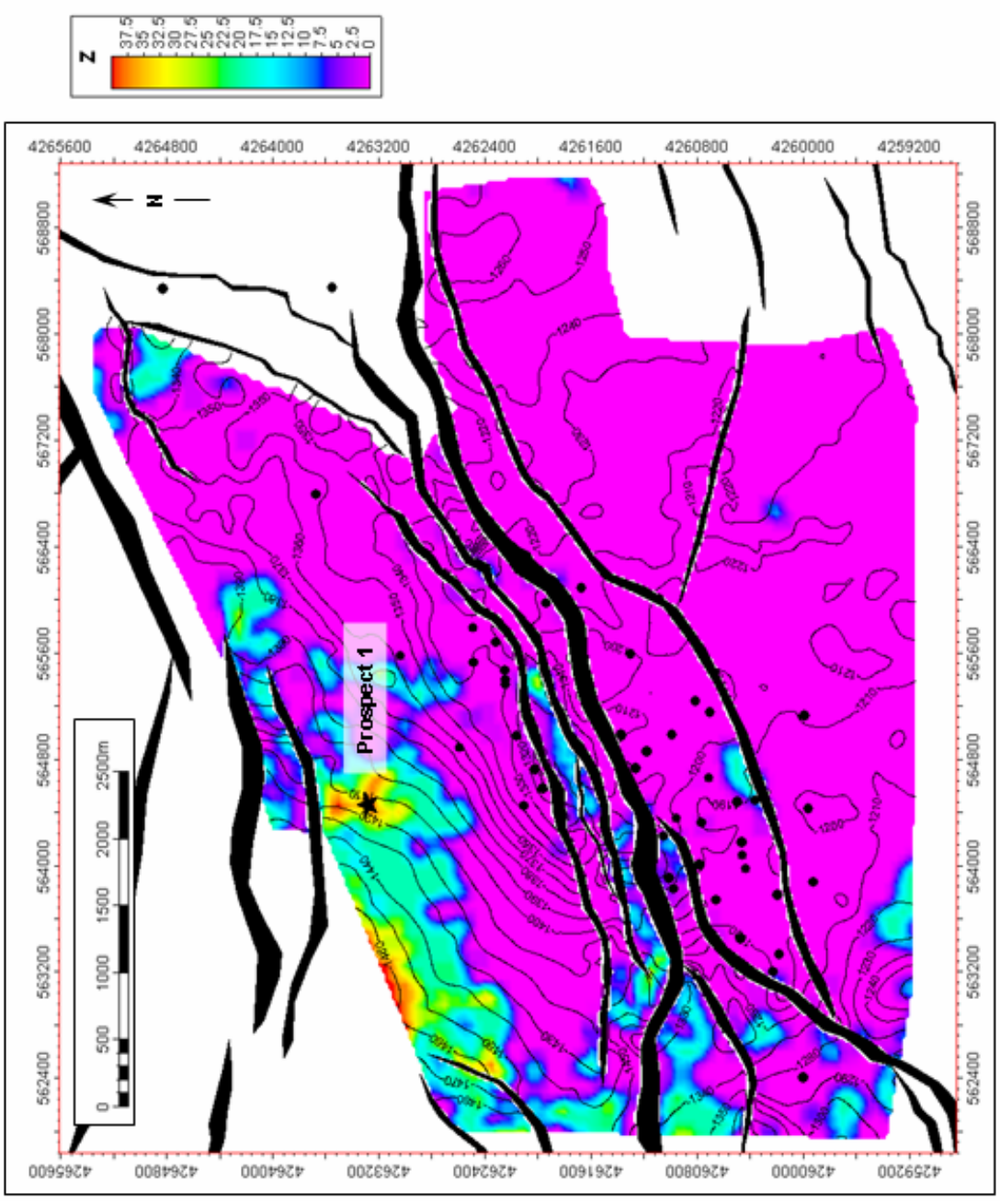
Z
37.5
35
32.5
30
27.5
25
22.5
20
17.5
15
12.5
10
7.5
5
2.5
0
N
Prospect 1
0
500
1000
1500
2000
2500m
4265600
4264800
4264000
4263200
4262400
4261600
4260800
4260000
4259200
568800
568000
567200
566400
565600
564800
564000
563200
562400

Figure 4.17

Figure 4.18. Total sand thickness map of interval G3 – G6. Sand-rich areas are represented by bright colors (low P- and S-impedance values) while floodplain (non-reservoir) facies are represented by a pink background (high P- and S-impedance values). Black dots represent well locations. Prospects 1 is located in block C, prospect 2 is located in the easternmost region of block D and prospect 3 is located in block D south. Prospect 1 is situated in a sand prone region 450 m wide and extends for about 1800 m in an NE-SW direction. Sandstone thickness reaches up to 22 m. Prospect 2 is situated in a sandstone fairway approximately 600 m wide and extends for at least 1300 m in a NE-SW direction. Maximum sandstone thickness is 39 m. Prospect 3 is placed in a region most likely characterized by laterally continuous sheet sandstones. This area of widespread sandstone deposition is at least 1250 m wide and extends for about 2300 m in a NE-SW direction. Maximum sandstone thickness is approximately 32 m.

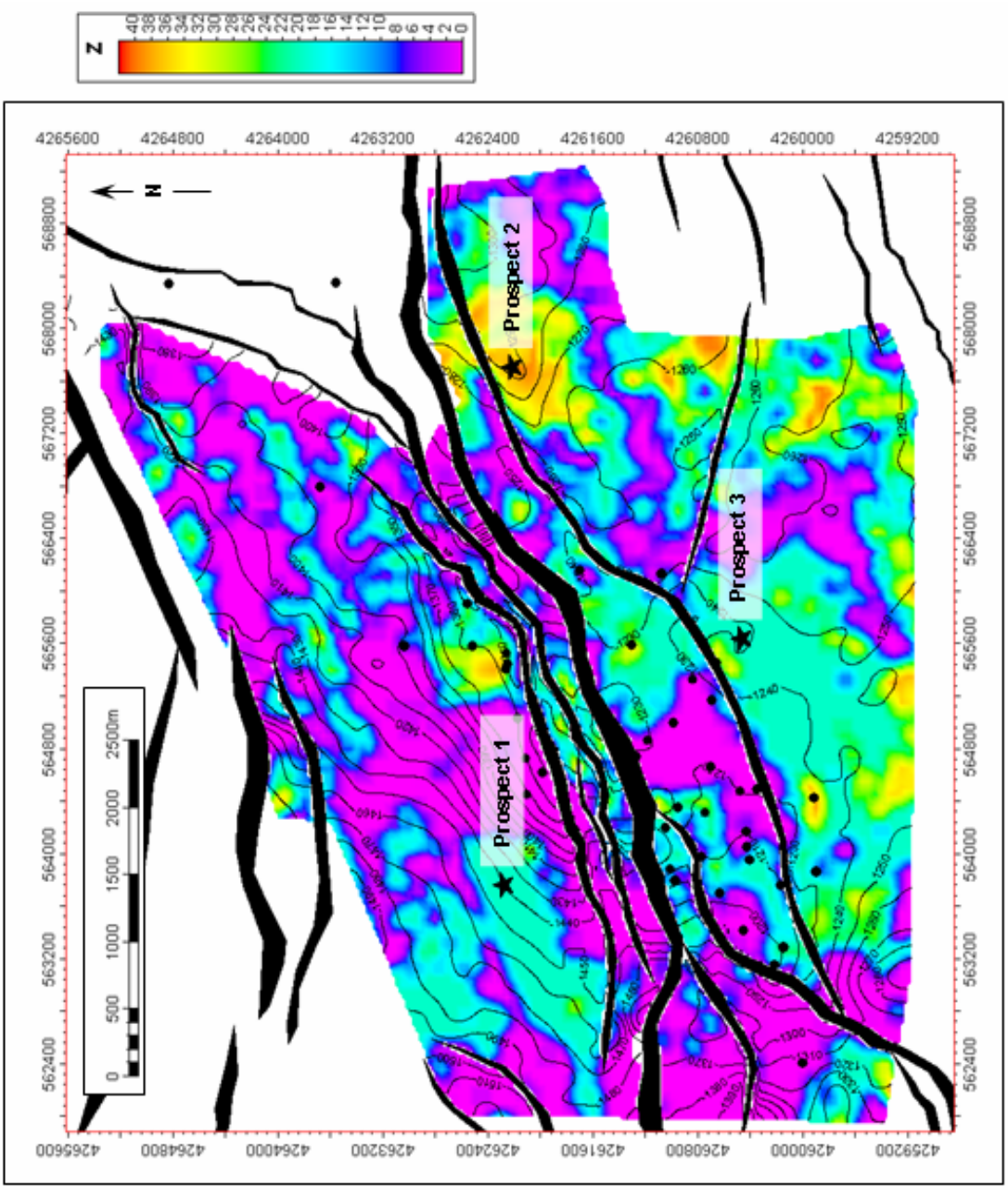
Z
40
38
36
34
32
30
28
26
24
22
20
18
16
14
12
10
8
6
4
2
0
4265600
4264800
4264000
4263200
4262400
4261600
4260800
4260000
4259200
568800
568000
567200
566400
565600
564800
564000
563200
562400
N
Prospect 1
Prospect 2
Prospect 3
0
500
1000
1500
2000
2500m

Figure 4.18

Figure 4.19. Total sand thickness map of interval G6 – G8. Sand-rich areas are represented by bright colors (low P- and S-impedance values) while floodplain (non-reservoir) facies are represented by a pink background (high P- and S-impedance values). Black dots represent well locations. Most of the sandstone fairways in this interval have already been tested and showed commercial accumulations of hydrocarbons. One additional prospect has been located in block D south. This prospect is situated in a sandstone fairway 580 m wide and extends roughly N-S for approximately 650 m. Maximum sandstone thickness is approximately 31 m.

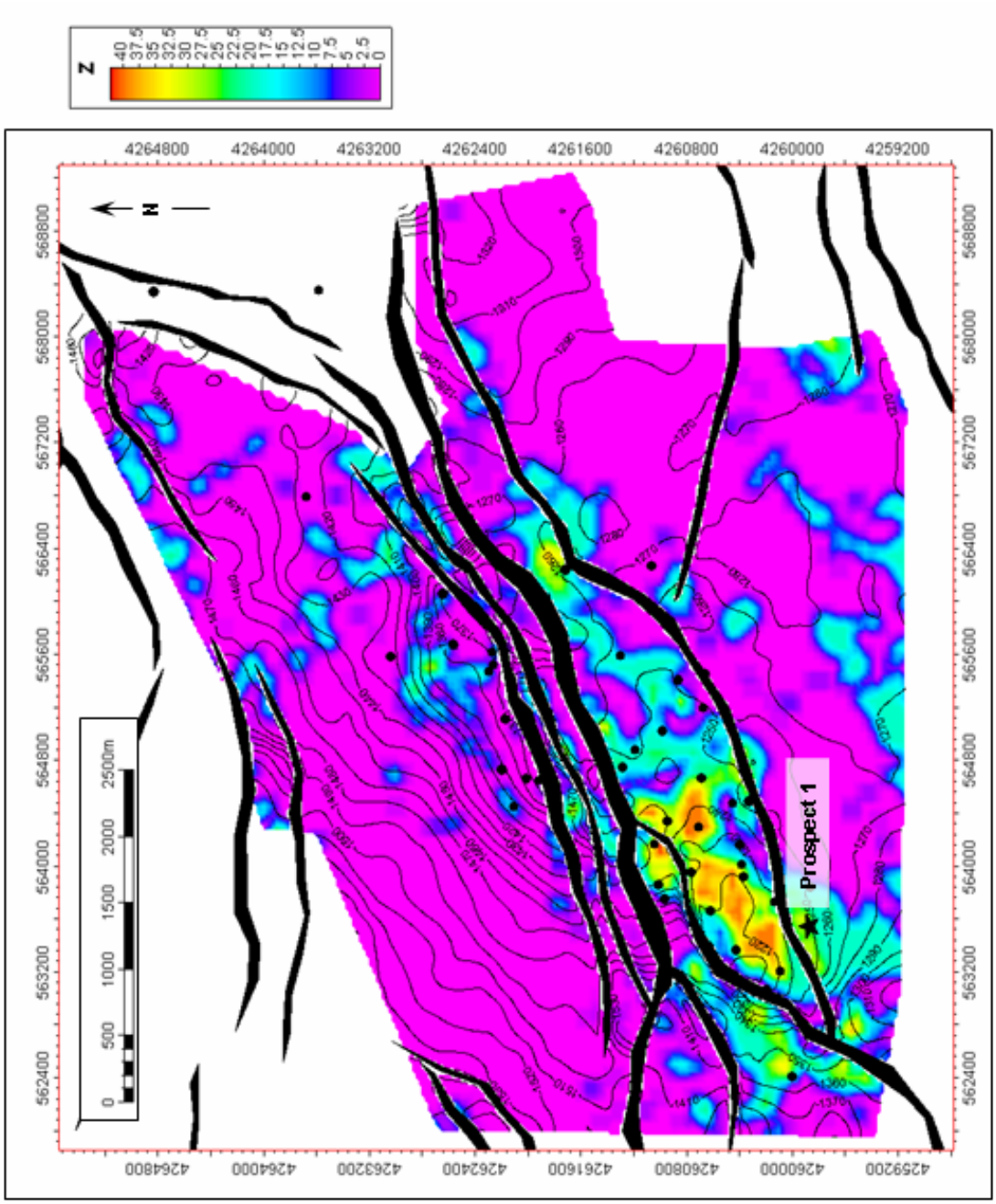
Z
40
37.5
35
32.5
30
27.5
25
22.5
20
17.5
15
12.5
10
7.5
5
2.5
0
N
4264800
4264000
4263200
4262400
4261600
4260800
4260000
4259200
568800
568000
567200
566400
565600
564800
564000
563200
562400
0
500
1000
1500
2000
2500m
Prospect 1

Figure 4.19

4.7.2 Reservoirs

Sandy channel-fill facies from the Guantao and Minghuazhen Formations are the most common type of sandstone reservoirs in the Zhao Dong field. Individual channel bodies when preserved range between 8 and 12 m thick (Minghuazhen Formation) and consist of coarse to fine-grained, locally very coarse, poorly to moderately well sorted, subangular to subrounded quartz-rich sandstones (Figures 3.8, 3.9, 3.10, 3.11 and Table 3.1). Porosities and permeabilities in Zhao Dong field range between 28 and 32% and 240 and 5500 mD, respectively (Roc Oil Company Limited, 2007).

4.7.3 Seal

Low permeability, silty floodplain facies provide important local seals in the Guantao and Minghuazhen sections (Figures 3.8, 3.9, 3.10 and 3.11). Intraformational shales within the reservoir serve both as top and lateral seal.

4.7.4 Structural vs. stratigraphic traps

Exploration in Zhao Dong field has focused largely on structural traps, which are easier to identify and evaluate using seismic data than stratigraphic traps. Stratigraphic traps that have been largely overlooked may represent a good exploration opportunity for future exploration.

Table 4.1 shows the main oil traps found in the Minghuazhen and Guantao sections of Zhao Dong field. The two main structural traps in the field are tilted-fault blocks along blocks C and D and formed within individual strike-slip-related flower structures (Figures 3.12b and 3.13b).

In these structural traps, a combination of fault seal, mainly through the juxtaposition of sandy reservoir and non-reservoir shaly rocks across the leading-edge fault, and dip closure provide the dominant closure mechanism (Figure 3.11). Combination traps are more common in block D south and the more distal portions of block C (Figures. 4.1). The channel-fill sandstones in these two areas trap hydrocarbons through a combination of fault seal, dip closure at the reservoir level and stratigraphic pinch-out.

4.7.5 Future potential

Besides the proposed locations (Figures 4.12, 4.13, 4.14, 4.15, 4.16, 4.17, 4.18 and 4.19), additional hydrocarbon potential may exist outside of the Zhao Dong concession area north of Block C (Figures. 3.18 and 3.24). This area has been less explored, and perhaps offers the most significant remaining exploration target within the larger 3D survey area (Figure 3.4). Well developed, non-channelized lobate sandstone bodies interpreted as fan deltas may represent improved exploration opportunities over the more linear channelized reservoirs within block C. The non-channelized lobate sandstone trend north of Block C forms a NE-oriented 10 km-long and 1.5 km wide sand-prone belt. Plays in this region are predicted to be in the same types of subtle structural/stratigraphic traps known from previous drilling in Block C (Figures. 3.18 and 3.24).

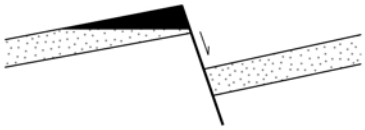	Tilted-fault block
	Horst-block
	Flower structure

Table 4.1 Main oil traps found in the Minghuazhen and Guantao sections of Zhao Dong field. The two main structural traps in the field are comprised by tilted-fault blocks (block C and flower structure compartments) and horst blocks (block D).

4.8 CONCLUSIONS

The most cost effective drilling program for an oil field requires the integration of conventional and unconventional geological and geophysical techniques. Accordingly, the main goal of this chapter was to apply a more robust method that more accurately delineates sand-rich reservoir bodies using multiple 3D seismic volumes validated by abundant well data. Seismic-derived P- and S-relative impedance volumes were used to image the shapes and spatial distribution of reservoir (channel-fill) facies within the Miocene Guantao and Pliocene Minghuazhen Formations, a complex fluvial environment characterized by abrupt lateral facies changes and thin sandstone bodies encased within massive shale units.

Impedance-derived total sand thickness maps revealed two main styles of sand distribution in Zhao Dong field: **channel-fill facies** in the Minghuazhen Formation are intermittently and locally deposited within a background matrix of high-impedance floodplain facies. The dominant trend of sandstone deposition consists of narrow (up to 470 m wide), confined, and slightly sinuous roughly E-W or N-S-oriented sandstone-filled channels. Wells in these trends penetrate up to 25 m of gross sandstone and generally display fining-upward or serrate well log patterns consistent with their fluvial origin. Channel-fill facies in the Guantao Formation form more areally extensive fluvial sandstone bodies that extend several hundred meters (up to 2300 m) along dip and strike directions. Individual fluvial channels in this part of the section are hardly preserved. Wells in these trends reach up to 55 m of gross sandstone and display blocky or coarsening-upward well log patterns (Figure 3.5).

Thirteen new locations have been proposed in this study based on the impedance-derived total thickness maps of eight different prospective intervals within the Guantao

and Minghuazhen Formation. At the time of this writing, I do not know whether any of these prospects have been identified by others or have been tested.

CHAPTER 5

Conclusions

5.1 CENOZOIC TECTONIC EVOLUTION OF THE BOHAI BASIN

Based on a regional basin analysis of megasequences, regional unconformities, fault systems, and, thickening trends and ages; I conclude that previously proposed models for orthogonal rifting (Ye et al., 1985) and late phase of Neogene strike-slip deformation (Hu et al., 2001) have both played important roles in the formation of the Bohai Basin.

The Cenozoic Bohai Basin contains two main depositional units, a late Paleocene to late Oligocene syn-rift section (MS2) of continental sedimentary rocks in half-grabens and an overlying early Miocene to recent post-rift sag section (MS3 and MS4) of continental sedimentary rocks deposited in broad depocenters or sag basins (Figures 2.6, 2.8, 2.9, 2.10, 2.11, 2.12 and 2.13). The syn-rift section developed in response to a regional late Paleocene – late Oligocene extension, which produced abundant basin-parallel northeast-striking and basin-oblique east-west structures (Figures 2.8, 2.9, 2.10, 2.11, 2.12, 2.13, 2.14 and 2.15). Paleogene extension was followed by a period of regional uplift and erosion during late Oligocene (Figures 2.6 and 2.11b). Subsidence analysis shows that the post-rift sag section developed in response to thermal subsidence, which was later followed by strike-slip deformation (Hu et al., 2001) (Figure 2.18).

The peak of strike-slip deformation occurred during late Miocene – early Pliocene and resulted in the reactivation of previous rift-related normal faults and in the formation of new E-W and WNW-ESE striking strike-slip faults (Figure 2.11b). Earthquakes indicate that right-lateral strike-slip faulting continues to the present-day in a pattern consistent with the regional-scale “lazy-Z” map pattern of the Cenozoic Bohai depocenter (Figure 2.4).

The widespread distribution of Eocene to Miocene rifts in the Bohai Basin and adjacent basins of east Asia (Figure 2.2a) supports the previous interpretation by Watson et al. (1987) and Schellart and Lister (2005) that this phase of extension was related to a previously proposed rollback of the Pacific plate subducted beneath the Bohai Basin (Figure 2.3a). Strike-slip deformation is attributed to a change in the direction of the convergence vector between the Eurasian plate and the subducting Pacific plate during early to late Miocene time (Northrup et al., 1985) (Figure 2.21b).

5.2 STRATIGRAPHY AND SEDIMENTOLOGY OF ZHAO DONG FIELD

The Miocene Guantao and Pliocene Minghuazhen Formations in Zhao Dong field developed during the post-rift thermal subsidence stage of the Bohai Basin in northeastern China (Chapter 2). These deposits are entirely fluvial in origin and can be grouped into four main facies associations: FA1 - channel-fill, FA2 - point-bar, FA3 - crevasse splay; and FA4 - interdistributary facies-associations (Figure 3.7).

The integrated application of fluvial sequence stratigraphic concepts together with the identification and correlation of A/S cycles (Ramon and Cross, 1997) on three-dimensional seismic and well-log data has resulted in a revised chronostratigraphic subdivision of the fluvial deposits of the Guantao and Minghuazhen Formations in Zhao

Dong field, Bohai Bay; northeastern China. The revised chronostratigraphic subdivision results in a more detailed prediction of reservoir sand distribution and connectivity and therefore increases the likelihood for successful wells drilled in the Zhao Dong field (Chapter 4).

Ten fieldwide correlatable accommodation/supply cycles were identified and correlated in the Guantao and Minghuazhen sections of Zhao Dong field (Figure 3.5c). Guantao Formation is made up of highly amalgamated fluvial sands deposited under low accommodation/supply conditions (Figures 3.8, 3.9, 3.10, 3.11 and 3.21). Amalgamated fluvial channel sandstone forms areally extensive bodies that extend several hundred meters along dip and strike directions. Minghuazhen Formation on the other hand is characterized by isolated channel systems encased by floodplain facies deposited under high accommodation/supply conditions (Figures 3.8, 3.9, 3.10, 3.11 and 3.21). The changes in the fluvial architecture between both formations are interpreted to reflect a progressive increase in accommodation space produced by strike-slip faulting (Chapter 2) that led to successively less amalgamation of the channel deposits.

Because Guantao and Minghuazhen Formations are fully fluvial successions, eustasy can be ruled out as an external control on their accommodation and stratigraphic cyclicity. Climatic fluctuations also appear to have been minor since climatic indicators such as paleosols and pollen assemblages did not vary markedly during their span of deposition (ref).

On the basis of data presented in this chapter, I conclude that regional tectonic subsidence - including syndepositional block faulting caused by strike-slip deformation - is the main control on changing accommodation and stratigraphic cyclicity of Miocene-Pliocene non-marine deposits of the Zhao Dong field. Autogenic processes such as lateral

migration and avulsion may also be superimposed effects on the autogenic processes recorded in the fluvial stratigraphy of the basin.

5.3 P- AND S-IMPEDANCE SEISMIC DERIVED VOLUMES

The most cost effective drilling program for an oil field requires the integration of conventional and unconventional geological and geophysical techniques. Accordingly, the main goal of this chapter was to apply a more robust method that more accurately delineates sand-rich reservoir bodies using multiple 3D seismic volumes validated by abundant well data. Seismic-derived P- and S-relative impedance volumes were used to image the shapes and spatial distribution of reservoir (channel-fill) facies within the Miocene Guantao and Pliocene Minghuazhen Formations, a complex fluvial environment characterized by abrupt lateral facies changes and thin sandstone bodies encased within massive shale units.

Impedance-derived total sand thickness maps revealed two main styles of sand distribution in Zhao Dong field: channel-fill facies in the Minghuazhen Formation are intermittently and locally deposited within a background matrix of high-impedance floodplain facies. The dominant trend of sandstone deposition consists of narrow (up to 470 m wide), confined, and slightly sinuous roughly E-W or N-S-oriented sandstone-filled channels. Wells in these trends penetrate up to 25 m of gross sandstone and generally display fining-upward or serrate well log patterns consistent with their fluvial origin. Channel-fill facies in the Guantao Formation form more areally extensive fluvial sandstone bodies that extend several hundred meters (up to 2300 m) along dip and strike directions. Individual fluvial channels in this part of the section are hardly preserved.

Wells in these trends reach up to 55 m of gross sandstone and display blocky or coarsening-upward well log patterns (Figure 3.5).

Thirteen new locations have been proposed in this study based on the impedance-derived total thickness maps of eight different prospective intervals within the Guantao and Minghuazhen Formation. At the time of this writing, I do not know whether any of these prospects have been identified by others or have been tested.

References

Alexander, J., J. S. Bridge, M. R. Leeder, R. E. L. Collier, and R. L. Gawthorpe, 1994, Holocene meander-belt evolution in an active extensional basin, southwestern Montana: Journal of Sedimentary Research, v. 64, p. 542-559.

Allen, M. B., D. I. M. Macdonald, Z. Xun, S. J. Vincent, and C. Brouet-Menzies, 1997, Early Cenozoic two-phase extension and late Cenozoic thermal subsidence and inversion of the Bohai Basin, northern China: Marine and Petroleum Geology, v. 14, p. 951-972.

Allen, M. B., D. I. M. MacDonald, Z. Xun, S. J. Vincent, and C. Brouet-Menzies, 1998, Transtensional deformation in the evolution of the Bohai Basin, northern China, in R. E. Holdsworth, R. A. Strachan, and J. F. Dewey, eds., Continental transpressional and transtensional tectonics, Geological society (London) Special Publication 135, p. 215-229.

Arnott, R. W. C., B. A. Zaitlin, and D. J. Potocki, 2002, Stratigraphic response to sedimentation in a net-accommodation-limited setting, Lower Cretaceous Basal Quartz, south-central Alberta: Bulletin of Canadian Petroleum Geology, v. 50, p. 92-104.

Avadhani, V. L. N., M. Anandan, B. J. Thattacherry, K. S. Murthy, B. C. Gariya, and A. K. Dwivedi, 2006, Acoustic impedance as a lithological and hydrocarbon indicator - a case study from Cauvery Basin: The Leading Edge, v. 25, p. 854-858.

Benabentos, M., S. Mallick, M. Sigismondi, and J. Soldo, 2002, Seismic reservoir description using hybrid seismic inversion: A 3D case study from the Maria Ines Oeste Field, Argentina: The Leading Edge, v. 21, p. 1002-1008.

Berge, T. B., F. Aminzadeh, P. de Groot, and T. Oldenziel, 2002, Seismic inversion successfully predicts reservoir, porosity, and gas content in Ibhubesi Field, Orange Basin, South Africa: The Leading Edge, v. 21, p. 338-348.

BGMRLP, 1989, Regional Geology of Liaoning Province, Bureau of Geology and Mineral Resources of Liaoning Province, Geological Publishing House, Beijing, p. 856.

Blum, M. D., and T. E. Tornqvist, 2000, Fluvial responses to climate and sea-level change: A review and look forward: Sedimentology, v. 47, p. 2-48.

Bordy, E. M., and O. Catuneanu, 2001, Sedimentology of the upper Karoo fluvial strata in the Tuli Basin, South Africa: Journal of African Earth Sciences, v. 33, p. 605-629.

Bose, A., V. Singh, A. K. Tandon, B. S. Josyulu, and M. Chandra, 2004, A case study of stratigraphic and lithologic interpretation of thin reservoirs through an integrated approach: The Leading Edge, v. 23, p. 966-972.

Cai, D., Y. Luo, C. Yao, J. He, S. Hu, H. Lu, and L. Wang, 2000, Structures of the Bohai petroliferous area, Bohai Bay basin: Acta Geologica Sinica, v. 74, p. 641-650.

Calais, E., M. Vergnolle, V. San'kov, A. Lukhnev, A. Miroshnitchenko, S. Amarjargal, and J. Deverchere, 2003, GPS measurements of crustal deformation in the Baikal-Mongolia area (1994-2002): Implications for current kinematics of Asia: Journal of Geophysical Research, v. 108, p. 1-13.

Carter, A., D. Roques, C. Bristow, and P. Kinny, 2001a, Understanding Mesozoic accretion in Southeast Asia: Significance of Triassic thermotectonism (Indosinian orogeny) in Vietnam: Geology, v. 29, p. 211-214.

Carter, A., D. Roques, C. Bristow, and P. D. Kinny, 2001b, Understanding Mesozoic accretion in Southeast Asia: Significance of Triassic thermotectonism (Indosinian Orogeny) in Vietnam: Geology, v. 29, p. 211.

Catuneanu, O., 2006, Principles of Sequence Stratigraphy: Amsterdam, Elsevier, 375 p.

Catuneanu, O., and D. Bowker, 2001, Sequence stratigraphy of the Koonap and Middleton fluvial formations in the Karoo foredeep South Africa: Journal of African Earth Sciences, v. 33, p. 579-595.

Catuneanu, O., and H. N. Elango, 2001, Tectonic control on fluvial styles: the Balfour Formation of the Karoo Basin, South Africa: Sedimentary Geology, v. 140, p. 291-313.

Catuneanu, O., M. A. Martins-Neto, and P. G. Eriksson, 2005, Precambrian sequence stratigraphy: Sedimentary Geology, v. 176, p. 67-95.

Chang, C., 1991, Geological characteristics and distribution patterns of hydrocarbon deposits in the Bohai Bay basin, East China: Marine and Petroleum Geology, v. 8, p. 98-106.

Chen, A., 1998, Geometric and kinematic evolution of basement-cored structures: Intraplate orogenesis within the Yanshan Orogen, northern China: Tectonophysics, v. 292, p. 17-42.

Chen, C., J. Huang, J. Chen, and X. Tian, 1984, Depositional models of Tertiary rift basins, eastern China, and their application to petroleum prediction: Sedimentary Geology, v. 40, p. 73-88.

Chen, W., and J. Nabelek, 1988, Seismogenic strike-slip faulting and the development of the North China Basin: Tectonics, v. 7, p. 975-989.

Christie-Blick, N., 1985, Deformation and basin formation along strike-slip faults, in K. T. Biddle, and N. Christie-Blick, eds., Strike-slip Deformation, Basin Formation, and Sedimentation: Society of Economic Paleontologists and Mineralogists - Special Publication No.37, p. 1-34.

Chung, S. L., C. H. Lo, C. Y. Lan, P. L. Wang, T. Y. Lee, H. Tran Trong, T. Hoang Huu, and A. Tran Tuan, 1999, Collision between the Indochina and South China blocks in the Early Triassic: Implications for the Indosinian Orogeny and closure of eastern Paleotethys: EOS, Transactions of the American Geophysical Union, v. 80, p. 1043.

CNOOC (China National Offshore Oil Corporation) -Limited, 2005, Key operating areas. http://www.cnoocltd.com/Operations/channel/opertions1295.asp#m1. [Accessed October 2006].

Curray, J. R., 1964, Transgressions and regressions, in R. L. Miller, ed., Papers in Marine Geology, New York, Macmillan, p. 175-203.

Dahle, K., K. Flesja, M. R. Talbot, and T. Dreyer, 1997, Correlation of fluvial deposits by the use of Sm-Nd isotope analysis and mapping of sedimentary architecture in the Escanilla Formation (Ainsa Basin, Spain) and the Statfjord Formation (Norwegian North Sea). Abstracts, Sixth International Conference on Fluvial Sedimentology, Cape Town, South Africa, p. 46.

DeAngelo, M. V., and L. J. Wood, 2001, 3-D seismic detection of undrilled prospective areas in a mature province, South Marsh Island, Gulf of Mexico: The Leading Edge, v. 20, p. 1282-1292.

Diessel, C., R. Boyd, J. Wadsworth, D. Leckie, and G. Chalmers, 2000, On balanced and unbalanced accommodation/peat accumulation ratios in the Cretaceous coals from Gates Formation, Western Canada, and their sequence-stratigraphic significance: International Journal of Coal Geology, v. 43, p. 143-186.

Du, Y., 1990, Eogene lacustrine carbonate rocks and sedimentary model in the Bohai Bay region: Shiyou yu tianranqi dizhi, v. 11, p. 376-392.

Duffaut, K., T. Alsos, H. Rogno, N. F. Al-Najjar, and M. Landro, 2000, Shear-wave elastic impedance: The Leading Edge, v. 19, p. 1222-1229.

Dvorkin, J., J. Walls, R. Uden, M. Carr, M. Smith, and N. Derzhi, 2004, Lithology substitution in fluvial sand: The Leading Edge, v. 23, p. 108-112.

Elsasser, W. M., 1971, Sea-floor spreading as thermal convection, v. 76, p. 1101-1112.

Energy Information Administration, China. http://www.eia.doe.gov/emeu/cabs/China/Oil.html. [Accessed February 2007].

Emery, D., and K. J. Myers, 1996, Sequence Stratigraphy: Oxford, Blackwell, 297 p.

Eriksson, P., W. Altermann, and O. Catuneanu, 2005, Some general advice for writing a scientific paper: Journal of African Earth Sciences, v. 41, p. 285-288.

Escalona, A., and P. Mann, 2003, Three-dimensional structural architecture and evolution of the Eocene pull-apart basin, central Maracaibo basin, Venezuela: Marine and Petroleum Geology, v. 20, p. 141-161.

Farrell, K. M., 2001, Geomorphology, facies architecture, and high-resolution, non-marine sequence stratigraphy in avulsion deposits, Cumberland Marshes, Saskatchewan: Sedimentary Geology, v. 139, p. 93-150.

Fletcher, C. J. N., W. R. Fitches, C. C. Rundle, and J. A. Evans, 1995, Geological and isotopic constraints on the timing of movement in the Tan-Lu Fault Zone, northeastern China: Journal of Southeast Asian Earth Sciences, v. 11, p. 15-22.

Forbes, China's 2006 oil import dependency at 47 percent, up 4.1 percentage points from 2005. http://www.forbes.com/business/feeds/afx/2007/02/12/afx3420562.html [Accessed March 2007].

Galloway, W. E., 1989, Genetic stratigraphic sequences in basin analysis, I. Architecture and genesis of flooding-surface bounded depositional units: AAPG Bulletin, v. 73, p. 125-142.

Galloway, W. E., and D. K. Hobday, 1996, Terrigenous Clastic Depositional Systems: Applications to Fossil Fuel and Groundwater Resources: Berlin, Springer-Verlag, 489 p.

Gilder, S. A., P. H. Leloup, V. Courtillot, Y. Chen, R. S. Coe, X. Zhao, W. Xiao, N. Halim, J.-P. Cogne, and R. Zhu, 1999, Tectonic evolution of the Tancheng-Lujiang (Tan-Lu) Fault via Middle Triassic to early Cenozoic paleomagnetic data: Journal of Geophysical Research, v. 104, p. 15,365-15,390.

Gluck, S., E. Juve, and Y. Lafet, 1997, High-resolution impedance layering through 3-D stratigraphic inversion of poststack seismic data: The Leading Edge, v. 16, p. 1309-1315.

Gong, Z.S., 1997. Giant Offshore Oil and Gas Fields in China. Petroleum Industry Press, Beijing, 396 p.

Gong, Z., 2004, Neotectonics and petroleum accumulation in offshore Chinese basins: Earth Science (Bejing, China), v. 29, p. 513-517.

Guo, L., 1983, Formation and evolution of the Mesozoic-Cenozoic active continental margin and island arc of the West Pacific: Acta Geologica Sinica, v. 57, p. 11-21.

Hamilton, D. S., and N. Z. Tadros, 1994, Utility of coal seams as genetic stratigraphic sequence boundaries in nonmarine basins: An example from the Gunnedah Basin, Australia: AAPG Bulletin, v. 78, p. 267-286.

Han, Z., L. Wu, Y. Ran, and Y. Ye, 2003, The concealed active tectonics and their characteristics as revealed by drainage density in the North China plain (NCP): Journal of Asian Earth Sciences, v. 21, p. 989-998.

Hardage, B. A., and R. Remington, 1999, 3-D seismic stratal-surface concepts applied to the interpretation of a fluvial channel system deposited in a high-accommodation environment: Geophysics, v. 64, p. 609-620.

Helland-Hansen, D., I. Magnus, A. Edvardsen, and E. Hansen, 1997, Seismic inversion for reservoir characterization and well planning in the Snorre Field: The Leading Edge, v. 16, p. 269-273.

Hellinger, S. J., K. M. Shedlock, J. G. Sclater, and Y. Hong, 1985, The Cenozoic evolution of the North China Basin: Tectonics, v. 4, p. 343-358.

Hidalgo, R., S. Haryono, M. Schneider, and R. Roden, 2001, 3-D seismic interpretation of thin gas sandstone reservoirs using multi-attribute analysis on poststack and AVO data, offshore SE Sumatra: The Leading Edge, v. 20, p. 364-370.

Hong, Y., K. M. Shedlock, S. J. Hellinger, and J. G. Sclater, 1985, The North China Basin; An example of a Cenozoic rifted intraplate basin: Tectonics, v. 4, p. 153.

Hsiao, L. Y., S. A. Graham, and N. Tilander, 2004, Seismic reflection imaging of a major strike-slip fault zone in a rift system: Paleogene structure and evolution of the Tan-Lu Fault system, Liaodong Bay, Bohai, offshore China: AAPG Bulletin, v. 88, p. 71-97.

Hu, J., S. Xu, X. Tong, and H. Wu, 1989, The Bohai Bay Basin, in X. Zhu, ed., Chinese Sedimentary Basins: Sedimentary basins of the World, volume 1, K, Hsu (series editor), Amsterdam, Elsevier, p. 89-105.

Hu, S., P. B. O'Sullivan, A. Raza, and B. P. Kohn, 2001, Thermal history and tectonic subsidence of the Bohai Basin, northern China: A Cenozoic rifted and local pull-apart basin: Physics of the Earth and Planetary Interiors, v. 126, p. 221-235.

Huang, C., 1978, An outline of the tectonic characteristics of China: Eclogae Geologicae Helvetiae, v. 71, p. 611-635.

Hubbard, R. J., 1988, Age and significance of sequence boundaries on Jurassic and Early Cretaceous rifted continental margins: AAPG Bulletin, v. 72, p. 49-72.

Jervey, M. T., 1988, Quantitative geological modeling of siliciclastic rock sequences and their seismic expression, in C. K. Wilgus, B. S. Hastings, C. A. Ross, H. Posamentier, J. Van Wagoner, and C. G. Kendall, eds., Sea-level changes: An integrated approach, SEPM - Special Publication 42, p. 47-69.

Kuykendall, M. D., J. B. O'Reilly, B. D. Patton, R. P. Mott, J. Yang-Logan, Q. Gui Ma, L. Ying, S. Hua, L. Xin Tian, and P. Fei Zhao, 2003, Petroleum geology of the Peng Lai 19-3 oil field, Bohai Bay, People's Republic of China, in M. T. Halbouty, ed., Giant Oil and Gas Fields of the Decade, 1990-1999, AAPG Memoir 78, p. 321–331.

Lan, C., S. Chung, L. Trinh Van, C. Lo, T. Lee, S. A. Mertzman, and J. Shen, 2003, Geochemical and Sr-Nd isotopic constraints from the Kontum Massif, central Vietnam on the crustal evolution of the Indochina block: Precambrian Research, v. 122, p. 7-27.

Lancaster, S., and D. Whitcombe, 2000, Fast track "coloured" inversion: Expanded abstracts, 70th SEG Annual Meeting, Calgary, p. 1572-1575.

Latimer, R. B., R. Davidson, and P. van Riel, 2000, An interpreter's guide to understanding and working with seismic-derived acoustic impedance data: The Leading Edge, v. 19, p. 242-256.

Lau, A., A. Gonzalez, S. Mallick, and D. Gillespie, 2002, Waveform gather inversion and attribute-guided interpolation: A two-step approach to log prediction: The Leading Edge, v. 21, p. 1024-1027.

Leckie, D. A., K. E. Wallace-Dudley, N. A. Vanbeselaere, and D. P. James, 2004, Sedimentation in a low-accommodation setting: Nonmarine (Cretaceous) Mannville and marine (Jurassic) Ellis groups, Manyberries field, southeastern Alberta: AAPG Bulletin, v. 88, p. 1391-1418.

Li, S., Y. Xiao, D. Liou, Y. Chen, N. Ge, Z. Zhang, S.-s. Sun, B. Cong, R. Zhang, S. R. Hart, and S. Wang, 1993, Collision of the North China and Yangtse Blocks and formation of coesite-bearing eclogites: Timing and processes: Chemical Geology, v. 109, p. 89-111.

Li, Y., X. Hu, C. Zhao, and G. L. Wang, 1998, Establishment of the GPS monitoring network in North China and relationship between the crustal horizontal motion and the stress field and seismicity: Earthquake research in China, v. 14, p. 116-125.

Liangmiao Ye., 1995, Paleosols in the Upper Guantao Formation (Miocene) of the Gudong Oil Field and Their Application to the Correlation of Fluvial Deposits: AAPG Bulletin, v. 79, p. 981-988.

Liu, G., 1987, The Cenozoic rift system of the North China Plain and the deep internal processes: Tectonophysics, v. 133, p. 277-285.

Liu, G., and E. B. Leopold, 1994, Climatic comparison of Miocene pollen floras from northern East-China and south-central Alaska, USA: Palaeogeography, Palaeoclimatology, Palaeoecology, v. 108, p. 217-228.

Lonergan, L., and N. White, 1997, Origin of the Betic-Rif mountain belt: Tectonics, v. 16, p. 504-522.

Lukie, T. D., R. W. Dalrymple, G. W. Ardies, and B. A. Zaitlin, 2002, Alluvial architecture of the Horsefly unit (Basal Quartz) in southern Alberta and northern Montana: Influence of accommodation changes and contemporaneous faulting: Bulletin of Canadian Petroleum Geology, v. 50, p. 73-91.

Ma, X., 2001, Global joint inversion for the estimation of acoustic and shear impedances from AVO derived P- and S-wave reflectivity data: First Break, v. 19, p. 557.

Ma, X., Q. Deng, Y. Wang, and H. Liu, 1982, Cenozoic graben systems in North China: Zeitschrift fuer Geomorphologie, v. 42, p. 96-116.

Mallick, S., X. Huang, J. Lauve, and R. Ahmad, 2000, Hybrid seismic inversion: A reconnaissance tool for deepwater exploration: The Leading Edge, v. 19, p. 1230-1237.

Mann, P., M. R. Hempton, D. C. Bradley, and K. Burke, 1983, Development of pull-apart basins: Journal of Geology, v. 91, p. 529-554.

McClay, K., and T. Dooley, 1995, Analogue models of pull-apart basins: Geology, v. 23, p. 711-714.

McClay, K. R., T. Dooley, P. Whitehouse, and M. Mills, 2002, 4-D evolution of rift systems: Insights from scaled physical models: AAPG Bulletin, v. 86, p. 935-959.

Mendez-Hernandez, E., R. Vila-Villasenor, A. Sosa-Patron, F. de la Vega, G. Hernandez-Carrera, C. Decker, M. Burnett, M. Eissa, D. O'Meara, and J. Castagna, 2003, Advanced seismic techonology improves prospect evaluation and reservoir

delineation in the mature Macuspana Basin, Mexico: The Leading Edge, v. 22, p. 1142-1147.

Meng, Q., and G. Zhang, 1999, Timing of collision of the North and South China blocks: Controversy and reconciliation: Geology, v. 27, p. 123-126.

Miall, A. D., 1985, Architectural-element analysis: A new method of facies analysis applied to fluvial deposits: Earth-Science Reviews, v. 22, p. 261-308.

Miall, A. D., 1996, The Geology of Fluvial Deposits: New York, Springer-Verlag, 598 p.

Millot, G., 1979, Clay: Scientific American, v. 240, p. 108-118.

Mitchum, R. M., Jr., P. R. Vail, and J. B. Sangree, 1977, Seismic stratigraphy and global changes of sea level; Part 6, Stratigraphic interpretation of seismic reflection patterns in depositional sequences, in C. E. Payton, ed., Seismic Stratigraphy: Applications to Hydrocarbon Exploration, AAPG Memoir 26, p. 135-144.

Molnar, P., and T. Atwater, 1978, Interarc spreading and Cordilleran tectonics as alternates related to the age of subducted oceanic lithosphere: Earth and Planetary Science Letters, v. 41, p. 330-340.

Molnar, P., and P. Tapponnier, 1975, Cenozoic tectonics of Asia: Effects of a continental collision: Science, v. 189, p. 419-426.

Morley, C. K., 1999, Basin evolution trends in East Africa, in C. K. Morley, ed., Geoscience of rift systems - Evolution of East Africa, AAPG Studies in Geology No. 44, p. 131-150.

Morley, C. K., 2002, A tectonic model for the Tertiary evolution of strike-slip faults and rift basins in SE Asia: Tectonophysics, v. 347, p. 189-215.

Nabelek, J., W. Chen, and Y. Hong, 1987, The Tangshan earthquake sequence and its implications for the evolution of the North China Basin: Journal of Geophysical Research, v. 92, p. 12,615-12,628.

Northrup, C. J., L. H. Royden, and B. C. Burchfiel, 1995, Motion of the Pacific plate relative to Eurasia and its potential relation to Cenozoic extension along the eastern margin of Eurasia: Geology, v. 23, p. 719-722.

Okay, A., and A. Sengor, 1992, Evidence for intracontinental thrust-related exhumation of the ultra-high-pressure rocks in China: Geology, v. 20, p. 411-414.

Plint, A. G., P. J. McCarthy, and U. F. Faccini, 2001, Nonmarine sequence stratigraphy: Updip expression of sequence boundaries and systems tracts in a high-resolution

framework, Cenomanian Dunvegan Formation, Alberta foreland basin, Canada: AAPG Bulletin, v. 85, p. 1967-2001.

Posamentier, H., and G. Allen, 1999, Siliciclastic Sequence Stratigraphy: Concepts and Applications: SEPM Concepts in Sedimentology and Paleontology, v. 9, 210 p.

Posamentier, H. W., M. T. Jervey, and P. R. Vail, 1988, Eustatic controls on clastic deposition; I, Conceptual framework, in C. K. Wilgus, B. S. Hastings, C. A. Ross, H. W. Posamentier, J. Van Wagoner, and C. G. Kendall, eds., Sea-level Changes: An Integrated Approach, SEPM - Special Publication 42, p. 109-124.

Posamentier, H. W., and P. R. Vail, 1988, Eustatic controls on clastic deposition; II, Sequence and systems tract models, in C. K. Wilgus, B. S. Hastings, C. A. Ross, H. W. Posamentier, J. Van Wagoner, and C. G. S. C. Kendall, eds., Sea-level Changes: An integrated Approach, SEPM Special Publication 42, p. 125-154.

Ramon, J. C., and T. A. Cross, 1997, Controles estratigraficos en la arquitectura de canales fluviales: Revision a los modelos de facies fluviales e implicaciones en caracterizacion de yacimientos: Memorias del Primer Congreso Latinoamericano de Sedimentologia, Sociedad Venezolana de Geologos, Tomo II, Noviembre, 1997, p. 209-215.

Ratcliffe, K. T., A. M. Wright, C. Hallsworth, A. Morton, B. A. Zaitlin, D. Potocki, and D. S. Wray, 2004, An example of alternative correlation techniques in a low-accommodation setting, nonmarine hydrocarbon system: The (Lower Cretaceous) Mannville Basal Quartz succession of southern Alberta: AAPG Bulletin, v. 88, p. 1419-1432.

Rigzone, 2006, Roc Oil Reduces Production at Zhao Dong Block. http://www.rigzone.com/news/article.asp?a_id=36962. [Accessed February 2007].

Roc Oil Company Limited, Zhao Dong Block Oil Fields, Bohai Bay, China C and D Oil Fields. http://www.rocoil.com.au/Public/Activities/China/Zhao_Dong_Oil_Fields.aspx [Accessed February 2007].

Ronghe, S., and S. Pambayuning, 2002, Depth-induced impedance variations in reservoir sands - Implications for predicting lithology and fluid distributions offshore Brunei Darussalam: The Leading Edge, v. 21, p. 388-393.

Ronghe, S., and K. Surarat, 2002, Acoustic impedance interpretation for sand distribution adjacent to a rift boundary fault, Suphan Buri Basin, Thailand: AAPG Bulletin, v. 86, p. 1753-1771.

Ronghe, S., and P. V. Trung, 2000, Acoustic impedance interpretation for hydrocarbon extent, offshore Brunei Darussalam: First Break, v. 18, p. 421-426.

Rowley, D.B. 1996. Age of initiation of collision between India and Asia: a review of stratigraphic data. Earth and Planetary Science Letters, 145, p. 1–13.

Schellart, W. P., 2004, Kinematics of subduction and subduction-induced flow in the upper mantle: Journal of Geophysical Research, v. 109 (B07401).

Schellart, W. P., 2005, Influence of the subducting plate velocity on the geometry of the slab and migration of the subduction hinge: Earth and Planetary Science Letters, v. 231, p. 197– 219.

Schellart, W. P., and G. S. Lister, 2005, The role of the East Asian active margin in widespread extensional and strike-slip deformation in East Asia: Journal of the Geological Society of London, v. 162, p. 959-972.

Schellart, W. P., G. S. Lister, and M. W. Jessell, 2002, Analogue modelling of asymmetrical back-arc extension: Journal of the Virtual Explorer online, v. 7, p. 25-42.

Schlager, W., 1993, Accommodation and supply - A dual control on stratigraphic sequences: Sedimentary Geology, v. 86, p. 111-136.

Searle, M.P., Windley, B.F. and Coward, M.P, 1987. The closing of Tethys and the tectonics of the Himalaya. Geological Society of America Bulletin, 98, 678–701.

Shanley, K. W., and P. J. McCabe, 1994, Perspectives on the sequence stratigraphy of continental strata: AAPG Bulletin, v. 78, p. 544-568.

Smith, P., J. I. Berg, S. Eidsvig, I. Magnus, F. Verhelst, and J. Helgesen, 2001, 4-D seismic in a complex fluvial reservoir: The Snorre feasibility study: The Leading Edge, v. 20, p. 270-276.

Sonnenfeld, M. D., 1996, Sequence evolution and hierarchy within the Lower Mississippian Madison Limestone of Wyoming, in M. W. Longman, and M. D. Sonnenfeld, eds., Paleozoic Systems of the Rocky Mountain Region, Rocky Mountain Section SEPM, place of publication, p. 165-192.

Steckler, M. S., and A. B. Watts, 1978, Subsidence of the Atlantic-type continental margin off New York: Earth and Planetary Science Letters, v. 41, p. 1-13.

Steinshouer, D. W., J. Qiang, P. J. McCabe, and R. T. Ryder, 1999, Maps showing geology, oil and gas fields, and geologic provinces of the Asia Pacific region, U. S. Geological Survey Open File Report 97-470F.

Sukmono, S., D. Santoso, A. Samodra, W. Waluyo, and S. Tjiptoharsono, 2006, Integrating seismic attributes for reservoir characterization in Melandong Field, Indonesia: The Leading Edge, v. 25, p. 532-538.

Sundermann, J., and S. Feng, 2004, Analysis and modeling of the Bohai sea ecosystem—a joint German–Chinese study: Journal of Marine Systems, v. 44, p. 127-140.

Tapponnier, R., G. Peltzer, A. Y. Le Dain, R. Armijo, and P. Cobbold, 1982, Propagating extrusion tectonics in Asia: New insights from simple experiments with plasticine: Geology, v. 10, p. 611-616.

Thorne, J. A., and D. J. P. Swift, 1991, Sedimentation on continental margins; VI, A regime model for depositional sequences, their component systems tracts, and bounding surfaces, in D. J. P. Swift, G. F. Oertel, R. W. Tillman, and J. A. Thorne, eds., Shelf Sand and Sandstone Bodies: Geometry, Facies and Sequence Stratigraphy, International Association of Sedimentologists - Special Publication 14, p. 189-255.

Tian, K., Y. Shi, R. Qin, N. J. McMillan, and P. J. Lee, 1996, Petroleum geology of the Huanghua basin, eastern China: Bulletin of Canadian Petroleum Geology, v. 44, p. 595-614.

Torres-Verdin, C., M. Victoria, G. Merletti, and J. Pendrel, 1999, Trace-based and geostatistical inversion of 3-D seismic data for thin-sand delineation: An application in San Jorge Basin, Argentina: The Leading Edge, v. 18, p. 1070-1077.

Tye, R. S., and J. M. Coleman, 1989, Evolution of Atchafalaya lacustrine deltas, south-central Louisiana: Sedimentary Geology, v. 65, p. 95-112.

Vail, P. R., R. M. Jr., R. Todd, and J. Sangree, 1977a, Seismic stratigraphy and global changes of sea level, in C. E. Payton, ed., Seismic stratigraphy - Application to hydrocarbon exploration, AAPG Memoir 26, p. 49-212.

Vail, P. R., R. M. Mitchum, Jr., and S. Thompson, III, 1977b, Seismic stratigraphy and global changes of sea level; Part 4: Global Cycles of Relative Changes of Sea Level in Payton, C.E., ed., Seismic stratgraphy; applications to hydrocarbon exploration. AAPG Memoir 26, p. 83-98.

van Gelder, A., J. H. van den Berg, G. Cheng, and C. Xue, 1994, Overbank and channel fill deposits of the modern Yellow River delta: Sedimentary Geology, v. 90, p. 293-305.

Van Horn, J., 2001, Sendji Formation reservoir delineation based on 2-D and 3-D inversion, Yombo Field, offshore Congo: The Leading Edge, v. 20, p. 435-441.

Van Wagoner, J. C., R. M. Mitchum, K. M. Campion, and V. D. Rahmanian, 1990, Siliciclastic sequence stratigraphy in well logs, cores, and outcrops: concepts for high-resolution correlation of time and facies: AAPG Methods in Exploration Series 7, 55 p.

Van Wagoner, J. C., H. W. Posamentier, R. M. Mitchum, Jr., P. R. Vail, J. F. Sarg, T. S. Loutit, and J. Hardenbol, 1988, An overview of the fundamentals of sequence stratigraphy and key definitions, in C. K. Wilgus, B. S. Hastings, C. A. Ross, H. W. Posamentier, J. Van Wagoner, and C. G. Kendall, eds., Sea-level Changes: An Integrated Approach, SEPM - Special Publication 42, place of publication, p. 39-45.

Veeken, P. C. H., and M. Da Silva, 2004, Seismic inversion methods and some of their constraints: First Break, v. 22, p. 47 - 70.

Wadsworth, J., R. Boyd, C. Diessel, and D. Leckie, 2003, Stratigraphic style of coal and non-marine strata in a high accommodation setting: Falher Member and Gates Formation (Lower Cretaceous), Western Canada: Bulletin of Canadian Petroleum Geology, v. 51, p. 275-303.

Wadsworth, J., R. Boyd, C. Diessel, D. Leckie, and B. A. Zaitlin, 2002, Stratigraphic style of coal and non-marine strata in a tectonically-influenced intermediate accommodation setting: The Mannville Group of the Western Canadian Sedimentary Basin, south-central Alberta: Bulletin of Canadian Petroleum Geology, v. 50, p. 507-541.

Walls, J. D., M. T. Taner, G. Taylor, M. Smith, M. Carr, N. Derzhi, J. Drummond, D. McGuire, S. Morris, J. Bregar, and J. Lakings, 2002, Seismic reservoir characterization of a U.S. Midcontinent fluvial system using rock physics, poststack seismic attributes, and neural networks: The Leading Edge, v. 21, p. 428-436.

Wan, T., and H. Zhu, 1996, The maximum sinistral strike-slip and formation age of the Tancheng-Lujiang fault zone: Geological Journal of Universities (Beijing, China), v. 2, p. 14-27.

Wang, G., M. Coward, W. Yuan, S. Liu, and W. Wang, 1995, Fold growth during basin inversion - Example from the East China Sea Basin, in J. Buchanan, and P. Buchanan, eds., Basin inversion: Geological Society (London) Special Publication 88, p. 493-522.

Wang, T., 1995, Oil-gas distribution regularity of the sedimentary basin to the east of Taihang Mountain, Shanxi: Journal of Geology and Mineral Resources of North China, v. 10, p. 399-414.

Wang, T., 1997, Oil and gas reservoir geology of rift basins in East China, Petroleum Industry Press, Beijing, China, 172 p.

Wang, W., Q. Jin, and Z. Ma, 1998, Meso-Cenozoic evolution of the Tanlu fault and formation of sedimentary basins: Acta Geologica Sinica, v. 72, p. 350-362.

Wang, Y., G. A. Houseman, G. Lin, F. Guo, Y. J. Wang, W. M. Fan, and X. Chang, 2005, Mesozoic lithospheric deformation in the North China block: Numerical simulation of evolution from orogenic belt to extensional basin system: Tectonophysics, v. 405, p. 47-63.

Wang, S. and L. Zhao., 1990, Offshore, in G. Zhai, ed., The petroleum geology of China, Petroleum Industry Press, Beijing, China, v.16, p. 3-260.

Watson, M. P., A. B. Hayward, D. N. Parkinson, and M. Zhang Zh, 1987a, Plate tectonic history, basin development and petroleum source rock deposition onshore China: Marine and Petroleum Geology, v. 4, p. 205-225.

Weinberg, R.F. and Dunlap, W.J., 2000. Growth and deformation of the Ladakh batholith, Northwest Himalayas: implications for timing of continental collision and origin of calc-alkaline batholiths. Journal of Geology, 108, 303–320.

WesternGeco/DCS Reservoir Services, 2004, Apache China Zhao Dong Field Inversion Project: Phase 2, internal report, 83p.

Wood, L. J., D. Pecuch, B. Schulein, and M. Helton, 2000, Seismic attribute and sequence stratigraphic integration methods for resolving reservoir geometry in San Jorge Basin, Argentina: The Leading Edge, v. 19, p. 952-962.

Wright, V. P., and S. B. Marriott, 1993, The sequence stratigraphy of fluvial depositional systems: The role of floodplain sediment storage: Sedimentary Geology, v. 86, p. 203-210.

Xu, G., Y. Wang, and H. She, 1998, The characteristics and formation of tectonic environments of the ophiolitic melange zones of the eastern Qinling-Dabieshan collision orogenic belt: Geological Survey of Finland - Special Paper, v. 26, p. 67.

Xu, J., 1993, Basic characteristics and tectonic evolution of the Tancheng-Lujiang fault zone, in J. Xu, ed., The Tancheng-Lujiang Wrench Fault System, John Wiley & Sons, United Kingdom, p. 17-50.

Xu, J., G. Zhu, W. Tong, K. Cui, and Q. Liu, 1987, Formation and evolution of the Tancheng-Lujiang wrench fault system: A major shear system to the northwest of the Pacific Ocean: Tectonophysics, v. 134, p. 273-310.

Xu, X., Q. Deng, R. Dong, C. Zhang, and W. Gao, 1992, Study on strong earthquake activity and risk areas in the Shanxi graben system: Seismology and Geology, v. 14, p. 305-316.

Xu, X., and X. Ma, 1992, Geodynamics of the Shanxi rift system, China: Tectonophysics, v. 208, p. 325-340.

Yan, Z., S. R, and Z. M, 1996, Epicentres of earthquakes 1:12,000,000, in X. Yuan, ed., Atlas of geophysics in China: Beijing, Geological Publishing House, p. 90 - 93.

Yang, M., P. Lu, X. Hua, and R. Song, 1989, Focal mechanism solutions of earthquakes, in X. Ma, G. Ding, W. Gao, H. Zhang, B. Zhang, and Z. Ma, eds., Lithospheric Dynamics Atlas of China, Beijing, China Cartographic Publishing House, p. 26.

Yang, S., C. Li, and J. Cai, 2006, Geochemical compositions of core sediments in eastern China: Implication for Late Cenozoic palaeoenvironmental changes: Palaeogeography, Palaeoclimatology, Palaeoecology, v. 229, p. 287-302.

Yang, Y., and T. Xu, 2004, Hydrocarbon habitat of the offshore Bohai Basin, China: Marine and Petroleum Geology, v. 21, p. 691-708.

Yao, Y., H. Liang, Z. Cai, X. Guan, Z. Zhao, Z. Cheng, Z. Sun, and S. Yang, 1994, Tertiary in Petroliferous Regions of China (IV): The Bohai Gulf Basin, Petroleum Industry Press, Beijing, 240 p.

Ye, H., K. M. Shedlock, S. J. Hellinger, and J. G. Sclater, 1985, The North China Basin: An example of a Cenozoic rifted intraplate basin: Tectonics, v. 4, p. 153-169.

Ye, H., B. Zhang, and F. Mao, 1987, The Cenozoic tectonic evolution of the Great North China: Two types of rifting and crustal necking in the Great North China and their tectonic implications: Tectonophysics, v. 133, p. 217-227.

Yi, S., S. Yi, D. J. Batten, H. Yun, and S.-J. Park, 2003, Cretaceous and Cenozoic non-marine deposits of the Northern South Yellow Sea Basin, offshore western Korea: palynostratigraphy and palaeoenvironments: Palaeogeography, Palaeoclimatology, Palaeoecology, v. 191, p. 15-44.

Yin, A., and S. Nie, 1993, An indentation model for the North and South China collision and the development of the Tan–Lu and Honam fault system, eastern Asia: Tectonics, v. 12, p. 801-813.

Zeng, H., 2004, Seismic geomorphology-based facies classification: The Leading Edge, v. 23, p. 644-645.

Zeng, H., T. F. Hentz, and L. J. Wood, 2001, Stratal slicing of Miocene-Pliocene sediments in Vermilion Block, 50-Tiger Shoal Area, offshore Louisiana: The Leading Edge, v. 20, p. 408-418.

Zha, Q., 1984, Jizhong Depression, China; its geologic framework, evolutionary history, and distribution of hydrocarbons: AAPG Bulletin, v. 68, p. 983-992.

Zhai, M., J. Guo, and W. Liu, 2005, Neoarchean to Paleoproterozoic continental evolution and tectonic history of the North China Craton: A review: Journal of Asian Earth Sciences, v. 24, p. 547-561.

Zhang, Q., Y. Li, and S. Mi, 1994, Two-dimensional basin modelling for the Damintun Sag: Petroleum Exploration and Development (Beijing, China), v. 21, p. 38-43.

Zhang G. C., Zhu L. and L. Shao, 2001, Pull-apart structures in Bohai Sea and petroleum exploration domain. Acta Petrolei Sinica 22, 14–18

Zhang, Y., S. Dong, and W. Shi, 2003, Cretaceous deformation history of the middle Tan-Lu fault zone in Shandong Province, eastern China: Tectonophysics, v. 363, p. 243-258.

Zhang, Y., Z. Wei, W. Xu, R. Tao, and R. Chen, 1989, The North Jiangsu-South Yellow Sea basin, in X. Zhu, ed., Chinese Sedimentary Basins: Sedimentary Basins of the World volume 1, K. Hsu (series editor), Amsterdam, Elsevier, p. 107-123.

Zhou, Z., J. Zhao, and P. Yin, 1989, Characteristics and tectonic evolution of the East China Sea, in X. Zhu, ed., Chinese Sedimentary Basins: Sedimentary Basins of the World volume 1, K. Hsu (series editor), Amsterdam, Elsevier, p. 165-179.

Zhu, G., Y. Wang, G. Liu, M. Niu, C. Xie, and C. Li, 2005, $^{40}Ar/^{39}Ar$ dating of strike-slip motion on the Tan-Lu fault zone, East China: Journal of Structural Geology, v. 27, p. 1379-1398.

Zhu, X., 1989, Remarks on the Chinese Mesozoic-Cenozoic sedimentary basins, in X. Zhu, ed., Chinese Sedimentary Basins: Sedimentary Basins of the World volume 1, K. Hsu (series editor), Amsterdam, Elsevier, p. 1-5.

Vita

Hugo Alberto Castellanos was born in Caracas, Venezuela on February 7, 1974, the son of Hugo Castellanos and Noris Gomez. After completing his work at Instituto Educacional Aragua High School in Maracay, Venezuela, he entered the Engineering Department of Universidad Central de Venezuela (UCV) in Caracas, Venezuela where he received the degree of Bachelor of Science in Geophysical Engineering in January 2000. Upon graduation, he joined the UCV-Department of Geophysical Engineering as lecturer in geophysics. In January 2001, he enrolled in The University of Texas at Austin for graduate studies (Ph.D.) in Geological Sciences. While a graduate research assistant at the Bureau of Economic Geology, he was nominated to the William S. Livingston Outstanding Graduate Employee Award in 2005. He was awarded a third place prize for his poster on the stratigraphy of the Bohai Basin in the Best Student Poster Awards Competition at the 2006 AAPG Annual Convention in Houston, Texas. He began working as a Geologist in the Exploration Technology Group of Apache Corporation in Houston, Texas, in October, 2006.

Permanent address: 2100 Bering Dr. Apt. 310
Houston, TX 77057

This dissertation was typed by the author.